PIEZOTRONICS/PIEZO-PHOTOTRONICS: DEVICES AND APPLICATIONS

A Dissertation
Presented to
The Academic Faculty

by

Ruomeng Yu

In Partial Fulfillment
of the Requirements for the Degree
Doctor of Philosophy in the
School of Materials Science and Engineering

Georgia Institute of Technology
May 2016

PIEZOTRONICS/PIEZO-PHOTOTRONICS: DEVICES AND APPLICATIONS

Approved by:

Dr. Zhong Lin Wang, Advisor
School of Materials Science and Engineering
Georgia Institute of Technology

Dr. Benjamin D.B. Klein
School of Electrical and Computer Engineering
Georgia Institute of Technology

Dr. Meilin Liu
School of Materials Science and Engineering
Georgia Institute of Technology

Dr. Oliver Brand
School of Electrical and Computer Engineering
Georgia Institute of Technology

Dr. Russell D. Dupuis
School of Electrical and Computer Engineering
Georgia Institute of Technology

Date Approved: [Feburary 12, 2016]

To my dearest family, Hongjun, Jie, Xinwei, Zhenggang and Chanyu

ACKNOWLEDGEMENTS

I would like to thank my advisor, Prof. Zhong Lin Wang, for his continuous support and kind advice through my last five years PhD studies. He provides me guidance and suggestions in both my research life and personal life. As the leader of our research group, he himself establishes a model as an outstanding and hard-working scientist for all of us to learn from. I really appreciate this opportunity to work in this world-wide famous research group. Many thanks also go to the committee members, Prof. Russell D. Dupuis, Prof. Meilin Liu, Prof. Oliver Brand and Prof. Benjamin Klein for their precious time and insightful suggestions on my doctoral research and thesis.

It is my great honor to join this research group with lots of kind and talented scholars. I received a lot of help from my friends in this group. Dr. Caofeng Pan was my first mentor in this group and he taught me everything about our research from the very beginning, trained me from a fresh PhD with no scientific research experiences to the person who I am today. I would also like to thank many group members for giving me warm care and helpful instructions in the past five year, especially during the time when I had a knee surgery, Prof. Lin Dong, Simiao Niu, Dr. Guang Zhu, Dr. Wenzhuo Wu, Dr. Youfan Hu, Dr. Wenxi Guo and many of my colleagues provided me huge help and cares. Besides, I would like to thank Xiaonan Wen, Dr. Yong Ding, Dr. Fengru Fan, Dr. Chen Xu, Prof. Zhaona Wang, Xingfu Wang, Wenbo Peng, Zhen Wen, Hengyu Guo, Long Lin, Dr. Sihong Wang, Jun Chen, Yusheng Zhou, Dr. Ying Liu, Dr. Yannan Xie, Peng Bai, Prof. Jin Yang, Prof. Ying Wu, Yuanjie Su, Dr. Ya Yang, Dr. Hulin Zhang, Prof. Jinhui Song, Prof. Sheng Xu, Prof. Yan Zhang, Dr. Yunlong Zi, Qingshen Jing, Xue Wang,

Jung-Il Hong, Sangmin Lee, Ken Pradel, Po-Kang Yang, Fang Yi, Li Zheng, Min-Hsin Yeh, Zong-Hong Lin, Gang Cheng, Tiejun Zhang, Yolande Berta, and many others, for their kind help in both my research and my personal life.

Last but not least, I would like to thank my loved ones. I am sincerely grateful to my parents, Hongjun Yu and Jie Shen, for giving me the best care in my childhood and offering me the best education opportunities throughout my college. I cannot become the person who I am today without their unconditional love. I would also express my gratefulness to my gorgeous wife, Xinwei Luo, who goes through every tough moment with me together and always gives me her strongest supports no matter what. I am blessed to spend the rest of my life with her.

TABLE OF CONTENTS

LIST OF FIGURES

SUMMARY

Piezoelectric effect has been widely used in electromechanical sensing, actuation and energy harvesting, which produces polarization charges under mechanical deformation in materials lacking inversion symmetry or with polarization domains. Conventional piezoelectric materials such as PZT and PVDF are electrically insulating and hence not feasible for constructing functional electronics or optoelectronics. The effect of mechanically-induced polarization on electronic and optoelectronic processes of charge carriers in piezoelectric materials has therefore been long overlooked. Semiconductor materials such as ZnO, GaN and CdS with wurtzite or zinc blende structures also possess piezoelectric properties but are not as extensively utilized in piezoelectric sensors and actuators as PZT due to their relatively small piezoelectric coefficients. The coupling of piezoelectric polarization with semiconductor properties in these materials has resulted in both novel fundamental phenomenon and unprecedented device applications, leading to the increasing research interests in the emerging field of piezotronics and piezo-phototronics. The basic of piezotronics and piezo-phototronics lies in the fact that strain-induced polarization charges at interface can effectively modulate the local band structure and hence the charge carrier transport across local junctions/contacts by exerting substantial influence on the concentration/distribution of free carriers and interfacial electronic charged states in the device. Fundamental physics about the piezotronics and piezo-phototronics are systematically illustrated at first in this dissertation. Functional electronic/optoelectronic devices based on piezoelectric semiconductor materials are presented to demonstrate the practical applications of the piezotronic and piezo-

phototronic effects, including nanowire/microwire transistors, nanowire logic circuits, bio/chemical sensors and photo detectors. By successfully applying the piezotronic and piezo-phototronic effects in a wide range of electronics/optoelectronics, we have shown the universality of these two effects to be utilized in various practical applications as effective approaches to modify the physical properties of charge carriers in piezoelectric semiconductors.

CHAPTER 1

INTRODUCTION

1.1 Motivation

In addition to the technology trajectory of miniaturizing components for enhanced performance as per Moore's law, which has been the dominating roadmap that drives the advancement of information technology in the last few decades, much effort has been paid on integrating individual micro/nanodevices with diversified functionalities into multi-functional micro/nano-systems and large-scale networks for structural health and environmental monitoring, personal electronics, human–machine interfacing and biomedical diagnosis/therapy.[1-6] Integration of these discrete devices with dedicated functionality toward self-powered smart systems is proposed to be one of the major roadmaps for electronics.[7-9] The miniaturized dimensions of nanomaterials and the capability of modulating their compositions/properties in well-controlled manners not only present the potential for addressing some of the critical challenges faced by silicon-based microelectronics, but also enable the technologies for developing electronics with tunable functionalities that are critical to emerging applications in consumer electronics, prosthetic devices, robotics, surgical instruments and biomedical therapy/treatments (Figure 1.1).[6, 10-15] Approaches for developing active and adaptive interactions between electronic devices and human/ambient are highly desired for realizing the above applications.

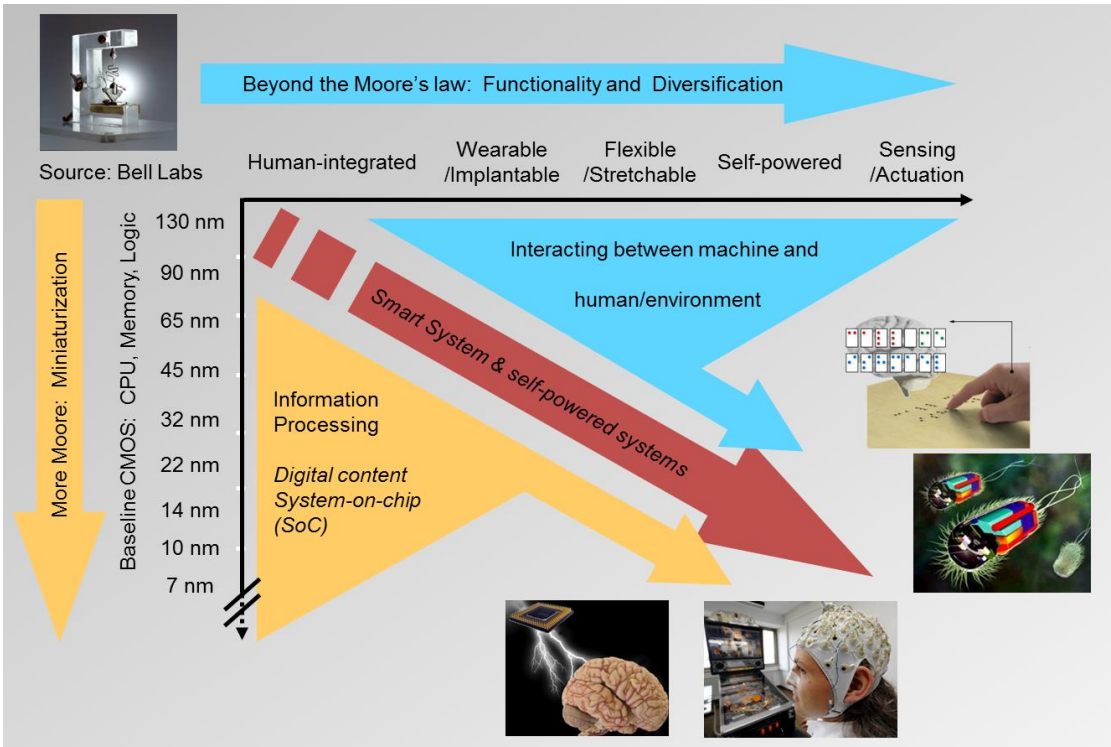

Figure 1.1 Perspective of electronics technology beyond Moore's law. The vertical axis represents the miniaturization of device dimension and the increase of integrated device density for more powerful data/signal processing. The horizontal axis represents the diversification and integration of device functionality for novel applications, such as wearable/implantable human-integrated electronics and self-powered technology for sensing and actuation. The future of electronics is an integration of more powerful data processing and more integrated functionalities.[16]

Vibration-based mechanical signals are ubiquitous in the environment and provide abundant actuation sources for potentially controlling the electronics.[16] It is, however, not facile to directly interface mechanical signals by silicon electronics without innovative designs. Traditionally, signals from strain sensitive transducers can be probed and acquired by electronic devices. These signals, however, cannot be directly utilized to control silicon electronics. One major focus in the current research of flexible electronics is to minimize/eliminate the effect of strain induced by the substrate on the operations of the electronic components, which can be termed as the passive flexible electronics. On

the other hand, the deformation introduced by the substrate can be utilized to induce electrical signals for directly controlling Si-based electronics.

Piezoelectric effect has been widely used in electromechanical sensing, actuation and energy harvesting,[17] which produces polarization charges under mechanical deformation in materials lacking inversion symmetry or with polarization domains. Conventional piezoelectric materials such as perovskite-structured $Pb(Zr_xTi_{1-x})O_3$ (PZT) and polyvinylidene fluoride (PVDF) are electrically insulating and hence not feasible for constructing functional electronics or optoelectronics. In addition, the extremely brittle nature of ceramic PZT films and the incorporation of lead impose issues, such as reliability, durability, and safety for long term sustainable operations, and hinder its applications in areas, such as biomedical devices. The effect of mechanically-induced polarization on electronic and optoelectronic processes of charge carriers in piezoelectric materials has therefore been long overlooked.

Semiconductor materials such as ZnO, GaN and CdS with wurtzite or zinc blende structure also possess piezoelectric properties but are not as extensively utilized in piezoelectric sensors and actuators due to their relatively small piezoelectric coefficients.[18] The coupling of piezoelectric polarization with semiconductor properties in these materials has resulted in both novel fundamental phenomenon and unprecedented device applications, leading to the increasing research interests in the emerging field of piezotronics and piezo-phototronics.[19-24] The core of piezotronics and piezo-phototronics lies in the fact that strain-induced polarization charges at interface can effectively modulate the local interfacial band structure and hence the charge carrier transport across junction/contact formed in piezoelectric semiconductor devices, by exerting substantial

influence on the concentration/distribution of free carriers and interfacial electronic charged states in the device.

The concept of piezotronics and piezo-phototronics is invented for implementing the active flexible electronics,[8, 9, 16] which enable the novel approaches for directly generating electronic controlling signals or enhancing electronic devices performances from mechanical stimuli. The role anticipated to be played by piezotronics is similar to mechano-sensation in physiology. The physiological foundation for the senses of touch, hearing, and balance is the conversion of mechanical stimuli into neuronal signals that are the electrical controlling signals. For instance, mechanoreceptors of the skin are responsible for touch, while tiny cells in the inner ear are responsible for hearing and balance. Furthermore, the piezo-phototronic effect is designed to effectively tune/control the charge transport across interface/junction and modulate the optoelectronic processes of charge carriers, such as generation, separation, diffusion and recombination. Therefore, it is necessary to understand the fundamental physics involved in the piezotronic and piezo-phototronic effects, and explore the practical applications of these two effects in functional electronics and optoelectronics.

1.2 Piezoelectric Property

Zinc oxide is used as the modular material system to elaborate the piezoelectric property. It is chosen not only because it is a representative piezoelectric semiconductor material, but also for its easy, low-cost and controlled synthesis at low temperature. The same principle applies to other piezoelectric semiconductors, such as GaN, CdS, CdSe and more. The absence of inversion symmetry gives rise to non-mobile piezoelectric

polarization charges at the interfaces in wurtzite-structured ZnO crystal upon mechanical straining. The effect of piezoelectric polarization can be partially screened by the moderate-level doping, but cannot be completely diminished due to the dielectric property of the material. These interfacial ionic charges are capable of inducing considerable modulation to charge carrier distribution in ZnO and the adjacent semiconductor/metal interface. [16]

1.2.1 Piezoelectric Polarization Charges

Wurtzite (ZnO) crystal has a hexagonal structure with a large anisotropic property in and perpendicular to the direction of the *c*-axis. The Zn^{2+} cations and O^{2-} anions are tetrahedrally coordinated, and the centers of charge of the positive and negatives ions overlap with each other. When applying a stress at an apex of the tetrahedron, the centers of the cations and anions charges are relatively displaced, inducing a dipole moment as shown in Figure 1.2a. A constructive addition of all the dipole moments within the crystal results in a macroscopic potential drop along the straining direction in the crystal. This is the piezoelectric potential (piezo-potential) (Figure 1.2b).[18] Piezo-potential is a strain-induced inner-crystal field, which is created by non-mobile and non-annihilative ionic charges. Therefore, piezo-polarization charges and piezo-potential exist as long as the applied strain is maintained. Piezo-potential can also drive the flow of electrons in the external load when the materials are subjected to mechanical deformation, which is the fundamental of the piezoelectric nanogenerator.[25, 26] The distribution of piezo-potential has been investigated based on two typical configurations of single nanowire (NW) devices: the transversely deflected NW and the axially strained NW (Figure 1.2b).

Transversely deflected NWs are normally utilized in energy harvesting applications,[27] while axially strained NWs are used in piezotronic applications on flexible substrates.[28] The finite conductivity possessed by the material can partially screen the piezo-polarization charges accordingly, but cannot completely diminish them due to the dielectric property of the material and the moderate doping level. Recently, theoretical study has also revealed that a strong piezoelectric field may be induced inside the NW heterostructures due to lattice mismatch, which may introduce significant effects on the charge-carrier transport and confinement.[29, 30]

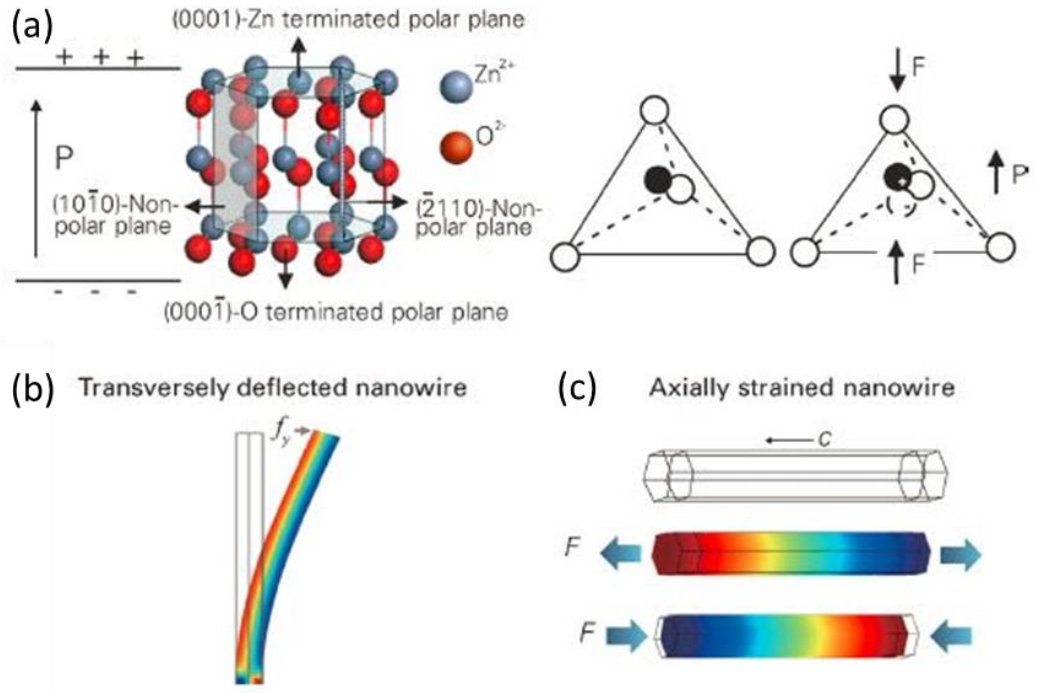

Figure 1.2 Piezo-potential in a wurtzite crystal. (a) Atomic model of the wurtzite-structured ZnO.[16] (b) Piezo-potential distribution along a transversely deflected ZnO NW calculated by numerical methods.[31] (c) Piezo-potential distribution along a ZnO NW under axial strain calculated by numerical methods.[32] The color gradient represents the distribution of piezo-potential in which red indicates positive piezo-potential and blue indicates negative piezo-potential. The growth direction of the NW is along the *c*-axis.

1.2.2 Piezoelectric Potential in Transversely Deflected NWs

The relationship between the piezo-potential distribution in a laterally bent NW and the dimensionality of the NW as well as the magnitude of the applied force at the tip has been derived analytically by applying the perturbation expansion of the linear equations,[31] which shows that the electric potential (in cylindrical coordinates) is independent of vertical height except for the regions very close to the fixed end of the NW. Moreover, the analytical solution also suggests that the electrostatic potential is directly related to the aspect ratio of the NW instead of its absolute dimensionality. For an NW with a fixed aspect ratio, the induced piezo-potential is proportional to the maximum deflection at the NW tip. The schematic illustration of the piezo-potential distribution in transversely deflected NWs is shown in Figure 1.2b. The validity of the derived analytical equation for the piezo-potential distribution in a transversely deflected NW has also been verified by comparing the analytical solutions and finite element method (FEM) calculation for a fully coupled electromechanical system,[31] showing that the difference between the results derived from the analytical equation and those from full numerical calculation is only 6%. The response in electrical transport and photoconduction behaviors of the transversely bent ZnO NW due to piezoelectric polarization has also been experimentally studied by in situ transmission electron microscopy.[33]

1.2.3 Piezoelectric Potential in Axially Strained NWs

Another commonly encountered configuration for the ZnO-NW-based nanoelectronic device incorporates the horizontally placed NW, with its two ends and adjacent regions fully covered by metal electrodes on the substrate (normally flexible

material). The dimension of NWs is orders of magnitude smaller than that of the supporting substrates, so that the mechanical behavior of the entire device is dictated by the substrate. In reality, various kinds of forces, including tensile, compression, twisting, and combinations of them, might act on the NW during operations.[32] The distribution of piezo-potential throughout the NW under these forces can be obtained by the FEM.[32] For simplicity and concentrating on how the piezo-potential would vary under different strains, it is assumed that there is no body force and no free-charge carriers in the NW. It can be seen from Figure 1.2c that piezo-potential continuously drops from one side of the NW to the other upon straining, indicating that electron energy also continuously increases from one end of the NW to the other. Meanwhile, the Fermi level remains flat all over the NW at equilibrium. Consequently, the electron energy barrier between ZnO and metal electrodes will be raised at one side and lowered at the other side, which should lead to experimentally observable asymmetric *I*–*V* characteristics for the NW device. This is the governing principle of piezotronics and piezo-phototronics.[16]

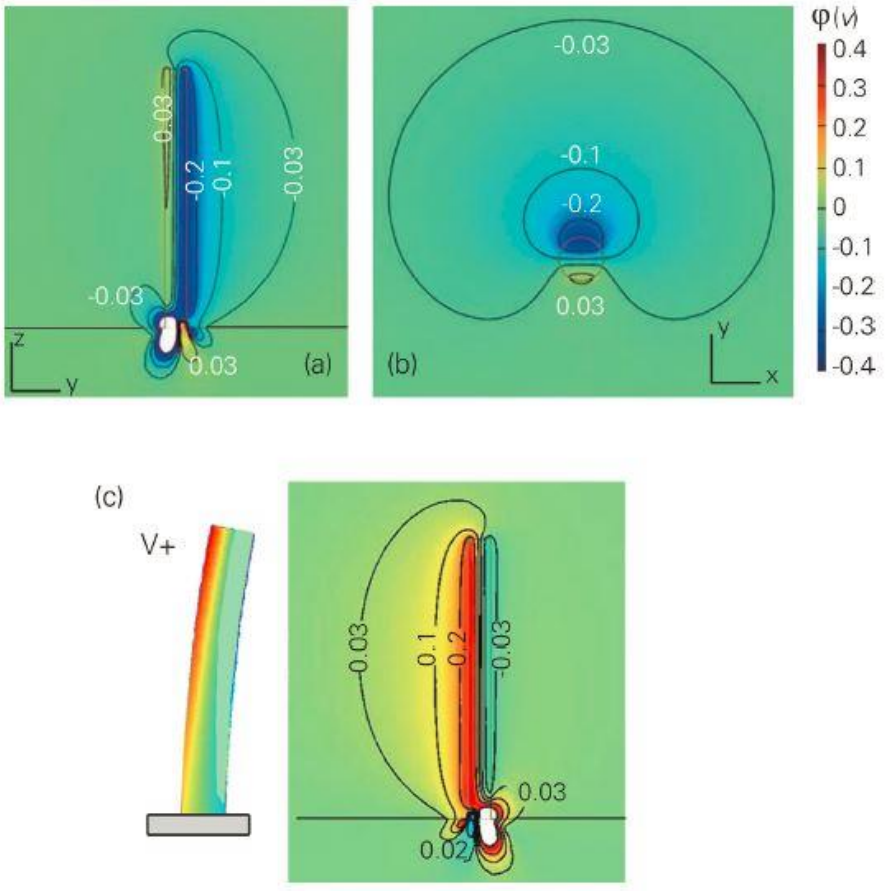

Figure 1.3 (a,b) Numerical calculation results of the piezo-potential distribution in an n-type ZnO NW considering finite doping with a donor concentration of 1×10^{17} cm^{-3}.[34] (c) Numerical calculation results of the piezo-potential distribution when the acceptor concentration in the ZnO NW is 1×10^{17} cm^{-3}.[35]

1.2.4 Piezoelectric Potential in Doped Semiconductor NWs

It is also important to point out that the above results are all based on an assumption that there are no free-charge carriers in materials.[32] The as-synthesized ZnO nanostructures are, however, intrinsically n-type with a typical donor concentration of 1×10^{17} cm^{-3}.[36] Taking the statistical electron distribution into account, the distribution of piezo-potential in a bent ZnO NW with moderate charge-carrier density can be calculated, showing that free electrons tend to accumulate at the positive piezo-potential side of the NW at thermal equilibrium.[34] Therefore, the effect of negatively charged carriers partially,

if not all, screens the positive piezo-potential, while no change to the negative piezo-potential can be observed. Figures 1.3a and 1.3b show the calculated piezo-potential when the donor concentration in the ZnO NW is 1×10^{17} cm^{-3}, which clearly presents the screening effect of finite donor concentration on the distribution of piezo-potential.[34] This is also consistent with the experimental observation that only negative pulses can be observed in an atomic force microscopy (AFM)-based nanogenerator experiment using n-type ZnO NWs, and the output negative potential peak appears only when the AFM tip touches the compressed side of the NW.[27] For even smaller systems, strong confinement effect requires quantum-mechanical considerations due to discrete bound states in the materials. In such a case, an elaboration of theory similar to two dimensional electron gas (2DEG) in GaN/AlGaN high-electron-mobility transistors (HEMTs) is necessary for investigating the effect of piezo-potential.[37] In addition to the n-type doping normally observed for as-synthesized ZnO NWs, it is also possible to receive stable p-type ZnO NWs.[35, 38-40] The stability of p-type doping in ZnO NWs is possible due to the dislocation-free volume and the presence of a high concentration of vacancies near the surface of the NWs.[41] The distribution of piezo-potential in a bent p-type ZnO NW has also been theoretically investigated. Figure 1.3c shows the calculated piezo-potential when the acceptor concentration in the ZnO NW is 1×10^{17} cm^{-3}.[35] With finite p-type doping, the holes tend to accumulate at the negative piezo-potential side. The negative side of piezo-potential is thus partially screened by holes, while the positive side of it is preserved.

1.3 Thesis Scope

In my doctoral research, I was dedicated to investigating the fundamental physics of the piezotronic and piezo-phototronic effects by understanding the piezoelectric polarization charges modified energy band profiles and charge carrier transport processes both theoretically and experimentally. Upon straining, piezoelectric polarizations are induced within semiconductor materials with non-central symmetric crystal structures. Such polarizations present at the vicinity of local interface of metal-semiconductor contact or p-n heterojunctions. The energy band profiles near local contacts are thus modified by the piezo-charges, leading to the tuning/controlling effect on the charge carriers' transport across the energy barriers at local interface. This is the piezotronic effect. Similarly, the piezo-phototronic effect is about utilizing strain-induced piezoelectric polarizations to modulate the optoelectronic processes of charge carriers, such as generation, separation, diffusion and recombination, by modifying the energy band structures at local contacts. Following the fundamental working principles of these two effects, several applications have been demonstrated to investigate the piezotronic and piezo-phototronic effects on a wide range of electronic and optoelectronic devices. Based on the piezoelectric semiconductors, such ZnO, GaN and CdS, the piezotronic and piezo-phototronic effects have been applied to nanowire/microwire transistors, nanowire logic circuits, bio/chemical sensors and photo detectors.

In this thesis, the major goal is to provide in-depth understanding about the fundamental physics as well as the practical applications of the piezotronic and piezo-phototronic effects from both theoretical and experimental points of view. Numerical calculations are conducted to simulate the modifications of energy band by the

piezoelectric polarizations under mechanical strains. Temperature dependence of the piezotronic and piezo-phototronic effects is also studied to derive insights about the charge carriers' transport process at various ambient temperatures. Experimental results of applying the piezotronic and piezo-phototronic effects to tune/control the general performances of various electronic and optoelectronic devices are presented to indicate the universality of these two effects as effective approaches to modify the physical properties of charge carriers in piezoelectric semiconductors.

CHAPTER 2

PIEZOTRONICS

2.1 Basics of Piezotronics

When applying a strain along the *c*-axis of ZnO NW, due to the coupling of piezoelectric and semiconducting properties, piezoelectric polarization charges created at the two ends of the NW induce the piezo-potential. This potential is capable of modulating characteristics of the contact formed between the NW and the electrodes by modifying the local Schottky barrier height (SBH).[18] Consequently, the transport of charge carriers in the device can be tuned by the externally applied strain. This is the piezotronic effect.[16, 18, 42] Electronics fabricated by using the inner-crystal piezo-potential as a 'gate' voltage to modulate the charge transport across a metal-semiconductor (M-S) interface is piezotronics, which is different from the basic design of a complementary metal-oxide-semiconductor (CMOS) field effect transistor (FET) and may enable potential applications in force/pressure-triggered/controlled electronic devices, sensors, biomedical diagnosis/therapy, human-computer interfacing, and prosthetics.

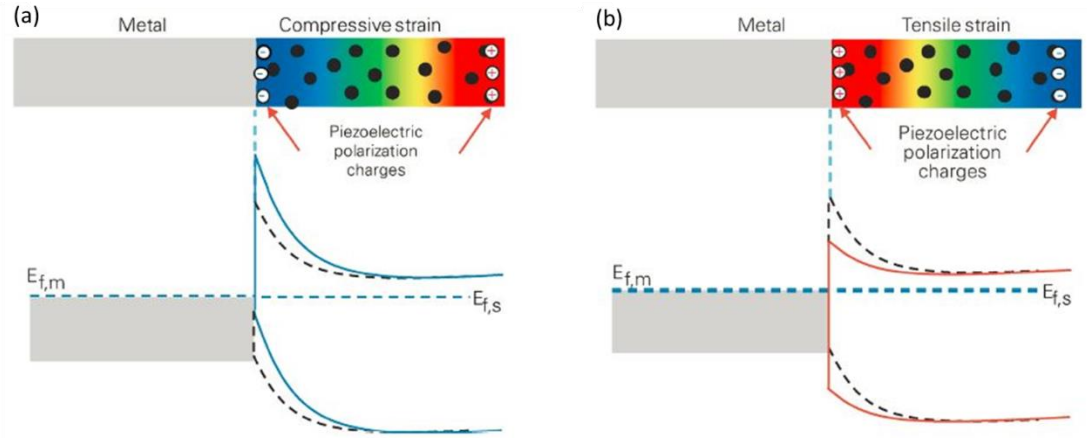

Figure 2.1 Schematic of energy diagram illustrating the effect of piezo-potential on M-S contact. (a) With compressive strain applied, the negative piezoelectric polarization ionic charges induced near the interface (symbols with '–') increases the local SBH. (b) With tensile strain applied, the positive piezoelectric polarization ionic charges induced near the interface (symbols with '+') decreases the local SBH. The color gradients indicate the distribution of piezo-potential, with red representing positive piezo-potential and blue representing negative piezo-potential. The band diagrams for the M-S contact with and without the presence of piezotronic effect are shown using the solid and black dashed curves, respectively. The black dots represent the free-charge carriers in the bulk semiconductor.[43]

2.1.1 Piezoelectric Polarization on Metal-Semiconductor Contact

The M-S contact is a fundamental structure of semiconductor electronics and optoelectronic.[44] When a metal and a semiconductor come into contact forming an M-S interface, a significant redistribution of charge takes place due to the overlap of wave functions from both the metal and the semiconductor.[45, 46] When the system reaches thermal equilibrium, Fermi levels on either side of the interface must be aligned, and thus a net charge transfer will occur at the interface. If the electron affinity of the semiconductor $e\chi$ (relative to free-electron energy or vacuum level E_0) is appreciably smaller than the work function of the metal $e\Phi_m$, then electrons flow into the metal from the semiconductor with the depletion region formed in the semiconductor near the interface. This leads to the deformation of energy bands in the semiconductor close to the M-S interface and consequently the formation of an abrupt discontinuity or an energy barrier at the interface, which is the Schottky barrier with a barrier height of $e\Phi_{Bn}$. Ideally, the intrinsic SBH can be determined by $e\Phi_{Bn} = e(\Phi_m - \chi)$ (for the n-type semiconductor). The SBH is a measure of the mismatch of energy levels for majority carriers across the M-S interface, which dictates the transport of charge carriers across the M-S interface and is of vital importance for the operation of a related semiconductor device. Current can only pass through the barrier if the externally applied positive bias on the metal is larger

than a certain threshold value Φ_i (for the n-type semiconductor). If the semiconductor material also possesses piezoelectric property, once the strain is induced in the semiconductor, the negative piezoelectric polarization charges and thus the negative piezo-potential induced at the semiconductor side can repel the electrons away from the interface, resulting in a further depleted interface and an increased local SBH (Figure 2.1a); on the other end, if the polarity of the induced strain is reversed, the positive piezoelectric polarization charges and the positive piezo-potential created at the semiconductor side near the interface can attract the electrons toward the interface, resulting in a less depleted interface and hence a decreased local SBH (Figure 2.1b).[18, 43] It is well known that the transport of charge carriers across the Schottky barrier is sensitively dictated by the SBH.[46] It can therefore be seen that piezo-potential is able to effectively modulate the local contact characteristics depending on the crystallographic orientation of the piezoelectric semiconductor material and the polarity of the applied strain.[18] Consequently, the transport of charge carriers across the M-S contact can be effectively modulated by the piezoelectric polarization charges, or more specifically, the local contact characteristics can be tuned and controlled by varying the magnitude and polarity of externally applied strains. The modulation and gating of charge transport across the interface by the strain-induced piezo-potential are the core of piezotronics.[18]

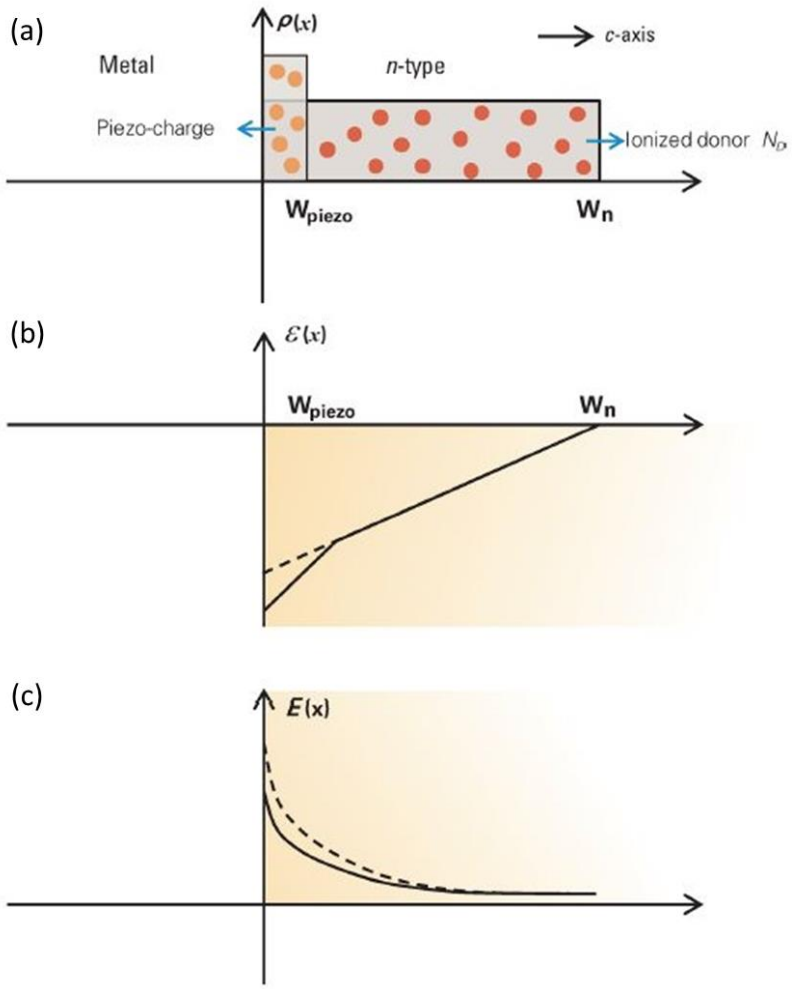

Figure 2.2 (a) Space charge distribution; (b) electric field, and (c) energy-band diagram for ideal metal-semiconductor Schottky contacts with the presence of piezoelectric polarization charges at the applied voltage V = 0 (thermal equilibrium). The dashed lines indicate the electric field and energy band with the absence of piezoelectric charges.[47]

2.1.2 Fundamentals of Piezotronics

By ignoring surface states and other anomalies, space charge distribution, electric field, and energy-band diagram in the M-S contact with the presence of piezoelectric polarization charges at the zero applied voltage (thermal equilibrium) are shown in Figure 2.2, in which W_n is the width of the region where ionized donors are distributed in the n-type semiconductor (ZnO here). When the strain is introduced in the semiconductor, the

induced polarization charges at the interface not only change the height of the Schottky barrier, but also the width of the depletion region. The carrier transport in the M-S contact is dominated by the majority carriers according to the diffusion theory for the Schottky barrier, and the current under the forward bias can be expressed as[48]

$$J_n \approx J_D \cdot [\exp(qV / kT) - 1],$$

Where

$$J_D \approx q^2 D_n N_C \cdot (kT)^{-1} \cdot \sqrt{[2qN_D(\Psi_{bi} - V) \cdot \varepsilon_s^{-1}]} \cdot \exp[-q\Phi_{Bn} \cdot (kT)^{-1}]$$

is the saturation current density. Here ε_s is the permittivity of the semiconductor material, D_n is the diffusion coefficient for electrons, N_C is the effective density of states in the conduction band, and N_D is the donor concentration in the semiconductor. The saturation current density with the absence of the piezoelectric polarization charge is

$$J_{D0} \approx q^2 D_n N_C \cdot (kT)^{-1} \cdot \sqrt{[2qN_D(\Psi_{bi0} - V) \cdot \varepsilon_s^{-1}]} \cdot \exp[-q\Phi_{Bn0} \cdot (kT)^{-1}],$$

where Ψ_{bi0} and Φ_{Bn0} are the built-in potential and SBH, respectively, with the absence of piezoelectric polarization charges. The effect of the piezoelectric charge can be considered as perturbation to the conduction-band edge.[47] The change in the effective SBH induced by piezoelectric polarization charges is then derived as

$$\Phi_{Bn} = \Phi_{Bn0} - q^2 \rho_{piezo} W_{piezo}^2 (2\varepsilon_s)^{-1},$$

where piezoelectric polarization charges are distributed in the region with a width of W_{piezo} near the barrier interface. In conventional piezoelectric theory, since the region within which the piezoelectric polarization charges are distributed is much smaller than the volume of the bulk crystal, it is reasonable to assume that piezoelectric polarization

charges are distributed at the surface region with the zero thickness of the bulk piezoelectric material. Such an assumption, however, does not hold true for NW devices. The current density across the Schottky barrier formed between the metal and strained n-type piezoelectric semiconductor can hence be rewritten as

$$J_n = J_{D0} \cdot \exp[q^2 \rho_{piezo} W_{piezo}^2 (2kT\varepsilon_s)^{-1}] \cdot \exp[qV \cdot (kT)^{-1} - 1].$$

A more specific expression can be obtained to reflect the effect of piezo-potential on M-S contact. If the induced strain is s_{33} along the *c*-axis of the ZnO NW, the piezoelectric polarization can then be obtained from

$$P_z = e_{33} s_{33} = q \rho_{piezo} W_{piezo},$$

where ρ_{piezo} represents the density of created piezoelectric polarization charges (in units of electron charge). The current density across the Schottky barrier is now expressed as

$$J \approx J_{D0} \cdot \exp[q e_{33} s_{33} W_{piezo} (2kT\varepsilon_s)^{-1}] \cdot \exp[qV \cdot (kT)^{-1} - 1].$$

It can be clearly seen that the current transported across the M-S interface is directly related to not only the magnitude, but also to the polarity of the induced strain. When positive piezoelectric polarization charges (positive ρ_{piezo}) due to tensile strain (positive s_{33}) are introduced locally to the Schottky barrier at work, the current transported across the barrier increases. A similar conclusion can also be achieved when the polarity of the induced strain is switched to compressive type. This is the fundamental mechanism of piezotronic devices, such as strain-gated transistors (SGTs).[21]

2.2 Devices and Applications

In this section, several applications of the piezotronic effect are presented following the theoretical understanding about the fundamentals illustrated in section 2.1.

By applying mechanical strains to various piezoelectric semiconductor based electronic devices, the piezotronic effect has been utilized to modify the transport properties of GaN nanobelts[49, 50], AlGaN/AlN/GaN heterostructures, logic devices,[51] bio/chemical sensors[52-54] and environmental sensors[55, 56]. The temperature dependence of the piezotronic effect[57] has also been investigated to better understand its working mechanism at low ambient temperatures. These results indicate that the piezotronic effect is a universal effect in various electronic devices fabricated by piezoelectric semiconductors.

2.2.1 Piezotronic Effect on Transport Properties of Semiconductors

Based on the investigations of the fundamental physics about the piezotronics, it is clear that one of the most straightforward applications of this effect is to tune/control the electric transport properties of nano/microwire transistors based on piezoelectric semiconductors. In this section, the piezotronic effect on the transport properties of *c*-axis GaN nanobelts,[49] *a*-axis GaN nanobelt[50] and AlGaN/AlN/GaN heterostructures are systematically studied as follows.

2.2.1.1 *c*-Axis GaN Nanobelts[49]

Due to the polarization of ions in a wurtzite structured crystal that has non-central symmetry such as GaN, a piezo-potential is created by applying a stress. Here we studied the piezotronic effect on the transport property of *c*-axis GaN nanobelts (NBs). The *I*-*V* characteristics of the *c*-axis oriented GaN NB are tuned when a compressive/tensile strain is applied on the NB due to the change in Schottky barrier height at the local contact. The

configurations of attaching the NB on flexible substrate are found to play a very important role in dictating the *I-V* characteristics.

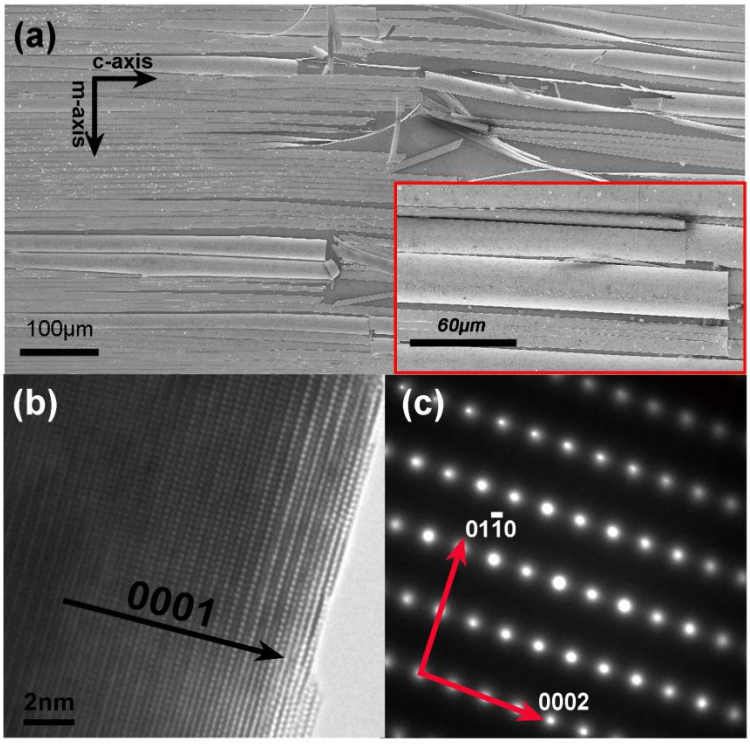

Figure 2.3 (a) SEM image of a GaN NBs. The inset is a high magnification SEM image, showing details of the GaN belt. (b) HRTEM image of a GaN NB, indicating that the GaN belt is single crystal and grown along *c*-axis. (c) Corresponding select area electron diffraction (SAD) pattern of the same GaN NB in (b).[49]

GaN NBs were fabricated *via* the method called strain-controlled cracking of thin solid films.[58] Figure 2.3a shows typical SEM images of as-fabricated GaN NBs, which can be seen clearly that the NBs are well separated, straight and parallel with each other, with lengths of several hundred microns and widths of 10 μm, the inset of Figure 2.3a is a high magnification SEM image, showing morphological details of the n-type GaN belts. A high resolution transmission electron microscopy (HRTEM) image and the corresponding select area electron diffraction (SAED) patterns taken from the end of a GaN NB are presented in Figures 2.3b and 2.3c, indicating that the GaN belt is a single

crystal with length direction of *c*-axis, surface normal plane of (-2110) and side surfaces (01-10).

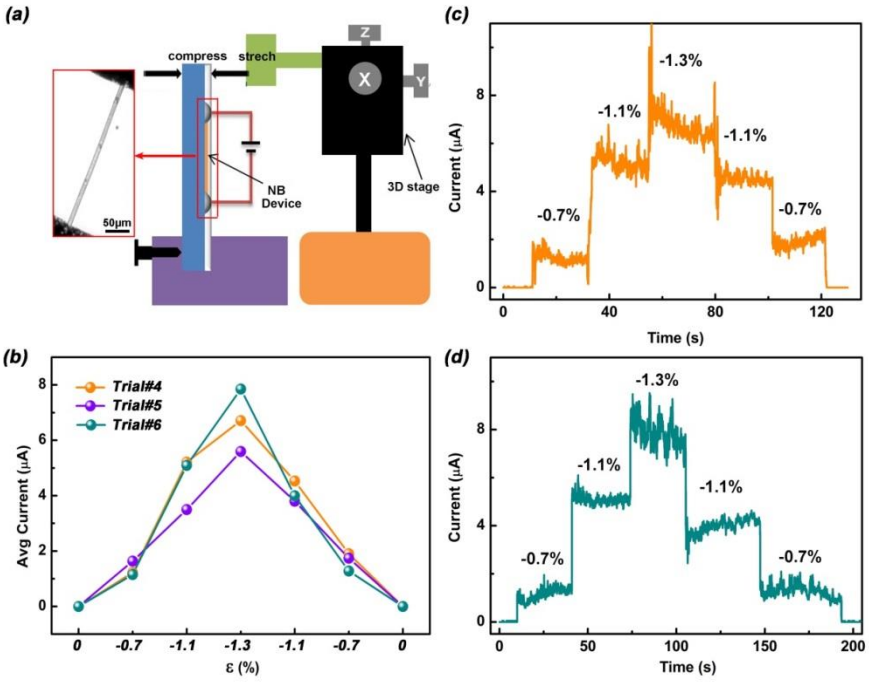

Figure 2.4 Reproducibility on the current response of the GaN NB device under different compressive strains. (a) Schematic of the measurement set-ups for studying the piezotronic effect in GaN NB, the inset is an optical image of a typical GaN NB device. (b) Plots of the average current responses *vs*. the applied strain. The data was extracted from (c-d), showing a good reproducibility of the GaN NB device. All of the data in (b-d) are obtained from the same device. (c-d) Current response of a GaN NB device under different compressive strains when the bias voltage was fixed at 3 V. The compressive strain applied on the device increased step by step from -0.7%, -1.1% to -1.3% and then fell back to -0.7%. The corresponding current of the GaN NB device increased first step by step as well, and then decreased, with a peak value at a strain of -1.3%.[49]

The device was fabricated by transferring and bonding an individual GaN NB laterally on the polystyrene (PS) substrate, with its *c*-axis in the plane of the substrate pointing to the source. Silver paste was used to fix the two ends of the NB, serving as source and drain electrodes, respectively. For such Ag-GaN NB-Ag device, it could be treated as a metal-semiconductor-metal (M-S-M) structure. A thin layer of polydimethylsiloxane (PDMS) was used to package the device. This PDMS thin layer

can not only enhance the adhesion of the silver paste to the PS substrate, but also prevent the GaN NB from contamination or corrosion by gases or liquid. Finally, a flexible, optically transparent, and well-packaged piezotronic device was fabricated. The schematic of the measurement set-up for studying the piezotronic effect on GaN NB device is presented in Figure 2.4a. One end of the PS substrate was fixed tightly on a sample holder, with the other end free to be bent. A three-dimensional (3D) mechanical stage with movement resolution of 1 μm was used to apply the strain on the free end of the PS substrate. A typical optical image of the as-fabricated GaN NB device is presented in Figure 2.4a.

I-t characteristics of the devices at different strains were recorded to investigate the piezotronic effect on GaN NB devices when compressive strains were applied to and released from the GaN NB device with the bias voltage being fixed at 3 V. The compressive strain applied to the device was increased step by step from -0.7%, -1.1% to -1.3% and then decreased step by step back to -0.7%. The corresponding current of the GaN NB device increased step by step as well first from 1.4 μA to 7.8 μA, and then fell back to 1.4 μA, with a peak value at the strain of -1.3%. Five more repeated tests were carried out on the same device to show the reproducibility and stability of the device. Due to the space limitation, only two of six results are presented in Figures 2.4c and 2.4d. The current reached almost the same value under the same strains in the two tests, and the current can fully recover when the strain was released. The average currents of the device under different strains at a bias of 3 V were extracted from three trials and plotted in Figure 2.4b, showing a good reproducibility and stability of the GaN NB device.

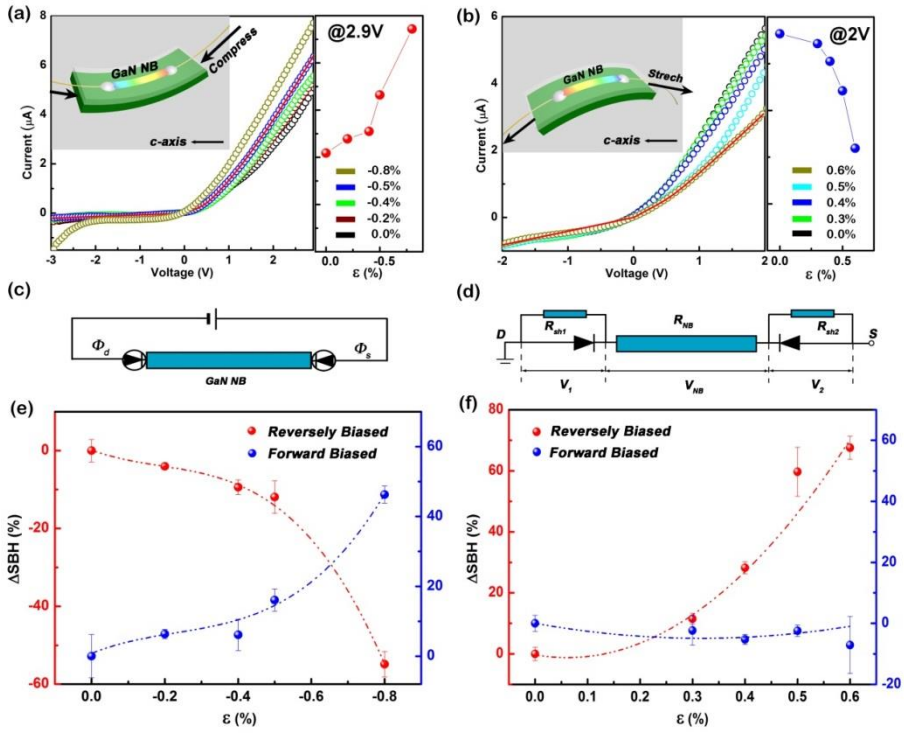

Figure 2.5 *I-V* curves of the GaN NB devices when they are compressed (a) or stretched (b) to different degrees of strain, with the *c*-axis of GaN NB parallel to the longitudinal axis of the PS substrate. The colorful lines are experimental data while the red lines are theoretical fitting. The plots of current *vs.* strain at a fixed bias are presented as well. The current increased with increasing the strain (a), noted as SU; decreased with increasing the strain (b), noted as SD. The insets are corresponding schematic diagrams of configurations of GaN NB devices under different strains. (c) Schematic of proposed sandwich model of MSM structure and (d) its equivalent circuit. (e-f) Relative changes of the forward and reversely biased Schottky barrier height (ΔSBH) *vs.* the applied strain. The ΔSBH data was extracted from the theoretical simulations corresponding to (a) SU, (b) SD.[49]

The piezotronic effect on GaN NBs is investigated and summarized in Figures 2.5a and 2.5b, showing obvious asymmetric *I-V* characteristics. The insets are corresponding schematic diagrams of configurations of GaN NB devices under different strains. The current value at a fixed bias under different strains was extracted from Figures 2.5a and 2.5b, plotted at most right side correspondingly, which shows clearly that compressive strain leads to a monotonous increasing current (Figure 2.5a) and tensile strain leads to a decreasing current (Figure 2.5b). These *I-V* characteristics clearly

demonstrate that there were Schottky barriers presenting at the two GaN/Ag contacts but with distinctly different barrier heights.[59-61] These Schottky barriers at the metal/semiconductor interfaces play a crucial role in determining the electrical transport property of the M-S-M structure. It is important to quantitatively fit the *I-V* curve in order to determine the nature of the electric transport across the M-S-M structure.[59, 60] The fitting of the *I-V* characteristics of the GaN NB under different strains was carried out using a GUI program PKUMSM developed by Peng *et al*[62], which worked under the theoretical model as described in follows:

When the device is supplied with a bias V over the two electrodes, the voltage V is distributed on the Schottky barriers and the unexhausted part of the GaN NB, denoted here by V_1, V_2, V_{NB} respectively, i.e.,

$$V = V_1 + V_2 + V_{NB} \tag{2.1}$$

The current–voltage relationships of the three components, i.e., the reverse biased Schokkty barrier (I_1–V_1), the NB (I_{NB}–V_{NB}) and the forward biased Schottky barrier (I_2–V_2) are given by

$$I_1 = S_1 J_r(V_1) + V_1 / R_{sh1} \tag{2.2}$$

$$I_2 = S_2 J_f(V_2) + V_2 / R_{sh2} \tag{2.3}$$

$$I_{NB} = V_{NB} / R_{NB} \tag{2.4}$$

where R_{sh1} and R_{sh2} are the shunt resistances associated with the two Schottky barriers, S_1 and S_2 are corresponding contact areas of the two metal-semiconductor junctions respectively. $J_r(V_1)$ is the current density passing through the reverse biased Schottky

barrier, and $J_f(V_2)$ is that through the forward biased Schottky barrier. For moderate bias, V is larger than $3kT/q$, i.e., 75 mV at room temperature, these current densities are given by

$$J_r(V_1) = \frac{A^*T\sqrt{\pi E_{00}}}{k}\left\{q(V_1-\xi)+\frac{q\phi_1}{\cosh^2(E_{00}/kT)}\right\}^{1/2}\times\exp(-\frac{q\phi_1}{E_0})\exp\left[qV_1(\frac{1}{kT}-\frac{1}{E_0})\right] \quad (2.5)$$

and

$$J_f(V_2) = A^*T^2\exp(-\frac{q\phi_2}{kT})\times\exp(\frac{qV_2}{nkT})\left[1-\exp(-\frac{qV_2}{kT})\right] \quad (2.6)$$

in which ϕ_1 and ϕ_2 are the effective height of the two Schottky barriers respectively, n is an ideality factor describing the deviation of the Schottky barrier (for an ideal barrier n =1), ξ is the distance between the Fermi level to the bottom of the conduction band for n-type NBs or to the top of the valence band for p-type NBs, T is temperature, $A^* = 4\pi m^* qk^2/h^3$ is the Richardson constant of the GaN NB, m^* is the effective mass of major carrier, q is the magnitude of electron charge and k is the Boltzmann constant. It should be noted that the Schottky barrier is not a constant during measurement. This quantity depends on the applied bias, and may be affected by such effects as the image force etc., and all these effects have been included in the present model by regarding be an effective barrier. The two important constants are given by

$$E_0 = E_{00}\coth(\frac{E_{00}}{kT}) \quad (2.7)$$

and

$$E_{00} = \frac{\hbar q}{2}\left[\frac{N_d}{m^*\varepsilon_s\varepsilon_0}\right]^{1/2} \quad (2.8)$$

where N_d is the doping concentration, ε_s is the relative permittivity of the semiconducting NB and ε_0 is the permittivity of free space.

The current flowing through each part of the M-S-M structure is the same for a steady current so that

$$I_1 = I_2 = I_{NB} \tag{2.9}$$

We may rearrange the above equations into a set of two equations

$$S_1 J_r(V_1) + V_1 / R_{sh1} = (V - V_1 - V_2) / R_{NS}$$

$$S_2 J_f(V_2) + V_2 / R_{sh2} = (V - V_1 - V_2) / R_{NS} \tag{2.10}$$

Once solving this set of equations for any given bias V, we can obtain the voltage distributions V_1, V_{NB} and V_2, the current density I passing through the M-S-M system and all the related parameters including ϕ_1 and ϕ_2 by fitting the experimental data.

Our device is considered as a single GaN NB sandwiched between two opposite Schottky barriers,[19] and an equivalent circuit is shown in Figures 2.5c and 2.5d. The fitting results were plotted as red lines in Figures 2.5a and 2.5b, together with the experimental data. It is clear that the fitting curves agree well with the experimental *I*-*V* curves in each case. Furthermore, the relative change of forward and reversely biased Schottky barrier heights (ΔSBH) of each device, corresponding to Figures 2.5a and 2.5b, are obtained and presented in Figures 2.5e and 2.5f. Apparently, the trends of forward biased SBH and reversely biased SBH are opposite to each other, which means that the change in barrier height was caused by the piezoelectric polarization charges at the two ends of the NB. It has been reported that the SBHs of GaN Schottky barrier[63] shift under

strain are attributed to a combination of band structure and piezoelectric effect.[63-65] The piezotronic effect is a polarized effect using the piezopotential as a "gate" voltage to tune/control charge carrier transport at a contact or junction within the GaN NB;[20, 66] while the piezoresistive effect and parasitic capacitance effect are both non-polar effects on the electric transport,[67] therefore, the electromechanical behaviors of our GaN NB devices were dominated by the piezotronic effect.

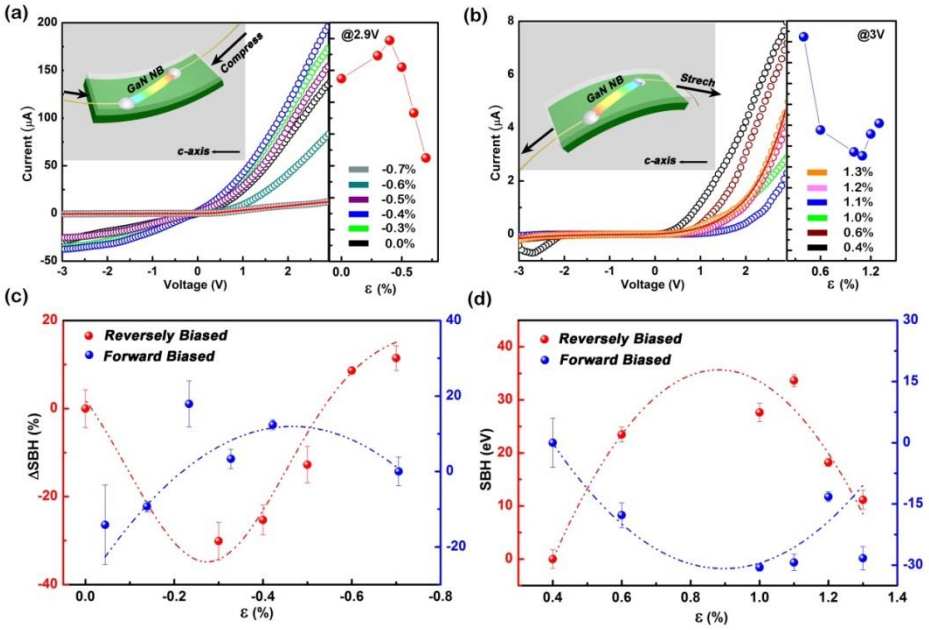

Figure 2.6 *I-V* curves of the GaN NB devices when they are compressed (a) or stretched (b) to different degrees of strain, with the *c*-axis of GaN NB off the longitudinal axis of the PS substrate. The colorful lines are experimental data while the red lines are theoretical fitting. The plots of current *vs.* strain at fixed bias are presented as well. The current increased first with increasing the strain, then decreased (a), noted as U&D; decreased first then increased (b), noted as D&U. The insets are corresponding schematic diagrams of configurations of GaN NB devices under different strains. (c-d) Relative changes of the forward and reversely biased Schottky barrier height (ΔSBH) *vs.* the applied strain. The ΔSBH data was extracted from the theoretical simulations corresponding to (a) U&D, (b) D&U.[49]

We found that the configurations of how the NBs being placed on the substrate plays a very important role in the shape of the *I-V* characteristics. For a device with the *c*-axis of GaN NB parallel to the longitudinal axis of the substrate, monotonous increasing

(Figure 2.5a, noted as SU) and decreasing (Figure 2.5b, noted as SD) *I-V* curves were derived when it was subjected to a compressive or tensile strain, respectively. For a device with the *c*-axis of the GaN NB slightly off aligning with the longitudinal axis of the substrate, more complicated *I-V* characteristics were derived when it was subjected to a strain, as shown in Figures 2.6a and 2.6b. Under an increasing compressive strain, the current increased first and then decreased (Figure 2.6a, noted as U&D); under an increasing tensile strain, the current decreased first and then increased (Figure 2.6b, noted as D&U). Current value at fixed bias was extracted from Figures 2.6a and 2.6b, plotted at most right side correspondingly, to give a clearer view on how it performed under different strains. Furthermore, the fitting results were presented as red lines in Figures 2.6a and 2.6b, which coincide with the experimental data very well. The corresponding plots of relative change of SBH *vs.* strains before and after applying strains are presented in Figures 2.6c and 2.6d. In each case, the reversely biased SBH and forward biased SBH were changing in opposite trends as a function of strain, which once again confirms the domination of piezotronic effect to the electromechanical behaviors of these GaN NB devices.

To make sure the configurations of how NBs being placed on the substrate can lead to different *I-V* curves (i.e. for device with *c*-axis of GaN NB parallel to the longitudinal axis of PS substrate, *I-V* curves of SU and SD types were received; for device with *c*-axis of GaN NB slightly off aligning with the longitudinal axis of PS substrate, *I-V* curves of U&D and D&U types were received), further investigation were carried out. The *I-V* curves of 24 devices were studied and classified into four types: SU (Figure 2.5a); SD (Figure 2.5b); U&D (Figure 2.6a); D&U (Figure 2.6b). Among the 24

devices we have studied, 5 of them were tensile strained, among which 2 are of SD type, 2 are of D&U type, 1 is SU type; 19 of the 24 devices were compressively strained, among which 3 are of SD type, 2 are of D&U type, 9 are of SU type, and 5 are U&D type.

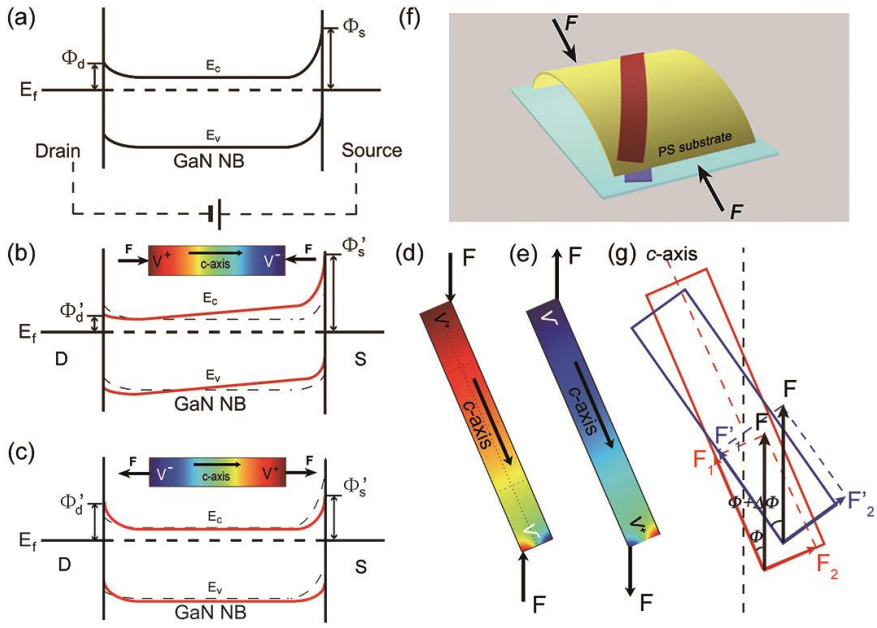

Figure 2.7 Schematic energy band diagrams illustrating the asymmetric Schottky barriers at the source and drain contacts of an (a) unstrained, (b) compressively strained, (c) and tensile strained GaN NB device. The insets of (c) and (d) are numerically calculated piezopotential distributions along GaN NB with its *c*-axis parallel to the longitudinal axis of the PS substrate. (d-e) Numerically calculated piezopotential distributions along GaN NB with its *c*-axis aligning 30 degrees off the longitudinal axis of PS substrate, under compressive and tensile strain, respectively. (f) 3-D schematic diagram illustrating the transverse twist of an off-axis compressed GaN NB, the twist is quite obvious. (g) A 2-D projection of the GaN NB device, showing the transverse twist of the GaN nanobelt during the compressive deformation. There is a maximum effective force exerted on the GaN NB as the external force increases, which is in accordance with the *I*-*V* behaviors of GaN NB devices shown in Figure 4.[49]

A theoretical model is proposed to explain the piezotronic effect on the electrical characterization, especially the SBH of the GaN NB using the energy band diagram, as shown in Figures 2.7a-c. For piezoelectric semiconductors such as ZnO and GaN, a piezoelectric potential is created inside the NB by applying a strain/pressure/force owing to the non-central symmetric crystal structure.[27] Once a strain is created in GaN NB, there

exists a piezopotential distribution along *c*-axis, with its polarity depending on the sign of the strain,[20] as shown in Figures 2.7b and 2.7c, respectively. A negative piezo-potential at the semiconductor side effectively increases the local SBH, while a positive piezo-potential reduces the barrier height. The role played by the piezo-potential is to effectively change the local contact characteristics through an internal field depending on the crystallographic orientation of the material and the sign of the strain,[68] thus, the charge carrier transport process is tuned at the M-S contact. When the GaN NB device is under compressive strain, as shown in Figure 2.7b, the drain has a positive potential leading to a lower SBH. Alternatively, by changing the compressive strain to tensile, as shown in Figure 5 (c), the drain this time has a negative potential along with a higher SBH.

For devices with GaN NB lying along the longitudinal axis of the substrate, which have SU and SD type *I-V* characteristics, when compressed with *c*-axis pointing to the source (Figure 2.7b), SBH at the drain will be lowered and then presents a SU type *I-V* curve. Similarly, if everything remains the same except for applying a tensile strain instead of a compressive one, SBH at the drain will be increased and gives out a SD type *I-V* curve. For devices with the *c*-axis of GaN NB lying off the longitudinal axis of PS substrate, which have U&D and D&U type *I-V* characteristics, the numerically calculated piezo-potential distributions along the GaN NB when it was subjected to an 30 degrees off-axis compressive and tensile strain are presented in Figures 2.7d and 2.7e, respectively. It can be seen that piezo-potential distributions here are similar to that of the GaN NB lying along the longitudinal axis of the substrate, as shown in Figures 2.7b and 2.7c. Therefore, the configuration of GaN NB device with its *c*-axis slightly off aligning

with the longitudinal axis of PS substrate is essential to U&D and D&U type *I-V* curves. From Figure 2.7f, it is obvious to see with such a configuration, once the device is compressed or stretched, a transverse twist is possible. Figure 2.7g shows a 2-D projection of the GaN NB device, making it much easier and clearer to see the twist of the GaN nanobelt during the compressive/tensile deformation. For an off-axis GaN NB device, the force applied on the substrate, noted as F, can be divided into two components: one is parallel to the *c*-axis of the GaN NB, noted as F_1 in Figure 2.7g, the other is perpendicular to the *c*-axis, noted as F_2 in Figure 2.7g. In a case of compressive strain (Figure 2.6a), the *I-V* characteristics were under control of the two components: F_1 has a positive effect on the current, while F_2 has a negative effect on the current. Under an increasing compressive strain, F_1 decreased, while F_2 increased. As a result, the competition between two effects could lead to a peak value of current as applied strain increased, which is the same situation as type U&D and D&U, as shown in Figures 2.6a and 2.6b.

In summary, the piezotronic effect on the transport properties of GaN NB has been demonstrated. The *I-V* characteristics of the device were tuned by the piezotronic effect when a compressive/tensile strain was applied on the GaN NB due to the change in Schottky barrier height, with good reproducibility and stability. The configurations was found to play a very important role in this process and different configurations of GaN NB devices would lead to different trends of *I-V* characteristics as well. A theoretical model is proposed to explain such effect on the electrical characterization, especially the SBH of the GaN NB using the energy band diagram. This effect would have potential

applications in strain and stress measurements in biomedical sciences, MEMS devices and structure monitoring.

2.2.1.2 *a*-Axis GaN Nanobelts[50]

Since the piezoelectric polarizations are highly dependent on the crystal orientations, the piezotronic effect should have distinguishable impacts on the electric transport properties of devices fabricated by semiconductors with different growth orientations. In this section, by using the GaN nanobelts synthesized along *a*-axis direction, the corresponding piezotronic effect is studied by measuring the electronic transport properties of single-nanobelt transistors. The physical mechanism is carefully illustrated and further confirmed by theoretical simulations *via* finite element analysis (FEA). Theoretical calculations are also conducted to reveal the spatial distributions of local carrier concentrations and the energy band diagrams of *a*-axis oriented GaN nanobelts under different straining conditions. This work systematically analyzes the transport properties of SGTs based on *a*-axis oriented GaN nanobelt, and the results provides fundamental understanding about the piezotronic effect along different crystal orientations, which can be useful for semiconductor-based electronics for logic computations, sensing systems, human-machine interfacing, implantable surgical instruments and biomedical diagnostics. [11, 12, 69-71]

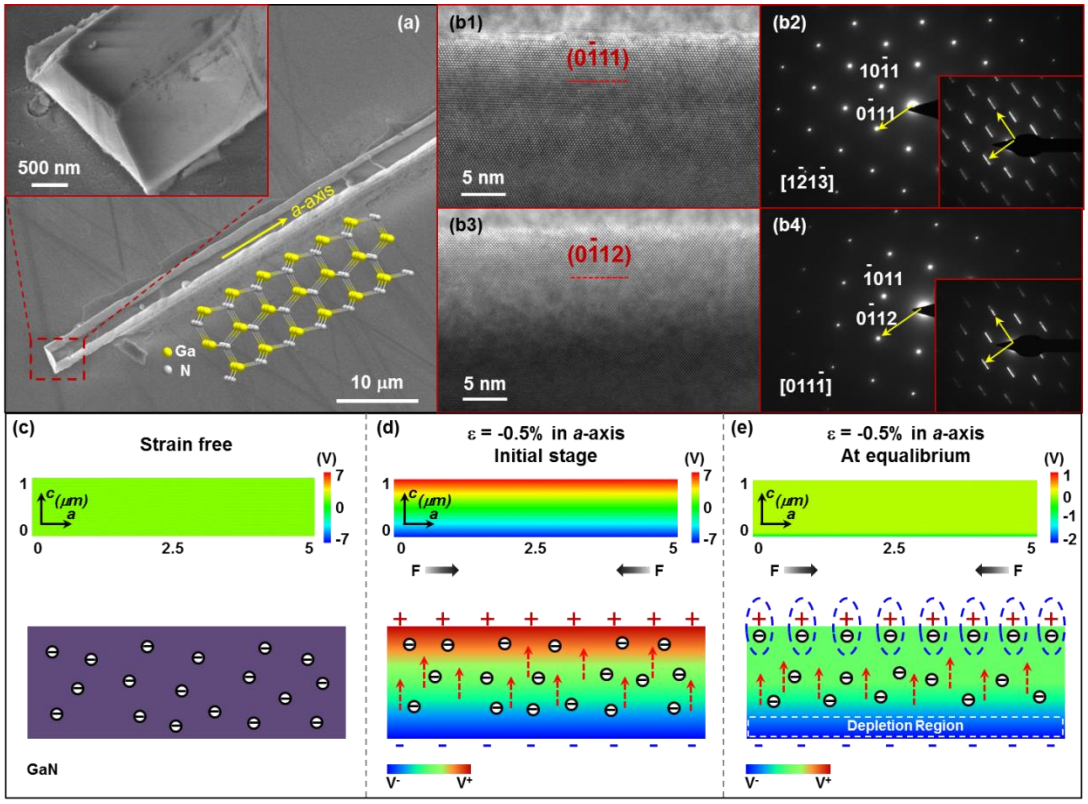

Figure 2.8 Characterizations and working mechanism of GaN nanobelt SGTs. (a) SEM images of the as-synthesized GaN nanobelt with trapezoidal cross section as the inset. (b) HRTEM images (b1, b3) and the corresponding SAED patterns (b2, b4) of GaN nanobelts. (c-e) Schematic illustration of the working mechanism of GaN nanobelt SGTs (c) under strain free condition; (d) as applying -0.5% compressive strains at the initial stage; (e) under -0.5% compressive strains at equilibrium. Top panels: FEA simulations of piezoelectric potential distributions; bottom panels: schematic illustration of carriers' motions.

Patterned silicon substrates used for GaN growth are fabricated by photolithography and wet chemical etching to form 800 nm deep trapezoidal grooves with two opposed Si (111) facets separated by a bottom Si (100) facet. GaN nanobelts are then synthesized on the patterned Si (100) substrate in a metal-organic chemical vapor deposition (MOCVD) reactor under 1050 ℃ and 400 mbar for 1800 seconds. The morphology of the as-synthesized GaN nanobelts are characterized by SEM as presented in Figure 2.8a, clearly showing a trapezoidal cross section as the inset with height of 1

μm, width of 2 μm and length of 100 ~ 200 μm. HRTEM images and the corresponding selected area electron diffraction (SAED) patterns presented in Figure 2.8b provide more insight information of the as-synthesized GaN nanobelts. Single crystal GaN is achieved as shown in Figures 2.8b1 and 2.8b3. The growth orientation is perpendicular to the normal directions of plane ($0\bar{1}11$) and ($0\bar{1}12$) as indicated by the SAED patterns in Figures 2.8b2 and 2.8b4. Therefore, it is confirmed that the GaN nanobelts used in this work is synthesized along $<2\bar{1}\bar{1}0>$ direction (*i.e. a*-axis oriented growth). The SGTs are fabricated by applying silver paste at both ends of the GaN nanobelt as source and drain electrodes.

The physical mechanism of piezotronic effect on electronic transport properties of *a*-axis GaN nanobelt SGTs under mechanical strains is investigated and schematically illustrated in Figures 2.8c-e. Motions of charge carriers under different straining conditions are depicted as bottom panels (Figures 2.8c-e), while the corresponding piezoelectric potential distributions are theoretically simulated *via* FEA and presented as top panels (Figures 2.81c-e). As a n-type semiconductor with donor concentration N_D = 2×10^{17} cm^{-3}, the as-synthesized *a*-axis GaN nanobelt presents electrons as majority charge carriers (Figure 2.8c, bottom) without piezo-potential distribution (Figure 2.8c, top) under strain free condition as shown in Figure 2.8c. By applying a compressive strain ε = -0.5% along *a*-axis direction (Figure 2.8d), at the initial stage, an instantaneous piezo-potential distribution is produced (Figure 2.8d, top) with positive piezoelectric polarization charges at the +*c* plane and negative piezo-charges at the –*c* plane (Figure 2.8d, top). Thus, mobile electrons are repelled by negative piezo-charges towards the +*c* plane as shown in the bottom panel of Figure 2.8d. At equilibrium, most of the positive

piezoelectric polarization charges at the +*c* plane are screened by mobile electrons,[72] while an electron depletion region is generated near negative piezo-charges at the –*c* plane as schematically shown in the bottom panel of Figure 2.8e. The corresponding piezo-potential distributions are calculated and presented in the top panel of Figure 2.8e. Considering the symmetric configuration of GaN nanobelt SGTs with respect to the *a*-axis, similar carrier motions and piezo-potential distributions are expected for tensile strain (along *a*-axis) scenarios, with electron depletion region induced at the +*c* plane and positive piezo-charges screened by electrons at the –*c* plane. Therefore, externally applied compressive/tensile strains tune/control the transport properties of *a*-axis GaN nanobelt SGTs as the gating by forming an electron depletion region to shrink the conducting channel and thus increase the resistance of the GaN nanobelts. This working mechanism is fundamentally new in physics and different from that in *c*-axis piezoelectric nanostructures, whose electric transport is determined by the asymmetric changes of barrier height at both Schottky contacts of the two-terminal devices as illustrated in previous sectino.[49]

Meanwhile, two Schottky barriers are formed between GaN and Ag when applying silver paste at both ends of the nanobelt for source and drain electrodes.[49] Upon compressive/tensile straining, negative piezoelectric polarization charges (Figure 2.8e) are presented at the local GaN/Ag interface after equilibrium; positive piezo-charges are screened by mobile carriers. The barrier heights at both Schottky contacts are therefore increased by negative piezo-charges and thus hinder the transport of electrons across the local energy barrier, which is equivalent to increasing the resistance of GaN nanobelts based transistors. Therefore, as applying more compressive/tensile strains, the resistance

of GaN nanobelts based transistors is increased owing to the formation of electron depletion region and the increased SBH.

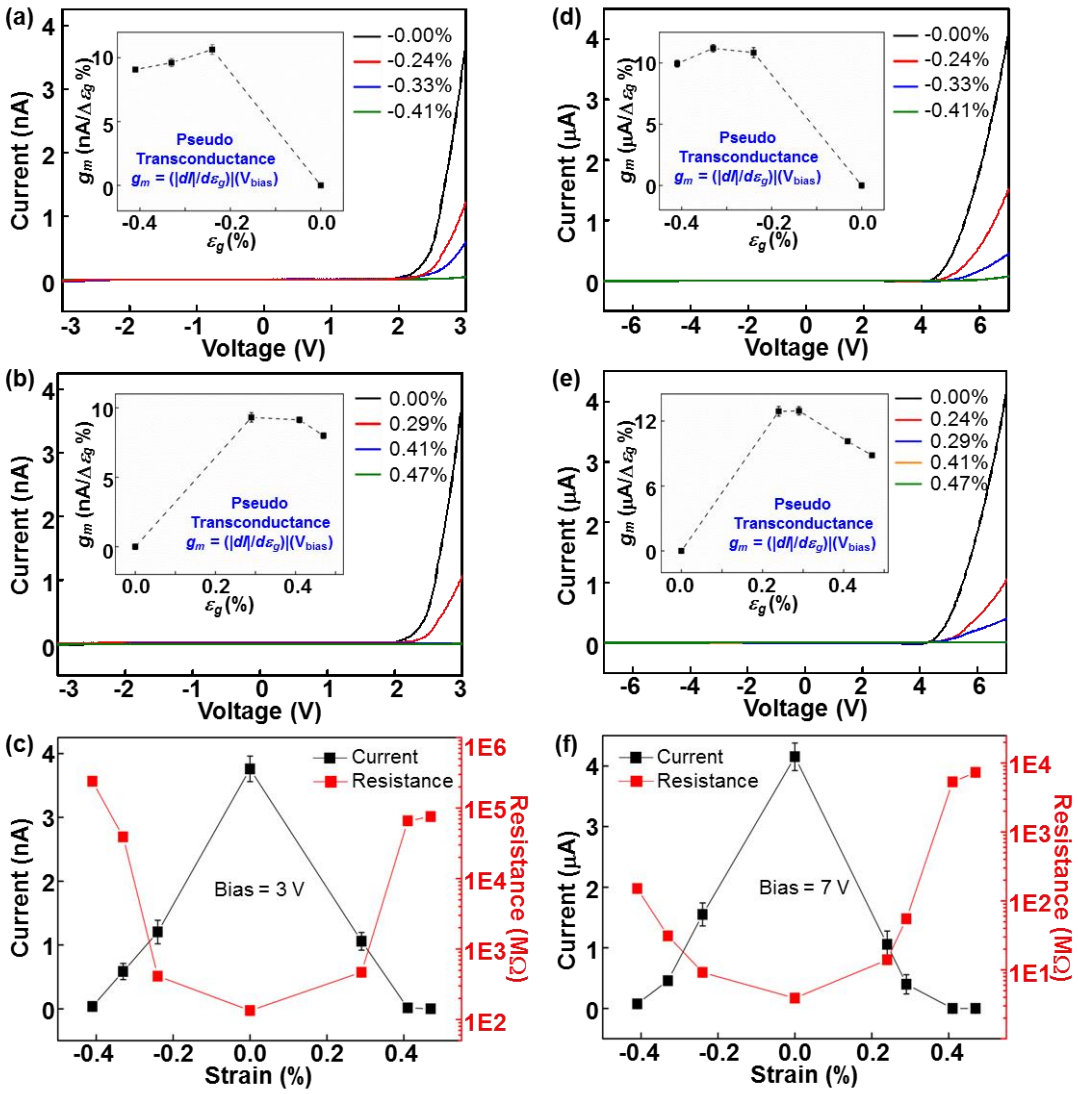

Figure 2.9 Piezotronic effect on *I-V* characteristics of *a*-axis GaN nanobelt SGTs. (a, b) *I-V* characteristics of GaN nanobelt SGTs under a series of (a) compressive and (b) tensile strains under triangular wave ranging from –3 V to +3 V. The insets are the corresponding pseudo-transconductance at 3 V. (c) Current and resistance response to strains at a bias voltage of 3 V. (d, e) *I-V* characteristics of GaN SGTs under a series of (d) compressive and (e) tensile strains under triangular wave ranging from –7 V to +7 V. The insets are the corresponding pseudo-transconductance at 7 V. (f) Current and resistance response to strains at a bias voltage of 7 V.[50]

Piezotronic effect on the transport properties of *a*-axis GaN nanobelt SGTs is systematically studied by applying different bias voltages on the devices under various straining conditions. The experimental set-ups and the optical images of the as-fabricated GaN nanobelt SGTs are presented in Figure 2.10a. *I-V* characteristics of GaN nanobelt SGTs under a series of compressive and tensile strains are measured and summarized in Figures 2.9a and 2.9b, respectively, by applying a triangular wave ranging from -3 V to +3 V. Obviously, the output currents of GaN nanobelt SGTs decrease as increasing compressive/tensile strains. The pseudo-transconductance $g_m = (|dI|/d\varepsilon_g)$ at a bias voltage of 3 V is derived by calculating the current differences per unit strain between strain-free and certain straining condition of the devices. The results are presented as insets of Figures 2.9a and 2.9b, indicating the gating effect of externally applied strains over the transport properties and output currents of *a*-axis GaN nanobelt SGTs. The maximum value of g_m is obtained under 0.29% tensile strain with the value of g_m = 12.9 (μA/ $\Delta\varepsilon_g$ %), at a bias voltage of 7 V (Figure 2.9e). Changes of current are plotted as a function of applied strains at a bias voltage of 3 V (Figure 2.9c, black), while the corresponding resistance changes are calculated and displayed in Figure 2.9c as red symbols. Obviously, the current decreases and the resistance increases by applying more compressive/tensile strains, which is distinguishable from the asymmetric changes of currents/resistances observed in *c*-axis nanostructures upon compressive and tensile straining[49] due to the different working mechanisms.

Based on the fact that the resistance of *a*-axis GaN nanobelts increases as applying both compressive and tensile strains, the electronic transport properties of GaN under strains are dominated by the piezotronic effect instead of the piezoresistive effect.

Because the piezoresistive effect is defined as $\frac{\Delta R}{R} = \pi\sigma$ (R is the resistance, π is the piezoresistive coefficient, σ is the stress), and the changes of resistance are inverse under compressive and tensile strains. Furthermore, the piezoresistive coefficient π is calculated by extracting the data at 3 V biased voltage (Figure 2.9a), with relative changes of resistance between unstrained and -0.41% compressively strained conditions $\frac{\Delta R}{R}$ = 73.2, stress $\sigma = \varepsilon \times E$ (E = 181 GPa is the Young's modulus of GaN). The calculated π is in the order of 1×10^{-7} Pa^{-1}, which is three orders in magnitude larger than the typical value in the 10^{-10} level.[73] This result further confirms that it is the piezotronic effect, rather than the piezoresistive effect, that plays an essential role in controlling the electronic transport properties of *a*-axial GaN nanobelt SGTs. More experimental measurements are conducted under 7 V (Figures 2.9d-f) biased voltages; similar performances are obtained under different straining conditions for both investigations. All the observed results indicate the increasing resistance and decreasing current under stronger compressive/tensile strains, as predicted by the proposed working mechanism. Over 50 devices are measured during the experiments, most of which possess similar electronic transport properties as described above, indicating the reliability and reproducibility of these results.

Theoretical calculations are performed to obtain insight understanding about the modifications of energy band structure and charge carrier distributions by piezotronic effect. Upon straining, charge carriers redistribute within GaN due to the electric field established by strain-induced piezoelectric polarization charges. The mechanical equilibrium and the direct piezoelectric effect are expressed as:[72]

$$\begin{cases} \sigma_p = c_{pq}\varepsilon_q - e_{pk}E_k \\ D_i = e_{iq}\varepsilon_q + \kappa_{ik}E_k \end{cases} \tag{2.11}$$

where σ is the stress tensor, ε is the strain tensor, E is the electric field, D is the electric displacement, c_{pq} is the mechanical stiffness tensor, e_{pk} and e_{iq} are the piezoelectric constant, κ_{ik} is the dielectric constant. The Voigt-Nye notation is used. By substituting the second equation into Gauss's law, the equation for the electric field is derived:

$$\nabla \bullet D = \frac{\partial}{\partial x_i}\left(e_{iq}\varepsilon_q + \kappa_{ik}E_k\right) = \rho = e\left(p - n + N_D^+ - N_A^-\right) \tag{2.12}$$

where p is the hole concentration in the valence band, n is the electron concentration in the conduction band, N_D^+ is the ionized donor concentration and N_A^- is the ionized acceptor concentration. $p = N_A^- = 0$ is adopted for n-type GaN nanobelts used in this work. Therefore, equation (2.12) transfers into:

$$\nabla \bullet D = \frac{\partial}{\partial x_i}\left(e_{iq}\varepsilon_q + \kappa_{ik}E_k\right) = \rho = e\left(-n + N_D^+\right) \tag{2.13}$$

The redistribution of electrons under thermodynamic equilibrium is given by the Fermi-Dirac statistics,

$$\begin{cases} n = N_c \dfrac{2}{\sqrt{\pi}} \displaystyle\int_{E_c(x)}^{\infty} \frac{\left[\left(E - E_c(x)\right)/kT\right]^{1/2}}{1 + \exp\left[\left(E - E_F\right)/kT\right]} \frac{dE}{kT} \\ N_c = 2\left(\dfrac{2\pi m_e kT}{h^2}\right)^{3/2} \end{cases} \tag{2.14}$$

where the conduction band edge $E_c(x)$ is a function of space coordinates. N_c, the effective state density of conduction band, is determined by the effective mass of conduction band electrons m_e and temperature T. Considering the obvious mechanical

deformation, the band edge shift ΔE_c is the sum of the electrostatic energy part and the deformation potential part,

$$\Delta E_c = E_c - E_{c0} = -e\varphi + \Delta E_c^{deform} = -e\varphi + a_c \frac{\Delta V}{V} \tag{2.15}$$

where E_{c0} is the conduction band edge of a free-standing unstrained GaN nanobelt; $\Delta E_c^{deform} = a_c \Delta V/V$ is the band edge shift due to the deformation potential, which is proportional to the relative volume change $\Delta V/V$, and a_c is the deformation potential constant. Finally, the activation process of the donors is given by:

$$N_D^+ = N_D \frac{1}{1 + 2\exp\left(\frac{E_F - E_D(x)}{kT}\right)} \tag{2.16}$$

where $E_D(x) = E_c(x) - \Delta E_D$ is the position-dependent donor energy level. The constant ΔE_D is the activation energy of the donors.

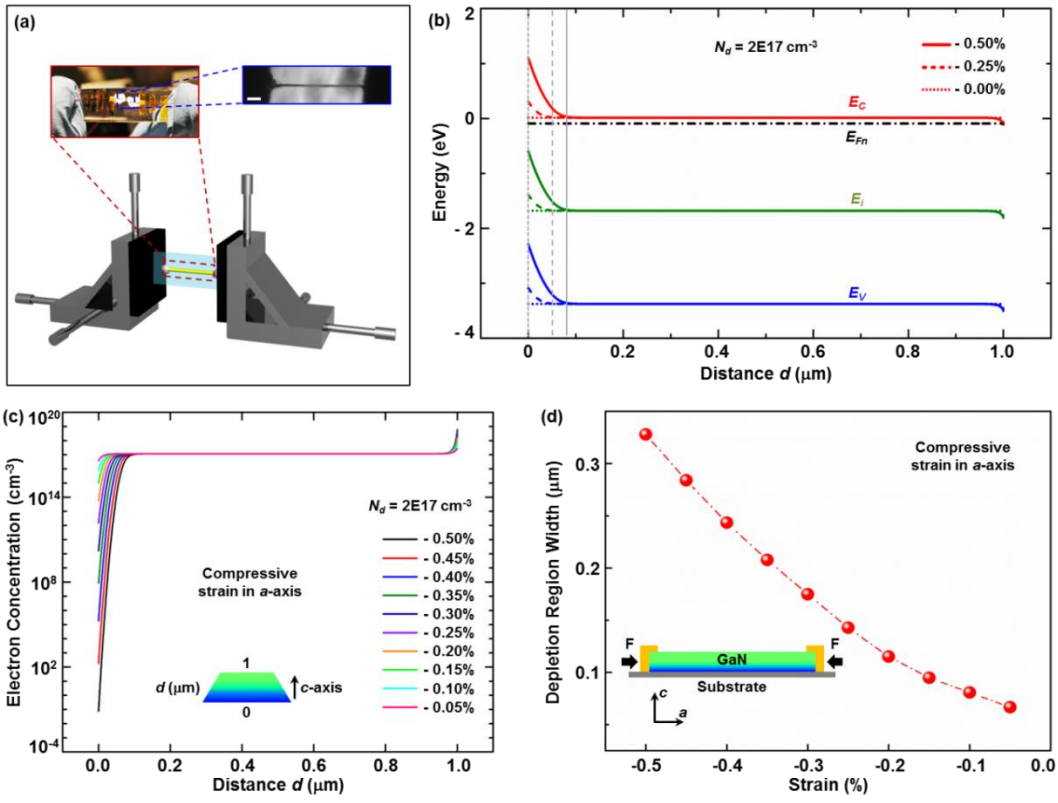

Figure 2.10 Theoretical simulations under compressive strains. (a) Experimental set-up and optical images of GaN nanobelt SGTs. Scale bar is 50 m. (b) Energy band diagram of GaN SGTs under 0% (short dot line), -0.25% (short dash line) and -0.50% (solid line) compressive strains. (c) Spatial distribution of local electron concentrations along *c*-axis within GaN under different compressive straining conditions. Donor concentration is $N_D = 2\times10^{17}cm^{-3}$. (d) Width of electron depletion region under different compressive strains along *a*-axis.[50]

With nonlinear partial differential equations (2.11) - (2.16) solved by FEA, the piezoelectric potential distributions (Figure 2.8c-e, top), energy band diagrams (Figure 2.10b) and local carrier concentrations (Figure 2.10c) in a GaN nanobelt under mechanical strains along *a*-axis direction are derived. Figure 2.10c displays the spatial distribution of electron concentrations along *c*-axis direction under a series of compressive straining conditions. Energy band diagrams of GaN under 0% (Figure 2.10b, short dot line), -0.25% (Figure 2.10b, short dash line) and -0.50% (Figure 2.10b, solid line) compressive strains are shown in Figure 2.10b, indicating different bending positions of the energy band edge. Depletion region width is determined by locating the bending position of energy band edge[74] and plotted as a function of compressive strains as shown in Figure 2.10d. It is clear that a wider electron depletion region is achieved under stronger compressive strains, which agrees well with experimental results and the proposed physical mechanism. Also, it rules out the role played by the piezoresistive effect in the measured transport characteristics. Same calculations are conducted for tensile strains (along *a*-axis) situations. Due to the symmetric configuration of GaN nanobelt SGTs, same behaviors are observed for energy band diagrams and local electron concentrations with opposite spatial distributions. The width of the electron depletion region also increases as applying more tensile strains.

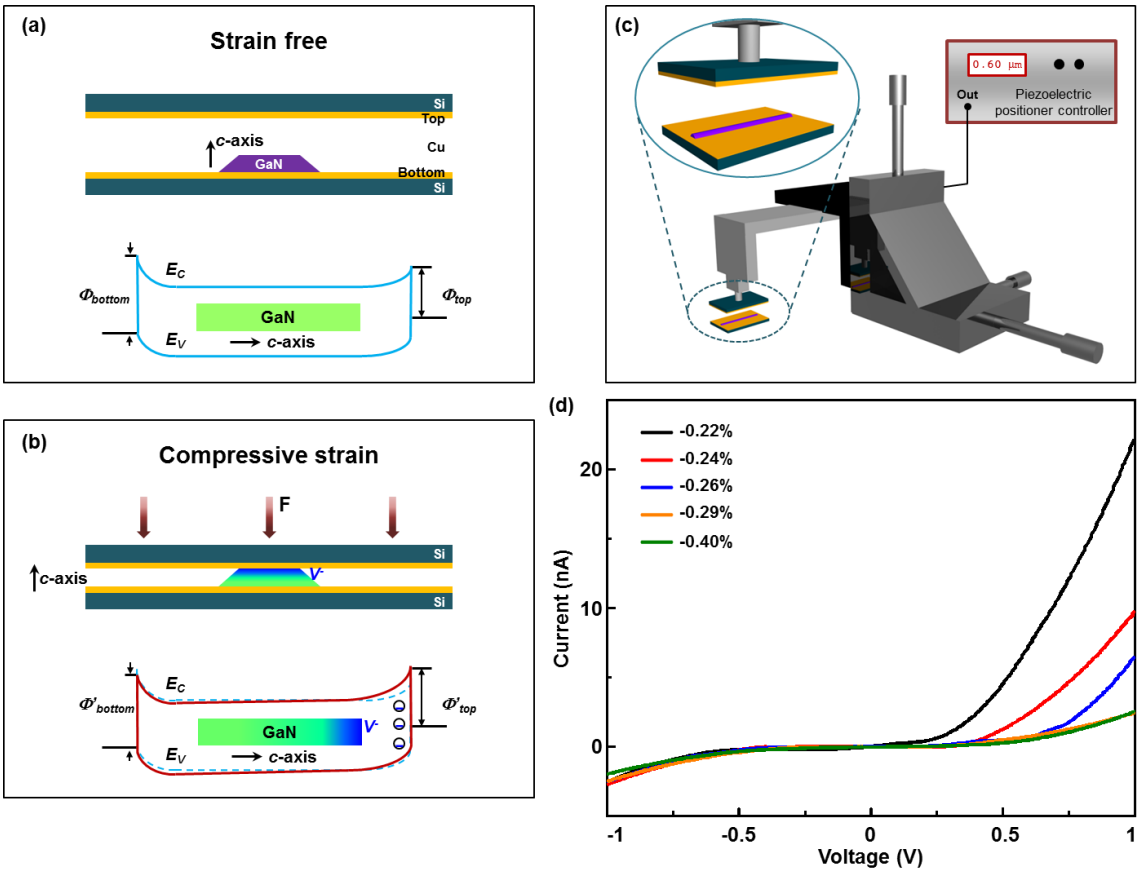

Figure 2.11 *I-V* characteristics of GaN nanobelt SGTs under *c*-axis strains. (a, b) Experimental set-up and the corresponding energy band diagram of GaN SGTs under (a) strain free condition and (b) compressive strains along *c*-axis. (c) Experimental set-up of the *c*-axis strain measurements. (d) *I-V* characteristics of GaN SGTs under various compressive strains along *c*-axis. Note: the current flow is along the *c*-axis.[50]

The dominate role played by the piezotronic effect in tuning/controlling the electronic transport processes of GaN nanobelt SGTs under mechanical strains is further confirmed by conducting control experiments to apply compressive strains along *c*-axis of the GaN nanobelt (Figure 2.11). Under strain free condition, GaN nanobelt is placed on the bottom Si wafer (1 cm by 1 cm) coated by copper as an electrode, with its *c*-axis pointing upwards (Figure 2.11a). Another copper coated Si wafer (1 cm by 1 cm) is attached to a piezoelectric positioner (movement resolution ~ 10 nm) as shown in Figure 2.11c to apply compressive strains and serves as the top electrode as well. By pressing

down the top Si wafer, compressive strains are applied on the GaN nanobelt along its *c*-axis orientation (Figure 2.11b). The corresponding energy band diagram is schematically presented in Figure 2.11b, with SBH between GaN and top electrode increasing, while the SBH between GaN and bottom electrode remaining unchanged, because negative piezoelectric polarization charges present at the +*c* plane, while positive piezo-charges are screened by mobile electrons and no obvious piezoelectric potential is observed at the –*c* plane. These energy band diagrams perfectly explain the obtained *I*-*V* characteristics of GaN nanobelt SGTs as shown in Figure 2.11d: output currents measured along the *c*-axis at +1 V biased voltage decrease as increasing the applied strains, since the barrier height of the corresponding reversely biased Schottky contact is increased; while the currents at -1 V remain unchanged, because the barrier height of the corresponding reversely biased Schottky contact is unchanged due to the screening effect.

Different from previous section that focus on fundamental study and applications of piezotronic effect on nanostructures grown along *c*-axis, *a*-axis GaN nanobelts are synthesized and fabricated as SGTs in this section. The piezotronic effect on the modifications of energy band structures and the corresponding electronic transport properties of GaN nanobelts SGTs is systematically investigated. *I*-*V* characteristics of GaN nanobelt SGTs are measured under different bias voltages and straining conditions. Upon stronger compressive/tensile straining, the resistance of GaN nanobelts is increased and the currents of SGTs are decreased by the piezotronic effect. Wider electron depletion region and increased SBH induced by more mechanical strains are accounted for the obtained electronic transport behaviors. Theoretical calculations/simulations *via* FEA are conducted to provide insight understanding of the physical mechanism of the

piezotronic effect. The spatial distributions of local carrier concentration along *c*-axis and the energy band diagrams of the *a*-axis GaN nanobelts under different straining conditions are presented to support the proposed working mechanism. This work systematically investigates the electronic transport behaviors of *a*-axis GaN nanobelt SGTs controlled by piezotronic effect and provides guidance to potential applications of piezotronic effect on semiconductor-based electronic devices for logic computations, sensing systems, human-machine interfacing, implantable surgical instruments and biomedical diagnostics.

2.2.1.3 AlGaN/AlN/GaN Heterostructures

AlGaN/GaN is one of the most promising material systems for creating heterojunction electron gas (HEG) due to its strong intrinsic polarizations,[75] and has been widely applied for high electron mobility transistor (HEMTs)[76] and other high-performances quantum electronics[77]. In previous reports, tuning alloy compositions and controlling the thickness of AlGaN layer are two most effective ways to tune/control the physical properties of HEG and thus essential to optimizing devices performances[78, 79]. However, the extreme complexity and high expenses of these two methods are preventing them from practical applications. Therefore, it is necessary to develop new approaches for easier and more effective modulations of HEG in HEMTs as alternatives. In this work, we proposed an easy and new approach to modulate the physical properties of HEG by introducing the piezotronic effect. The conductance of AlGaN/AlN/GaN microwires is increased by 165% under -1.78% compressive strains and reduced by 48% under 1.78% tensile strains at room temperature, due to the modulations of HEG by the strain-induced

piezotronic effect. This modulating effect is further improved at 77 K by 890% and 940% under compressive and tensile strains, respectively, indicating the enhanced piezotronic effect at low ambient temperature. This study provides in-depth understandings about the piezotronic-effect modulation of low-dimensional electron gas in heterostructured nanomaterials and indicates potential applications in high electrons mobility transistors (HEMTs) and MEMS/NEMS.

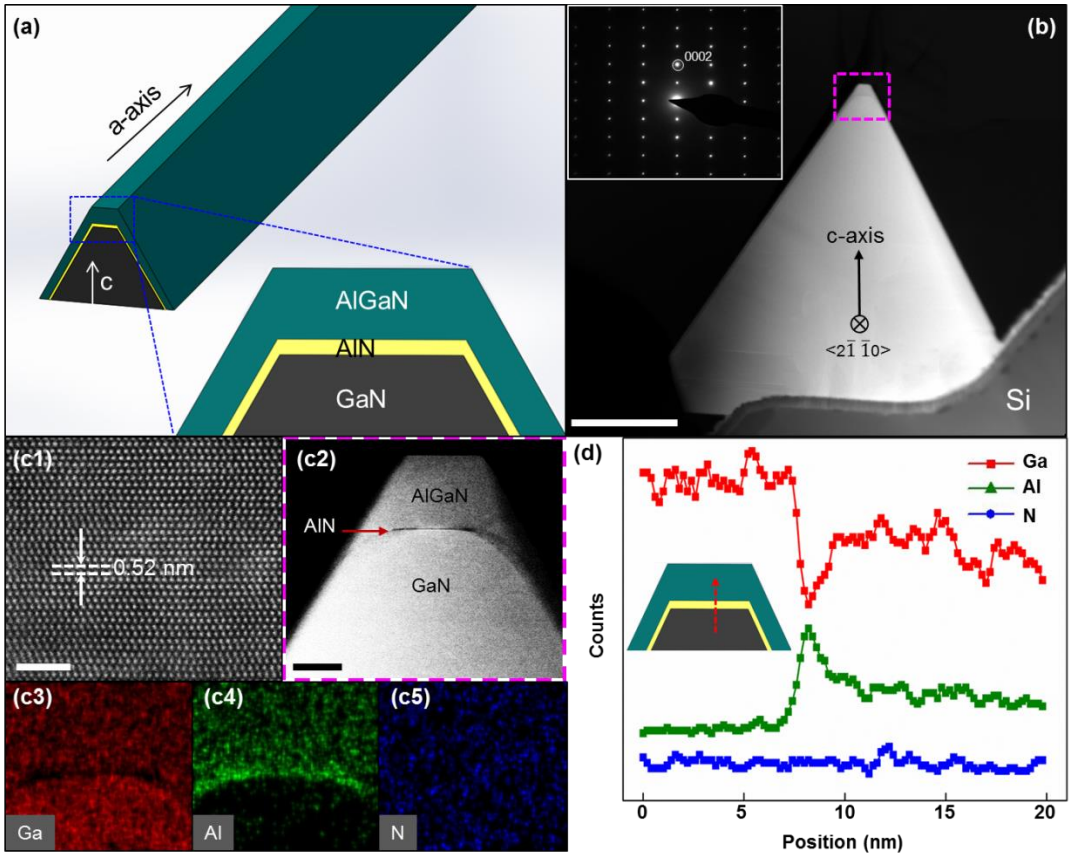

Figure 2.12 Structure characterizations of AlGaN/AlN/GaN heterostructures microwire. (a) Schematic diagram of an individual heterostructure microwire and magnified cross-sectional view of a microwire facet highlighting AlGaN/AlN/GaN structure. (b) The cross-section HAADF-STEM image of an individual AlGaN/AlN/GaN heterostructure microwire. The scale bar is 500 nm. Inset: Corresponding electron diffraction pattern. (c1) High-resolution transmission electron microscope image acquired from GaN. The scale bar is 5 nm. (c2) The magnified HAADF-STEM image collected from the labeled area in Fig. 1b. The scale bar is 20 nm. (c3-5) STEM energy-dispersive X-ray spectroscopy (EDX) elemental mapping of the AlGaN/AlN/GaN heterojunction. (d) The EDX line profiles for Ga (red), Al (green) and N (blue) elements.

AlGaN/AlN/GaN heterostructure microwires used in this work are synthesized on patterned Si substrate by MOCVD as shown in Figure 2.12a. Undoped single-compound GaN microwires with uniform lateral facets are grown firstly and serve as a platform to sequentially deposit undoped AlN and AlGaN layers. The cross-section high-angle annular dark-field scanning transmission electron microscopy (HAADF-STEM) image of an individual AlGaN/AlN/GaN heterostructure microwire is presented in Figure 2.12b, showing a trapezoidal cross section with top width of ~100 nm, bottom width of ~1.5 μm and height of ~1.5 μm. The corresponding selected area electron diffraction (SAED, Tecnai G2) patterns indexed along the *a*-axis (Figure 2.12b, inset) and the high-resolution transmission electron microscope (HRTEM, FEI F30) image (Figure 2.12c1) are presented to characterize the crystal structure of AlGaN/AlN/GaN heterostructure microwire as non-centrosymmetric wurtzite single crystal orientated along nonpolar < $2\bar{1}\bar{1}0$ > (i.e. *a*-axis) direction with polar *c*-axis pointing to its top surface. The magnified HAADF-STEM image collected from the labeled area in Figure 2.12b is shown in Figure 2.12c2, clearly presenting a dark contrast line (ultrathin AlN interlayer) sandwiched by the top AlGaN layer and bottom GaN. The thicknesses of AlGaN and AlN layers are estimated to be 40 nm and 1.6 nm, respectively. STEM energy-dispersive X-ray spectroscopy (EDX) elemental mapping (Figures 2.12c3-5) of AlGaN/AlN/GaN heterojunction clearly reveals the spatial distributions of Ga, Al, and N elements, confirming that the contrasts in Figure 2.12c2 are from the variation of chemical compositions. The corresponding line profile extracted from EDX mapping is presented in Figure 2.12d.

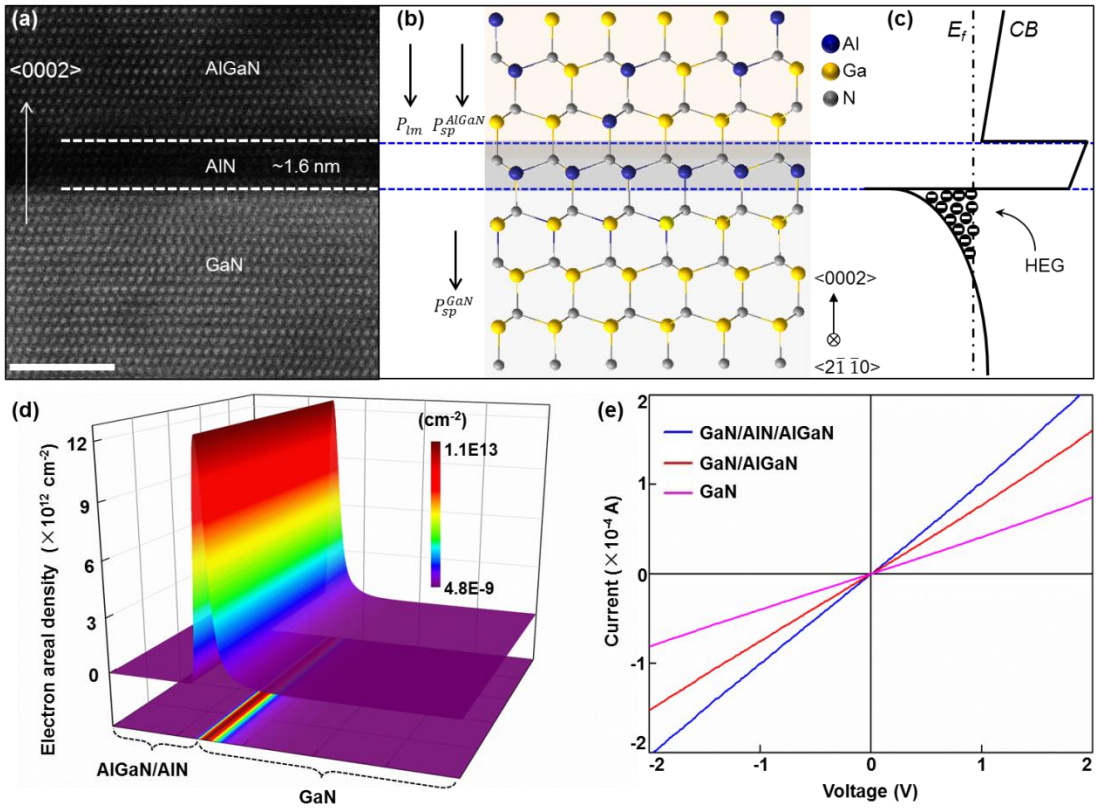

Figure 2.13 HEG distributed at AlGaN/AlN/GaN heterojunctions. (a) The lattice-resolved HAADF-STEM image of the interfacial region of AlGaN/AlN/GaN heterostructure. (b) Corresponding atomic structure model. (c) Corresponding conduction band profile and the distribution of HEG. (d) The calculated electron density distribution in AlGaN/AlN/GaN heterostructure microwire. (e) *I-V* characterizations of microwire devices based on AlGaN/AlN/GaN heterostructure microwire, AlGaN/GaN heterostructure microwire and homogeneous single-compound GaN microwire.

The existence of HEG at AlGaN/AlN/GaN heterojunctions is confirmed by experimental characterizations and theoretical simulations as shown in Figure 2.13. The lattice-resolved HAADF-STEM image shown in Figure 2.13a indicates that the interfaces of AlGaN/AlN and AlN/GaN are atomically uniform and sharp without obvious boundary defects or dislocations. These results confirm the absence of strain relaxation in AlGaN and AlN epitaxy layers, and suggest that scattering due to surface roughness should be reduced in this heterostructure microwire. The corresponding atomic structure model and conduction band energy profile of the AlGaN/AlN/GaN heterostructure are

shown in Figures 2.13b and 2.13c, respectively. Owing to its non-centrosymmetric crystal structure, there are two different types of intrinsic polarizations presented in AlGaN/AlN/GaN heterojunctions: (i) the spontaneous polarization *PAlGaN sp* and *PGaN sp* existing in AlGaN and GaN, respectively; (ii) lattice-mismatch-induced piezoelectric polarizations existing in AlGaN layer (P_{lm}) due to the different lattice constants between AlGaN epitaxy layer and GaN relaxed "substrate"[80]. These polarizations lead to the accumulation of net positive fixed charges at AlGaN/AlN/GaN interface. Meanwhile, the conduction band of GaN lies below that of AlGaN, leading to the formation of a triangle-shaped quantum potential well in GaN layer near the AlN/GaN interface (Figure 2.13c). As a result, the electrons in heterostructure microwire are attracted and confined in this potential well and HEG is generated. In order to further confirm the existence of HEG, the electron density distribution in the AlGaN/AlN/GaN heterostructure microwire is calculated and shown in Figure 2.13d, indicating the formation of HEG with a high electron density of 1×10^{13} cm^{-2} locating at a narrow region in GaN layer close to the heterojunction interface. Besides, the ultrathin AlN interlayer is utilized to reduce the alloy scattering from AlGaN layer and provide a large conduction band discontinuity for better confinement of electrons in the potential well.

Enhancements on the electric transport properties of heterostructure microwires by HEG and AlN interlayer are investigated by synthesizing three different microwires: AlGaN/AlN/GaN heterostructure microwire, AlGaN/GaN heterostructure microwire and homogeneous single-compound GaN microwire. Typical *I-V* characteristics of these three types of microwires based two-terminal Ohmic devices are compared in Figure 2.13e, showing better conductance of AlGaN/GaN microwires than that of GaN due to the

existence of HEG, and the best conductance of AlGaN/AlN/GaN microwires because of the reduced electrons scattering from ultrathin AlN interlayer.

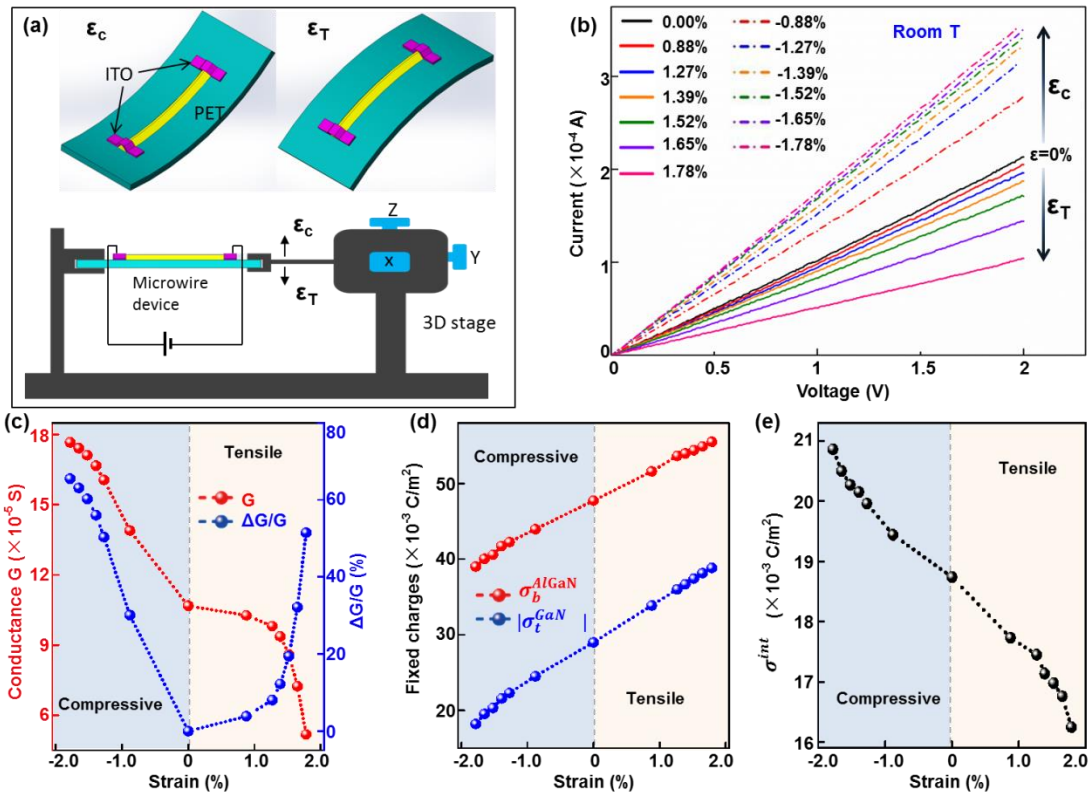

Figure 2.14 Piezotronic effect and fixed charges distribution in AlGaN/AlN/GaN heterostructure. (a) Experimental set-ups (lower) and the schematics of the microwire devices experiencing compressive (upper left) and tensile strain (upper right). (b) *I-V* characteristics of the as-fabricated microwire devices under strain free and a series of compressive and tensile strains condition. (c) The conductance (*G*) and the corresponding relative changes (*ΔG/G*) of the microwire devices as a function of strains. (d) The fixed polarization charges distributed at the bottom surface of AlGaN layer (σ_b^{AlGaN}) and the absolute value of fixed polarization charges distributed at the top surface of GaN ($|\sigma_t^{GaN}|$) as a function of applied external strains. (e) The effective net fixed polarization charges (σ^{int}) at AlGaN/AlN/GaN heterojunctions as a function of externally applied strains.

The piezotronic effect modulations on the HEG and electric transport properties of AlGaN/AlN/GaN microwire devices are systematically studied under various straining conditions as shown in Figure 2.14. The experimental set-ups and the schematics of the

microwire devices under compressive and tensile strain are presented in Figure 2.14a. *I-V* characteristics of the as-fabricated microwire devices under a series of compressive and tensile strains are measured and summarized in Figure 2.14b, demonstrating Ohmic transport property. Obviously, the output currents of heterostructure microwire devices increase as increasing compressive strains, and decrease as increasing tensile strains. The conductance of the microwire devices (G) and the corresponding relative changes ($\Delta G/G$) are extracted and plotted as a function of applied strains as shown in Figure 2.14c. It clearly indicates that the conductance of the AlGaN/AlN/GaN heterostructure microwire increases/decreases with the compressive/tensile strain.

The superposition among piezotronic-induced polarization P_{pz}, intrinsic spontaneous polarization P_{sp}^{AlGaN} and P_{sp}^{GaN} and lattice-mismatch-induced piezoelectric polarization P_{lm} is explored by calculating the fixed polarization charges distributions at the interfaces of AlGaN/AlN/GaN heterostructure. The fixed polarization charges distributed at the bottom surface of AlGaN layer (σ_b^{AlGaN}) and the absolute value of fixed polarization charges distributed at the top surface of GaN ($|\sigma_t^{GaN}|$) as a function of externally applied strains are firstly calculated and summarized in Figure 2.14d. Then, the effective net fixed polarization charges (σ^{int}) at the AlGaN/AlN/GaN heterojunction as a function of externally applied strains are also calculated and shown in Figure 2.14e. It is clear that σ^{int} is always positive with or without external strains with the value increasing/decreasing as compressive/tensile strains. Therefore, more effective polarization charges accumulate at the heterojunctions as increasing compressive strains, while less effective polarizations present as applying more tensile strains to the devices.

These changes agree well with the observed *I-V* curves in Figure 2.14b and are resulted from the modulations of energy band profiles at heterojunctions by the piezotronic effect.

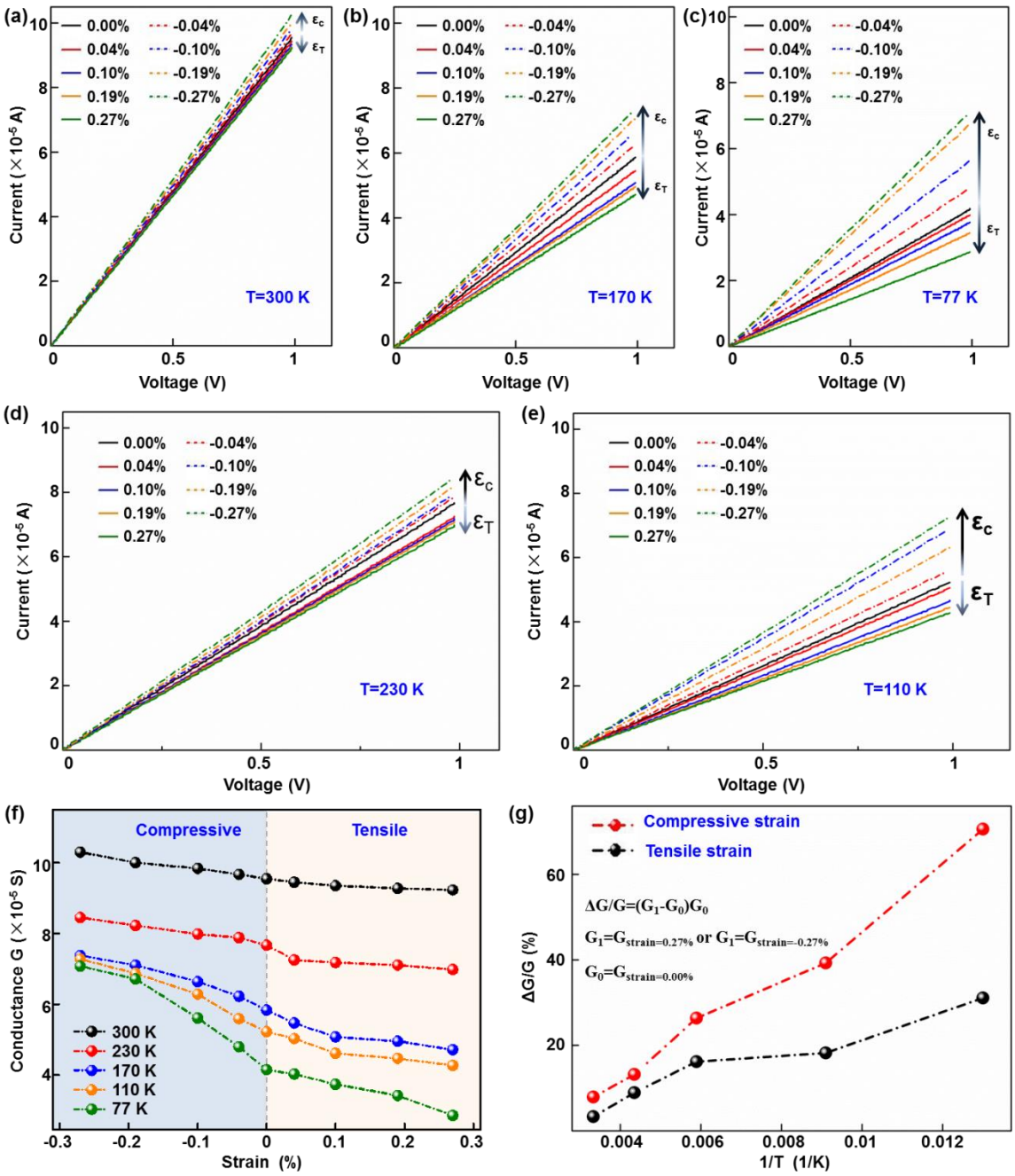

Figure 2.15 Temperature dependence of the modulation of HEG by the piezotronic effect. *I-V* characteristics of AlGaN/AlN/GaN heterostructure microwire devices at 300 K (a), 170 K (b), 77 K (c), 230 K (d) and 110 K (e) under externally applied compressive and tensile strains along *a*-axis. (f) Conductances (*G*) of AlGaN/AlN/GaN heterostructure microwire devices under each temperature condition as a function of external strains. (g)

The relative changes of conductance under compressive (red) and tensile (black) strain conditions.

Temperature dependence of the piezotronic effect modulations of HEG at AlGaN/AlN/GaN heterojunctions is systematically investigated as shown in Figure 2.15. *I-V* characteristics of AlGaN/AlN/GaN heterostructure microwire devices are measured at 300 K, 230K, 170 K, 110 K and 77 K (Figure 2.15a-e) by externally applying compressive and tensile strains along *a*-axis. Obviously, the output currents increase as applying compressive strains and decreases as applying tensile strains at each temperature condition but with distinguishable magnitudes. As the system temperature decreases, the changes of *I-V* curves become more and more significant, and the difference among output currents derived under various straining conditions become most explicit at 77 K. These results are resulted from the enhanced piezotronic effect at low temperature as freeze-out effect reduces the screening again piezo-polarizations at lower temperature,[81] and thus the enhanced piezotronic effect at lower temperature condition plays a more significant role in modifying the energy profiles and physical properties of HEG at AlGaN/AlN/GaN heterojunctions.

Conductances (*G*) of the AlGaN/AlN/GaN heterostructure microwire devices at each temperature as a function of external strains are plotted in Figure 2.15f. Obviously, the conductance of the microwire devices at each straining condition increases with the temperature since higher carrier mobility obtained at higher temperature due to more thermal energies. Moreover, at each temperature condition, the conductance of heterostructure microwire devices shows a consistent increasing and decreasing tendency as the increasing of compressive and tensile strain, respectively. This variation tendency becomes more and more significant as changing the temperature from 300 K to 77 K.

Further study of the temperature dependence of piezotronic effect modulation of HEG at heterojunctions is conducted by calculating the relative changes of conductance $\Delta G/G=(G_1-G_0)G_0$, where $G_0=G_{strain=0.00\%}$; $G_1=G_{strain=-0.27\%}$ *or* $G_1=G_{strain=0.27\%}$ as shown in Figure 2.15g. For compressive strains, the calculated $\Delta G/G$ increases by 890% as changing the ambient temperature from 300 K to 77 K; for tensile strains, the calculated $\Delta G/G$ increases by 940% from 300 K to 77 K. These results indicate that the modulations of HEG and electric transport properties of AlGaN/AlN/GaN heterostructure microwires become substantially more effective at lower temperature due to the enhanced piezotronic effect.

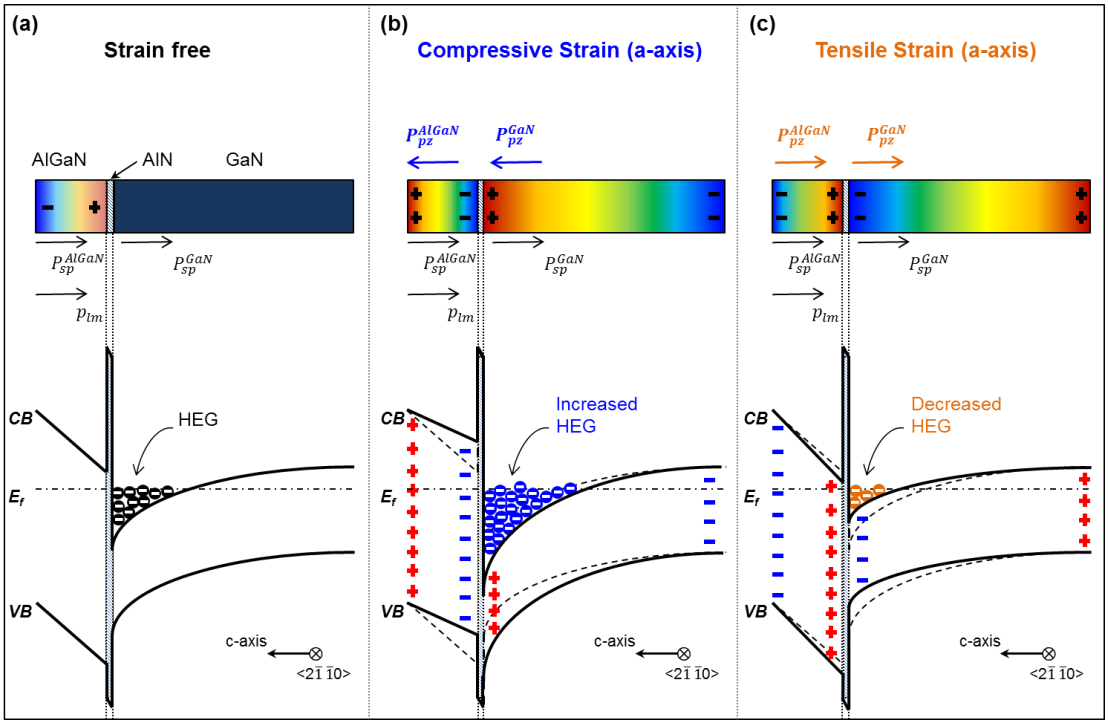

Figure 2.16 Working mechanism of the piezotronic effect modulations of HEG. The coupling of spontaneous polarization, lattice-mismatch-induced polarization, piezotronic-effect-induced polarization, corresponding energy band profiles and the distribution of HEG in AlGaN/AlN/GaN heterostructures microwire under (a) strain free, (b) compressive strain along *a*-axis and (c) tensile strain along *a*-axis condition.

Energy diagrams of the AlGaN/AlN/GaN heterostructure microwire along *c*-axis are carefully analyzed under different straining conditions to illustrate the working mechanism of piezotronic effect modulations of HEG at heterojunctions. Under strain free condition (Figure 2.16a), a triangle-shape potential well is formed in GaN close to AlN/GaN interface due to the co-existence of P_{sp}^{AlGaN}, P_{lm} and P_{sp}^{AlGaN} and the large band discontinuity between AlGaN and GaN. The net fixed charges at AlGaN/AlN/GaN heterojuctions σ^{int} are always positive with or without strains (Figure 2.14e). Therefore, free electrons within the microwire close to the heterostructur interface are attracted by σ^{int} and confined in the potential well, giving rise to the formation of HEG as shown in Figure 2.16a. Under compressive strain along *a*-axis of the microwire (*i.e.* tensile strain along *c*-axis), positive piezo-charges are induced at +*c* plane while negative piezo-charges at –*c* plane. The energy band of AlGaN close to AlGaN/AlN interface tilts upward by the negative piezo-charges and the energy band of GaN near GaN/AlN interface is bent downward by positive piezo-charges as shown in Figure 2.16b. Thus the potential well becomes "deeper" to confine more electrons in it due to the modulations of energy profile at heterojunctions. Meanwhile, the increased σ^{int} under compressive strain attracts more free electrons, thus the sheet density of HEG increases. This agrees well with the enhanced electric transport of heterostructure microwire shown in Figure 2.14b. In contrast, under tensile strain along *a*-axis (Figure 2.16c), energy band of AlGaN close to AlGaN/AlN interface is bent downward by the positive piezo-charges and the energy band of GaN near GaN/AlN interface is elevated by negative piezo-charges. Thus the potential well becomes "shallower" compared to strain free condition and the corresponding electrons confinement is weakened. Meanwhile, the decreased σ^{int} under

tensile strain releases a certain amount of the confined free electrons from the potential well and thus decreases the sheet density of HEG. This leads to the reduced electric transport of heterostructure microwire, which is consistent with the experimental result shown in Figure 2.14b.

The piezotronic effect is applied to AlGaN/AlN/GaN heterostructure microwires as a novel approach to modulate the physical properties of HEG and thus tune/control the electric transport process of carriers across heterojunctions. Unlike previously reported methods by either modifying the alloy components or controlling the thickness of each layer to modulate the HEG properties, here we utilize strain-induced piezoelectric polarization charges to modify the energy band profile at local heterojunctions as an effective way for physical properties modulations of HEG. Compared with traditional methods, this approach is fundamentally new in science and possesses huge advantages, such as easy-to-fabricate and low costs. By introducing the piezotronic effect to AlGaN/AlN/GaN heterostructure microwires, at room temperature, the conductance is increased by 165% under -1.78% compressive strains, and reduced by 48% under 1.78% tensile strains; at 77 K, this modulating effect is further improved by 890% and 940% under compressive and tensile strains, respectively, due to the enhanced piezotronic effect at low ambient temperature. This study provides in-depth understanding about the piezotronic-effect modulation of low-dimensional electron gas in heterostructured nanomaterials, with potential applications in high electrons mobility transistors (HEMTs) and MEMS/NEMS.

2.2.2 Piezotronics Logic Devices and Computations[51]

In this work, by utilizing the piezoelectric polarization charges created upon straining at metal-GaN NB interface to modulate transport of local charge carriers across the Schottky barrier, the piezotronic effect has been applied to convert mechanical stimuli into electronic controlling signals in wurtzite-structured GaN NB, leading to the GaN NB SGTs. By further assembling and integrating GaN NB SGTs, universal logic devices such as NOT, AND, OR, NAND, NOR and XOR gates have been demonstrated for performing mechanical-electrical coupled piezotronic logic operations. Moreover, basic piezotronic computation such as one-bit binary addition over the input mechanical strains with corresponding computation results in electrical domain by half-adder has been implemented for the first time. The strain-gated piezotronic logic devices may find novel applications in human-machine interfacing, active flexible/stretchable electronics, MEMS, biomedical diagnosis/therapy and prosthetics.

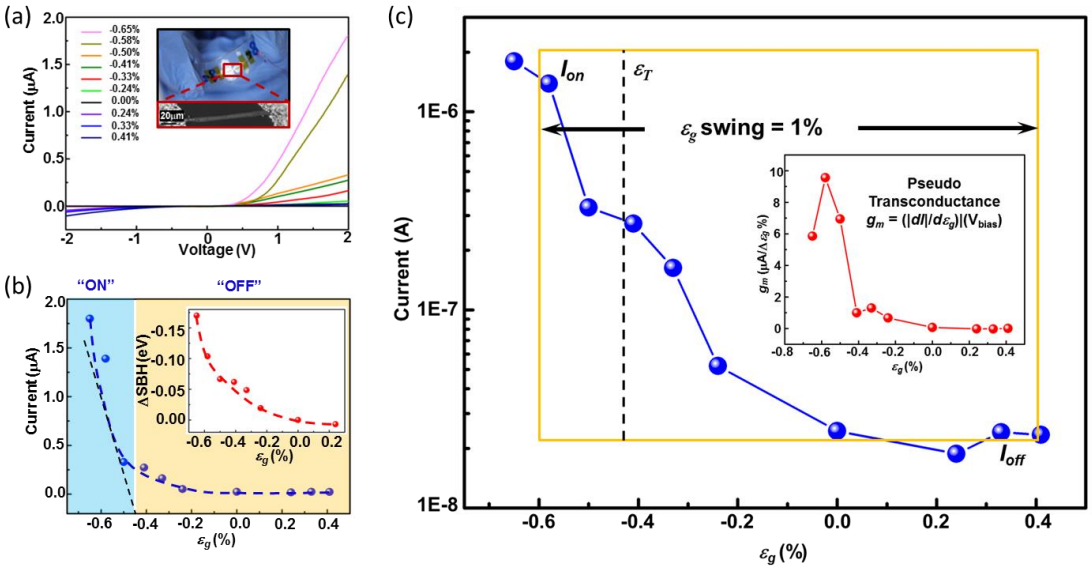

Figure 2.17 GaN NB piezotronic transistor. (a) I_{DS}-V_{DS} characteristics of GaN NB piezotronic transistor under different strains. The inset is a digital image and an optical image of a typical piezotronic transistor. (b) I_{DS}- $_g$ curve of a typical GaN piezotronic transistor measured at fixed bias of 2 V. The intersection between *x*-axis ($_g$) and the

black dashed line (tangent of the maximum slope region) indicates the threshold gate strain $_T$ is -0.43%. The inset presents the change of SBH *versus* applied strains. (c) Current-strain transfer characteristics of GaN NB SGT. The yellow square defines the 1% gate strain swing window. On and off currents are defined as the values derived at $_{g(on)}$ = $_T$ – 0.2% and $_{g(off)}$ = $_T$ + 0.8%. The inset presents the pseudo transconductance for this GaN NB SGT with bias voltage of 2 V.[51]

GaN NBs used in this study is the same as those used in previous section 2.2.1.1, where detailed materials properties have already been carefully characterized. The optical images of an as-fabricated GaN NB piezotronic SGT is shown in Figure 2.17a (Inset). Once the substrate was bent, a tensile/compressive strain was created in the NB since the mechanical behavior of the entire structure was determined by the substrate.[82, 83] I_{DS}-V_{DS} characteristic for single GaN NB SGT was obtained as a function of the strains induced in the SGT (Figure 2.17a), which exhibited the asymmetric trend in current response to strains at source and drain electrodes, as dictated by piezotronic effect. For piezotronic SGT, the applied mechanical strains produce the piezopotential which can effectively change the SBH at the M-S contact and thus function as the controlling input signal to gate/modulate the electrical transport in the SGT. The magnitude and the sign of applied strains can be calculated following the method reported elsewhere.[21, 83] The I_{DS}-ε_g curve of a typical GaN NB SGT measured at a fixed bias of 2 V (Figure 2.17b) shows that I_{DS} decreases as the strain gate ε_g increases (the tensile/compressive strains are defined as positive/negative respectively) and the threshold gate strain ε_T is determined as -0.43%. The I_{on} and I_{off} of the SGTs can be determined as 1.8 μA and 0.0188 μA respectively at $\varepsilon_{g(on)} = \varepsilon_T - 0.2\%$ and $\varepsilon_{g(off)} = \varepsilon_T + 0.8\%$, so that 20% of the ε_g swing below the threshold strain ε_T turns the piezotronic transistor on, while the rest 80% defines the "off" state, as illustrated in Figure 2.17c. The corresponding I_{on}/I_{off} ratio of 95.7 is comparable to

previously reported values from semiconductor nanowire based FET driven by electrical signals and piezotronic SGTs based on ZnO NWs.[21, 84]

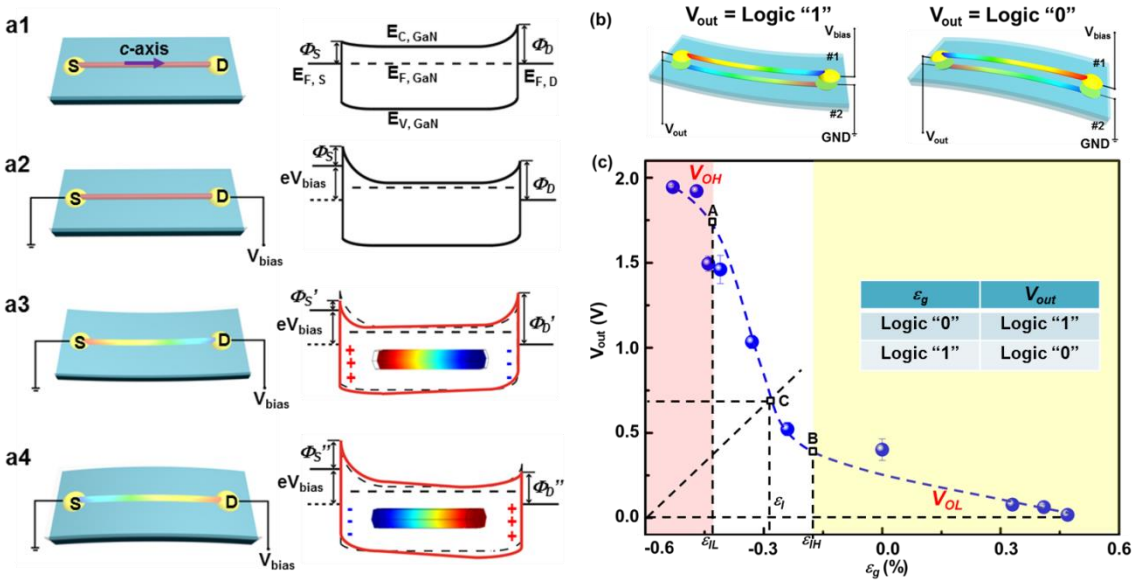

Figure 2.18 Working mechanism and GaN NB piezotronic inverter. (a) Schematic and band structure of GaN NB piezotronic transistor under (a1) strain free condition and no bias voltage; (a2) strain free condition and bias voltage V_{bias}; (a3) compressive strains and bias voltage V_{bias}; (a4) tensile strains and bias voltage V_{bias}. The crystallographic *c*-axis of the NB directs from source to drain as labeled. (b) Schematics of a GaN piezotronic inverter performing logic operations in responding to the strain inputs, which is defined as strains applied on #2 SGT. (c) The strain-voltage transfer characteristic (SVTC) and noise margins of the GaN NB piezotronic inverter at fixed bias of 2 V. The slope of black dashed line connecting origin and point C is 1; the slopes of the tangent at point B and C are both -1. Inset presents the truth table of a piezotronic inverter.[51]

The working principle of the GaN NB SGTs is explained using band diagrams as shown in Figure 2.18a. A strain-free GaN NB SGT formed Schottky contacts of different barrier heights (Φ_S and Φ_D) with metal electrodes at both ends (Figure 2.18a1). The transport characteristics of M-S-M structure based SGT devices are dominated by the reversely biased Schottky contact. When the drain was forward biased, the quasi-Fermi levels at the source ($E_{F, S}$) and the drain ($E_{F, D}$) were separated by an amount of eV_{bias}, where V_{bias} corresponds to the applied bias (Figure 2.18a2). Once a strain was applied

onto GaN NB, distribution of piezopotential was induced along *c*-axis, with its polarity depending on the sign of the strain (Figure 2.18a3, a4).[47] A negative piezopotential at the semiconductor side effectively increases the local SBH, while a positive piezopotential reduces the barrier height. When the GaN NB SGT was under compressive strain (Figure 2.18a3), SBH at the reversely biased source contact was reduced by the strain-induced positive piezopotential, which gave rise to an increased current in the device and hence the "on" state. Alternatively, by changing the compressive strain to tensile, as shown in Figure 2.18a4, SBH at the reversely biased source contact was increased by the strain-induced negative piezopotential, resulting in the decreased current and the "off" state. Therefore, by changing the externally applied strains from compressive to tensile, the electrical output of piezotronic SGTs can be tuned from "on" to "off". The role played by piezopotential is to effectively change the local contact characteristics through an internal field which depends on the crystallographic orientation of the material and the sign of the strain. The changes in SBH under different strains can be derived as[28]:

$$\ln[I(\varepsilon_g)/I(0)] = -\Delta\Phi_S/kT \quad (1)$$

where $I(\varepsilon_g)$ and $I(0)$ are the currents measured through the SGT at a fixed bias with and without applied strains, respectively. The corresponding $\Delta\Phi_S$-ε_g curve clearly presents the modulation effect of strains on contact characteristics (Figure 2.17b).

The GaN NB based piezotronic logic gates can be realized by assembling GaN NB SGTs. Figure 2.18b shows the schematic of a GaN NB piezotronic inverter (NOT gate). Two GaN NB SGTs were packaged on the top and bottom surfaces of the same flexible substrate. By defining the strain applied on #2 SGT (the bottom one) as the mechanical logic input of this inverter, an experimental truth table and strain-voltage

transfer characteristic (SVTC) for piezotronic strain-gated inverter can be obtained (Figure 2.18c). When the inverter was bent upward (Figure 2.18b, left), a compressive strain of -0.6% was induced in #1 transistor, while a tensile strain of same magnitude was simultaneously created in #2 transistor, leading to the complementary "on" and "off" states in #1 and #2 SGTs, respectively. In this case, an electrical logic "1" output (high voltage output) was observed. On the other hand, if the inverter was bent downward (Figure 2.18b, right), #1 SGT was now turned "off" and #2 SGT was "on", with an electrical logic "0" output (low voltage output) observed. The GaN piezotronic strain-gated inverter thus operates in a similar way to the conventional complementary metal oxide semiconductor (CMOS) inverters and performs logic inversion operation between mechanical and electrical domains.

The SVTC and noise margins[21] of the GaN NB piezotronic inverters were obtained by plotting the measured output voltages *versus* the applied external strains, as shown in Figure 2.18c. V_{OH} and V_{OL} represent the high and low output voltage of the piezotronic inverter, with theoretical values of $V_{OH} = V_{bias}$ = 2 V and V_{OL} = 0 V. Here the experimental values of V_{OH} and V_{OL} are 1.94 V and 0.017 V, respectively. The difference between experimental and theoretical values was probably caused by the voltage drop across the SGT device which was "on" during the measurement. The logic swing of the piezotronic inverter is defined as (V_{OH} - V_{OL}) = 1.92 V. The switching threshold strain of the piezotronic inverter ε_I, at which the electrical output of the inverter switches between logic "1" and "0" states, is determined at point C with corresponding strain value of -0.29% (Figure 2.18c). The numerical value for slope of the dashed line connecting the origin and point C is 1. In order to characterize the effect of mechanical input (strain gating signal)

on the electrical output of inverter, two positions where the numerical value for slope of the SVTC curve equals -1 is labeled as point A and B (Figure 2.18c). Point A (ε_{IL} = -0.44%) and B (ε_{IH} = -0.17%) represent the largest input strain corresponding to output logic "1" and the smallest input strain corresponding to output logic "0", respectively. When the applied strain lies within the region where $\varepsilon < \varepsilon_{IL}$ (pink zone in Figure 2.18c), the electrical output of the inverter is logic "1"; when the applied strain lies within the region where $\varepsilon > \varepsilon_{IH}$ (yellow zone in Figure 2.18c), the electrical output of the inverter is logic "0". In the logic low mechanical input region, #1 SGT is "on" and #2 SGT is "off"; while in the logic high mechanical input region, #1 SGT is "off" and #2 SGT is "on".

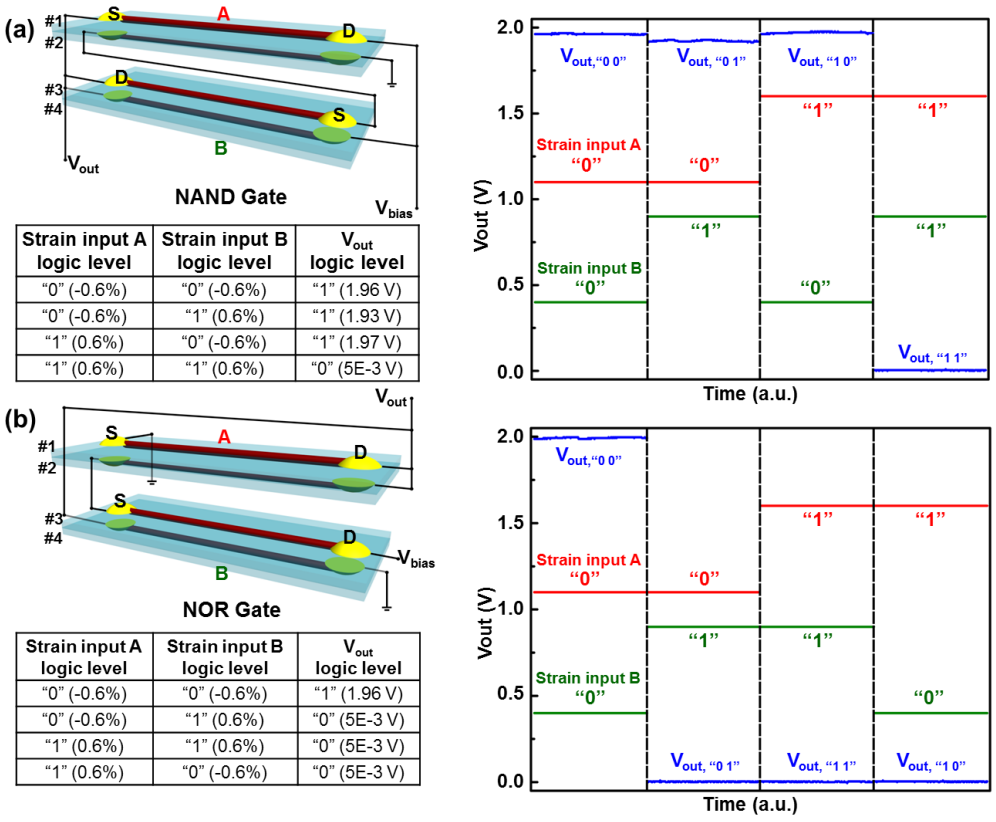

Strain input A logic level	Strain input B logic level	V_{out} logic level
"0" (-0.6%)	"0" (-0.6%)	"1" (1.96 V)
"0" (-0.6%)	"1" (0.6%)	"1" (1.93 V)
"1" (0.6%)	"0" (-0.6%)	"1" (1.97 V)
"1" (0.6%)	"1" (0.6%)	"0" (5E-3 V)

Strain input A logic level	Strain input B logic level	V_{out} logic level
"0" (-0.6%)	"0" (-0.6%)	"1" (1.96 V)
"0" (-0.6%)	"1" (0.6%)	"0" (5E-3 V)
"1" (0.6%)	"1" (0.6%)	"0" (5E-3 V)
"1" (0.6%)	"0" (-0.6%)	"0" (5E-3 V)

Figure 2.19 GaN NB piezotronic NAND and NOR logic gates. Schematic of the GaN NB piezotronic (a) NAND gate and (b) NOR gate. Experimental truth table is presented with physical values following each corresponding logic level. The right part shows the measured electrical output voltages of NAND/NOR gate *vs.* the mechanical input strains.

Blue lines are the electrical output voltages of NAND/NOR gate, red and green lines represent the mechanical strains input applied on inverter A and B correspondingly.[51]

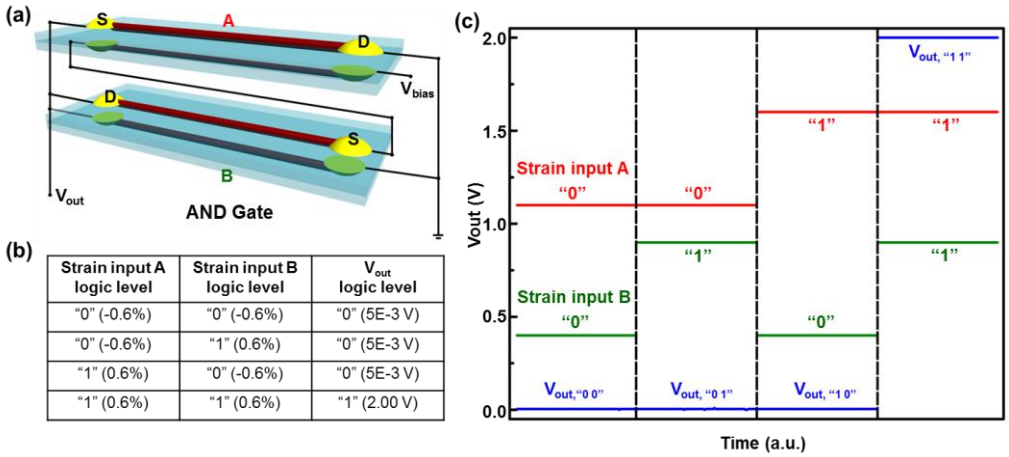

(b)

Strain input A logic level	Strain input B logic level	V_{out} logic level
"0" (-0.6%)	"0" (-0.6%)	"0" (5E-3 V)
"0" (-0.6%)	"1" (0.6%)	"0" (5E-3 V)
"1" (0.6%)	"0" (-0.6%)	"0" (5E-3 V)
"1" (0.6%)	"1" (0.6%)	"1" (2.00 V)

Figure 2.20 GaN NB piezotronic AND logic gate. (a) Schematic of the GaN NB piezotronic AND gate. (b) Experimental truth table of piezotronic AND logic gate, with physical values following each corresponding logic level. (c) Measured electrical output voltages of AND gate *versus* the mechanical input strains. Blue lines are the electrical output voltages of AND gate, red and green lines represent the mechanical strains input applied on inverter A and B correspondingly.[51]

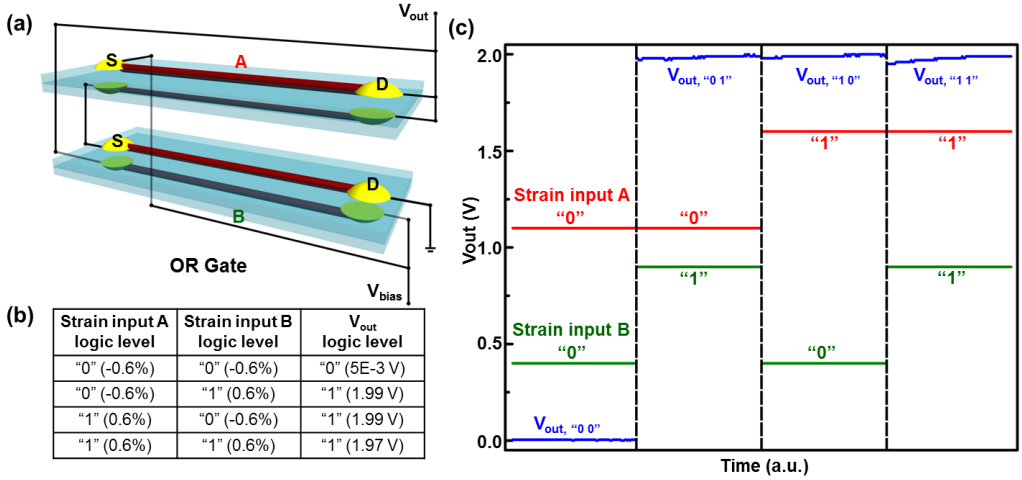

(b)

Strain input A logic level	Strain input B logic level	V_{out} logic level
"0" (-0.6%)	"0" (-0.6%)	"0" (5E-3 V)
"0" (-0.6%)	"1" (0.6%)	"1" (1.99 V)
"1" (0.6%)	"0" (-0.6%)	"1" (1.99 V)
"1" (0.6%)	"1" (0.6%)	"1" (1.97 V)

Figure 2.21 GaN NB piezotronic OR logic gate. (a) Schematic of the GaN NB piezotronic OR gate. (b) Experimental truth table of piezotronic OR logic gate, with physical values following each corresponding logic level. (c) Measured electrical output voltages of OR gate *versus* the mechanical input strains. Blue lines are the electrical output voltages of OR gate, red and green lines represent the mechanical strains input applied on inverter A and B correspondingly.[51]

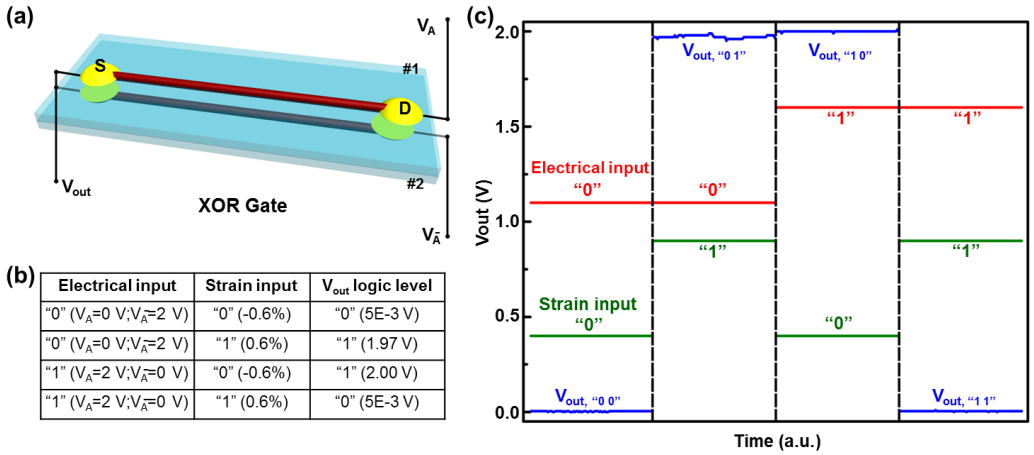

Electrical input	Strain input	V_{out} logic level
"0" (V_A=0 V;$V_{\bar{A}}$=2 V)	"0" (-0.6%)	"0" (5E-3 V)
"0" (V_A=0 V;$V_{\bar{A}}$=2 V)	"1" (0.6%)	"1" (1.97 V)
"1" (V_A=2 V;$V_{\bar{A}}$=0 V)	"0" (-0.6%)	"1" (2.00 V)
"1" (V_A=2 V;$V_{\bar{A}}$=0 V)	"1" (0.6%)	"0" (5E-3 V)

Figure 2.22 GaN NB piezotronic XOR logic gate. (a) Schematic of the GaN NB piezotronic XOR gate. Strain input was defined as strains applied to #2 SGT; electrical complementary input was defined as labeled in (b) Experimental truth table of piezotronic OR logic gate, with physical values following each corresponding logic level. The drain electrode of #1 (#2) SGT was connected to the electrical input V_A ($V_{\bar{A}}$). (c) Measured electrical output voltages of XOR gate *versus* the inputs. Blue lines are the electrical output voltages of XOR gate, red lines represent the electrical complementary input and the green lines represent the mechanical strains input.[51]

More universal piezotronic logic operations can be achieved by systematically integrating GaN NB piezotronic inverters which are gated individually by separate strain inputs. Figures 2.19a and b show the schematics of GaN NB piezotronic NAND gate and NOR gate respectively, by connecting two GaN NB piezotronic inverters properly in each case. The measured electrical output voltages of NAND gate (NOR gate) *versus* the mechanical input strains were plotted in the right part of Figure 2.19a (2.19b). Blue lines are the experimentally measured electrical output voltages of NAND gate (NOR gate), while red and green lines represent the logic levels of input mechanical strains applied on inverter A and B respectively. The physical values of the output and input signals were listed in the experimental truth tables in Figure 2.19. The strain input A was defined as the strain applied on #2 SGT in NAND gate and #1 SGT in NOR gate, while the strain input B was defined as the strain applied on #3 SGT in NAND gate and #4 SGT in NOR

gate. In a similar manner, piezotronic strain-gated AND gate, OR gate and XOR gate have also been realized by integrating piezotronic inverters. The corresponding schematics and experimental results for these piezotronic logic gates are presented in Figures 2.20-2.22, respectively.

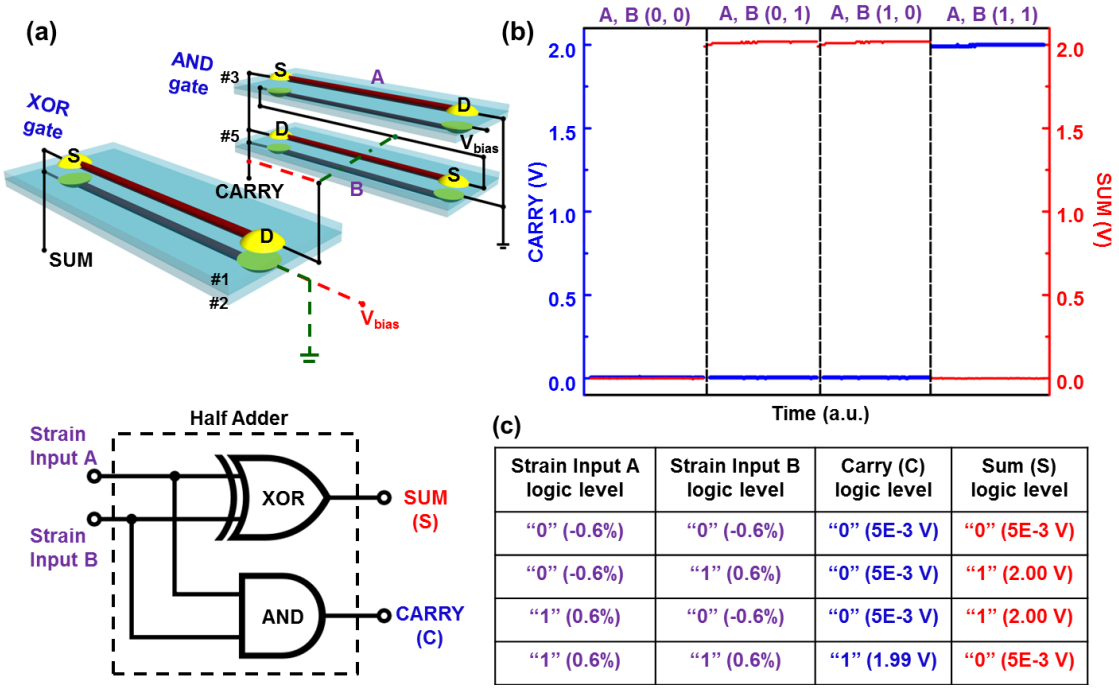

Strain Input A logic level	Strain Input B logic level	Carry (C) logic level	Sum (S) logic level
"0" (-0.6%)	"0" (-0.6%)	"0" (5E-3 V)	"0" (5E-3 V)
"0" (-0.6%)	"1" (0.6%)	"0" (5E-3 V)	"1" (2.00 V)
"1" (0.6%)	"0" (-0.6%)	"0" (5E-3 V)	"1" (2.00 V)
"1" (0.6%)	"1" (0.6%)	"1" (1.99 V)	"0" (5E-3 V)

Figure 2.23 GaN NB piezotronic Half Adder. (a) Schematics of GaN NB piezotronic half adder by integrating one piezotronic XOR gate and one piezotronic AND gate. (b) Measured electrical output voltages of the half adder. Blue lines represent the CARRY output; red lines represent the SUM output. The symbol "A, B (0, 1)" means mechanical strain input A is logic "0" and mechanical strain input B is logic "1", the rest are defined in a similar way. (c) Experimental truth table of GaN NB piezotronic half adder, physical values following the corresponding logic levels.[51]

By further integrating two different piezotronic strain-gated logic gates in a specific way, the piezotronic logic computation based on GaN NBs was demonstrated for the first time, which performed arithmetic operations over mechanical signals and provided corresponding electrical outputs. Figure 2.23a presents the schematic of a piezotronic strain-gated one-bit half adder, which consists of a piezotronic XOR gate and

a piezotronic AND gate. The strain input for piezotronic XOR gate and the strain input for inverter B in piezotronic AND gate was unified and noted as strain input B for the half adder (Figure 2.23); the electrical complementary input for XOR gate and the strain input for inverter A in piezotronic AND gate was unified and noted as strain input A for half adder (Figure 2.23). The unification of two strain inputs into strain input B for the half adder is straightforward by defining the strain applied to #2 SGT in XOR gate and #5 SGT in AND gate as the strain input B. To unify the electrical complementary input for XOR gate and the strain input for inverter A in AND gate, input V_A of XOR gate needed to be unified with strains applied to #4 SGT in the AND gate, which was defined as strain input A of the half adder. When the mechanical strain input A of half adder was logic "0", XOR gate was connected to AND gate by the red dashed lines, as shown in Figure 2.23a; when the mechanical strain input A was logic "1", XOR gate was connected to AND gate by the green dashed lines (Figure 2.23a). It is in this way that the electrical complementary input for XOR gate and the mechanical strain input for AND gate were unified into one mechanical input and being kept consistent to each other to perform addition computations in a similar manner to the conventional electrically-controlled half adder. Two measured electrical outputs of the piezotronic half adder, labeled as CARRY and SUM, were plotted in blue and red lines respectively, as shown in Figure 2.23b. The corresponding experimental truth table (with the physical values and logic levels of input and output signals) of piezotronic strain-gated half adder is presented in Figure 2.23c, which confirms clearly that piezotronic strain-gated half adder performs the one-bit binary addition over input mechanical strains and provides corresponding computation results in electrical domain. As demonstrated by the above strain-gated logic operations,

in contrary to traditional FET, the two-terminal strain-gated piezotronic SGTs process/interface mechanical strains input directly with the electrical controlling output signals under the influence of the self-generated inner-crystal potential (piezo-potential).

In summary, by utilizing the piezoelectric polarization charges created upon straining at metal-GaN NB interface to modulate transport of local charge carriers across the Schottky barrier, the piezotronic effect has been applied to convert mechanical stimuli into electronic controlling signals in GaN NB SGTs. By further assembling and integrating GaN NB SGTs, universal logic devices such as NOT, AND, OR, NAND, NOR and XOR gates have been demonstrated for performing mechanical-electrical coupled piezotronic logic operations. Moreover, basic piezotronic arithmetic operation such as one-bit binary addition by half-adder has been implemented for the first time to perform computations over mechanical signals and provide corresponding electrical output results. The demonstrated concept of strain-gated piezotronic logic operation/computation may find novel applications in human-machine interfacing, MEMS, biomedical diagnosis/therapy and prosthetics.

2.2.3 Piezotronics Sensors

Schottky-contacted structure provides a new approach for design, fabrication and application of ultrasensitive sensors with fast response time and outstanding response signals in various sensing systems. The SBH at local M-S interface plays a dominant role in determining the overall charge carriers transport process of these Schottky-contacted sensors. The sensitivity, response signals as well as recovery time of these sensors are all determined by the changes of SBH upon the adsorption of analyte molecules in a passive

manner. The original barrier height of local Schottky contact is essential to the performances of these sensors and a moderate starting point of SBH leads to optimized performances under various conditinos[85]. However, the barrier height is usually built-in with a fixed value in those sensors and the performances of sensors cannot be modified actively based on ambient environment. Therefore, it is essential to develop an effective method to modulate the starting point of SBH actively to guarantee the delivery of an ultrasensitive sensor with expected performances to the maximum extent.

Piezotronic effect[16] is a two-way coupling effect between semiconducting and piezoelectric properties of materials with non-central symmetry, such as wurtzite and zinc blende family. Upon straining, a piezoelectric potential (piezo-potential) distribution is induced inside the nanostructure along a certain crystal orientation, with piezoelectric polarization charges presented at local M-S interface in the semiconductor side. Considering the non-mobile, ionic charges nature, these strain-induced piezoelectric charges can only be partially screened instead of completely cancelled by free charge carriers. As for Schottky-contacted sensors fabricated with piezoelectric semiconductor materials, external strains can be utilized as a "strain gate" to tune/control the SBH by inducing piezoelectric polarization charges at the vicinity of local M-S interface. In this section, we present the piezotronic effect as an effective approach to enhance/optimize the performances of Schottky-contacted nanostructure sensors for pH,[52] glucose,[54] protein,[53] gas[56] and humidity[55] sensing applications.

2.2.3.1 Piezotronics pH Sensors[52]

The fabrication of a ZnO NW pH sensor follows the method reported by us previously[86]. The ZnO NW was synthesized *via* a vapor-solid (VS) method, which gave high quality and long NWs. The morphology of the as-fabricated ZnO NWs is presented in Figure 2.24a, with lengths of several hundreds of micrometers and diameters varying from tens of nanometers to several micrometers. An enlarged SEM image of an individual ZnO NW is shown as an inset in Figure 2.24a. Then, a long ZnO NW was chosen and dispersed onto a polyethylene terephthalate (PET)/or a polystyrene (PS) substrate; both ends of the ZnO NW were fixed by silver paste, serving as electrodes as well. After that a layer of epoxy was used to fully cover the two silver electrodes, preventing them from exposing in the buffer solution during the following test. An optical microscopy image of an as-fabricated device is presented in Figure 2.24b, showing that the length of the ZnO NW reaches over hundreds of micrometers. A real device is given in Figure 2.24c.

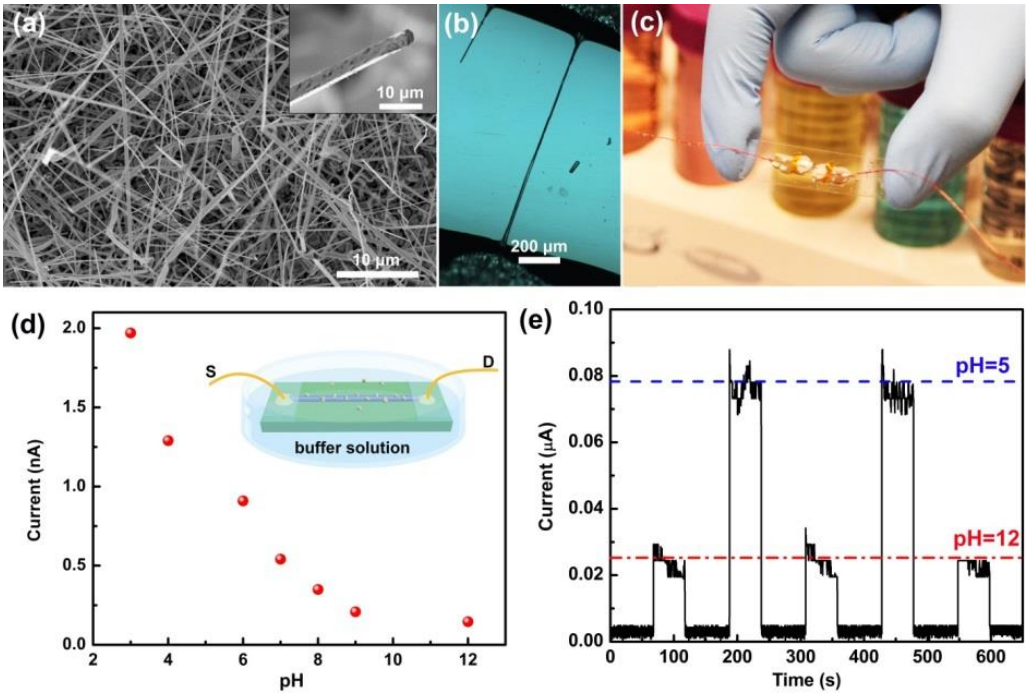

Figure 2.24 SEM image of the morphology of the as-synthesized ZnO NWs. The insert is a high-magnification image of an individual wire. (b,c) Optical microscopy and digital image of a ZnO NW pH sensor. (d) The response of the sensor to the pH varying from 3 to 12, no external strain was applied, just like traditional NW based sensors. (e) The repeatability of the ZnO sensor pH sensor at pH 5 and 12.[52]

The response of the NW sensor to the pH was tested by measuring its transportation properties in different buffer solutions. During this test, no strain was applied on the device, thus the signal level is at nA range, just like traditional NW based sensors. The results in Figure 2.24d demonstrate that signal of the ZnO NW sensor increased stepwise with discrete changing in pH from 12 to 3, showing a good response to the pH changing. These results are controlled by the "floating gate", and can be understood by considering the surface functionality of the ZnO NWs in different buffer solutions. At low pH, H^+ is adsorbed on the surface of the ZnO NW, and acts as a positive gate, which increases the electron carriers in the n-type ZnO NW and thus increases the conductance. At high pH, OH^- is adsorbed on the surface of the ZnO NW, which correspondingly depletes the electron carriers, and causes a decrease in conductance[1]. The response of the NW sensor to the pH changing is stable and repeatable (Figure 2.24e).

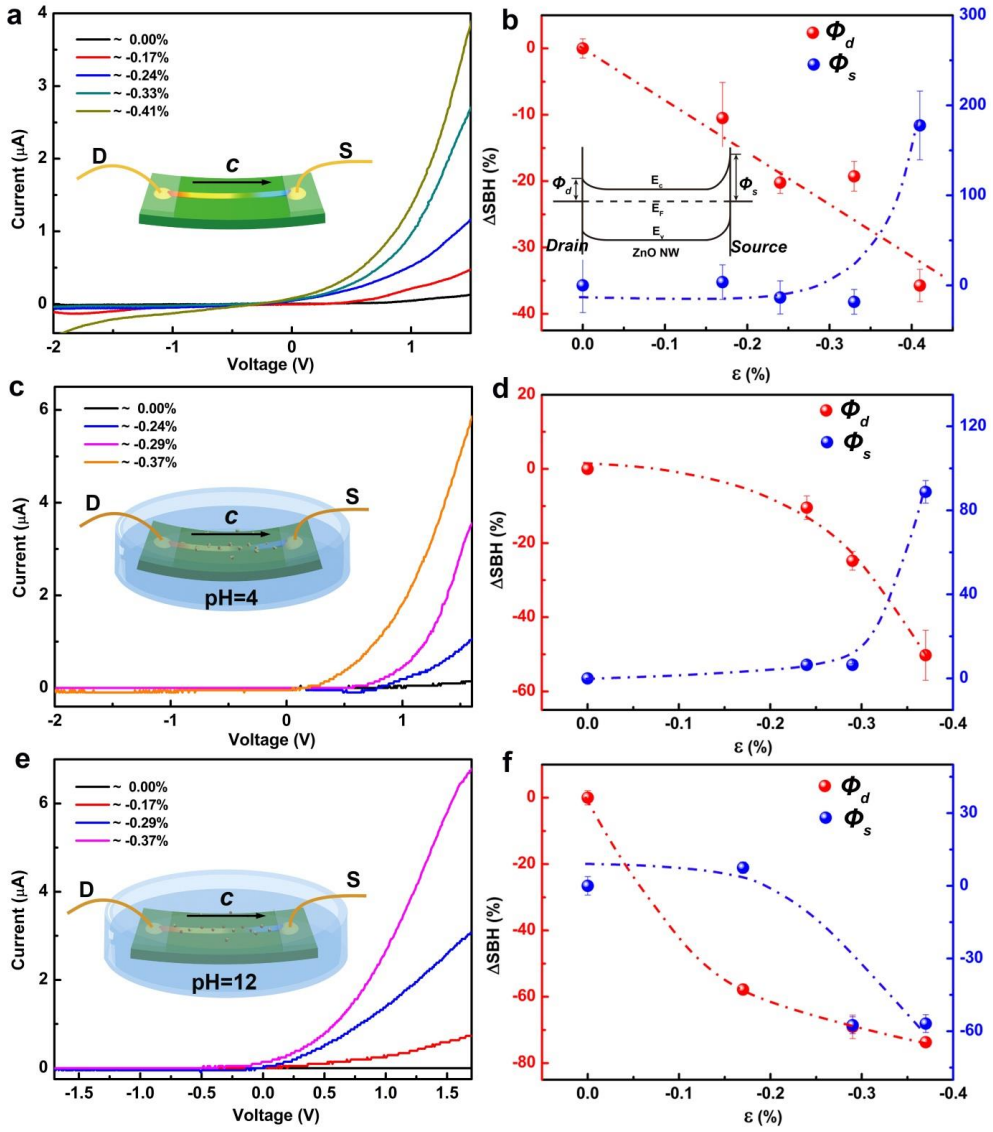

Figure 2.25 The stability and repeatability of the device under external applied strain in different environments, such as in ambient and buffer solutions. (a, c, e) I-V curves of the sensor when they are under different strains when the device is in ambient air (a), in a buffer solution pH = 4 (c), and in a buffer solution pH = 12 (e), with the *c*-axis of ZnO NW parallel to the longitudinal axis of the PS substrate. The right side are the corresponding relative changes of the forward and reversely biased Schottky barrier height (ΔSBH) *vs.* the applied strain extracted from the theoretical simulations corresponding to (a, c, e), respectively. An energy band diagram of such MSM structure is presented in (b).[52]

Figure 2.25 shows the stability and repeatability of the device under external applied strain in different environments, such as in ambient and buffer solutions. Since

the tensile strain could easily cause the failure of the ZnO NW, only compressive strain was applied on the device. One end of the PS substrate was fixed tightly on a manipulation holder, with the other end free to be bent. A three-dimensional (3D) mechanical stage with movement resolution of 10 μm was used to apply a strain on the free end of the PS substrate, which can be calculated according to Yang *et al.'s* work[87]. *I-V* characteristics of the devices at different strains in different solution (pH = 4 and 12) were recorded in Figure 2.25, with the *c*-axis of the ZnO wire pointing from drain to source. The insets in Figures 2.25a, c and e are corresponding test conditions. We can find that the device has similar behaviors when it is subjected to an external strain, either in the buffer solutions or in the ambient environment. An energy band diagram of such an M-S-M structure was presented as insets in Figure 2.25b. It is clear that a compressive strain leads to a signal current increasing from nA to μA with a strain about -0.4% applied when the device is subjected to a bias voltage of 1.5 V, which is mainly controlled by the Schottky barrier Φ_d in such an M-S-M structure[49, 59, 62, 88]. The Schottky barrier heights Φ_d and Φ_s at the drain and source sides in Figure 2.25a, c and e were quantitatively extracted through a GUI program PKUMSM developed by Peng *et al.*[62]. The relative changes of the Schottky barrier heights (ΔSBH) at both sides are presented at the right-hand side of Figure 2.25.

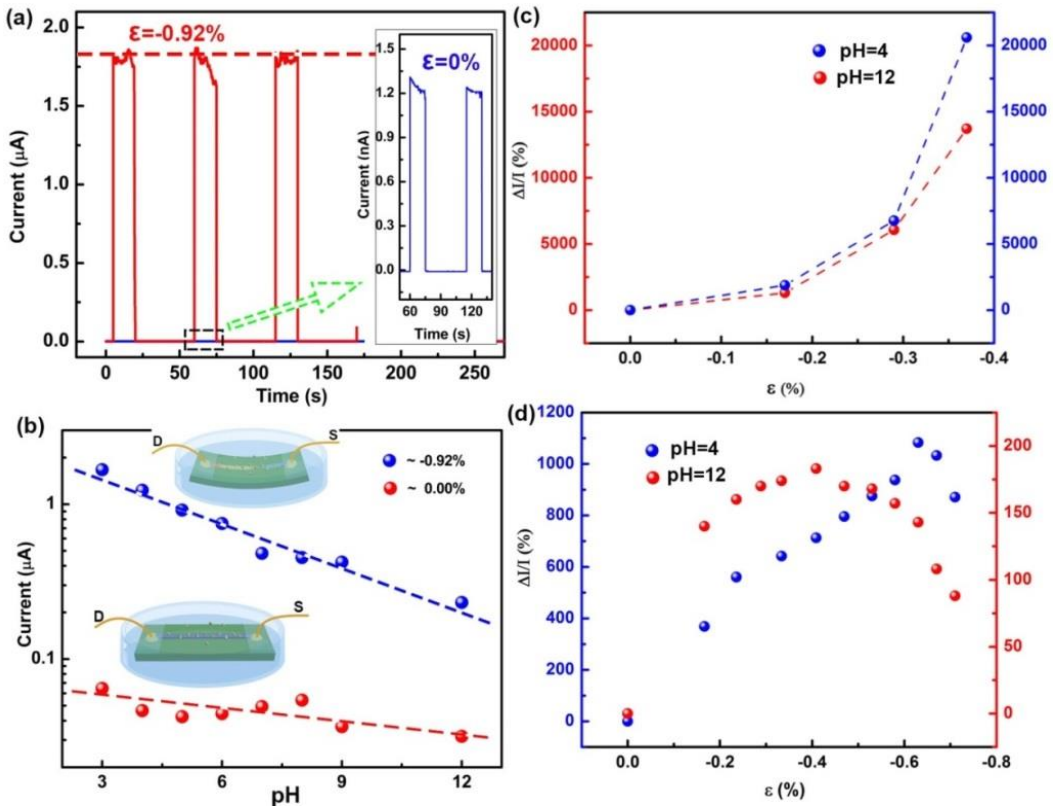

Figure 2.26 The signal level and the sensitivity of the sensor are increased by the piezotronics effect. (a) The output signal of a sensor in a buffer solution with pH = 5 when the strain is "off" (blue) and "on" (red). The signal is increased about 1500 times when a compressive strain of ε = -0.92% was applied. (b) The response of the sensor to the pH varying from 3 to 12, when the device is strain off (red) and on (blue). (c, d) The relative change of the signal current responses to the strain applied on the device in the buffer solution with pH = 4 (blue) and 12 (red), respectively, which can be divided into two categories: (c) monotone increasing, (d) the signal current showing a maximum in responding to the applied strain.[52]

The signal level of the device is increased, and the sensitivity of the device is enhanced as well by the piezotronics effect, as shown in Figure 2.26. When a strain-free sensor was immersed in a buffer solution with pH = 5, the signal level in the device was only 1.2 nA when a bias voltage of 0.5V was applied, as the blue curve shown in the insect of Figure 2.26a. Thereafter, this current jumped to 1.75 μA when a compressive strain of ε = -0.92% was applied, increased by nearly 1500 times in magnitude. The responses of the ZnO NW pH sensor to the full pH changing range when the external

strain was “off” (red curve) and “on” (blue curve) are presented in Figure 2.26b. It indicates the same phenomenon at the full pH scale that the response signal level of the device is at nA level when the ZnO NW is strain free, and the current response of the device is at μA level when the ZnO NW is compressive strained to ε = -0.92%. The piezotronic effect can increase not only the signals level of the sensor, but also the sensitivity, as can be seen from the slope of the current-pH relationship in Figure 2.26b. Larger slope means higher sensitivity and better selectivity for the pH sensor.

The piezotronic effect increases the signal level of the device, and enhances the sensitivity of the device by tuning the effective heights of the two SBs and thus the characteristic of the NW sensor. The decrease of the Φ_d increases the signal current level, while the increase of the Φ_s decreases the signal current. As a result, two kinds of characteristic relationships between the sensor performance and the applied strain have been observed. The first one is that the signal current increases with applied strain, as shown in Figure 2.26c, showing the stepwise monotone increased signal current from nA to μA range at pH = 4 (red curve) and 12 (blue curve). In the second case, the signal current shows a maximum in responding to the applied strain.

2.2.3.2 Piezotronics Glucose Sensors[54]

ZnO NWs used in this work were synthesized *via* a high temperature thermal evaporation process[19, 89, 90], with length of several hundreds of micrometers and diameter varying from tens of nanometers to a few micrometers. The glucose sensor was fabricated by transferring and bonding an individual ZnO NW laterally onto a polyethylene terephthalate (PET)/or a polystyrene (PS) substrate, with its *c*-axis in the plane of the

substrate pointing to the source. Silver paste was used to fix the two ends of the NW, serving as the source and drain electrodes, respectively. A thin layer of epoxy was applied to isolate both end-electrodes from the environment in order to avoid potential contacting between electrodes and the glucose solution during the measurements. For the surface decoration, 0.005 ml GOx with a concentration of 10 mg ml^{-1} was added onto the NW and incubated for two hours in the fume hood to dry naturally[91], this process was repeated four times followed by rinsing with deionized (DI) water to remove those non-firmly adsorbed GOx, then the devices were ready to perform as glucose sensors. A schematic in Figure 2.27a shows a GOx-decorated strain free ZnO NW glucose sensor in glucose solution. The same device under compressive strain is presented in Figure 2.27b. A real device is given in Figure 2.27d as the inset.

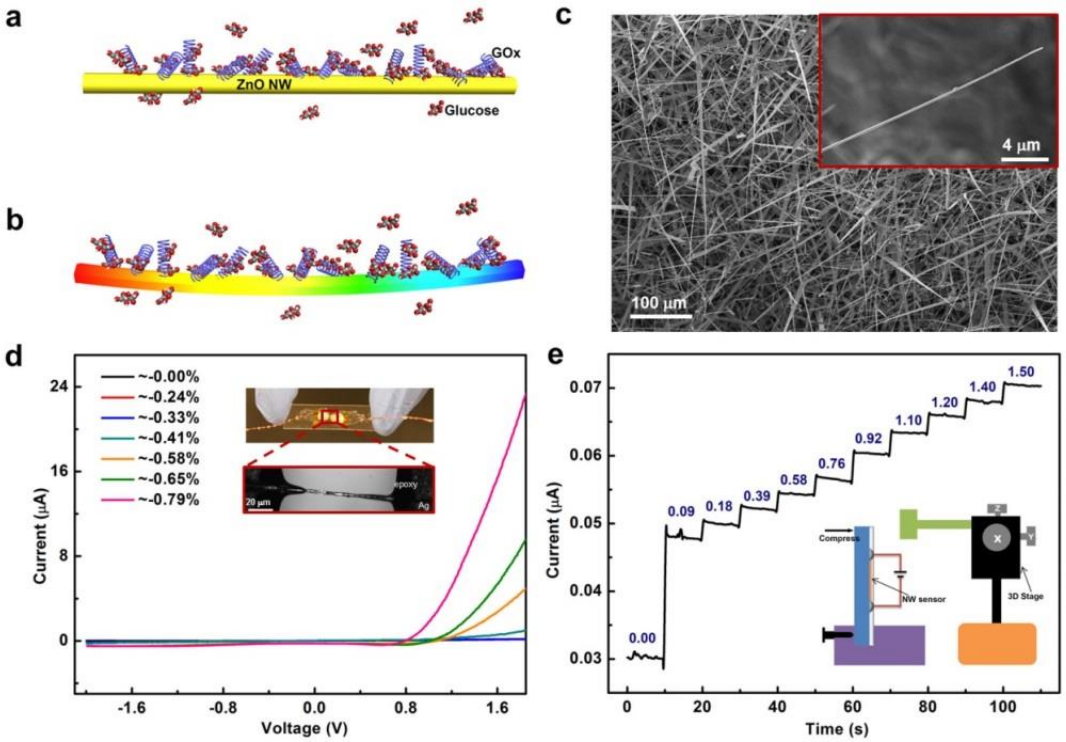

Figure 2.27 A schematic of ZnO NW decorated with GOx surrounded by glucose molecules under (a) no strain and (b) compressive strain. (c) SEM image of the morphology of the as-synthesized ZnO NWs. The inset presents a single ZnO NW in higher resolution. (d) *I-V* characteristics of a ZnO NW glucose sensor under different

compressive strains, no glucose added. The inset shows a digital image and an optical microscopy image of the ZnO NW glucose sensor. (e) *I-t* characteristics of another ZnO NW glucose sensor in different glucose concentrations, numbers labeled in unit of (g L^{-1}), no external strains applied. The inset presents a schematic of the experiments set-up.[54]

The response of the ZnO NW glucose sensors to different strains was investigated by applying a compressive strain step by step, up to -0.79%, with the sensors totally immersed in the pure DI water instead of glucose solution. Experiment set-up is shown in Figure 2.27e as the inset, one end of the device was fixed tightly on a manipulation holder, while the other end was free to be bent by a three-dimensional (3D) mechanical stage with movement step resolution of 10 μm. The magnitude of compressive strains can be calculated according to Yang *et al.*'s work[87]. Figure 2.27d presents the *I-V* characteristics of a device when applied different compressive strains. It is obvious to see that the output signal, i.e. currents here, experienced a tremendous increase as the device was compressively bent. At a bias voltage of 1.8 V, the current increased from 0.15 μA all the way to more than 25 μA, indicating a 150 times increase in magnitude as -0.79% compressive strain was applied.

The response of a strain free ZnO glucose sensor to different glucose concentrations is presented in Figure 2.27e, measured at a fixed bias of 2 V. By gradually adding glucose into the solution drop by drop, the output signal clearly increased step by step as expected. At each step, the current stayed at a distinguishable value for more than 10 seconds, which shows a good response and stability of the ZnO NW glucose sensors. Being able to response to the glucose concentrations ranging from 0.09 g L^{-1} to 1.5 g L^{-1}, the ZnO NW glucose sensor can cover the typical range of human body blood sugar level which is 0.8 g L^{-1} to 1.2 g L^{-1}, making it a qualified candidate for glucose monitoring system.

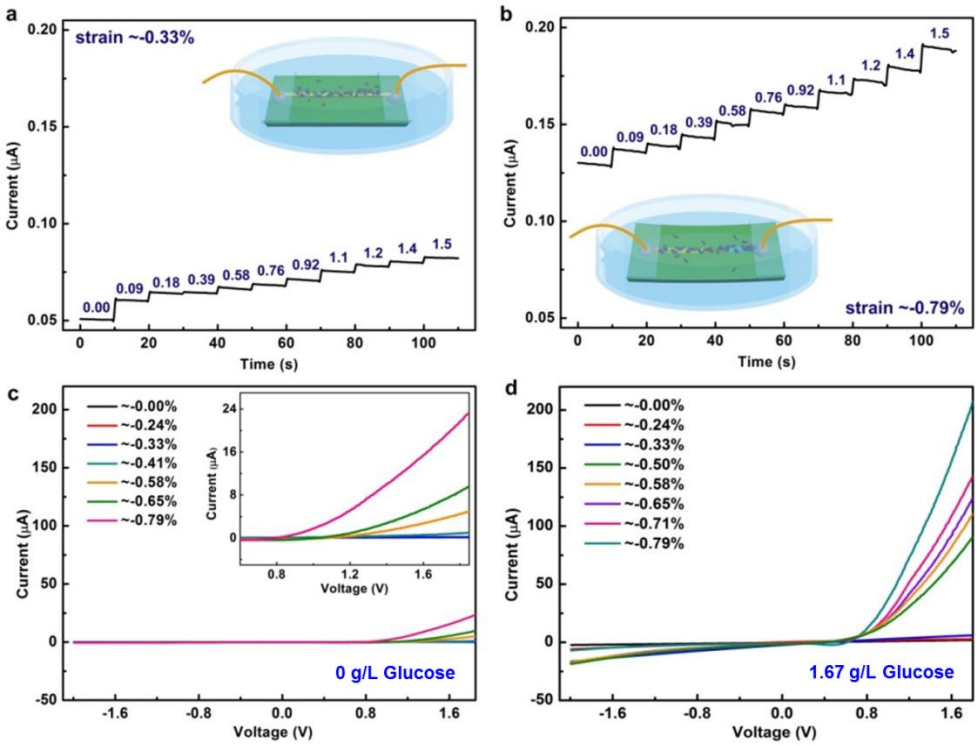

Figure 2.28 *I-t* characteristics of a ZnO NW glucose sensor in different glucose concentrations, numbers labeled in unit of (g L^{-1}), under (a) -0.33% compressive strain and (b) -0.79% compressive strain. The insets are schematics of adding glucose step by step to the glucose sensor under -0.33% and -0.79% compressive strain, respectively. *I-V* characteristics of the ZnO NW glucose sensor under different compressive strains, in a certain glucose concentration of (c) 0 g L^{-1} and (d) 1.67 g L^{-1}. The inset of (c) is an enlarged *I-V* curve to present more details.[54]

I-t and *I-V* characteristics of the devices at different strains and various glucose concentrations were recorded to investigate the piezotronic effect on the performances of ZnO NW based glucose sensors. Two series of experiments were carried out by changing the strains and glucose concentrations simultaneously: the first series experiments were conducted by adding glucose solution step by step under a fixed compressive strain at each time, the *I-t* characteristics of a glucose sensor under compressive strain -0.33% and -0.79% are presented in Figure 2.28a and b, respectively. It can be seen that the overall output signals were increased by a large amount when increased the compressive strain.

Moreover, it is easier to tell the current difference between two glucose concentrations as increasing the externally applied strain. This result indicates that the piezotronic effect can improve the sensing resolution of the glucose sensor, which is due to the non-linear *I-V* transport properties created by the Schottky barrier at the contacts of the M-S-M structure, similar to an amplification effect. By resolution here we mean the ability of the smallest concentration change that can be distinguished by the sensor and the measuring system. The second series experiments were conducted by applying compressive strains step by step in glucose solution of a certain concentration at each time, the *I-V* characteristics of a device in glucose solution of concentration 0 g L^{-1} and 1.67 g L^{-1} are shown in Figure 2.28c and d, respectively. It is obvious that the current went up by tens of times in magnitude when the glucose concentration was increased. This result again confirms the former conclusion that the higher the glucose concentration, the higher the output signals.

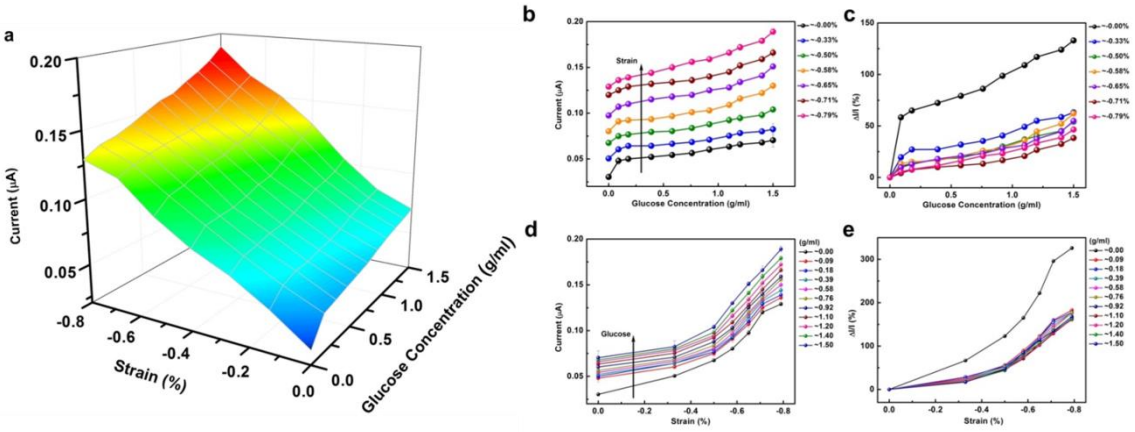

Figure 2.29 Piezotronic effect on the performances of ZnO NW glucose sensors. (a) 3D surface graph indicating the current response of the ZnO NW glucose sensor under different strains and glucose concentrations. (b-c) Absolute and relative current response of the ZnO NW glucose sensor in different glucose concentrations, with compressive strain ranging from 0 to -0.79%, respectively. (d-e) Absolute and relative current response of the ZnO NW glucose sensor under different compressive strains, with glucose concentration ranging from 0 to 1.50 g L^{-1}, respectively. Data of (b-e) were extracted from (a).[54]

By systematically investigating the glucose sensors response to continuously changed compressive strains and glucose concentrations, a 3-dimensional (3D) surface graph was plotted, as presented in Figure 2.29a. An overall trend of how the output signal varied with changing both the compressive strains and glucose concentrations can be simultaneously derived from this 3D graph. The current clearly went up as the glucose concentration or the compressive strain increased. Four 2D graphs are shown in Figures 2.29b-e for more details and information, which are extracted from Figure 2.29a by projecting on I-Strain surface and I-Glucose Concentration surface, respectively. Figures 2.29b and c show the absolute and relative current response of ZnO NW glucose sensors to various glucose concentrations when the compressive strain was fixed in each curve, ranging from -0.00% to -0.79%, respectively. Figures 2.29d and e present the absolute and relative current response of ZnO NW glucose sensors to different compressive strains under a certain glucose concentration in each curve, differing from 0.00 g L^{-1} to 1.50 g L^{-1} step by step. The results in Figure 2.29b show that the slope of curves became deeper and deeper when the applied strain increased, which means the sensing resolution is improved by the piezotronic effect. The same improvement can be derived more easily from Figure 2.29d, which indicates that the current difference between two certain glucose concentrations was significantly enlarged when applying more compressive strain. From Figure 2.29c it can be seen, the relative change in current by adding glucose can be as large as 130% and mostly around 25% to 50%. In Figure 2.29e, this relative change in current has the largest value more than 300% and mostly around 150%, when applied more compressive strains. These results indicate that, applying strains can significantly improve the sensitivity of glucose sensors; the relative change of output

signals in this case is even much larger than that in the case of adding glucose. Therefore, the performance of the glucose sensor was generally enhanced by the piezotronic effect when applying a -0.79% compressive strain on the device, and the output signal level was increased by more than 200% in magnitude; the sensing resolution and sensitivity of sensors were improved by more than 200% and 300%, respectively.

2.2.3.3 Piezotronics Protein Sensors[53]

ZnO NWs used in this experiment were synthesized *via* a high temperature thermal evaporation process[89, 90, 92], with length of several hundreds of micrometers and diameter ranging from tens of nanometers to a few micrometers. The device was fabricated by transferring and bonding an individual ZnO NW laterally onto a PET/PS substrate, with its *c*-axis in the plane of the substrate pointing to the source. Silver paste was used to fix the two ends of the NW, serving as source and drain electrodes as well, respectively. For such a Ag-ZnO NW-Ag device, it could be treated as a M-S-M structure[92]. A thin layer of epoxy was used to fully cover both end-electrodes in order to rule out possible contacting between electrodes and the solution when the device is immersed into protein solution. Then gold nanoparticles-anti Immunoglobulin G conjugates (Au NP-anti IgG) was assembled onto the surface of ZnO NW by adding 0.01 ml of Au NP-anti IgG colloidal solution (purchased from Tedpella, used directly without further purification) on the NW and incubated for one hour in the fume hood. Before carrying out protein Immunoglobulin G (IgG) test, the devices were modified with a blocking buffer (BB) (0.1% Tween 20 (purchased from Tedpella), 0.1% fish gelatin (purchased from Tedpella), and 1% BSA (purchased from Sigma-Aldrich)). It was

reported that BB could efficiently block the nonspecific binding of IgGs to the devices.[93] Thus, treating the device with BB can effectively diminish the undesirable response from the nonspecific binding to the device and is necessary for the specific function of the sensor. Devices with BB were dried for two hours at room temperature and then washed with PBS buffer. After that, 0.005 mL of IgG (Sigma-Aldrich) sample with a given concentration was pipetted onto the device for protein binding for one hour, followed by washing and drying. A schematic in Figure 2.30a shows the principle of a strain free and Au NP-anti IgG decorated ZnO NW protein sensor, with target protein IgG bonded. The same device applied by external compressive strains is presented in Figure 2.30b.

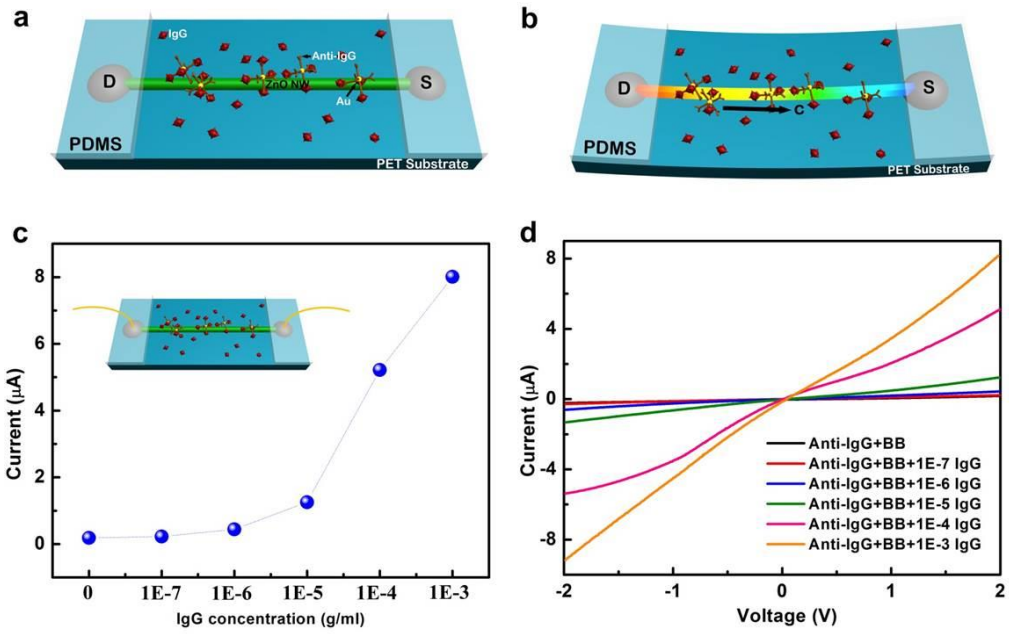

Figure 2.30 Schematic and target protein IgG response of a ZnO NW sensor. (a) Gold nanoparticle-anti IgG surface functionalized ZnO NW protein sensor bonding with target protein IgG. (b) ZnO NW protein sensor under compressive strain. (c) Target protein IgG response of ZnO NW devices at a fixed voltage of 2 V, with the IgG concentration varying from 0 to 1E-3g/ml, no external strain was applied. Inset is a schematic of the corresponding ZnO NW device. (d) *I-V* curves of ZnO NW devices at different IgG concentrations, no external strain was applied.[53]

The response of the ZnO NW protein sensor on different IgG concentrations is presented in Figure 2.30c, which was measured at a fixed bias of 2 V. The response signal of the device (i.e. current here) increased significantly from nA scale to several μA with the increasing of the targeting protein IgG concentrations from 0 to 1E-3 g/ml, since more target protein IgG being adsorbed onto the surface of the ZnO NW. This result indicates that the Anti-IgG decorated ZnO NW device has a good response to IgG concentrations. Further detailed examinations were carried out by measuring the current-voltage (*I*-*V*) curves of the sensor, with a bias voltage ranging from -2 to 2 V. *I*-*V* curves of a ZnO NW device under different IgG concentrations are presented in Figure 2.30d, which indicates that the output signals of the device are much stronger at higher IgG concentrations.

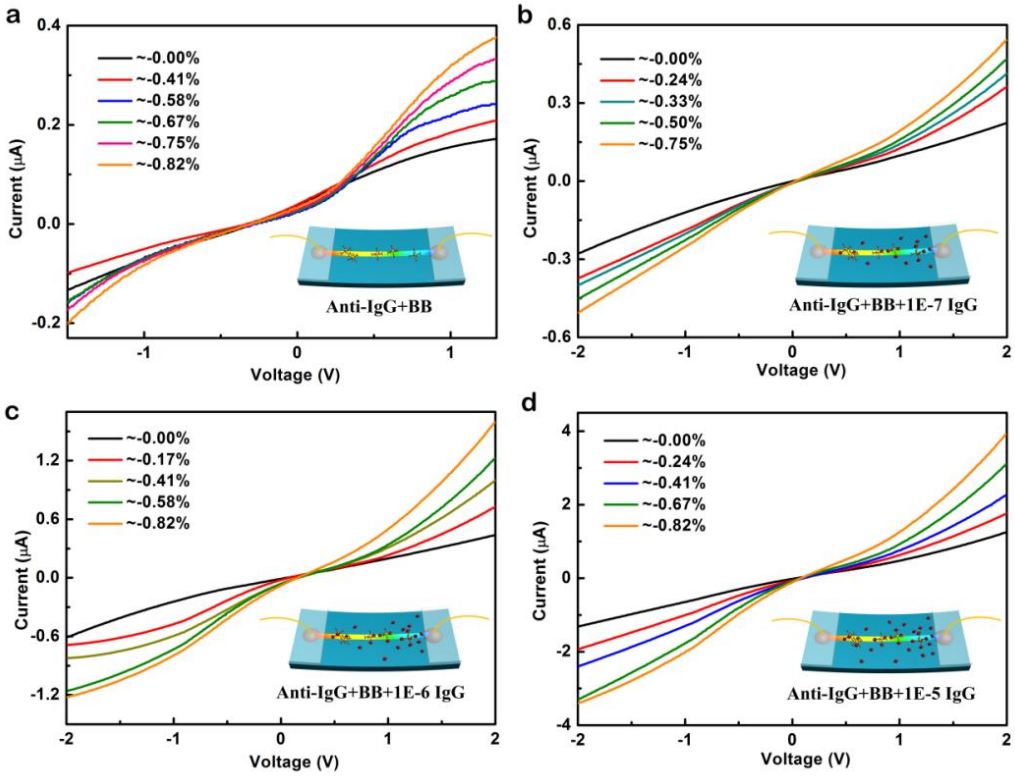

Figure 2.31 *I–V* curves of the ZnO NW protein sensor under different degrees of compressive strain, when the device was decorated with (a) Anti-IgG and BB, (b) Anti-

IgG and BB bonding with 1E-7g/ml target protein IgG, (c) Anti-IgG and BB bonding with 1E-6g/ml target protein IgG, (d) Anti-IgG and BB bonding with 1E-5g/ml target protein IgG. Insets are the schematics of corresponding ZnO NW devices.[53]

Piezotronics effect on the performance of these ZnO NW sensors was examined under compressive strains, which can be calculated according to Yang et al's work[87]. Figure 2.31 shows four sets of *I-V* curves corresponding to different IgG concentrations with protein sensors under compressive strains. Take Figure 2.31a as an example to illustrate how piezotronic effect tuned the performance of ZnO NW protein sensors. The current increase obviously, and the shape of *I-V* curves changes from an "Ohmic type" to the "Schottky type" when the externally applied strain increased from 0%, -0.41%, -0.58%, -0.67%, -0.75% to -0.82%[87]. Similar trends are observed for all the other three sets of *I-V* curves. It is necessary to notice that, the variation of the *I-V* curves of ZnO biosensors was attributed to a combination of bulk resistance change (piezoresistance effect) and the piezotronic effect, as reported in previous work[94]. In our case, the piezoresistance effect effectively lowered down the barrier heights at both ends, hence increased the output currents at both +2V and -2V; on the other hand, piezotronic effect increased the output current at +2V, while decreased that at -2V. *I-V* curves shown in Figure 2.31 were derived under the influence of both piezotronic effect and piezoresistance effect, dominated by piezotronic effect though[49, 95]. Therefore, the *I-V* curves here are not similar to those of a diode, but the relative change of currents at +2V is larger than that at -2V, since the barrier height was decreased by both of two effects at one end, while increased by piezotronics effect and decreased by piezoresistance effect at the other end. The change in transport characteristics indicates that the piezotronic effect in ZnO NW tunes the effective height of the Schottky barrier at local contacts, which

played a very important role in tuning the performance of protein sensors. The non-linear effect introduced by piezotronic effect in current transport can significantly enhance the sensitivity of the sensor.

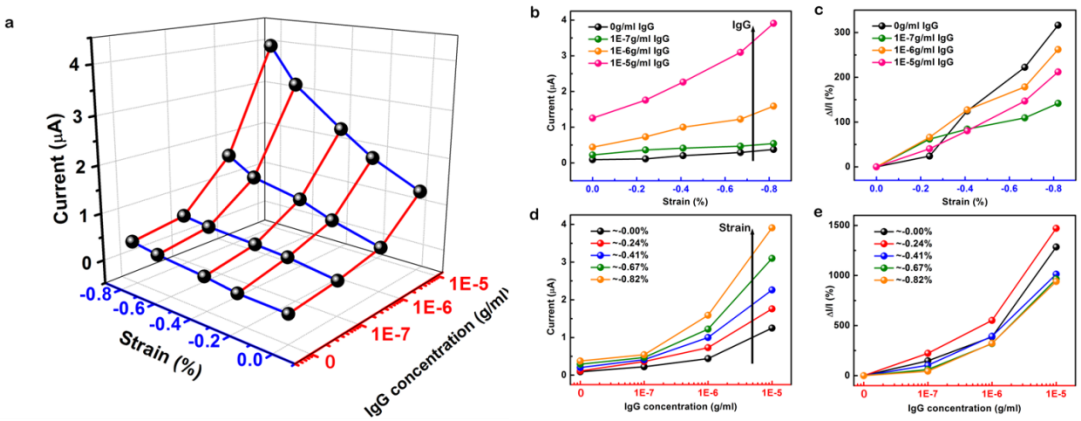

Figure 2.32 Piezotronic effect on the performances of ZnO NW protein sensors. (a) 3D graph depicting the current response of ZnO NW protein sensor under different strains and IgG concentrations. (b-c) Absolute and relative current response of ZnO NW protein sensor under different compressive strains, with IgG concentration ranging from 0 to 1E-5g/ml, respectively. (d-e) Absolute and relative current response of ZnO NW protein sensor at different IgG concentrations, with compressive strain ranging from 0 to -0.82%, respectively. Data of (b-e) were extracted from (a).[53]

By systematically investigating the sensor response on the changing external strain and targeting protein concentration, the results were extracted and plotted in a 3-dimentional (3D) graph, as shown in Figure 2.32a. It is straightforward to see that current increases as the IgG concentrations or compressive strains increases. Four 2D graphs are shown in Figures 2.32b-e for more details and information, which are extracted from Figure 2.32a by projecting on *I-Strain* surface and *I-IgG* concentration surface, respectively.

Figures 2.32b and c show the absolute and relative current response of ZnO NW protein sensor under different compressive strains when the concentration of target

protein was fixed at 0, 1E-7, 1E-6 and 1E-5 (g/ml), respectively. These 2D graphs present four curves at four IgG concentrations, each was derived by measuring the output current of ZnO NW protein sensor under different compressive strains. For each curve, as increasing the strain, the difference between currents related to two adjacent IgG concentrations was enlarged. It means that the piezotronic effect largely enhanced the resolution of the protein sensors, which is the result of the non-linear *I-V* transport properties as created by the Schottky barrier at the contacts of the M-S-M structure. Figures 2.32d and e present the absolute and relative current response of ZnO NW protein sensor at different IgG concentrations, with compressive strain fixed in each curve, ranging from 0 to -0.82%, respectively. It can be seen from this graph that at a fixed IgG concentration, the larger the strain the higher the output current: at a very low IgG concentration, without applying external strains, the output current might be too small to be detected, while applying a compressive strain; the output signal could be enhanced large enough to be detected. That is to say, piezotronic effect can improve the detection limit or sensitivity of ZnO NW protein sensors.

2.2.3.4 Piezotronics Gas Sensors[56]

In this work, we designed and fabricated Schottky-contact ZnO micro/nanowire sensors for flammable/toxic gas detections. By surface decorating the ZnO nanowire (NW) with Pd nanoparticles, hydrogen detection is demonstrated since the adsorbed hydrogen atoms acting as donors to induce a charge accumulation layer[96] on the NW surface, and thus increasing the carrier density within n-type ZnO NWs. By exposing ZnO NW devices to NO_2 atmosphere, the adsorbed NO_2 molecules consume electrons in

the conduction band and subsequently produce a charge depletion layer near surface, which effectively decreases the conductivity of the device. Piezotronic effect is introduced by externally applying strains to the ZnO micro/nanowire sensors to enhance/optimize their performances. Experimental results show that the detection sensitivity and resolution are obviously improved; the output current is significantly enhanced by 5,359% for H_2 and 238.8% for NO_2 detection. Strain-induced piezo-polarization charges play an essential role in modifying the band structure at M-S contact and hence gating the charge carrier transport process across the Schottky barrier. This study provides a promising approach to improve the detection sensitivity and enhance the general performance of Schottky-contact gas sensors.

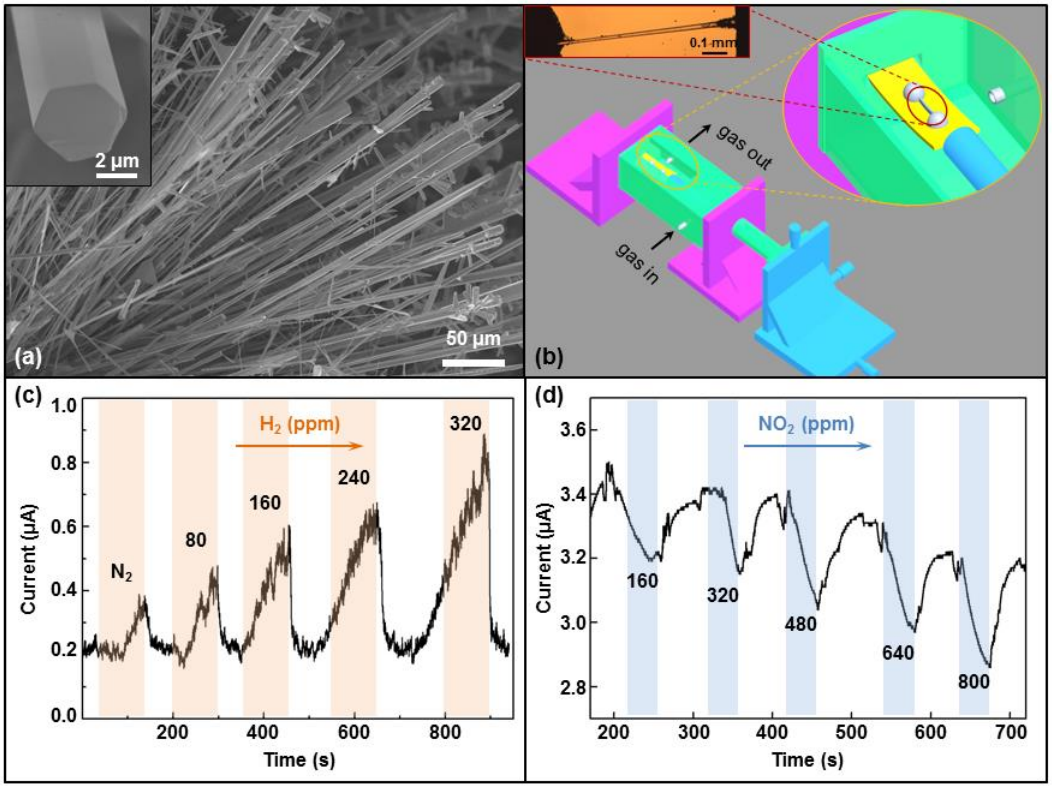

Figure 2.33 (a) Scanning electron microscopy (SEM) images of the as-grown ZnO NWs. (b) Schematic illustration of the experimental setups. Inset: the optical image of an as-fabricated gas sensor device. (c) Current response of a Pd-functionalized H_2 sensor to

different hydrogen concentrations. (d) Current response of a NO_2 sensor to different NO_2 concentrations.[56]

High-quality ZnO micro/nanowires used in this work were grown by a vapor-liquid-solid process at 1000 ℃, with lengths of several hundreds of microns and diameters varying from tens of nanometers to several microns (Figure 2.33a). An enlarged SEM image of an individual ZnO NW is shown as the inset of Figure 2.33a. Schematic illustrations of the experimental setup are presented in Figure 2.33b, showing that one end of the device is fixed inside the chamber, while the other end is free to be bent by a positioner through a 3D mechanical stage with movement resolution of 10 μm. An optical image of the as-fabricated ZnO micro/nanowire gas sensor is shown as the inset of Figure 2.33b. The response of ZnO micro/nanowire sensors to flammable/toxic gas is evaluated by measuring its transport characteristics under different gas concentrations at room temperature, with bias voltage fixed at 3V for H_2 sensor and 5V for NO_2 sensor, respectively.

The current response of a Pd-functionalized ZnO micro/nanowire H_2 sensor is presented in Figure 2.33c. By varying the hydrogen concentrations inside the measuring chamber, the current of the sensor increases stepwise with the hydrogen concentrations from 0.56 μA (80 ppm) to 0.82 μA (320 ppm), showing a sensitive response to the hydrogen atmosphere changes. The response time is about 100 s, the recovery time is about 10 s. The observed response and recover properties of the Pd-functionalized H_2 sensor are mainly contributed to the "spillover effect" reported previously by others[97]. Performances of a ZnO micro/nanowire NO_2 sensor are shown in Figure 2.33d, which is obtained by applying a 254 nm UV illumination for 10 minutes before the measurements to pre-remove the oxygen adsorbed on the ZnO surface. The current decreases with the

increase of the NO_2 concentration, from 3.20 μA (160 ppm) to 2.87 μA (800 ppm). The response time is about 60 s, and the recovery time is about 30 s. It can be seen that the current incompletely recovers to the original level after evacuating the NO_2 in each cycle, indicating a partial desorption and decomposition process of the main adsorbed nitrates[98].

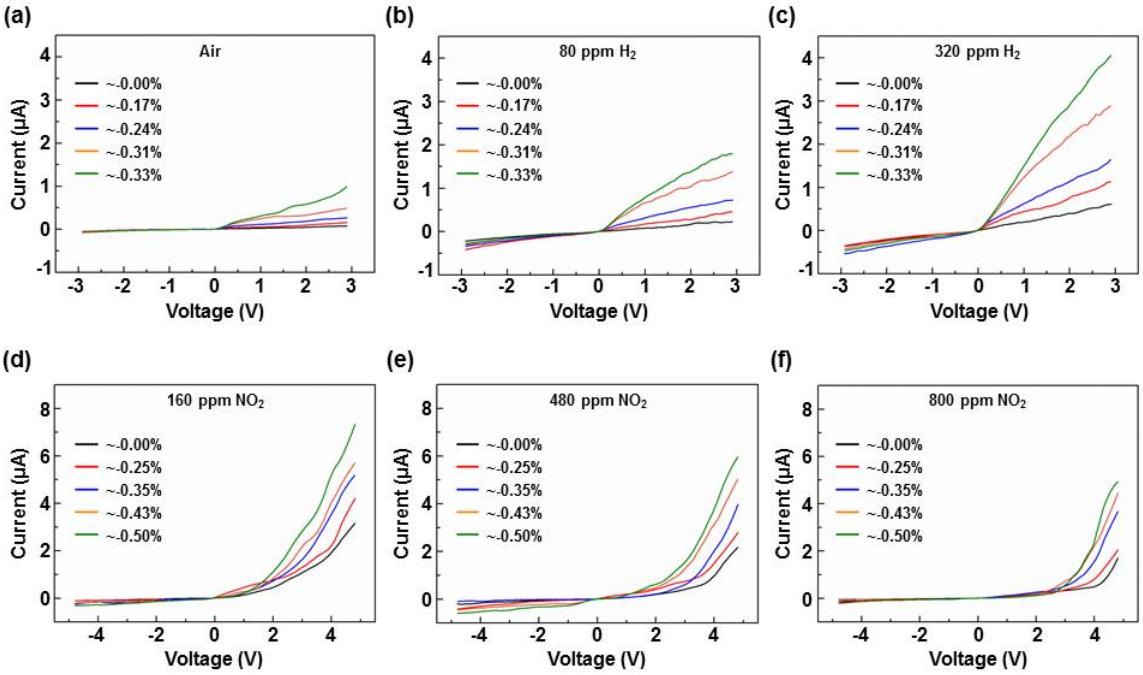

Figure 2.34 General H_2 and NO_2 sensing performances. (a-c) *I-V* characteristics of the H_2 sensor under different compressive strains (a) in air; (b) 80 ppm and (c) 320 ppm H_2 atmosphere. (d-f) *I-V* characteristics of the NO_2 sensor under different compressive strains in (d) 160 ppm, (e) 480 ppm and (f) 800 ppm NO_2 atmosphere.[56]

Systematic measurements of ZnO micro/nanowire gas sensors response to H_2 and NO_2 are conducted and summarized in Figures 2.34 *via* *I-V* characteristics at room temperature. Among air, 80 ppm and 320 ppm H_2 atmosphere, the Pd-functionalized H_2 sensors are measured under different strain conditions, showing increase in output current by either introducing more H_2 or applying more strains (Figures 2.34a, b and c). For example, under strain-free condition (Figures 2.34a, b and c, black line), the current of the gas sensor increases from 0.074 μA to 0.23 μA, then to 0.61 μA as the test

environment changes from air to 80 ppm H_2 and then to 320 ppm H_2, showing a good hydrogen response of the device. In air atmosphere, the current increases from 0.074 μA to 0.94 μA (by 1170%) as the applied compressive strain varying from -0.00% to -0.33% (Figure 2.34a). In 320 ppm H_2 atmosphere, the current increases from 0.61 μA to 4.05 μA (by 564%) as the compressive strain changes from -0.00% to -0.33% (Figure 2.34c). These results clearly show the significant enhancements in output current of ZnO micro/nanowire sensors under compressive strains by piezotronic effect.

Similar responses are derived for NO_2 detection as shown in Figures 2.34d, e and f. Under strain-free condition, the current decreases from 2.88 μA to 2.10 μA and then to 1.47 μA, as the NO_2 concentration increases from 160 ppm to 480 ppm then to 800 ppm (Figures 2.34d,e and f, black line). In 160 ppm NO_2 atmosphere, the current increases from 2.88 μA (-0.00% strain) to 7.19 μA (-0.50% strain), corresponding to an enhancement of 149.7% (Figure 2.34d). In 800 ppm NO_2 atmosphere, the current increases from 1.47 μA (-0.00% strain) to 4.98 μA (-0.50% strain) with a relative change of 238.8% as shown in Figure 2.34f. The enlarged output currents in different NO_2 atmosphere significantly facilitate the detection and clearly indicate the enhancements induced by piezotronic effect under externally applied compressive strains.

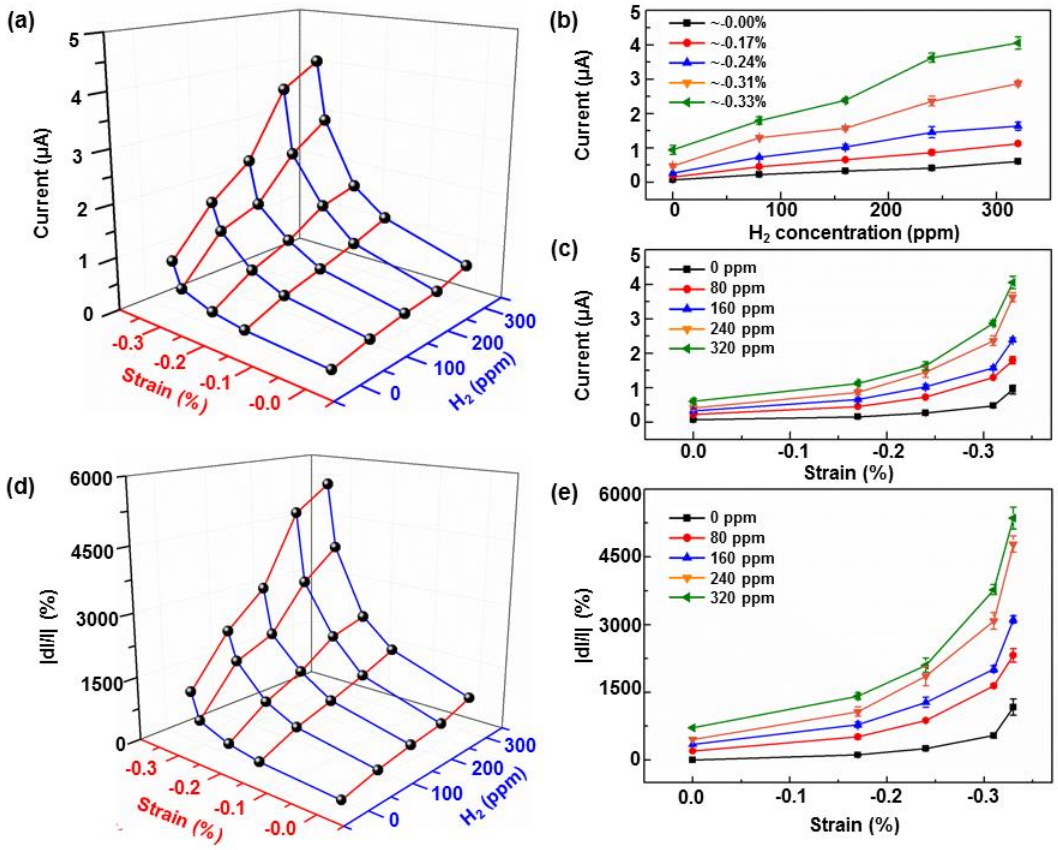

Figure 2.35 Piezotronic enhancements on H_2 sensing. (a) 3D graph depicting the current response of the H_2 sensor to strain and H_2 concentrations at a bias voltage of 2.9 V. (b) Absolute current response to different H_2 concentrations, with compressive strains ranging from -0.00% to -0.33%. (c) Absolute current response to different compressive strains, with H_2 concentrations ranging from 0 to 320 ppm. (d)3D graph and its corresponding (e) 2D projection indicating the relative changes of current under H_2 concentrations ranging from 0 to 320 ppm with respect to the value at -0% strain in air.[56]

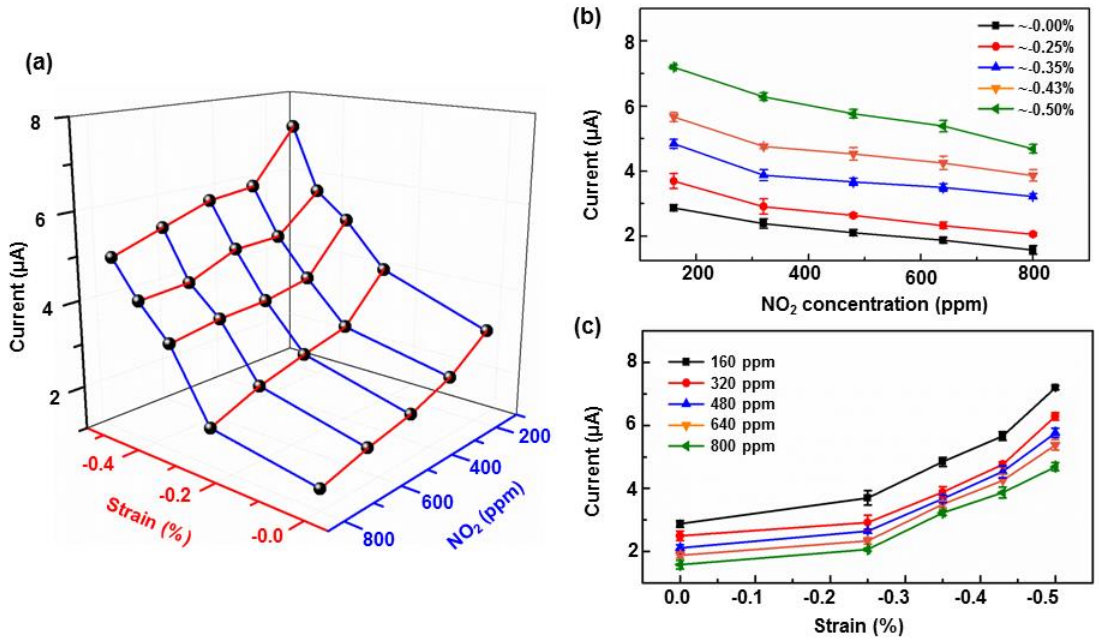

Figure 2.36 Piezotronic enhancements on NO_2 sensing. (a) 3D graph depicting the current response of the NO_2 sensor to strain and NO_2 concentrations at a bias voltage of 4.8 V. (b) Absolute current response to different NO_2 concentrations, with compressive strains ranging from -0.00% to -0.50%. (c) Absolute current response to different compressive strains, with NO_2 concentrations ranging from 160 to 800 ppm.[56]

A 3D plot is presented in Figure 2.35a to indicate the overall trend of current response to H_2 atmosphere and externally applied strain conditions for hydrogen detection, clearly showing that the current increases with the increase of H_2 concentration or compressive strain. Two corresponding 2D graphs are plotted in Figures 2.35b and c to illustrate the enhancements on detecting sensitivity and sensing resolutions by piezotronic effect after applying external strains. Figure 2.35b presents the absolute current response of Pd-functionalized H_2 sensors to different H_2 concentrations, with compressive strain fixed in each curve, ranging from -0.00% to -0.33%. The detection sensitivity of H_2 sensors are characterized by the slope of each curve, showing higher sensitivity under stronger compressive strains. Figure 2.35c shows the current response of H_2 sensors to different strains, with H_2 concentrations fixed in each curve (from 0 to 320 ppm). The

sensing resolution is clearly improved by piezotronic effect under compressive strains, since the difference of current response between two adjacent H_2 concentrations is increased by applying more compressive strains on the devices.

To better illustrate the enhancements on detection sensitivity of hydrogen sensors by piezotronic effect, the relative current change of the Pd-functionalized H_2 sensor in different H_2 concentration and strain conditions is calculated and summarized in Figures 2.35d and e, by defining the detection sensitivity as $dI/I = (I_{hydrogen,\,\varepsilon}-I_0)/I_0$, where I_0 is the current in air atmosphere under strain-free condition, and $I_{hydrogen,\,\varepsilon}$ is the current under certain H_2 concentration and strain conditions. It is obvious that the detection sensitivity under each H_2 concentration is significantly enhanced by piezotronic effect through applying compressive strains on the devices, with the highest value of 5,359% as sensitivity in 320 ppm H_2 atmosphere, under -0.33% compressive strain (Figure 2.35e). These results agree well with the increase in curve slope (Figure 2.35b) and indicate the obvious enhancements on detection sensitivity of hydrogen sensors by the piezotronic effect. Similar enhancements on detection sensitivity and sensing resolutions are also observed and presented in Figure 2.36 for NO_2 sensors. Both the slope of I *vs.* NO_2 concentration curves and the difference between output currents corresponding to two adjacent NO_2 concentrations increase when applying more compressive strains, indicating the improvements to the performances of ZnO micro/nanowire based NO_2 sensors by the piezotronic effect.

2.2.3.5 Piezotronics Humidity Sensors[55]

A ZnO micro/nanowire was utilized in this work to fabricate Schottky-contacted humidity sensors based on an M-S-M structure. By introducing the piezotronic effect, the signal level, sensitivity and sensing resolution of the humidity sensor were largely enhanced by applying an external strain. Since a higher Schottky barrier largely reduces the signal level while a lower Schottky barrier decreases the sensor sensitivity due to increased ohmic transport, an optimum 0.22% compressive strain was determined to enhance the performances of the humidity sensor with the largest responsivity of 1,240%. The physical mechanism behind the observed mechanical-electrical behavior was carefully studied by using band structure diagram. This work provides a promising way to largely enhance the overall performance of a Schottky-contact structured microwire sensor.

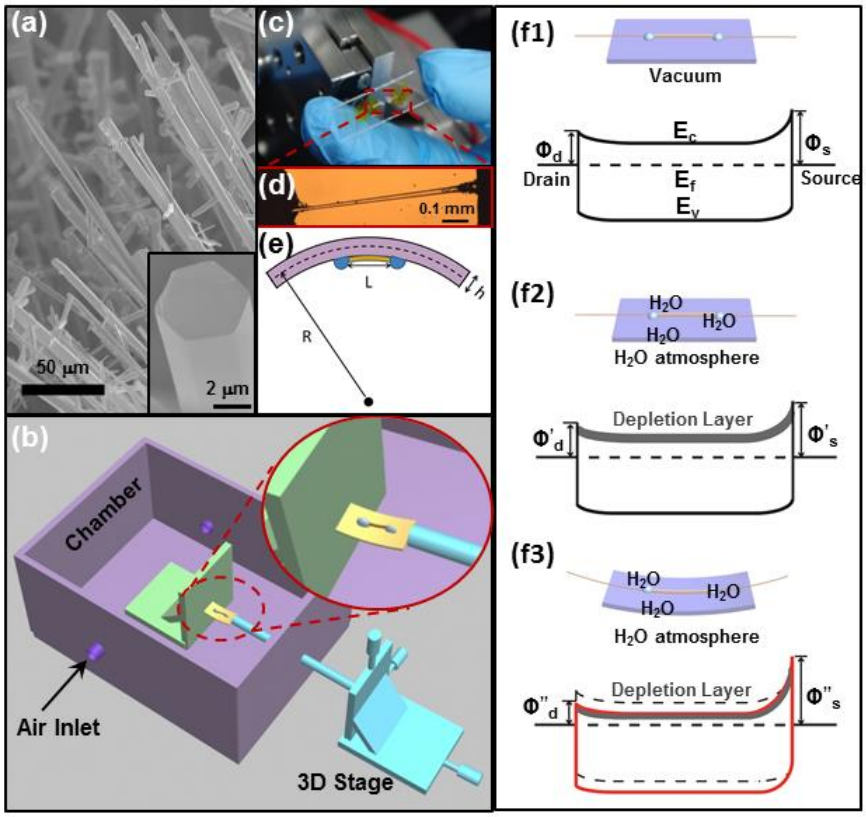

Figure 2.37 (a) Scanning electron microscopy (SEM) image of the as-grown ZnO NWs; Inset: enlarged SEM image of an individual ZnO NW, showing a perfect hexagonal cross-section. (b) Schematic of the measurement setups. (c) The optical image of an as-fabricated humidity sensor; (d) The optical microscopy image of the as-fabricated device. (e) Schematic shows the calculation of the compressive strain applied to the device. (f) Schematic energy band diagrams of ZnO NW humidity sensors, (f1) vacuum, (f2) H2O atmosphere, (f3) compressively strain in H2O atmosphere.[55]

ZnO NWs were grown by a vapor-liquid-solid process at 960℃, showing a hexagonal cross section with several hundred micrometers in lengths and hundreds of nanometers to several micrometers in diameters, as characterized by SEM image presented in Figure 2.37a. Then, a long ZnO micro/nanowire was chosen and dispersed onto a polyethylene terephthalate (PET)/or a polystyrene (PS) substrate; both ends of the ZnO micro/nanowire were fixed by silver paste, serving as electrodes. After that a layer of epoxy was used to fully cover the two silver electrodes, preventing them from exposing in the air during the following test. An as-fabricated ZnO micro/nanowire humidity sensor was sealed in a humidity chamber with one end tightly fixed on the holder as schematically shown in Figure 2.37b. Piezotronic effect was introduced by bending the other end of the device through moving a positioner, which was attached to a 3D mechanical stage with movement resolution of 10 μm located outside the chamber, up and down to apply external strains. A typical digital image together with an optical microscopy image focusing on the micro/nanowire and metal electrodes of the device are presented in Figure 2.37c and 2.37d, respectively. The external strains applied to the device can be calculated according to Yang *et al.*'s work. ε=h/2R, where ε is the strain of ZnO, h is the thickness of the substrate film, and R is the radius of the bending substrate, as shown in Figure 2.37e[99].

A theoretical model is proposed to explain the piezotronic effect on the performances of ZnO micro/nanowire humidity sensors by utilizing energy band diagrams. Figure 2.37f1 presents the energy band diagram of an M-S-M structured strain free ZnO micro/nanowire humidity sensor with its *c*-axis pointing from drain to source electrode. When introducing humid air into the chamber, water molecules were adsorbed onto the surface of ZnO micro/nanowire, where water dissociation occurred at surface oxygen vacancies (V_{Ox}) sites[100], leading to the formation of two bridging hydroxyl groups[101]. This process reduces the carrier concentrations and forms an electron depletion layer at the micro/nanowire surface, leading to a decrease of conductance of the whole device, as shown in Figure 2.37f2. The higher the RH, the lower the carrier density in ZnO micro/nanowire, and therefore the lower the output signals of the humidity sensor. If externally applying a compressive strain to the device at the same time, a strain-induced polarization piezo-charges would occur at local M-S contacts at both ends with the *c*-axis pointing at the negative charge side owing to the non-central symmetric crystal structure of ZnO[102]. Such piezo-charges could be only partially screened instead of completely cancelled out since they are non-mobile ionic charges[103], although hydronium (H_3O^+) would be dissociated by water molecules to produce hydroxyl ion (OH^-) in a moisture environment,[104-106], and thus lead to a directional movement of free electrons towards the piezo-charges in a moisture environment. As a result, the SBH at drain electrode, Φ_d, was reduced due to the presence of positive piezo-charges, while the SBH at source electrode was increased on the other end as shown in Figure 2.37f3.

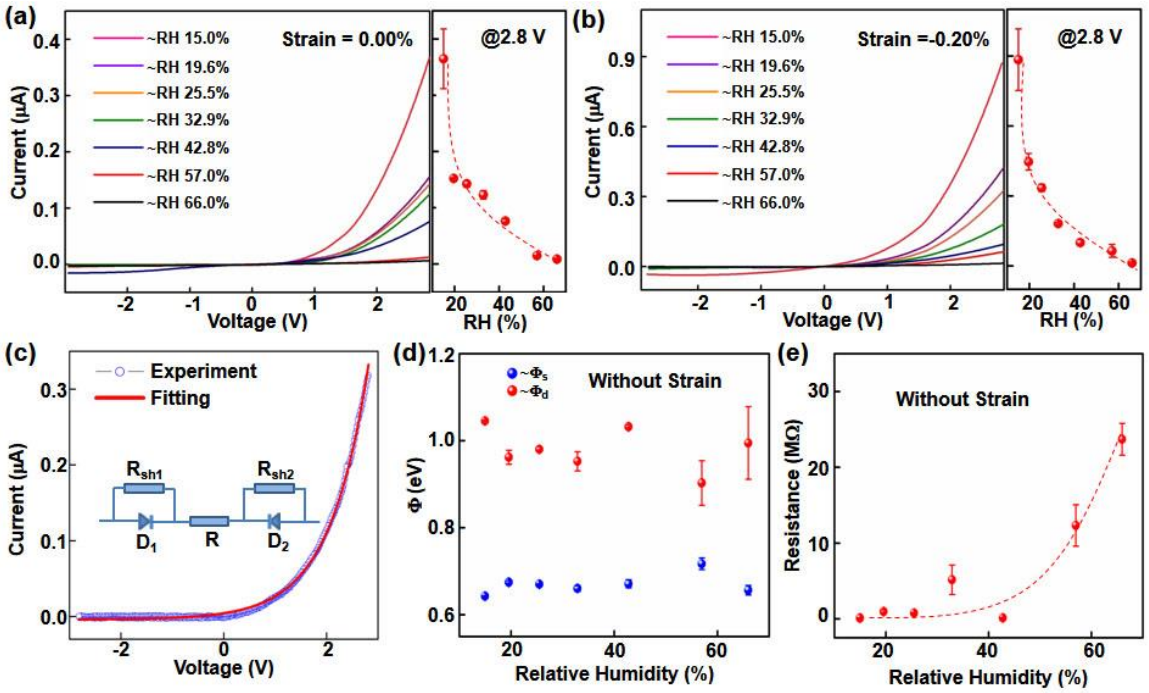

Figure 2.38 (a-b) I-V curves of the humidity sensor at different RHs, the compressive strain was 0.00% (a) and 0.20% (b) respectively. (c) Equivalent circuit model and quantitative fitting result of an individual ZnO NW-based humidity sensor. (d) The fitting results of the two Schottky barrier height changes with RHs from 15% to 66% without strain. (e) The fitting results of the resistance of the device with RHs from 15% to 66% without strain.[55]

Systematic measurements of humidity sensors were conducted under different RH and strain conditions at room temperature. For a strain free and a -0.20% compressively strain ZnO micro/nanowire humidity sensor, typical *I-V* characteristics under different RHs are presented in Figures 2.38a and 2.38b, respectively. The derived non-linear and non-symmetrical *I-V* curves indicate that the barrier heights at two Schottky contacts are distinguishable (Figure 2.37). As predicted by the working principles described above (Figure 2.37f2), the output signals (i.e. current) decreased when increasing the RH in a monotonous manner for both cases, a clear trend can be observed by extracting current value at fixed 2.8 V with drain electrode reversely biased as presented at most right side of Figure 2.38a and b correspondingly. Under 0.00% strain (Figure 2.38a), the current

decreased from 365.0 nA to 8.72 nA when the RH increased from ~15.0% to ~66.0%, while the current decreased from 884 nA to 12.9 nA under -0.22% compressive strains, indicating the enhanced resolution ($\Delta I/\Delta RH$) of the humidity sensors by the piezotronic effect. These *I-V* characteristics clearly demonstrate that there were Schottky barriers presenting at the two ZnO/Ag contacts but with distinctly different barrier heights. These Schottky barriers at the metal/semiconductor interfaces play a crucial role in determining the electrical transport property of the M-S-M structure. To better understand the behavior of this humidity sensor, an equivalent circuit model (inset of Figure 2.38c) is built to simulate the *I-V* characteristics of the devices by using a GUI program PKUMSM developed by Peng et al[107]. The fitting results are plotted as a red line in Figure 2.38c, together with the experimental data in blue dots. Furthermore, the changes of SBH at both ends, Φ_d and $\Phi_{s,}$ as well as the resistance of a strain free ZnO micro/nanowire humidity sensor are also calculated under different RHs as presented in Figures 2.38d and 2.38e. Apparently, the SBHs changed randomly with the RHs, while the resistance increased with the increasing of RHs, which can be accounted for the decrease of output signal observed in Figures 2.38a and b.

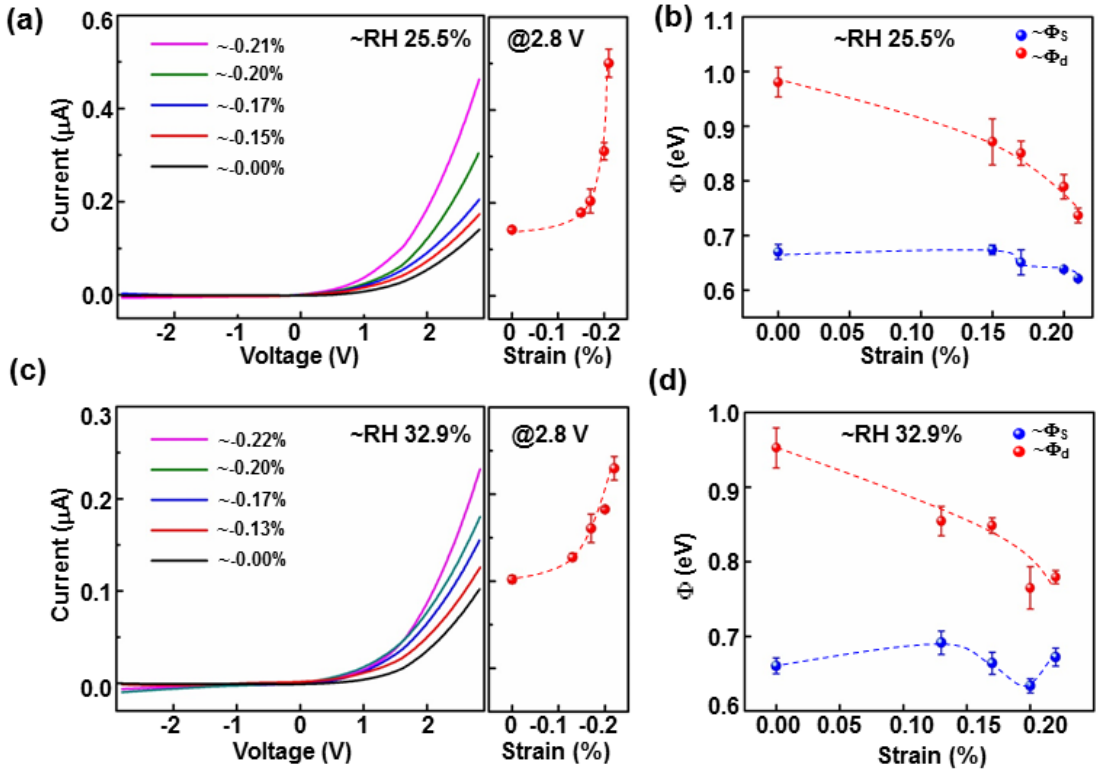

Figure 2.39 (a)&(c) I-V curves of the humidity sensor at different compressive strains, the RH was 25.5% (a) and 32.9% (c), respectively. (b)&(d) The fitting results of the two Schottky barrier height changes with compressive strains from 0 to 0.22%, the RH was 25.5% and 32.9% respectively.[55]

Figures 2.39a and 2.39c show the typical *I-V* characteristics together with the extracted current changes under a fixed 2.8 V bias voltage (drain electrode reversely biased) for two typical RH 25.5% and 32.9%, respectively. It can be seen the output signal increases monotonously with increasing the externally applied compressive strains at a fixed RH as indicated by the working principle of ZnO micro/nanowire humidity sensors when drain electrode was reversely biased. Theoretical simulations were also conducted to derive the changes of SBH at both ends (Figures 2.39b and 2.39d), showing that Φ_d decreased with increasing the compressive strains in both RH cases.

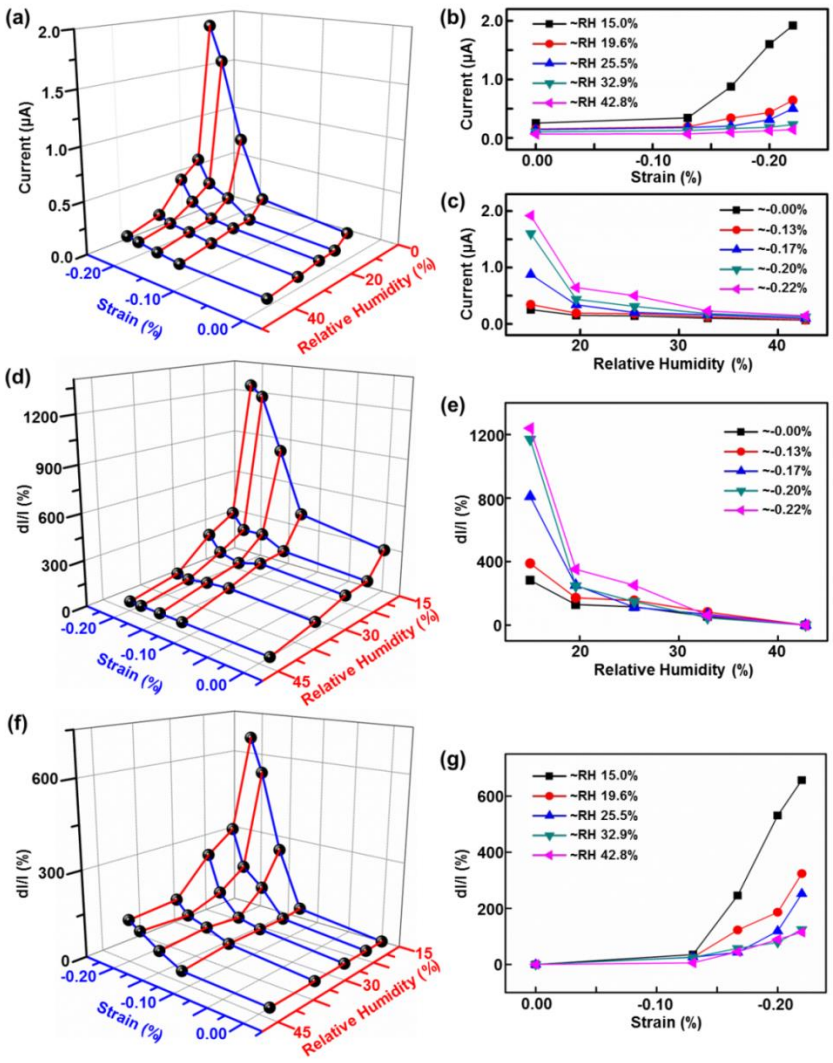

Figure 2.40 (a) 3D graph depicting the current response of the ZnO NW humidity sensor to strain and relative humidity at a bias voltage equal to 2.8 V. (b) Absolute current response to different compressive strains, with relative humidity ranging from 15.0% to 42.8%. (c) Absolute current response to different relative humidities, with compressive strains ranging from -0.00%to -0.22%. (d) 3D graph and its corresponding 2D projection (e) indicate the relative changes of current with respect to the value at 42.8% RH, under different compressive strains ranging from -0.00% to -0.22%. (f) 3D graph and its corresponding 2D projection (g) indicate the relative changes of current with respect to the value at 0.0% strain, under different RHs ranging from 15.0% to 42.8%. [55]

A 3-dimensional (3D) scatter plot is presented in Figure 2.40a to show the humidity sensor's performances at a fixed bias of 2.8 V under different humidity and strain conditions. The overall trend of output signals changes can be concluded

straightforwardly by correlating it with RH and compressive strains. The current monotonously increases with the increasing of compressive strain, while decreases with the increasing of RH. Two 2D graphs are extracted from Figure 2.40a to display the outputs response to different compressive strains and RHs under certain circumstances as shown in Figure 2.40b and 2.40c, respectively. As a 2D projection of the 3D plot on *I-strain* surface, five curves immersed in five different RHs were derived by measuring the output current of the ZnO humidity sensor under different compressive strains in each case, as shown in Figure 2.40b. Overall, the current decreased with increasing the RH due to the adsorption of water molecules as explained above. For each curve, the output signals increased with the increasing compressive strains, confirming that the piezotronic effect can enhance the general performances of humidity sensors at different RH by rising up the signal levels. Moreover, by looking into the current differences between two certain RHs under different strain conditions in Figure 2.40b, it is concluded that such differences were significantly enlarged by applying more compressive strains, which indicates a huge improvement of the sensing resolution of ZnO micro/nanowire humidity sensors by the piezotronic effect. For example, the current increased from 0.15 μA (~RH 15.0%) to 0.25 μA (~RH 19.6%) under no strain, where a 66.7% relative change in current was obtained; while this same current difference appeared to be from 0.64 μA (15.0% RH) to 1.92 μA (~RH 19.6%) under -0.22% compressive strain, with a 200% relative change in current achieved. These results clearly show a significant enhancement of the sensing resolution of our humidity sensors by the piezotronic effect. A similar conclusion can be obtained by projecting the same 3D plot on *I-RH* surface as presented in Figure 2.40c. Moreover, the slope of curves became deeper and deeper when the

applied strain increased, which means the sensitivity of humidity sensors was improved by the piezotronic effect as well.

To optimize the performances of the ZnO micro/nanowire humidity sensor, the relative changes of output current with respect to changing compressive strains and RHs are plotted as another two 3D scatter graphs as shown in Figures 2.40d and 2.40f, from which two 2D graphs are extracted to provide more details and information as shown in Figures 2.40e and 2.40g. By looking into the relative current response to various RHs under each certain strain condition, it is obvious to conclude that the larger the compressive strain, the larger the relative changes can be obtained from output signals. Therefore, a -0.22% compressive strain in our case can optimize the performances of ZnO micro/nanowire humidity sensor by achieving a largest responsivity of 1,240%.

2.2.4 Temperature Dependence of Piezotronics[57]

In this work, the temperature dependence of the piezotronic effect is investigated in GaN nanobelts (NBs) synthesized along the non-polar *a*-axis orientation. As cooling the system from 300 K to 77 K, the piezotronic effect in *a*-axis GaN is enhanced by over 440% owing to the increased effective piezoelectric polarizations resulted from the reduced screening effect caused by the decreased charge carriers mobility and density. The corresponding piezo-potential distributions, the energy band diagrams and the depletion region induced by the piezo-charges are calculated *via* finite element analysis (FEA) at various temperatures. This study presents in-depth understandings about the temperature dependence of the piezotronic effect in *a*-axis GaN and provides guidance to

their potential applications in high-performances electromechanical/optoelectronic devices.

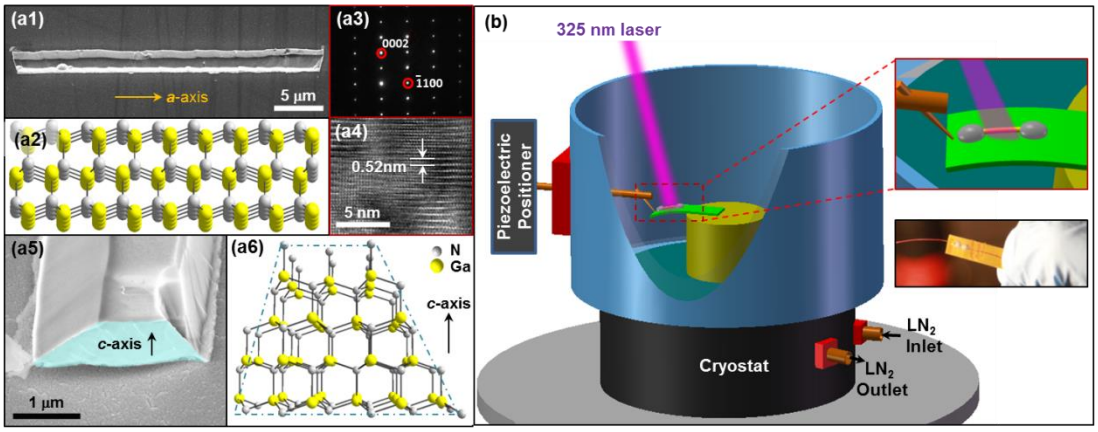

Figure 2.41 Structure characterizations and current response of GaN NBs devices. (a1) SEM image and (a2) the corresponding atomic model of the GaN NB synthesized along *a*-axis. (a3) SAED pattern, (a4) HRTEM image, (a5) SEM image and (a6) the corresponding atomic model of the cross section of the *a*-axis GaN NB. (b) Schematic illustration of the experimental set-up and the digital image of a real device.[57]

GaN NBs used in this work are synthesized on patterned silicon substrates by a metal-organic chemical vapor deposition (MOCVD) system as described elsewhere[108]. A typical scanning electron microscope (SEM, Hitachi SU8010) image of the as-synthesized GaN NB is shown in Figure 2.41a1, with the length ranging from tens of micrometers to several hundred micrometers. The corresponding atomic structure model (top view) of the GaN NB is shown in Figure 2.41a2, indicating the GaN NB is synthesized along the nonpolar $<2\bar{1}\bar{1}0>$ (i.e. *a*-axis) direction. The non-centrosymmetric wurtzite single crystal structure of GaN NBs is confirmed by the selected area electron diffraction (SAED, Tecnai G2) patterns indexed along the *a*-axis (Figure 2.41a3) and the corresponding high-resolution transmission electron microscope (HRTEM, FEI F30) image (Figure 2.41a4), with the polar *c*-axis pointing to the top surface of the GaN NB.

The enlarged SEM image of the trapezoid-shaped end surface and the corresponding atomic structure model are shown in Figures 2.41a5 and 2.41a6, respectively.

The piezotronic effect on the electric transport properties of *a*-axis GaN NBs based devices are measured in a micro-manipulation cryogenic probe system (Janis, model ST-500-2) as schematically illustrated in Figure 2.41b. By circulating liquid nitrogen (LN_2) through the cryostat of the measurement system, the temperature of the chamber is controlled between 77 K and 300 K. Reliable thermal equilibrium between the GaN NB and the cryostat is achieved by adopting aluminum foils (76 μm in thickness) covered with a layer of Kapton tape (30 μm in thickness) as the substrate (1 cm × 3 cm), which features with excellent thermal conductivity, an insulating surface and satisfactory mechanical flexibility. The thermal expansion coefficients of aluminum and Kapton tape are $23.1\times10^{-6}/℃$ and $20\times10^{-6}/℃$,[109] respectively. Substrate deformations due to the mismatch of thermal expansion coefficients can therefore be neglected. The device is fabricated by transferring and bonding an individual GaN NB laterally on this substrate with its *a*-axis parallel to the long edge. Silver paste are applied to fix both ends of the NB, serving as source and drain electrodes. A digital image of the as-fabricated *a*-axis GaN device is shown in the lower right of Figure 2.41b. One end of the device is fixed on the sample mount (Figure 2.41b, upper right) of the probe station system with the other end free to be bent. Mechanical strains are introduced through a micro-manipulating probe attached to one of the probing station arms moving in three dimensions. The values of the externally applied tensile strains are calculated following the method reported previously by *Yang et al*.[87] A beam of 325 nm UV laser is introduced to provide optical stimuli for characterizing optoelectronic performances of the GaN NB devices under a

series of strains with the temperature varying from 77 K to 300 K. The electric output signals are measured and collected by computer-controlled program through a GPIB controller.

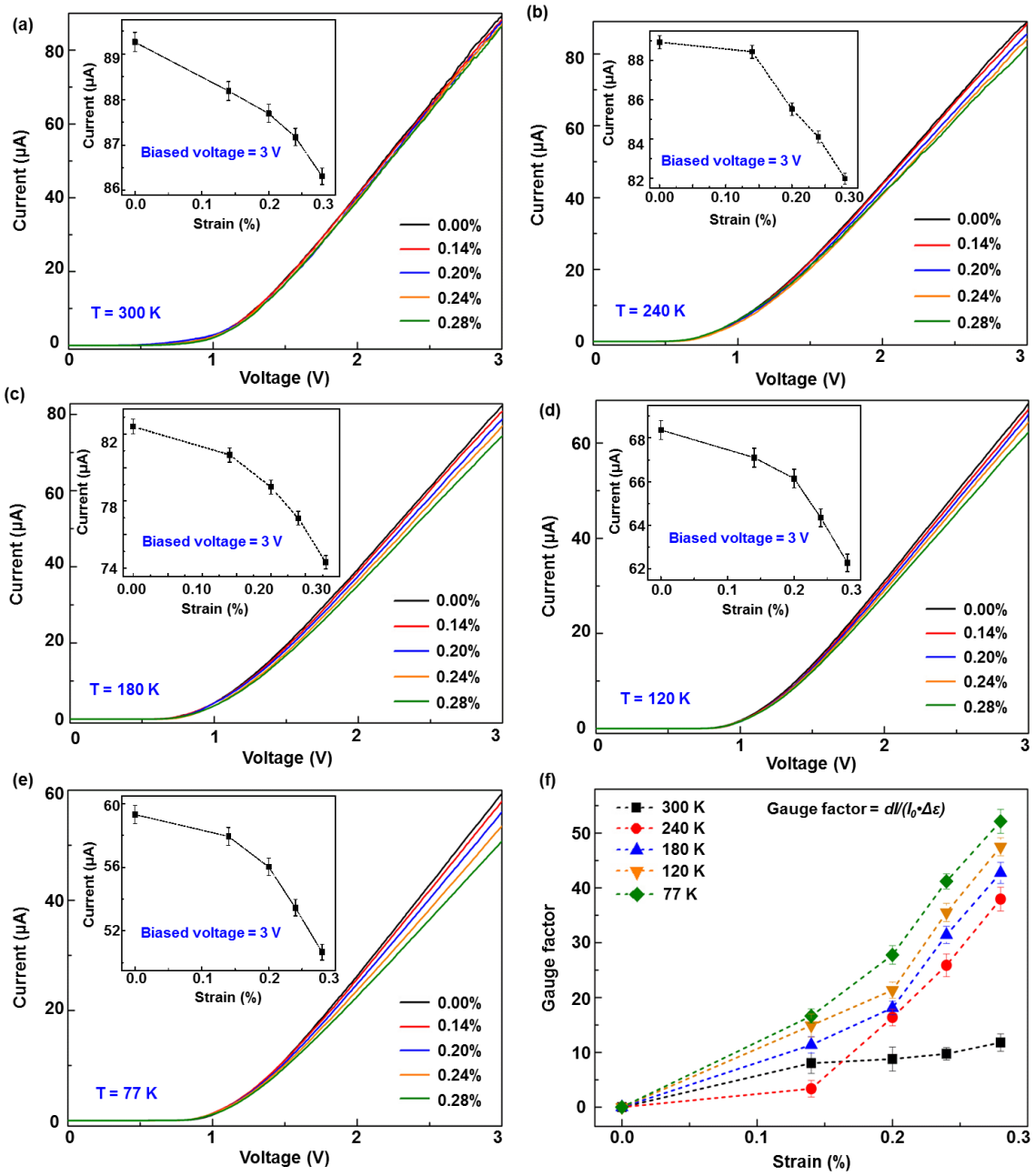

Figure 2.42 Temperature dependence of the piezotronic effect in *a*-axis GaN NB. Under dark condition, the piezotronic effect on the *I-V* characteristics of the GaN devices at (a) 300 K, (b) 240 K, (c) 180 K, (d) 120 K, (e) 77 K. The insets are the corresponding current

responses to various strains at 3 V biased voltage. (f) Gauge factor $dI/(I_0 \bullet \Delta\varepsilon)$ *vs.* the applied strains at a series of temperatures.[57]

Temperature dependence of the piezotronic effect in *a*-axis GaN is systematically investigated by applying a series of mechanical strains to the device at various temperatures and dark condition. *I-V* characteristics of a-axis GaN devices are measured at 300 K (Figure 2.42a), 240 K (Figure 2.42b), 180 K (Figure 2.42c), 120 K (Figure 2.42d) and 77 K (Figure 2.42e) by externally applying strains ranging from 0 to 0.28%. Obviously, the output currents decrease as applying more tensile strains at each temperature condition but with distinguishable magnitudes. As the system temperature decreases, the changes of *I-V* curves become more and more significant, and the difference among output currents derived under various tensile strains become the most explicit at 77 K. These observed experimental results are caused by increased effective piezoelectric polarization charges at low temperature due to the reduced screening effect by free charge carriers, since more mobile charges are trapped in the shallow impurities centers (*i.e.* freeze-out effect) at lower temperature. In order to quantitatively characterize the temperature dependence of the piezotronic effect in *a*-axis GaN NB devices, a gauge factor is defined as the relative changes of output currents per unit strain: $dI/(I_0 \bullet \Delta\varepsilon)=(I_\varepsilon - I_{\varepsilon=0\%})/(I_{\varepsilon=0\%} \bullet \varepsilon)$, where I_ε and $I_{\varepsilon=0\%}$ correspond to the output currents under strain ε and strain-free condition, respectively. The corresponding piezotronic gauge factors are calculated at different temperatures and straining conditions as plotted in Figure 2.42f. The results indicate that the piezotronic effect is enhanced by over 440% as the system temperature decreasing from 300 K to 77 K under 0.28% tensile strains. The obtained enhancement presents similar trend as reported in previous investigations on the

temperature dependence of the piezotronic effect in *c*-axis ZnO[109] nanowires, where the effective piezoelectric polarizations are also increased by cooling the system.

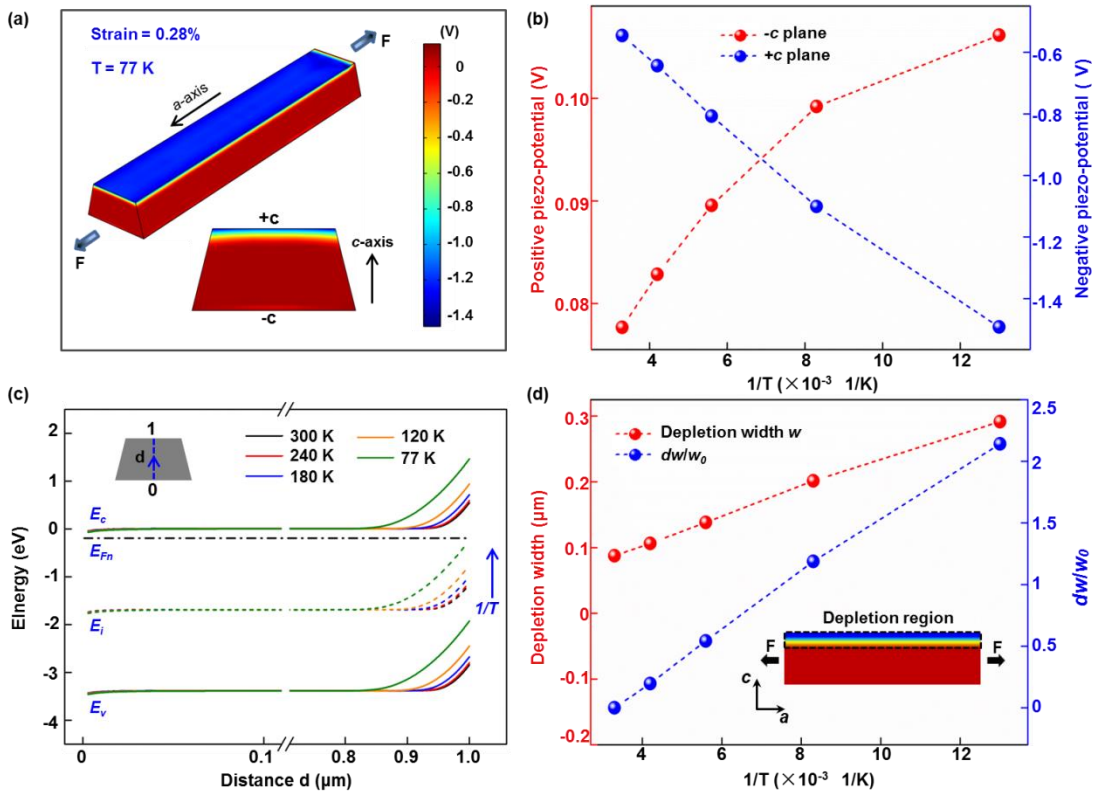

Figure 2.43 Theoretical simulations of the temperature dependence of the piezotronic effect. (a) Finite element simulation of the piezoelectric potential distribution in the *a*-axial GaN NB under 0.28% tensile strain along *a*-axis at 77 K. (b) The piezoelectric potential at +*c* plane (blue) and –*c* plane (red) as a function of the system temperature. (c) Energy band diagrams of *a*-axis GaN NB at different system temperatures under 0.28% tensile strain. (d) Electron depletion width (red) and its relative changes (blue) near the +*c* plane at different temperatures under 0.28% tensile strain.[57]

Physical mechanism of temperature dependence of the piezotronic effect is carefully studied by theoretical simulations *via* finite element analysis (FEA) as shown in Figures 2.43. Following the same calculation procedures presented in section 2.2.1.2, by solving the nonlinear partial differential equations (2.11) - (2.16) *via* FEA, the piezo-potential distributions (Figure 2.43a) and energy band diagrams (Figure 2.43c) in *a*-axis GaN NB are derived. Under 0.28% tensile strains, the piezo-potential distribution in *a*-

axial GaN NB at 77 K is simulated and presented in Figure 2.43a with the overall view (upper) and cross-section view (lower), showing that positive piezo-potential is induced at $-c$ plane and negative piezo-potential at $+c$ plane. The corresponding piezo-potential values at both $+c$ and $-c$ planes are extracted from Figure 2.43a and plotted in Figure 2.43b as a function of temperatures. Generally, the absolute values of the effective negative piezo-potential are one order of magnitude larger than those of the effective positive piezo-potential. This is because the free electrons with relatively high mobility in GaN NB screen most of the positive piezo-polarizations, while the negative piezo-polarizations are only partially screened considering the poor mobility of positive ionized donors (N_D^+). Besides, as decreasing the temperature from 300 K to 77 K, both the negative and positive piezo-potential increases due to the reduced screening effect, since more electrons/N_D^+ are trapped at lower temperature to reduce the density of free charge carriers. Furthermore, the non-completely screened negative piezo-potential presented near $+c$ plane effectively repulse the free electrons and produce an electron depletion region to modify the conducting channel width of *a*-axis GaN NB controlled by the external strains. The corresponding energy band diagrams under 0.28% tensile strains at various temperatures are calculated and plotted in Figures 2.43c. By locating the bending point of energy band diagrams (Figure 2.43c), the electron depletion region width under 0.28% strain is determined[74] and plotted in Figure 2.43d. It is obvious that the depletion region width w (Figure 2.43d, red) increases as decreasing the system temperature. Moreover, the relative changes of w is defined as $dw/w_0=(w_T-w_{T0})/w_{T0}$, where w_T and w_{T0} are the depletion region width at temperature T and T_0 = 300 K, respectively, and plotted

in Figure 2.43d (blue) as well. These results further confirm that the piezotronic effect is significantly enhanced at low temperature.

CHAPTER 3

PIEZO-PHOTOTRONICS

3.1 Basics of Piezo-Phototronics

When light illumination is taken into account, the three-way coupling among piezoelectricity, semiconductor behavior, and photon excitation characteristics gives rise to novel effect and applications. The presence of the localized piezoelectric polarization charges can significantly modulate/control the charge-carrier generation, separation, transport, and/or recombination at an interface/junction for achieving superior optoelectronic processes. This is the piezo-phototronic effect[16, 18] that can significantly affect the performances of optoelectronic devices, such as LEDs, photodetectors, and solar cells.[22, 24, 110-112] Devices fabricated by using the inner-crystal piezo-potential as a 'gate' voltage to tune/control the optoelectronic processes at the vicinity of a p-n junction is piezo-phototronics

3.1.1 Piezoelectric Polarization on p-n Junction

P-n junction is used for demonstration purpose here to elaborate the modulation of interfacial characteristics by strain-induced piezo-polarization charges. The same principle applies to other interfaces and junctions. A p-n junction consists of two semiconductor regions with opposite doping types, which is a fundamental building block in modern electronics and optoelectronics.[113] When the p-type and n-type semiconductors form a junction, the holes on the p-type side and the electrons on the n-type side adjacent to the metallurgical junction tend to diffuse across the junction into the n-type/p-type

region where few holes/electrons are present and redistribute to balance the local potential and reach thermal equilibrium. This diffusion process leaves ionized donors or acceptors behind, creating the charge depletion zone close to the junction that is depleted of mobile carriers. The ionized donors and acceptors induce an electric field that in turn results in the drift of charged carriers, moving in the opposite direction to that of the diffusion process. The diffusion of carriers continues until the drift current balances the diffusion current, thereby reaching the thermal equilibrium of the system, as indicated by the aligned Fermi energy across the system. As per the discussions on piezo-potential in the previous sections, the presence of such a carrier depletion zone can significantly enhance the piezotronic effect due to the fact that the piezoelectric polarization charges will be preserved, since the amount of regional residual free carriers is negligible in the charge depletion zone.[18] For simplicity, the p–n homojunction is considered here with the same band gaps for both p- and n-type materials. Meanwhile, only the n-type is piezoelectric material. Once the strain is applied on the n-type semiconductor, the positive piezoelectric polarization charges and hence the positive piezo-potential induced in the n-type region close to the junction interface attract the electrons toward the interface, resulting in the trapping or accumulation of electrons adjacent to the interface and thus a dip in the local band profile (Figure 3.1a),[18] which might be beneficial for promoting the electron-hole recombination and improving the efficiency of LED applications.[24, 110] Furthermore, the inclined band profile can also modulate the mobility of charged carriers moving toward the junction. On the other hand, if the polarity of the induced strain is reversed, the negative piezo-potential created in the n-type region close to the junction interface can repel the electrons away from the interface, resulting in the

depletion of electrons adjacent to the interface and thus a shoulder in the local band profile (Figure 3.1b).[18] This may result in the suppression of the electron-hole recombination rate in the device, which could be detrimental for related optoelectronic applications. More complicated situations involving p-n heterojunctions (in which the band gaps for p-type and n-type materials are different) can be discussed accordingly. Similar discussions can also be easily extended to cases including p-type piezoelectric semiconductor materials.

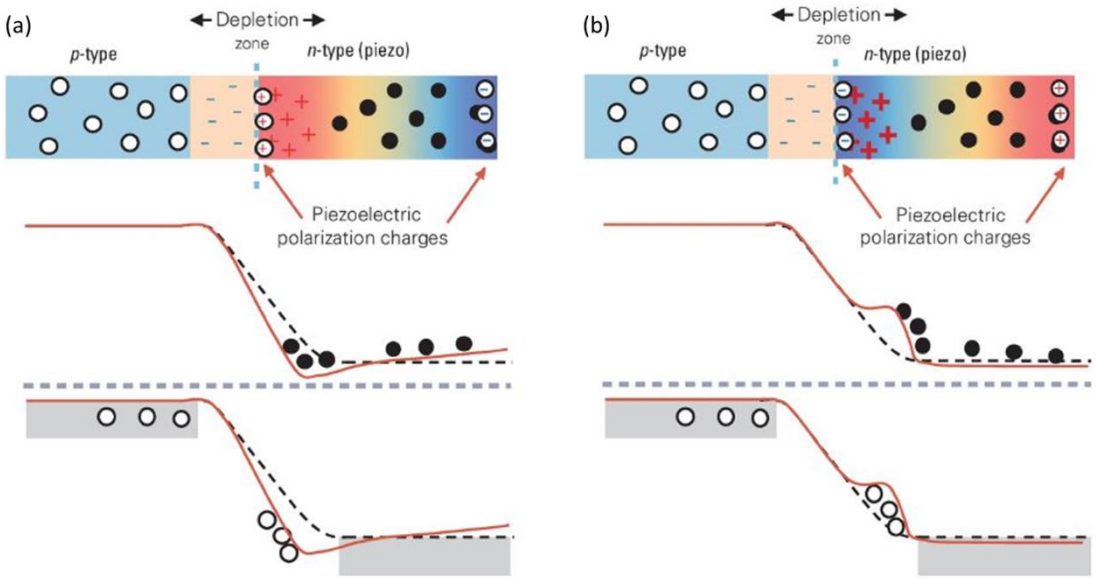

Figure 3.1 Schematic of energy diagram illustrating the effect of piezo-potential on modulating characteristics of the p-n junction. By applying strains, the piezoelectric polarization ionic charges are induced near the junction interface. The color gradients in (a) and (b) indicate the distribution of piezo-potential, with red representing positive piezo-potential and blue representing negative piezo-potential. The band diagrams for the p-n junction with and without the presence of piezotronic effect are shown using the red solid and black dashed curves, respectively. The black dots and empty circles represent the free-charge carriers in the semiconductor. Symbols '+' and '–' represent the ionized donors and acceptors in respective regions.[43]

3.1.2 Fundamentals of Piezo-Phototronics

Shockley theory provides the fundamental of *I-V* characteristics of piezoelectric p-n junctions.[114] For simplicity, we assume that the p-type region is non-piezoelectric and

n-type region is piezoelectric. Since ZnO NW grows along the direction of *c*-axis, the positive charges are created at the n-type side of the p-n junction by applying a compressive stress along the *c*-axis. An abrupt junction model is used here, in which the impurity concentration in a p-n junction changes abruptly from the acceptor N_A to the donor N_D. The built-in potential is given by

$$\Psi_{bi} = q \cdot (2\varepsilon_s)^{-1} \cdot (N_A W_{Dp}^2 + \rho_{piezo} W_{piezo}^2 + N_D W_{Dn}^2),$$

where $N_D(x)$ is the donor concentration, $N_A(x)$ is the acceptor concentration, and W_{Dp} and W_{Dn} are the depletion layer widths in the p-side and the n-side, respectively.[47]

This suggests that the change in the built-in potential can be modulated by the strain-induced piezoelectric charges. For a simple case in which the n-type side has an abrupt junction with the donor concentration N_D, and locally $p_{n0} >> n_{p0}$, where p_{n0} is the thermal equilibrium hole concentration in an n-type semiconductor, and n_{p0} is the thermal equilibrium electron concentration in a p-type semiconductor, the total current density of the p-n-junction based piezotronic transistor is given by

$$J = J_{C0} \cdot \exp[q^2 \rho_{piezo} W_{piezo}^2 (2kT\varepsilon_s)^{-1}] \cdot \exp[qV \cdot (kT)^{-1} - 1],$$

where J_{C0} is the saturation current density with the absence of piezo-potential.[47] It shows that the current transported across the p-n junction is an exponential function of the density of local piezo-charges, the sign of which depends on the type of strain. Therefore, the carrier transport can be effectively modulated by not only the magnitude of the strain, but also by the sign of the strain (tensile or compressive).

3.2 Devices and Applications

In this section, several applications of the piezo-phototronic effect are presented following the theoretical understanding about the fundamentals illustrated in section 3.1. By applying mechanical strains to various piezoelectric semiconductor based optoelectronic devices, the piezo-phototronic effect has been utilized to modify the photo-induced charge carriers' generation, separation, recombination and transport processes in photo detectors[115-117] and logic circuits[118]. The temperature dependence of the piezo-phototronic effect has also been investigated in both CdS nanowires[81] and *a*-axis GaN nanobelts[57] to better understand its working mechanism at low ambient temperatures. These results indicate that the piezo-phototronic effect is a universal effect in various optoelectronic devices fabricated by piezoelectric semiconductors.

3.2.1 Piezo-Phototronics Photodetectors (PDs)

As one of the most widely used optoelectronics, photodetectors have been extensively studied for several decades. The photo sensing performances of PDs highly depend on the separation efficiency of photo-generated electron-hole pairs. In this section, we have applied the piezo-phototronic effect to enhance the performances of 3 different types of PDs, GaN nanobelts PDs,[115] p-Si/n-ZnO PDs,[116] optical fiber (OF)/NWs hybridized PDs,[117] by utilizing the strain-induced piezoelectric polarization charges at interfaces to modify the local energy band profile and thus improve the carrier separation efficiency. These results indicate the universality of the piezo-phototronic effect as an effective approach to enhance the photo sensing performances.

3.2.1.1 GaN Nanobelts PDs[115]

In this work, the piezo-phototronic effect has been employed to modify the SBH at local M-S contact and thus enhance the sensing performances of Schottky-contacted GaN NB based PDs. In general, the response level of PDs was obviously enhanced by the piezo-phototronic effect when applying strains on devices. The optimized external strain, indicating an optimal SBH at M-S contact, was found to be -0.53%, at which the responsivity of the PD was increased by 18%. The sensitivity of GaN NB based PDs was enhanced by from 22% to 31% under a -0.53% compressive strain, when illuminated by a beam of 325 nm laser with intensity ranging from 12 to 2 W/cm^2.

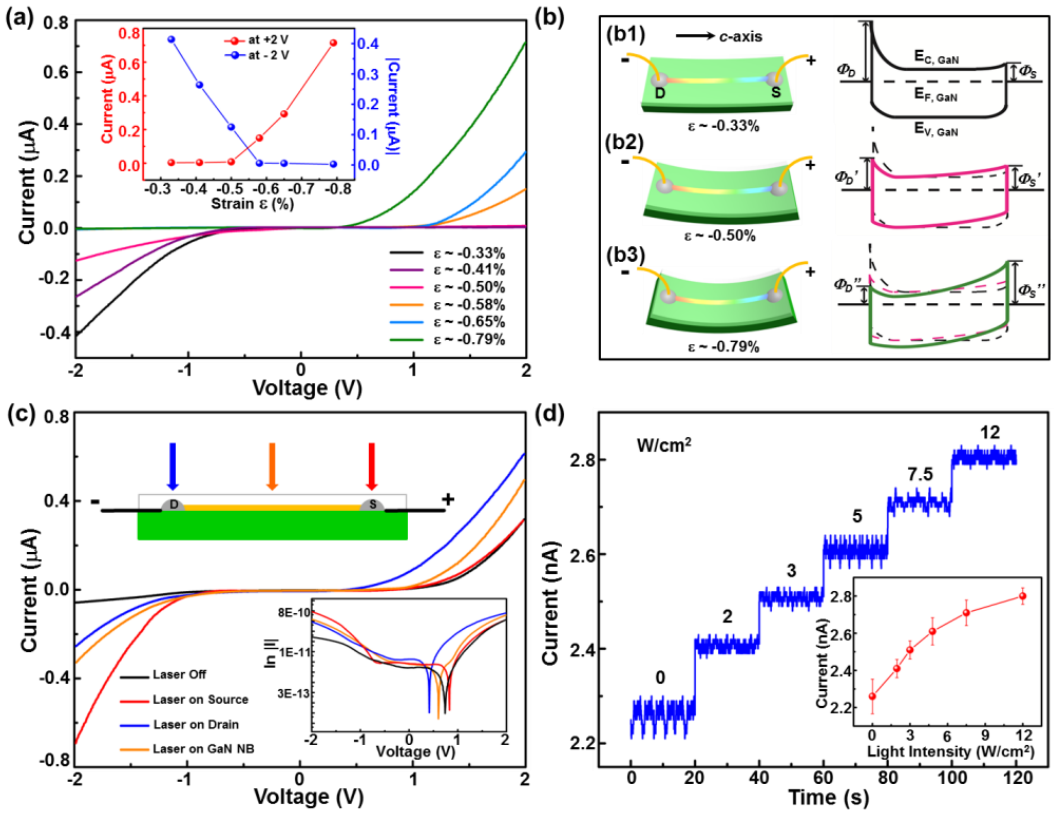

Figure 3.2 (a) *I-V* characteristics of a GaN NB based PD under a series of compressive strains, with a triangular wave swiping from -2 V to +2 V across the device. The inset is the plot of |*I*| *vs. strain* at -2 V and +2 V. (b) Band structure illustrating the *I-V* characteristics of a GaN NB based PD shown in (a), with the crystallographic *c*-axis of the NB directing from drain to source as labeled. (b1) Schematic and band structure of a

device under -0.33% compressive strain (presented as black solid line in (b1), black dashed line in (b2) and (b3)). (b2) Schematic and band structure of a device under -0.50% compressive strain (presented as pink solid line in (b2), pink dashed line in (b3)). (b3) Schematic and band structure of a device under -0.79% compressive strain (presented as olive solid line in (b3)). (c) *I-V* characteristics and schematic (inset) of a strain-free GaN NB based PD under 5 W/cm^2 laser illuminating on source electrode, GaN NB and drain electrode, respectively, with a triangular wave swiping from -2 V to +2 V across the device. The inset is the plot of *ln |I| vs. voltage*. (d) *I-t* characteristics of a strain-free GaN NB based PD under different 325 nm laser light intensities focused on drain electrode, which was reversely biased at a fixed 2 V. The inset is the corresponding *I vs. light intensity* curve.[115]

GaN NBs used to fabricate UV photo detectors in this study is the same as those used in previous section 2.2.1.1, where detailed materials properties have already been carefully characterized. By applying a series of compressive strains on the GaN NB based PD, *I-V* characteristics of a single PD was derived as a function of strains as shown in Figure 3.2a. A clearly asymmetric electromechanical behavior in current response to strains at both electrodes was obtained under a triangular wave swiping from -2 V to +2 V across the device, as dictated by the piezotronic effect. It confirms the electron transport process of the PD was dominated by the piezotronic effect, an interfacial effect asymmetrically tuning the local contacts characteristics, rather than piezoresistive effect, which is a symmetric volume effect without polarity. The data of |I| *vs.* strain at -2 V and +2 V were plotted as inset of Figure 3.2a. The band structure diagrams of GaN based PDs are presented in Figure 3.2b to illustrate the observed *I-V* characteristics. By swiping a triangular wave from -2 V to +2 V across the device, the drain electrode was reversely biased at V >0 side, while the source electrode was reversely biased at V <0 side, as shown in the schematics of Figure 3.2b. Externally applied compressive strains produced a positive piezo-potential at drain electrode, and a negative piezo-potential at source electrode. Therefore, the SBH was reduced step by step at drain electrode, while the SBH

at source electrode was increased when applying a series of compressive strains on the PD. This provides a good explanation to the *I-V* characteristics presented in Figure 3.2a.

The response of GaN NB based PD to laser illumination at different spots was derived by shinning the 325 nm laser at drain electrode, the middle of the GaN NB and source electrode, respectively (inset of Figure 3.2c), with a triangular wave swiping from -2 V to +2 V across the device. *I-V* characteristics of the device shown in Figure 3.2c clearly indicate that, when the laser was focused on source electrode, the current increased significantly under bias voltage ranging from -2 V to -1 V, in which case the source electrode was reversely biased; a similar increase was also observed for laser illumination at drain electrode. This concludes that the current of GaN NB based PD will be enhanced as long as the laser illuminates at the reversely biased electrode. As for the case when laser focused on GaN NB, the current of the device increased at both ends, with smaller increases in magnitude compared to either laser on drain electrode or source electrode, though. The observed optoelectronic behavior agrees very well with the above proposed physical mechanism of GaN NB based PD. Since the laser illumination at reversely biased electrode can effectively reduce the local SBH, which dominates the electron transport process of the whole device, it therefore has more significant influence on the PD current than that of the case merely more electron-hole pairs were generated inside the conducting channel when laser focused on GaN NB. A plot of ln |I| *vs.* voltage is presented as inset of Figure 3.2c, in which the opposite trends of current under forward and reversely biases are apparent, showing a typical character of the pizotronic effect.

With the drain electrode of a strain-free PD reversely biased at a fixed voltage of 2 V, *I-t* characteristics were obtained as a function of light intensities presented in Figure

3.2d. The increases of current were obviously observed as increasing the light intensity from 0 to 12 W/cm^2, with the beam of 325 nm laser illuminating at the drain electrode precisely. Extracted from the *I-t* characteristics, I *vs.* light intensity data was plotted in Figure 3.2d inset.

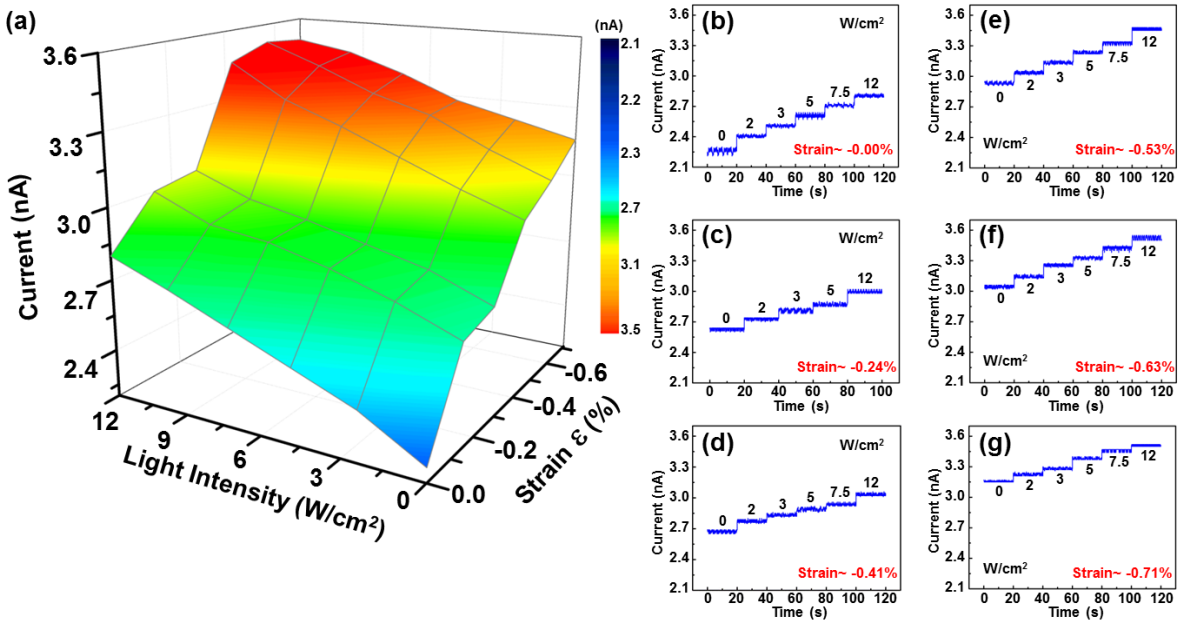

Figure 3.3 Piezotronic effect on the GaN NB based PD. (a) 3D surface graph illustrating the current response of a GaN NB based PD to strains and light intensities. *I-t* characteristics of a GaN NB based PD with 325 nm laser illuminating on drain electrode, which was reversely biased at a fixed 2 V, of light intensity ranging from 0 W/cm^2 to 12 W/cm^2 under a compressive strain of (b) -0.00%; (c) -0.24%; (d) -0.41%; (e) -0.53%; (f) -0.63%; (g) -0.71%.[115]

By systematically investigating the response of GaN NB based PD to a series of strains as well as light intensities with drain electrode reversely biased at a fixed voltage of 2 V under a beam of 325 nm laser illuminating at drain electrode, a 3-dimensional (3D) surface plot was derived (Figure 3.3a) by extracting from data plotted in Figures 3.3b-g. A straightforward overall trend of how the current of PD varied with changing both strains and light intensities can be concluded easily from Figure 3.3a, which coincides

with the *I-t* characteristics presented in Figures 3.3b-g that either more strain or stronger light intensity lead to a higher response current of the PD.

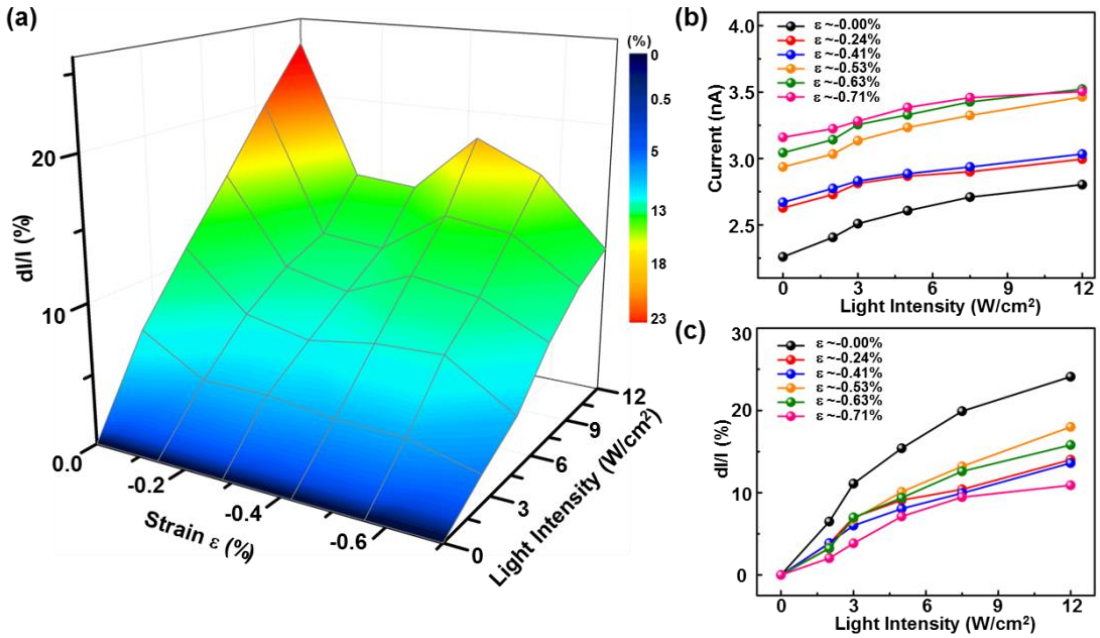

Figure 3.4 (a) 3D surface graph illustrating the relative change of current of a GaN NB based PD with respect to strains (*x*-axis) and light intensities (*y*-axis), with 325 nm laser illuminating on drain electrode, which was reversely biased at a fixed 2 V. (b) Absolute and (c) relative current response of a GaN NB based PD under different light intensities, with compressive strain ranging from -0.00% to -0.71%, respectively.[115]

To optimize the performances of GaN NB based PDs, the relative change of response current with respect to externally applied strains and 325 nm laser light intensities were plotted as another 3D surface graphs in Figure 3.4a. The absolute and relative current response of GaN NB based PD to various light intensities when the compressive strain was fixed in each curve, ranging from -0.00% to -0.71%, were presented in Figures 3.4b and c, respectively. As can be seen from Figure 3.4b, the response current of PD at very weak light intensity was increased by applying a -0.71% compressive strain, in which case an enhancement in the detecting limit of the device by as much as 44% was achieved. From the relative current response to light intensities

shown in Figure 3.4c, it seems that the most relative change of current was obtained with no strain applied. However, the current output signal at extremely low light intensity was too weak to be detected by the system when no external strains applied. Considering both the restriction of detecting limit and the responsively, it was under -0.53% compressive strain (yellow line in Figure 3.4c) rather than strain-free the best performance of GaN PD was achieved. Under this optimized externally applied strain, the responsivity of the PD was enhanced by 18%.

3.2.1.2 p-Si/n-ZnO PDs[116]

Silicon-based pn junction photodetectors (PDs) play an essential role in optoelectronic applications for photosensing due to their outstanding compatibility with well-developed integrated circuit technology. Piezo-phototronic effect, a three way coupling effect among semiconductor properties, piezoelectric polarizations and photon excitation, has been demonstrated as an effective approach to tune/modulate the generation, separation and recombination of photo-generated electron-hole pairs during the optoelectronic processes in piezoelectric-semiconductor materials. In this work, we designed and fabricated a p-Si/n-ZnO NWs hybridized PD by utilizing strain-induced piezo-polarization charges in piezoelectric n-ZnO side to modulate the optoelectronic process initiated in p-Si side and thus optimize the performances of the photosensing device. Experimental results indicate that silicon-based ZnO NWs hybridized PDs can effectively response to visible range optical signals. The general performances of the PD are optimized and significantly enhanced after introducing piezo-phototronics effect[16, 18] by externally applying strains to modify the interface properties at the Si/ZnO

heterojunction. Under a compressive strain of -0.10‰, a photoresponsivity *R* of 7.1 A/W was obtained, corresponding to an enhancement factor of 177%; the fastest rising time of 101 ms was achieved with 87% improvement. The optimal performances are attributed to the strain-induced piezo-polarization charges at Si/ZnO heterojunction interface, where the generation, separation and recombination of electron-hole pairs are modulated through the modifications of depletion region and band structures. These results indicate the capability of piezo-phototronic effect to effectively enhance/optimize the performances of silicon-based optoelectronic devices.

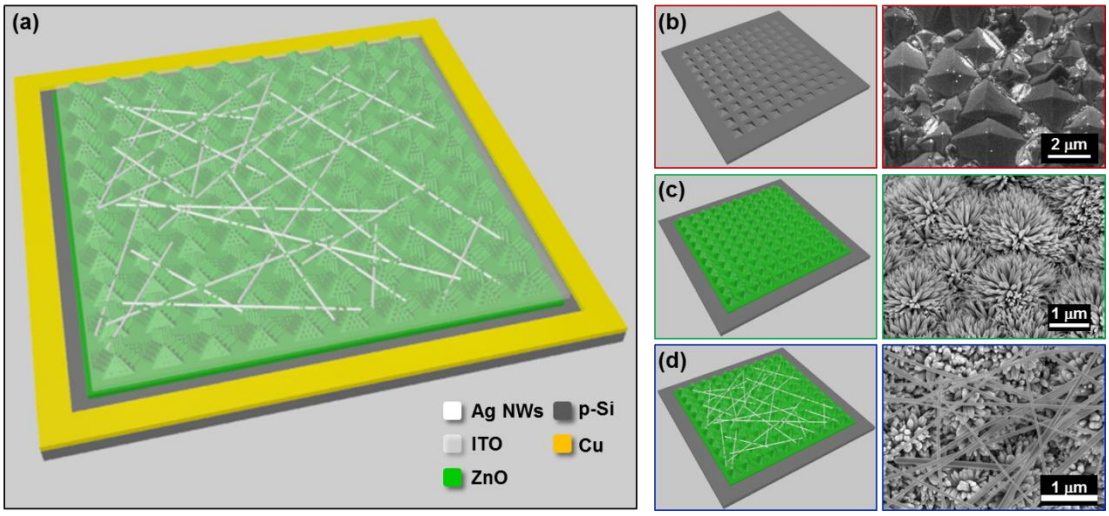

Figure 3.5 Device fabrication. (a) Schematic structure of a p-Si/n-ZnO NWs hybridized PD. (b-d) Schematic structure (left panel) and SEM images (right panel) of (b) etched Si wafer, p-Si/n-ZnO heterojunctions (c) before and (d) after spin coating Ag NWs.[116]

The structure of an as-fabricated pn junction PD is schematically illustrated in Figure 3.5a. A textured p-type Si wafer with micro-pyramids in the size of 2–4 μm (Figure 3.5b) is produced by etching Si wafer[119] to increase the surface area for better light absorptions. The obtained Si micro-pyramid structure is then covered by a thin layer of ZnO as seed layer and ZnO nanowires as antireflection coating to improve the energy-conversion efficiency,[120, 121] forming p-Si/n-ZnO heterojunctions with highly dense ZnO

NWs grown perpendicular to the surface of Si micro-pyramids along *c*-axis direction as shown in Figure 3.5c. To increase the conductivity of the top electrode, Ag nanowires are dispersed on ZnO NWs array as shown in Figure 3.5d. Finally, ITO layer and copper are sputtered on the ZnO NWs array and the p-type Si as the transparent top-electrode and the bottom-electrode, respectively.

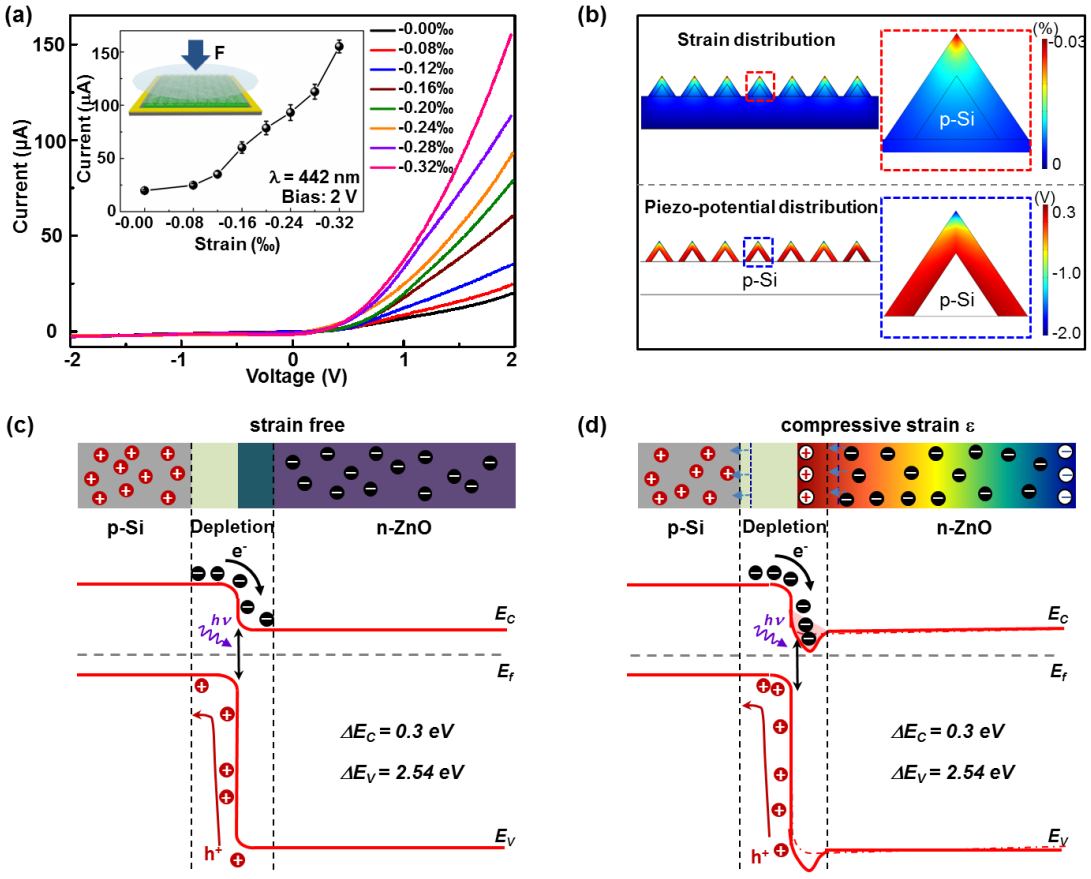

Figure 3.6 Working mechanism. (a) *I-V* characteristics of the device under different strain conditions without illumination of laser. The inset shows the current changes with the external strains when 2 V bias is applied. (b) Simulation results of strain distribution (top panel) and piezoelectronic potential distribution (bottom panel) in the ZnO nanowires array by FEA. (c, d) Schematic band diagrams of p-Si/n-ZnO heterojunction (c) without and (d) with compressive strain applied to illustrate the working mechanism of piezo-phototronic effect optimized pn junction PDs.[116]

The output signals of p-Si/n-ZnO NWs hybridized PDs under different external strain conditions and without any illumination were firstly measured and plotted in Figure 3.6a. The amount of strains applied onto ZnO NWs are estimated based on Young's modulus ratio among different materials by assuming a uniform distribution of forces through the stack up of the device at the mechanical equilibrium;[110] tensile strain is defined as positive and compressive strains as negative. The stronger the externally applied strain is, the higher output current is observed as shown in *I-V* characteristics of the pn heterojunction PDs. Inset of Figure 3.6a indicates a near-linear increase of output current from 20 μA (strain free) to more than 155 μA (-0.32‰ strain) when bottom electrode (p-Si) is biased at 2 V. Significantly, the rectifying performance of the p-Si/n-ZnO heterojunction is obviously enhanced, indicated by the rectification ratio I_F/I_R (I_F and I_R represent the forward and reverse currents, respectively)[122] increasing from 8 to 63. Therefore, by simply applying external strains, the interface properties of pn heterojunction are improved.

Based on a 2D physical model using real dimensions of p-Si/n-ZnO NWs hybridized structure as parameters, a finite element analysis is conducted to simulate the strain/piezoelectric potential distributions in ZnO NWs arrays as shown in Figures 3.6b. When pressing the device with a force of 10 N, the simulation results clearly show that the compressive strain mainly distribute in ZnO NWs near the tips of micro-pyramids (top panel in Figure 3.6b). The corresponding piezo-potential distributions are also illustrated in color codes as shown in Figure 3.6b (bottom panel) by knowing the polarity of external strains (compressive) and the crystalline orientation of ZnO NWs (*c*-axis pointing outwards perpendicular to the surface of micro-pyramid Si).[16] Positive piezo-

potential distributes at the local interface of n-ZnO/p-type Si heterojunction, effectively modulating the separation process of light-generated electron-hole pairs by tuning the energy band structure of piezoelectric ZnO NWs array. Negative piezo-potential distributes at the tip of micro-pyramid where ZnO NWs forming contacts with ITO top-electrode, this is equivalent to applying an additional forward bias voltage on the PD. Thus, the output current increases when applying more compressive strains as shown by the *I-V* characteristics in Figure 3.6a.

The influence of compressive strain on the photo-generated carriers transport process at p-Si/n-ZnO interface is understood from the expansion of the depletion width in p-Si side[123] and the modification of band diagram based on Anderson's model[124] (Figures 3.6c and 3.6d). The band gap and electron affinity values for Si and ZnO are $E_{g,Si}$=1.12 eV,[124] χ_{Si}=4.05 eV,[124] $E_{g,ZnO}$=3.36 eV, χ_{ZnO}=4.35 eV,[125] respectively. Once forming a pn heterojunction, a conductive band offset ΔE_c=0.3 eV and a valence band offset ΔE_v=2.54 eV[122] present at the local interface as shown in Figure 3.6c. Upon visible light (442 nm) illuminations, photons pass through the n-ZnO layer and are mostly absorbed in the underlying p-Si considering the band gaps of both materials, generating electron-hole pairs and thus increasing the output current. Under compressive strains, the depletion region expands and shift toward the p-Si side[123] because of the presence of positive piezoelectric charges at the junction. This expansion of depletion region in p-Si side effectively increases the photon-absorption volume and thus lead to a larger amount of charge carriers generated under illumination especially for visible light that mostly excite the electron-hole carriers at the Si side. On the other hand, the positive piezo-polarization charges displayed at pn heterojunction interface in n-ZnO side also attract

and trap some of the photo-generated electrons, which is equivalent to forming a dip at both conduction and valence bands of ZnO NWs (Figure 3.6d). This trapping mechanism retards the effective separation of photo-generated electron-hole pairs and therefore reduces the photocurrent. The above described two processes compete against each other with the increase of strains, and thus there exists an optimum strain at which the performance of the PD is maximized. Our experimental results will show such a result. This is the fundamental working principle of piezo-phototronic effect optimized performances of p-Si/n-ZnO hybridized visible PDs.

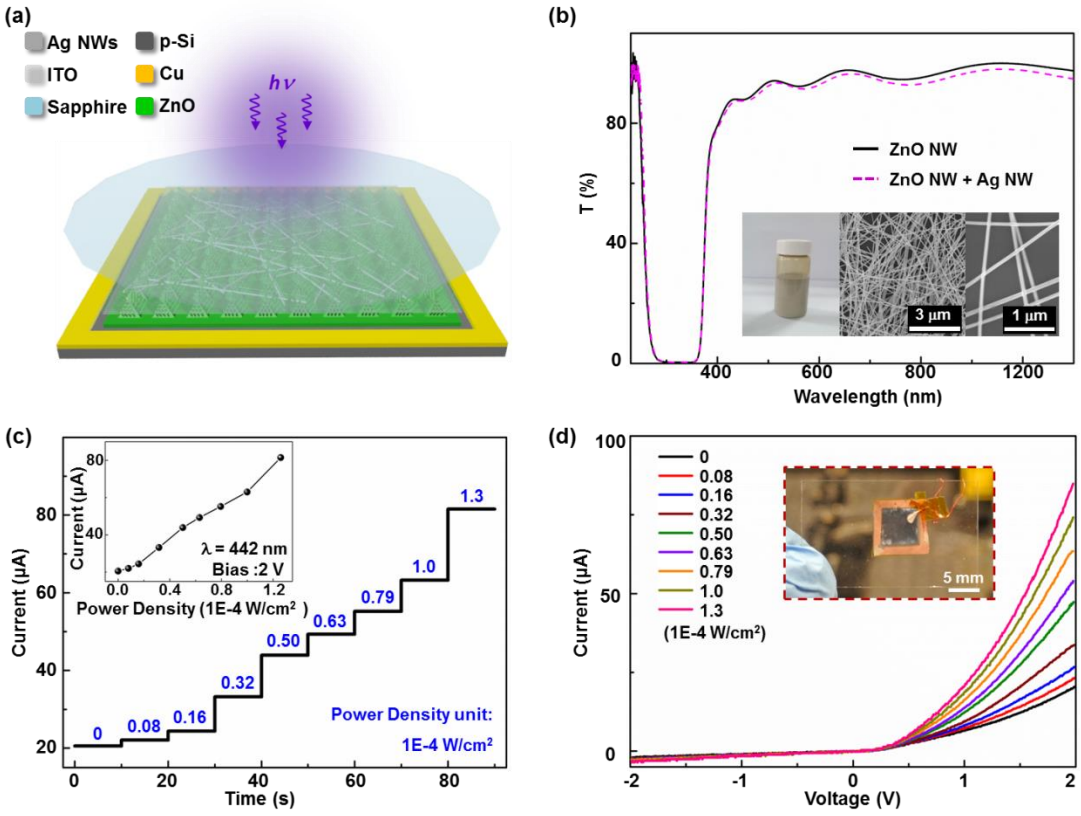

Figure 3.7 General photoresponse of p-Si/n-ZnO NWs hybridized PDs. (a) Schematic illustration of the experimental setup. (b) Transmission spectra of ZnO NWs array on the glass (black solid line) and the ZnO NWs coated with Ag NWs (purple dashed line). The insets are the photograph and SEM images of Ag NWs. (c) *I-t* response of the device under different illumination power densities at 2 V bias voltage. The inset shows the current change with the power density. (d) *I-V* characteristics of the device under

different illumination power densities when a triangle wave is applied. The inset shows a photograph of the real device.[116]

General photon-response performances of p-Si/n-ZnO NWs hybridized PDs are carefully investigated and summarized in Figure 3.7 by applying 442 nm laser illuminations (Figure 3.7a). The transmission spectra of ZnO NWs synthesized on glass substrate (black solid line) under the same growing conditions as those on p-Si and ZnO NWs array covered by Ag NWs (purple dashed line) are presented in Figure 3.7b, together with the photograph and SEM images of Ag NWs as the insets. It is obvious that both ZnO and Ag NWs are almost transparent to the 442 nm lasing (T ~ 90%), indicating the photo-generation process happens mostly in p-Si side at local junction/interface. By fixing the forward bias voltage at 2.0 V, the light response of p-Si/n-ZnO NWs hybridized PDs under 442 nm laser illumination to nine different power densities ranging from 0 to 1.3×10^{-4} W/cm^2 is presented in Figure 3.7c. The output current increased from 20.5 μA (dark current), through 43.9 μA (5×10^{-5} W/cm^2) to 81.5 μA (1.3×10^{-4} W/cm^2). The inset current *vs.* power density plot clearly shows a linear relationship between the output current and the power density, indicating the calibration for practical applications. By applying a triangular wave across the device, the corresponding *I-V* characteristics are also presented in Figure 3.7d together with a photograph of the real device.

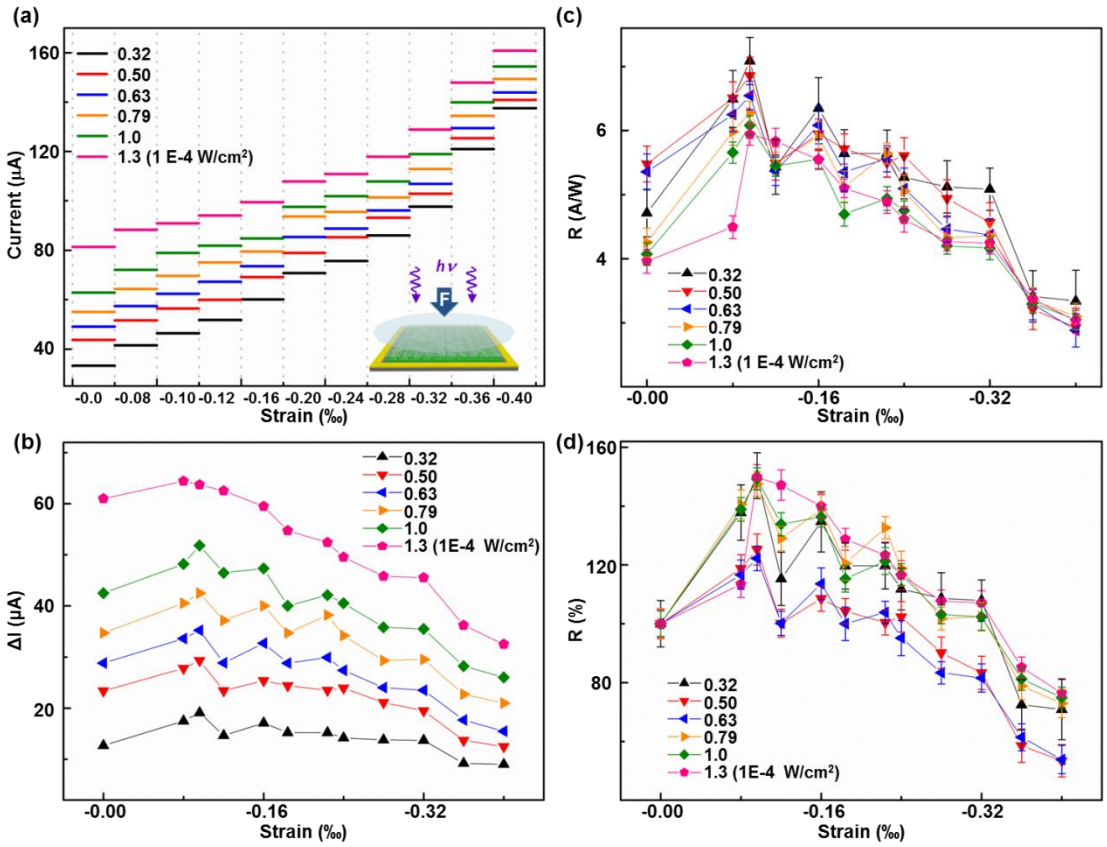

Figure 3.8 Piezo-phototronic effect. (a) Output current of the PDs under different strain and illumination conditions at 2 V bias voltage. The inset shows the schematic illustration of experimental setup. (b) Photocurrent, (c) photoresponsivity and (d) relative changes of photoresponsivity of the device under different strain and illumination conditions, biased at 2 V.[116]

Piezo-phototronic effect optimized performances of p-Si/n-ZnO NWs hybridized PDs are systematically investigated by applying a series of light power densities as well as external strains to the devices. The output current I of the PDs are measured and summarized in Figures 3.8a by applying a fixed bias voltage of 2 V across the pn junction. Under each power density (from 3.2×10^{-5} to 1.3×10^{-4} W/cm^2), eleven different strains ranging from -0.00‰ to -0.40‰ are exerted onto the PD to measure its optoelectronic behavior, indicating an obvious increase in output currents either by increasing the light power density or the external strains. The photocurrent $\Delta I=I-I_{dark,s}$ ($I_{dark,s}$ represents the

corresponding dark current under certain strains) are calculated and presented in Figure 3.8b, clearly showing that under each strain condition, the photo-current increases as increasing the power density of illumination. Moreover, a local maximum value of photo-current ΔI is obtained at -0.10‰ compressive strain under illuminations with the power density from 3.2×10^{-5} W/cm^2 to 1.3×10^{-4} W/cm^2, indicating the optimization of PDs performances by the piezo-phototronic effect.

As a critical parameter of PDs, the photoresponsivity R is also calculated as shown in Figure 3.8c for all the power densities and external strain conditions with bottom-electrode 2 V biased. The photoresponsivity[126] R is defined as $R = \frac{I_{light,s} - I_{dark,s}}{P_{ill}} = \frac{\eta_{ext} q}{h\nu} \cdot \Gamma_G$, where $P_{ill} = I_{ill} \times S$ is the illumination power on the PD; $I_{light,s}$ and $I_{dark,s}$ represent the photon and dark current under the corresponding external strain, respectively; Γ_G is the internal gain; η_{ext} is the external quantum efficiency (EQE); q is the electronic charge; h is Planck's constant; ν is the frequency of the light; I_{ill} is the excitation power density; S is the effective area of the PD. A maximum value of R is obviously concluded from Figure 3.8c under each power density, with the highest value of 7.1 A/W under -0.10‰ strain at a power density of 3.2×10^{-5} W/cm^2, corresponding to a relative enhancement of 177%. This achieved R value is larger than that of a commercial Si photodiode PD (in the range of 0.1-0.2 A/W at 442 nm);[127] and near 100 times larger in magnitude than that obtained from a Si/ZnO core-shell NW array PD (1.0×10^{-2} A/W, 480 nm, -1 V);[128] also larger than that of a Si/CdS core-shell NW network PD (<1 A/W, 480 nm, -1 V).[129]

To illustrate the piezo-phototronics effect on photoresponsivity more clearly, relative changes of photoresponsivity R with respect to R_0 (corresponding photoresponsivity at no strain) are calculated and summarized in Figure 3.8d. It is observed that, under each power density, the relative change of R is varying with applied strains in a similar manner to that of photo-current ΔI (Figure 3.8b) and photoreponsivity R (Figure 3.8c), displaying a maximum value at the external strain of -0.10‰. The maximum value derived in photo-current, photoresponsivity and relative change of R is attributed to the simultaneously existing competition between the expansion of depletion region in p-Si and the trapping mechanism to the photo-generated carriers as a dip in energy band of n-ZnO upon straining.

3.2.1.3 Optical Fiber/Nanowires Hybridized PDs[117]

In this work, we demonstrate the implementation of direct integration between optical communication system and PDs by designing and fabricating UV/visible photosensing devices with optical fiber – nanowires hybridized structure (Figure 3.9a). ZnO/CdS nanowires (NWs) heterojunctions are synthesized coaxially around an optical fiber (OF) to fulfill ultraviolet and visible light detections. The PD works in two modes: axial and off-axial illumination modes. Upon straining, piezo-polarization charges presented at the ZnO/CdS heterojunction interface effectively tune/control the charge transport across the interface/junction and modulate the optoelectronic processes of local carriers, such as generation, separation, diffusion and recombination. The performances of OF/NWs hybridized PDs have been enhanced/optimized by up to 718% in sensitivity and 2067% in photoresponsivity by the piezo-phototronic effect.

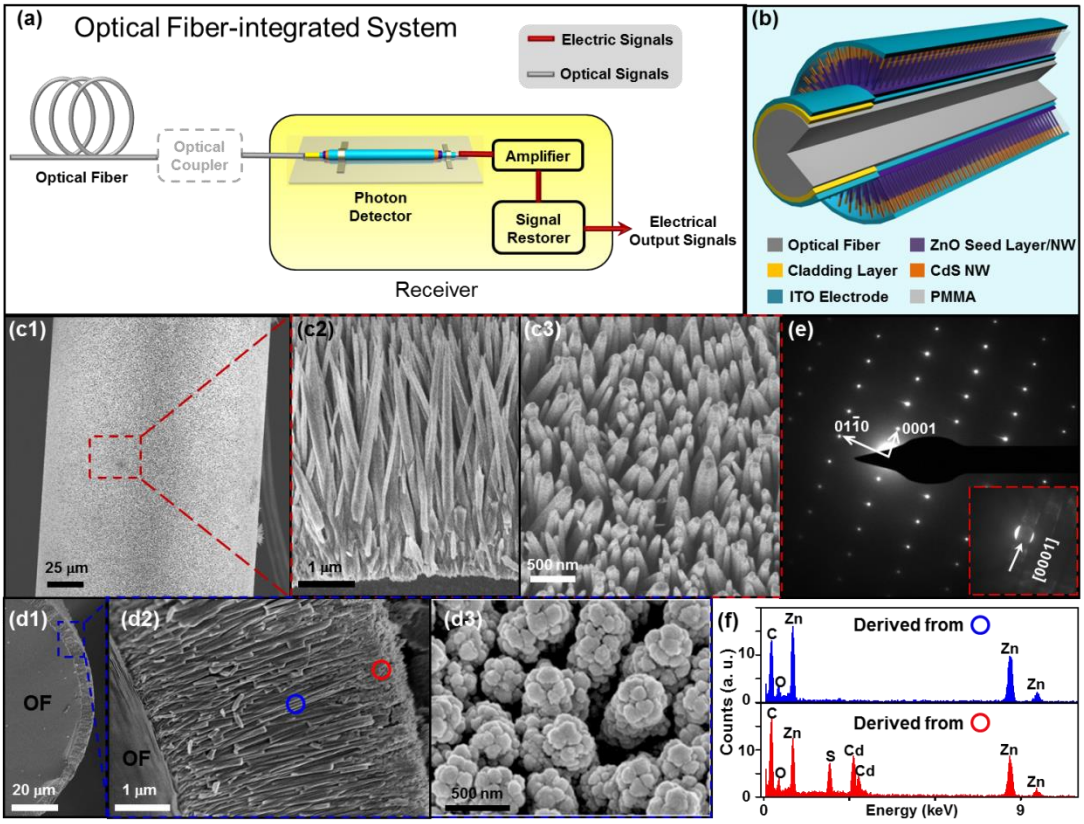

Figure 3.9 Structure and characterization of OF-NWs hybridized dual-mode PDs. (a) Schematic illustration of direct integration with optical communication system in a coupler-free manner. (b) Schematic demonstration of the structure of an OF-NWs hybridized dual-mode PD. (c, d) SEM images of NWs array synthesized coaxially around the OF with enlarged (c2, c3) side view and top view before, (d2, d3) after forming ZnO/CdS heterojunctions. (e) The corresponding select area electron diffraction (SAED) pattern of ZnO NWs. (f) Energy dispersive X-ray (EDX) spectra of single NWs collected from corresponding areas marked by blue and red circles shown in (d2).[117]

The structure of an OF-NWs hybridized UV/visible PD is schematically illustrated in Figure 3.9b. Top-view and side-view scanning electron microscopy (SEM) images presented in Figures 3.9c and d confirm the PD configuration, showing an OF core uniformly and compactly covered by ZnO NWs array with diameters of 150-250 nm and lengths of 3-4 μm (Figure 3.9c); as well as a layer of CdS NWs on top with thickness of about 1 μm (Figure 3.9d). ZnO NWs array is grown along *c*-axis coaxially in outwards radial direction of the OF as indicated by select area electron diffraction (SAED) pattern

from a single ZnO NW (Figure 3.9e). The existence of heterojunction interface between ZnO and CdS NWs is verified by taking energy dispersive X-ray (EDX) spectra (Figure 3.9f) of a single nanowire collected from the corresponding areas as marked in Figure 3.9d2 by red and blue circles. Only ZnO presents at inner layer (blue circle), while both ZnO and CdS are observed at outer layer (red circle) where the heterojunction formed.

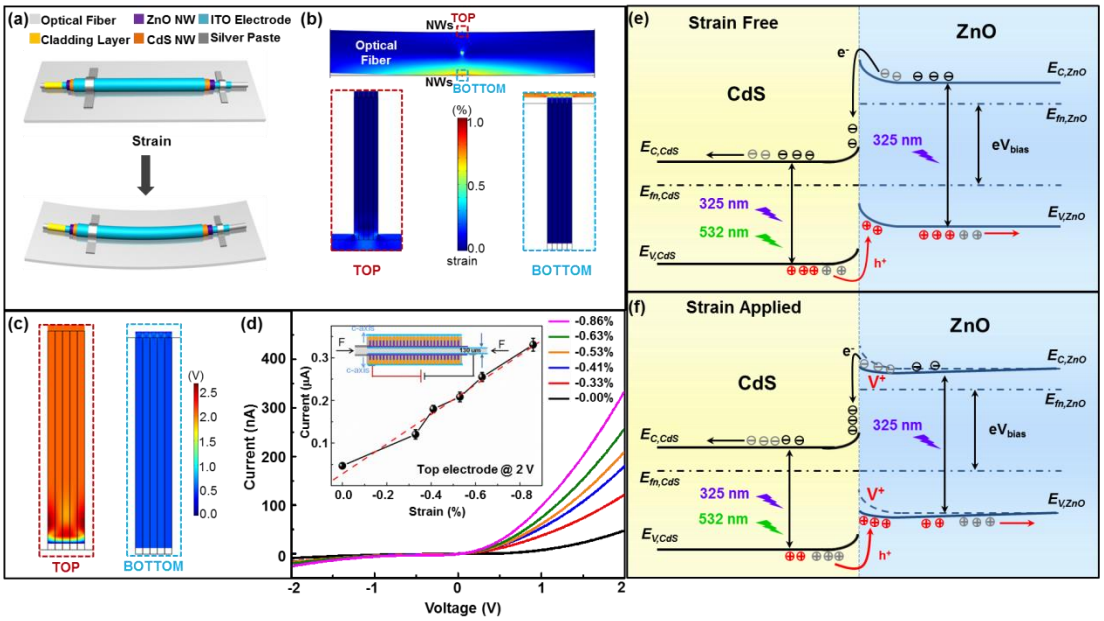

Figure 3.10 Piezo-phototronics and working mechanism of OF-NWs hybridized PDs. (a) 3D schematic demonstration of OF-NWs hybridized PDs without (top) and with strain (down). (b) Simulation results of strain distributions of OF-NWs hybridized PDs by finite element analysis method when bending the optical fiber concave up with a displacement of 10 m. The physical model is based on the dimensions of real devices. Enlarged strain distribution within ZnO NWs for both top (in red square) and bottom (in blue square) sides are presented. (c) Simulation results of piezoelectric potential distribution within ZnO NWs array on top (in red square) and bottom (in blue square) sides of the optical fiber. A positive piezo-potential is produced within top side ZnO NWs. (d) *I–V* characteristics of an OF-NWs hybridized dual-mode PD under different compressive strains by applying a triangular wave across the device, no light illumination involved. The inset shows a schematic experiment set-up and an *I-strain* curve when top-electrode is biased at 2 V. (e, f) Schematic band diagrams of ZnO/CdS heterojunctions (e) without and (f) with external strain applied to illustrate the working mechanism of OF-NWs hybridized dual-mode PDs.[117]

External strains are applied onto the OF-NWs hybridized PD by bending one end of the device with a 3D mechanical stage (movement resolution ~ 10 μm), while fixing the other end on a manipulation holder. Considering the symmetric configuration of this device, when bending it concave up as shown in Figure 3.10a (or down), a compressive strain along the longitudinal direction of OF induces a tensile strain along the *c*-axis of ZnO NWs at the top (or bottom) side of the OF, while no strain experienced by ZnO NWs that are distributed at the bottom (or top) side of the OF due to the spacing between loosely assembled NWs in the local region (Figure 3.10c).[130] Based on a 2D physical model using real dimensions of OF-NWs hybridized structure as parameters, a finite element analysis is conducted to simulate the strain/piezoelectric potential distributions within ZnO NWs arrays upon straining as shown in Figures 3.10b and c. When bending the OF concave up, the simulation results clearly confirm the strain distribution analysis presented above that NWs near the OF at top side are under tensile strains, while NWs at the bottom are strain-free (Figure 3.10b). The piezo-potential distributions are also illustrated in color codes by knowing the sign of externally applied strain (tensile strain on top side ZnO NWs along its *c*-axis) as well as crystalline orientation of ZnO NWs (*c*-axis pointing outwards along radial direction of OF).[16, 49] As shown in Figure 3.10c, positive piezo-potential distributes along ZnO NWs on the top side due to tensile strains, and no obvious potential observed for strain-free ZnO NWs at the bottom side. The values indicated in Figure 3.10d correspond to the longitudinal strain along the OF[87] with tensile strain defined as positive and compressive strain as negative.

The influence of strain on the photonic excitation process at ZnO/CdS interface can be understood from the band diagram. An energy barrier is formed at ZnO/CdS

heterojunction interface (Figure 3.10e) due to the shift of ZnO conduction band[131] upward by eV_{bias} when ZnO NWs are reversely biased as shown in the inset of Figure 3.10d. When applying an external strain, positive piezo-polarization charges are induced at heterojunction interface, which effectively reduce the barrier height by lowering both conduction and valence band of ZnO NWs (Figure 3.10f). Dominated by reversely-biased barrier height, the electronic transport process is therefore significantly enhanced as local charge carriers passing through heterojunction interface more easily. The higher the externally applied strain, the lower the barrier height, and thus the higher output current is observed as shown as *I-V* characteristics in Figure 3.10d. Inset of Figure 3.10d indicates a linear increase of output current from 47 nA (strain free) to more than 331 nA (-0.86% strain) when top electrode (CdS NWs) is biased at 2 V. Upon light illumination, the separation process of light-generated electron-hole pairs at vicinity of heterojunction interface is profoundly promoted by lowered barrier height owing to the presence of strain-induced positive piezo-polarization charges. This is the fundamental of piezo-phototronic effect enhanced performances of OF-NWs hybridized UV/visible PDs.

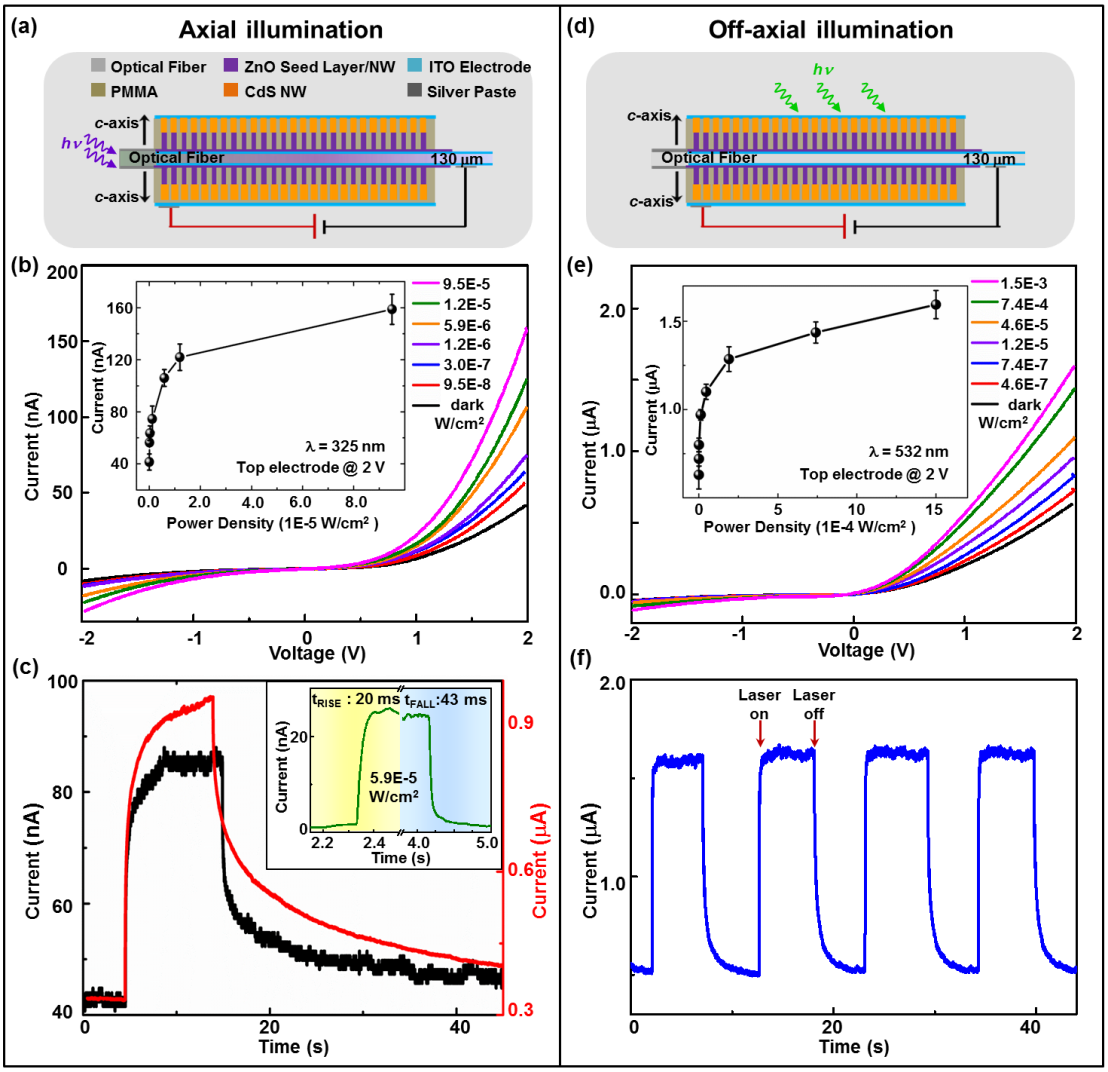

Figure 3.11 Demonstration of UV/visible detections of OF-NWs hybridized PDs. UV detections (left panel). (a) Schematic illustration, (b) *I–V* characteristics, and (c) response time of an OF-NWs hybridized PD under 325 nm axial illuminations. The inset of (b) presents the current change with power density when top electrode is biased at 2 V. The inset of (c) presents the response time of a PD under 325nm off-axial illuminations with power density of 1.5×10^{-5}W/cm^2.
Visible detections (right panel). (d) Schematic illustration, (e) *I–V* characteristics, and (f) time response of an OF-NWs hybridized PD under 532 nm off-axial illuminations. The inset of (e) presents the current change with power density when top electrode is biased at 2 V.[117]

UV/visible detections are firstly investigated by applying incident light signals (325 nm laser as UV source, 532 nm laser as visible source) in two different manners as

schematically shown in Figures 3.11a and d. A beam of 325 nm laser is focused at the cladding-layer-covered end of OF (Figure 3.11a) as UV stimuli for axial illumination mode. Higher light absorbance and detection sensitivity are expected for PD under this working mode as consequences of total internal reflection as well as multi-scattering within OF. By varying the power densities of incident light, a series of *I-V* characteristics are measured and summarized in Figure 3.11b, showing a good photoresponse in output current, increasing from 41.4 nA (dark) to 158.8 nA (9.5×10^{-5} W/cm^2) when top electrode (CdS NWs) is biased at 2 V. A beam of 532 nm laser is shinned from outside onto the surface of PDs for off-axial illumination mode visible detection. Although the construction of these PDs merely allows one side of NWs under direct illuminations, most NWs can still interact with the incident light when considering both transmitting and scattering of the beam by transparent OF core, which cannot be obtained from traditional substrate such as carbon fiber[16]. A similar optoelectronic behavior is observed for visible detection under off-axial illumination mode as shown in Figure 3.11e, with output current increasing from 630 nA (dark) to 1594 nA (9.5×10^{-4} W/cm^2) when top electrode (CdS NWs) is biased at 2 V.

Response time of OF-NWs hybridized PDs is carefully studied and presented in Figures 3.11c and f for both UV and visible detections. UV response presented in Figure 3.11c were obtained under 325 nm axial illumination with intensity of 5.9×10^{-6} W/cm^2 for 0% (black curves in Figure 3.11c) and -0.86% (red curves in Figure 3.11c) strain condition. By carefully studying the rise/fall edges of response time curves, a second-order exponential function is employed [132, 133] to calculate the rise and fall times. Upon straining (-0.86%), the UV detection rise time decreases from 0.63 s to 0.61 s; the fall

time decreases from 4.88 s to 1.26 s. The improved response time is resulted from strain-induced piezo-polarization charges presented at the vicinity of CdS/ZnO heterojunctions, which effectively reduce the barrier height (Figure 3.10f), facilitate the separation and transport process of photo-generated carriers, and thus improve the response time at rise/fall edges. Visible response were derived under 532 nm off-axial illumination with intensity of 1.5×10^{-3} W/cm^2 as shown in Figure 3.11f. The corresponding rise and fall times are calculated to be 25 ms and 452 ms following the same exponential fitting function as above. The shortest response time was observed under 325 nm off-axial illumination with intensity of 5.9×10^{-5} W/cm^2 as shown in the inset of Figure 3.11c, with rise time of 20 ms and fall time of 43 ms. These performances are competitive and impressive compared with other reported nanostructure UV detectors.[132, 134, 135]

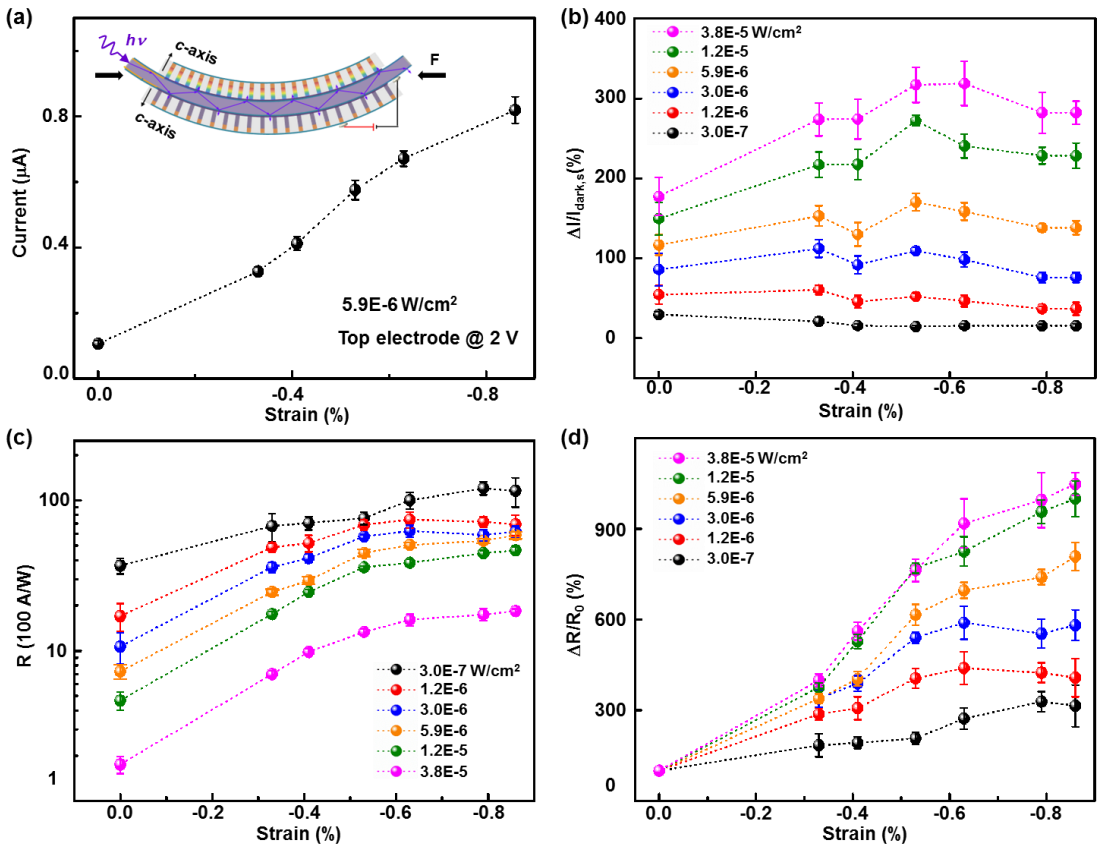

Figure 3.12 Piezo-phototronic effect on OF-NWs hybridized UV PDs under axial illuminations. (a) *I-strain* curve of an OF-NWs hybridized UV PD under 325 nm axial illuminations with power density of 5.9×10^{-6} W/cm^2 when top electrode is biased at 2 V. The inset shows a corresponding schematic experiment set-up. (b) Sensitivity, (c) photoresponsivity *R* and (d) relative changes of *R* of an OF-NWs hybridized UV PD operating in axial illumination mode under a series of power density and external strain conditions, when top electrode is biased at 2 V. $I_{dark,s}$ is dark current under the corresponding external strain, ΔI is the difference between photo and dark current. R_0 is photoresponsivity under no strain. ΔR is the difference between photoresponsivity under strained and unstrained conditions.[117]

Piezo-phototronic effect is then applied to enhance/optimize the performances of OF-NWs hybridized PDs for UV detection. A series of strains (from 0% to -0.86%) are externally applied onto the device working under 325 nm laser axial illumination with various power densities. The optoelectronic behaviors are monitored and presented in Figures 3.12a, showing an obvious enhancement in photoresponse with output current increasing linearly as applying more strains onto PDs. This linear relationship between current and strains provides a potential application for real-time dynamic strain monitoring. To clearly show the mechanism of current increasing, the relative difference between photocurrent and dark current under each certain power density and strain condition with respect to the corresponding dark current is defined as $\Delta I / I_{dark,s} = \frac{I_{light,s} - I_{dark,s}}{I_{dark,s}}$, $I_{light,s}$ and $I_{dark,s}$ are photo and dark current under certain external strain (indicated by subscript "s") , respectively. The photosensitivity of the OF-NWs hybridized UV PD under different power density and strains is derived and summarized in Figure 3.12b. Generally, a better sensitivity is achieved when higher strains are applied. A local maximum is observed under strong light illumination (pink, green and orange lines in Figure 3.12b), while fading away as reducing the power density

(blue, red and black lines in Figure 3.12b). These phenomena are attributed to the screening effect against piezo-polarization charges induced by light-generated free charge carriers.[22] Under strong illumination, a huge amount of free carriers are generated to partially screen the piezo-polarization charges presenting at vicinity of ZnO/CdS heterojunction interface, forming a competing mechanism and thus leading to an local maximum; while under weak illumination, strain-induced piezo-charges are still in dominance without a local extreme obtained in sensitivity.

Another critical parameter to evaluate performances of PDs, photoresponsivity *R*, is also calculated and analyzed comprehensively as shown in Figure 3.12c under each strain and power density conditions when top electrode is biased at 2 V. A monotonously increase of *R* with applied strains is concluded from Figure 3.12c under each power density, with the largest *R* value reaching 1.2×10^{4} A/W when applying a -0.86% strain onto the PD under 325 nm laser axial illumination with a power density of 3.0×10^{-7} W/cm^2. By assuming EQE equals to 1, the internal gain of this PD is calculated as 4.58×10^{4}, which can be induced by the heterojunction at the interface of ZnO and CdS nanostructures and the presence of oxygen-related hole-trapping states at the NW surface.[132] The achieved photoresponsivity *R* value is much larger than that of commercial UV PDs (mostly in the range of 0.1-0.2 A/W),[136, 137] and also near 10^5 times larger in magnitude than that obtained from a Si/ZnO core-shell NW array PD (1.0×10^{-2} A/W, 480 nm, -1 V);[128] 10^3 times larger in magnitude than that of a Si/CdS core-shell NW network PD (<1 A/W, 480 nm, -1 V).[129] Lower photoresponsivity *R* observed at higher power density could be a consequence of saturation absorption of photons by the semiconductors, as reported previously in a ZnO nanowire based UV light PD.[22] It is

because the difference between photo and dark current is not linearly proportional to light intensity, and R decreases with increasing the power density of incident light. A better insight of piezo-phototronic effect on photoresponsivity R can be derived by calculating the relative changes of R as $\Delta R/R_0$ (R_0 is the corresponding R under strain-free condition) under each power density (Figure 3.12d). This value increases as applying either stronger incident light or larger external strains as shown in Figure 3.12d, featuring with the largest value of 1048% under strongest power density (3.8×10^{-5} W/cm^2) and largest external strains (-0.86%) when the PD is working under 325 nm laser axial illumination mode.

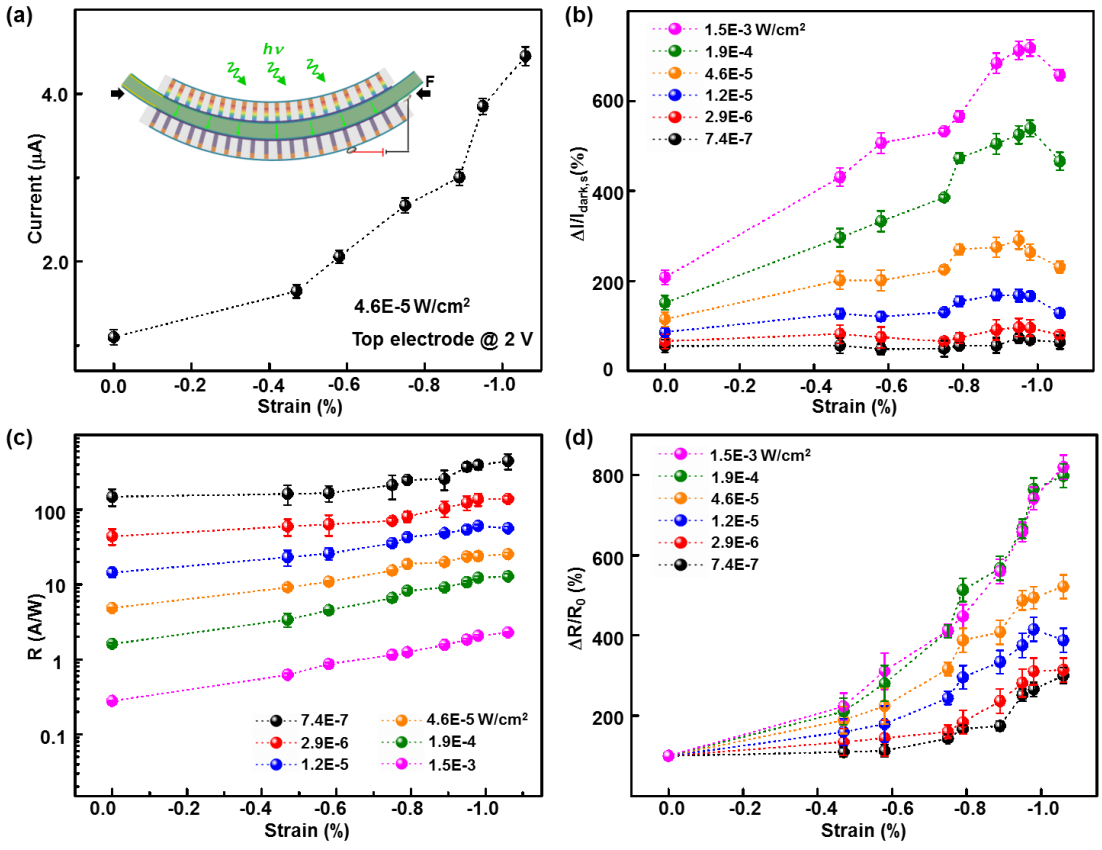

Figure 3.13 Piezo-phototronic effect on OF-NWs hybridized visible PDs under off-axial illuminations. (a) *I-strain* curve of an OF-NWs hybridized visible PD under 532 nm off-axial illuminations with power density of 4.6×10^{-5} W/cm^2 when top electrode is biased at 2 V. The inset shows a corresponding schematic experiment set-up. (b) Sensitivity, (c)

photoresponsivity R and (d) relative changes of R of an OF-NWs hybridized visible PD operating in off-axial illumination mode under a series of power density and external strain conditions, when top electrode is biased at 2 V. $I_{dark,s}$ is dark current under the corresponding external strain, ΔI is the difference between photo and dark current. R_0 is photoresponsivity under no strain. ΔR is the difference between photoresponsivity under strained and unstrained conditions.[117]

Piezo-phototronic effect enhanced visible detections of these OF-NWs hybridized PDs are also carefully studied in a similar manner under 532 nm off-axial illuminations. *I-V* characteristics, sensitivity, photoresponsivity R and its relative changes are all systematically investigated and summarized in Figures 3.13 under all power density and strain conditions, showing similar changes to those shown in Figure 3.12. Under 532 nm off-axial illuminations, the highest relative sensitivity of 718% was achieved (Figure 3.13b) by applying a -0.98% strain on the PD at a power density of 1.5×10^{-3} W/cm^2; the largest photoresponsivity R of 446 A/W (Figure 3.13c) was derived at -1.06% strain and a power density of 7.4×10^{-7} W/cm^2; the largest relative change of R of 820% (Figure 3.13d) was obtained at -1.06% strain and 1.5×10^{-3} W/cm^2 power density. These results indicate the capability of our OF-NWs hybridized PDs for visible detections.

OF-NWs hybridized UV/visible PDs possess novel designed configurations mainly in two aspects. First, optical fiber is employed as the foundation of this PD, enabling two working modes, axial illumination with light propagating inside OF due to its light guiding feature and internal multi-reflection; off-axial illumination with incident light applied on its surface to interact with most NWs through transmitting and scattering of light by transparent OF core. Also direct integration with optical communication system can be achieved by utilizing fiber welding technology in a coupler-free manner. Second, the newly designed engineering method and OF-NWs hybridized concept

demonstrated in this work can be extended to other materials combinations,[138-142] including infrared-sensitive materials and piezoelectric materials, and thus broaden the spectra ranges for more practical applications. Based on these newly designed OF-NWs hybridized PDs, we achieved a response time as fast as 20 ms and R as high as 1.2×10^4 A/W, both of which are competitive and impressive compared with other reported nanostructure PDs.[143, 144] Introduction of the three-way coupling piezo-phototronic effect provides a feasible approach to enhance/optimize the performances of these PDs. Utilizing positive piezo-polarization charges induced at vicinity of ZnO/CdS heterojunction interface upon straining to effectively modulate the barrier height formed at local interface, piezo-phototronic effect successfully tune/control the electronic transport and optoelectronic processes, when charge carriers travel across the heterojunction interface. Enhancement/optimization in PD sensitivity by up to 718% (-0.98% strain, 1.5×10^{-3}W/cm^2 at 532 nm off-axial illumination) and photoresponsivity by up to 2067% (-0.86% strain, 9.5×10^{-4}W/cm^2 at 325 nm off-axial illumination) are derived under externally applied strains. Possible applications of this newly designed piezo-phototronic PD may include energy-efficient optical communication system, unreachable areas and weak signals detection, safety monitoring of optical communication systems, damage-free mapping of electromagnetic field distribution in isolated systems, and bio-compatible optoelectronic probes.

3.2.2 Piezo-Phototronics Logic Circuits[118]

Emerging applications in wearable technology, pervasive computing, human-machine interfacing, implantable surgical instruments and biomedical diagnostics

demand active and adaptive interactions between electronics and ambient/host (e.g. human body). Direct detecting, processing and control of the information encoded in environmental stimuli by logic units may therefore be necessary. In this work, we report the implementation of piezo-phototronic logic operations (logic gates) and binary computations, such as half/full addition and subtraction, over optical and mechanical dual-inputs through cascaded logic circuits in cadmium sulfide (CdS) nanowire networks. Using polarization charges created at metal-CdS interface under strain to gate/modulate electrical transport and optoelectronic processes of local charge carriers, the piezo-phototronic effect has been applied to design two-terminal transistors, which process mechanical and optical stimuli on the devices into electronic controlling signals. The nanowire networks have been further demonstrated for achieving gated D latch to store information carried by these stimuli. The piezo-phototronic logic devices may have applications in optical micro-/nano-electromechanical systems, tunable bio-optoelectronic probes, adaptive optical computing and communication.

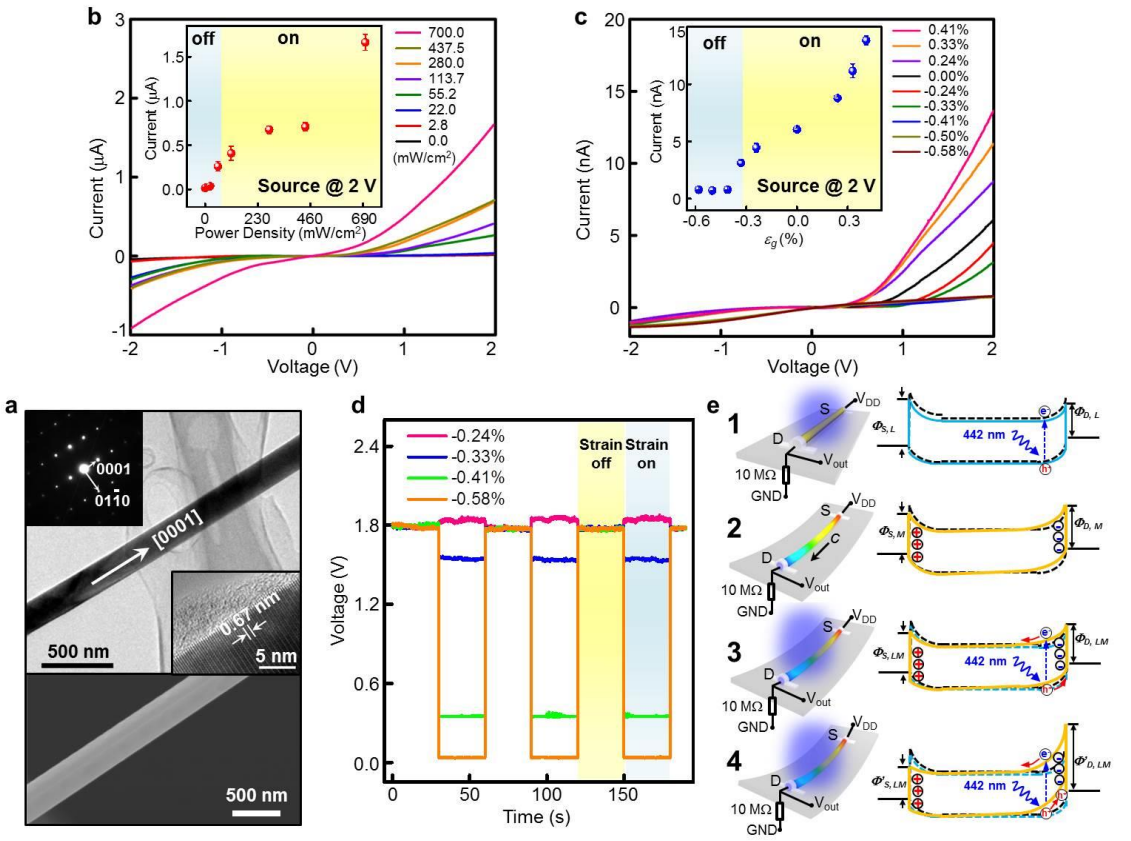

Figure 3.14 Characterization and working principle of light-strain dual-gated transistors (LSGTs). (a) SEM, TEM, HRTEM and corresponding selected area electron diffraction (SAED) pattern of a CdS NW; (b) *I-V* characteristics of a typical LSGT under different light power densities of a 442 nm laser beam, a triangular wave swiping from -2 V to 2 V was applied across the device. The inset shows a current *vs.* power density curve with source electrode biased at 2 V; (c) *I-V* characteristics of a typical LSGT under different strain conditions without light illumination, a triangular wave swiping from -2 V to 2 V was applied across the device. The inset presents a current *vs.* strain curve with source electrode biased at 2 V; (d) *V-t* characteristics of a typical LSGT under 700 mW/cm^2 illumination of a 442 nm laser beam, by applying four different strains periodically on the device; (e) Schematic illustration of LSGTs and the corresponding band diagrams under (1) 442 nm illumination; (2) small compressive strains; (3) small compressive strain and 442 nm illumination; (4) large compressive strain and 442 nm illumination.[118]

CdS NW is of particular interest for investigating piezo-phototronic effect and implementing related applications, due to its visible-range optical response and intrinsic piezoelectric property. CdS NWs used in this work were synthesized through a vapor-liquid-solid (VLS) process[145]. A typical transmission electron microscopy (TEM) image

of the as-synthesized NWs is shown in Figure 3.14a, indicating that the single crystalline CdS NWs grow along [0001] direction (*c*-axis) and possess non-centrosymmetric wurtzite structure[146]. A single CdS NW was then transferred onto a polyethylene terephthalate (PET) substrate for fabricating a flexible two-terminal M-S-M device (Figure 3.14a), with drain and source electrodes fabricated at two NW ends. Figure 3.14b shows the photo-response of an as-fabricated device to visible light illumination with energy (wavelength = 442 nm) above the band gap of CdS (~ 2.4 eV). When intensity of the illuminating laser exceeds a threshold value (~ 50 mW/cm^2, Figure 3.14b inset), a significant enhancement in photocurrent (from 15.6 nA to 261 nA) is observed under moderate source bias, due to the photon generation of free carriers within the CdS NW (Figure 3.14e1)[147]. The shape of photocurrent response is consistent with the formation of two back-to-back Schottky contacts between Ag electrodes and CdS NW, with Schottky barrier heights (SBHs) at both source and drain contacts lowered under photo-excitation (Figure 3.14e1)[148]. Optical illumination with appropriate energy and intensity can therefore modulate the conductivity of the CdS NW device and turn it into electrically "on" state (Figure 3.14b inset).

Carrier transport in the CdS NW device can also be controlled by mechanical strain. Figure 3.14c shows the device's drain-source current in the dark condition as a function of applied strain. The asymmetric trend observed in dark current at the source and drain electrodes in responding to strains indicates the characteristics of the piezotronic effect[18], which is the modulation of local interfacial band structure and charge carrier transport across junction/contact formed in piezoelectric semiconductor devices by strain-induced polarization charges at the interface. When a compressive strain is

applied onto the CdS NW, positive and negative piezoelectric polarization charges appear in the vicinity of Schottky barrier interfaces at the source and drain contacts, respectively, owing to the *c*-axis orientation of the wurtzite CdS NW (Figure 3.14a and 3.14e2). Positive polarization charges attract the free electrons toward the barrier interface, giving rise to a reduced depletion width and therefore decreased local barrier heights at source contact; while the negative polarization charges repel the electrons away from the interface, resulting in a expanded depleted zone and thus increased local barrier heights at drain contact (Figure 3.14e2). Similarly, negative (positive) piezoelectric polarization charges induced at source (drain) barrier by applying tensile strains increase (decrease) the corresponding local SBHs. Since electronic transport in M-S-M structure is dictated by the contact with reversely biased Schottky barrier[149], a change in SBH at the reversely biased drain contact due to strain-induced polarization charges results in the observed transport curves in Figure 3.14c, showing a significant increase of current from 0.8 nA (at -0.58% strain) to 3.1 nA (at -0.33% strain), 6.1 nA (strain free) and 13.8 nA (at 0.41% strain) when source electrode is biased at 2 V. The mechanical strain hence effectively controls the signal in two-terminal CdS NW device (Figure 3.14c inset) as a "strain-gate".

We have further studied the piezo-phototronic effect in two-terminal CdS NW device by introducing both optical illumination and mechanical strain to the device. A pull-down resistor (10 MΩ) is connected between the drain electrode and ground. The voltage across the resistor is monitored when CdS NW is under different illuminations and strains. For example, the output voltage under 700 mW/cm^2 illumination increases from 1.8 V to 1.85 V under -0.24% compressive strain, while the value decreases from 1.8 V to 1.53 V, 0.35 V and 0.03 V when compressive strain further increases to -0.33%,

-0.41% and -0.58%, respectively (Figure 3.14d). The negative polarization charges induced under small compressive strains (-0.24%) increases the local electric field intensity in the depletion region at the drain barrier. The modified band profile hence promotes the separation and mitigates the recombination of photo-induced electron-hole pairs by accelerating the drift of both charge carriers (Figure 3.14e3). Consequently, photo-conductivity of the CdS NW device increases when small compressive strains are applied, as evidenced by the increase in output voltage across the pull-down resistor (Figure 3.14d, for the -0.24% strain case). When the applied compressive strain is high enough, however, the edge of the CdS NW's valence band at the interface is raised above the Fermi level of the electrode. As a result, an energy barrier for holes is formed at the drain barrier interface, which hinders the separation of photo-induced electron-hole pairs and promotes the recombination of them, with the photo-generated holes trapped at the drain barrier (Figure 3.14e4). The significantly increased SBH at reverse-biased drain barrier further reduces the photo-current. Therefore, photo-conductivity of the CdS NW device decreases when large-enough compressive strains are applied, as indicated by the decrease in output voltage (Figure 3.14d, for the -0.33%, -0.41% and -0.58% strain cases). When the illumination intensity is low, on the other hand, separation of photo-excited electron-hole pairs is nearly complete. Change in device conductivity is therefore dominated by the change of band profiles at reversely biased drain barrier due to strain-induced polarization charges[21, 51, 150]. With less screening of the polarization charges by photo-induced free carriers under low-intensity illumination, the energy barrier for hole transport at drain barrier forms under even smaller compressive strains.

Using polarization charges created at M-S interface under strain to gate/modulate electrical transport and optoelectronic processes of local charge carriers *via* the piezo-phototronic effect, we are therefore able to implement the shown two-terminal light-strain-gated-transistor (LSGT), which processes mechanical and optical stimuli on the devices into electronic controlling signals (Figure 3.14d). Significantly, these data demonstrate that two distinct states are observed with on/off ratio larger than 60. For example, after 700 mW/cm^2 illumination is applied, conductance of LSGT changes by ~10^3 times as strain inputs vary between 0 ("strain off") and -0.58% ("strain on") (Figure 3.14d), with the output voltage switching from 1.8 V to 0.03 V, respectively. We define the low-resistance state as electrically "on" and the high-resistance state as electrically "off" of the LSGT. This is different from the voltage-gated operation of traditional FET. Neither of the above programmed state shows degradation over prolonged period. The stable programmability of individual LGSTs between the "on" and "off" states allows further construction of distinct functional circuits from cascaded network of LGSTs as described below.

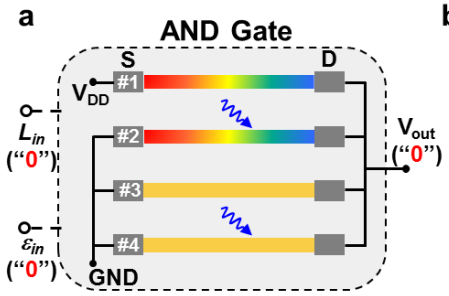

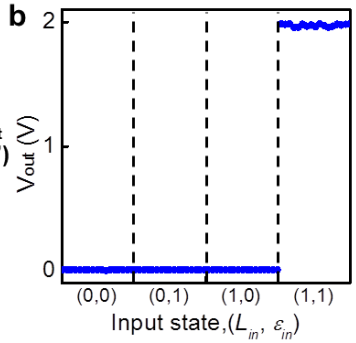

c

L_{in}	ε_{in}	V_{out}
"0"	"0"	0 (5E-3 V)
"0"	"1"	0 (5E-3 V)
"1"	"0"	0 (5E-3 V)
"1"	"1"	1 (1.98 V)

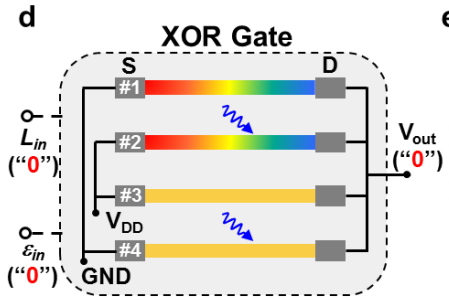

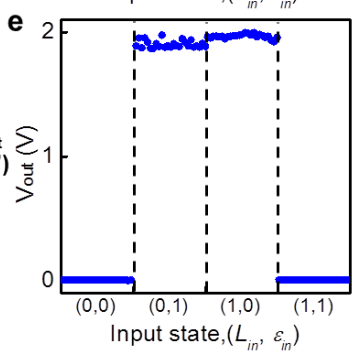

f

L_{in}	ε_{in}	V_{out}
"0"	"0"	0 (5E-3 V)
"0"	"1"	1 (1.90 V)
"1"	"0"	1 (1.97 V)
"1"	"1"	0 (5E-3 V)

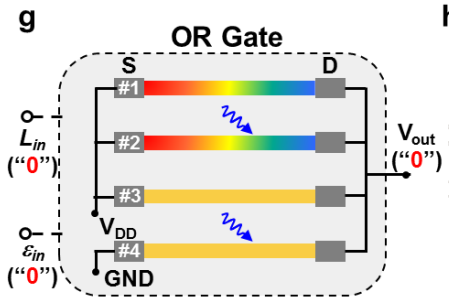

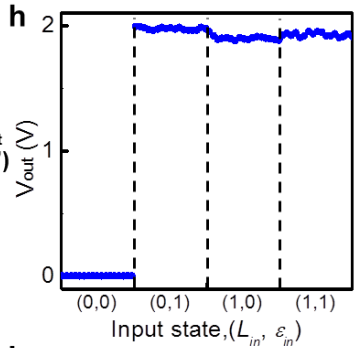

i

L_{in}	ε_{in}	V_{out}
"0"	"0"	0 (5E-3 V)
"0"	"1"	1 (1.98 V)
"1"	"0"	1 (1.90 V)
"1"	"1"	1 (1.93 V)

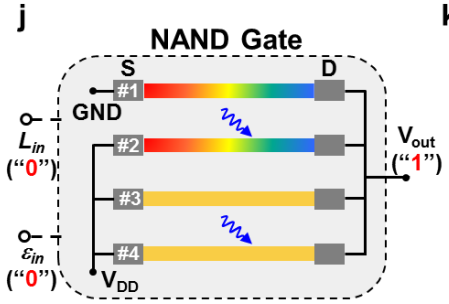

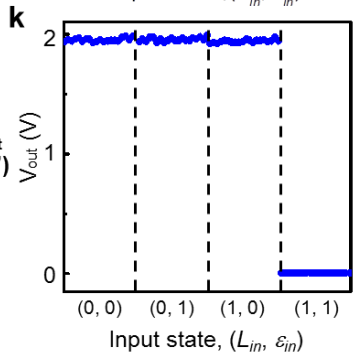

l

L_{in}	ε_{in}	V_{out}
"0"	"0"	1 (1.95 V)
"0"	"1"	1 (1.96 V)
"1"	"0"	1 (1.94 V)
"1"	"1"	0 (5E-3 V)

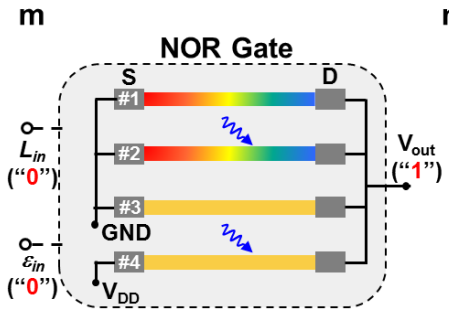

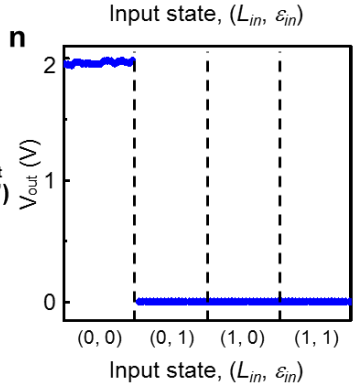

o

L_{in}	ε_{in}	V_{out}
"0"	"0"	1 (1.96 V)
"0"	"1"	0 (5E-3 V)
"1"	"0"	0 (5E-3 V)
"1"	"1"	0 (5E-3 V)

Figure 3.15 Light-strain controlled piezo-phototronic logic gates and some basic operations. Schematic configuration, electric output signals and experimental truth table with physical values of piezo-phototronic logic (a-c) AND gate, (d-f) XOR gate, (g-i) OR gate, (j-l) NAND gate, (m-o) NOR gate.[118]

We first investigate the potential of these "dual-gate" programmable LSGTs for building fundamental logic gates with four coupled NW elements (Figure 3.15). Each of these four LGSTs has two independently configurable gate controlling signals, L_{in} and ε_{in}, for optical and mechanical inputs, respectively. The output from these logic units is electrical voltage. In our demonstration, the logic "0" state for optical input L_{in} is defined as focusing the 442 nm laser with intensity of 700 mW/cm^2 on #2 and #4 LSGTs; the logic "1" state for optical input L_{in} is defined as focusing the 442 nm laser with intensity of 700 mW/cm^2 on #1 and #3 LSGTs. The logic "0" state for mechanical input ε_{in} is defined as applying -0.58% compressive strains on #1 and #2 LSGTs; the logic "1" state for mechanical input ε_{in} is defined as applying -0.58% compressive strains on #3 and #4 LSGTs (Figure 3.15). These definitions are adopted in all demonstrations here and afterward. Figures 3.15a, d, g j and m illustrate the configurations of piezo-phototronic AND, XOR, OR, NAND and NOR logic gates comprising of four LGSTs. These piezo-phototronic logic operations are experimentally verified as shown in Figure3.15b, e, h, k and n with low electric output (logic "0" output) at around 0 V and high electric output (logic "1" output) at around 2 V, which is the bias voltage V_{DD}. The physical values of input and output signals are presented in the experimental truth table in Figure 3.15c, f, I, l and o. Only the instances when both L_{in} and ε_{in} are logic "0" are illustrated in Figure 3.15a, d, g, j and m as examples, with the distribution of piezoelectric polarizations highlighted.

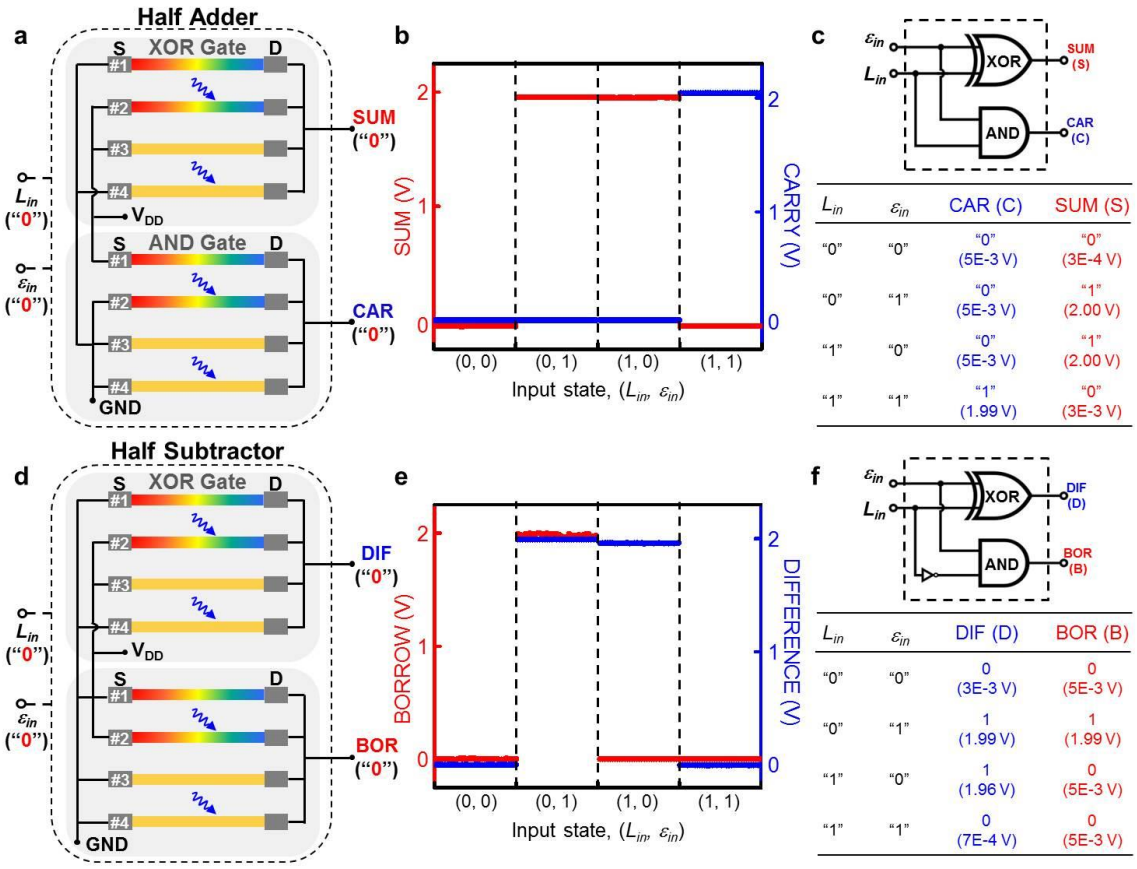

Figure 3.16 Light-strain controlled piezo-phototronic logic computations. Schematic configuration, electric output signals, logic diagram and experimental truth table with physical values of (a-c) piezo-phototronic half adder and (d-f) piezo-phototronic half subtractor.[118]

Piezo-phototronic arithmetic logic computations such as one-bit half adder and subtractor have been further implemented by assembling the above fundamental logic gates with external wiring (Figure 3.16). The operation of piezo-phototronic half-adder is programmed as shown in Figure 3.16a by integrating XOR and AND logic units, which computes the summation of two inputs L_{in} and ε_{in}. The outputs SUM (S) and CAR (C) represent the sum and carry-out of the summation of the two inputs, respectively, with $S=L_{in} \oplus \varepsilon_{in}$ and $C=L_{in} \cdot \varepsilon_{in}$. The symbols '$\oplus$' and '$\cdot$'represent logical XOR and AND. Typical operations of the resulting circuit for V_{DD} = 2.0 V (Figure 3.16b) show that, as

the input levels of L_{in} and ε_{in} are swept from logic state '0' to logic state '1', the outputs S and C switch between logic '0' (both ~0 V) and logic '1' (2.0 and 1.99 V, respectively). Further tests show that the output of S and C for four typical input combinations (Figure 3.16b) all had similar output ranges: ~ 0 V for logic state '0' and 1.9-2.0 V for logic state '1'. The expected and experimental results for a piezo-phototronic half adder are summarized in the truth table (Figure 3.16c), which shows good consistency for this fundamental logic unit. By designing the wiring layout, piezo-phototronic half-subtractor has also been presented. The two outputs of the circuit, DIF (D) and BOR (B), represent the difference and borrow, respectively, of the subtraction of inputs L_{in}-ε_{in}, with $D=L_{in} \oplus \varepsilon_{in}$ and $B=\overline{L_{in}} \cdot \varepsilon_{in}$, where $\overline{L_{in}}$ is the logical negation of L_{in}. Measurements of D and B for different input combinations (Figure 3.16e) show that the output voltage levels for logic state '0' (0.003-0.007 V) and logic state '1' (1.96-1.99 V) are well separated and represent robust states. Moreover, the truth table (Figure 3.16f) summarizing the expected and experimental results for the half subtractor shows consistent logic for this unit.

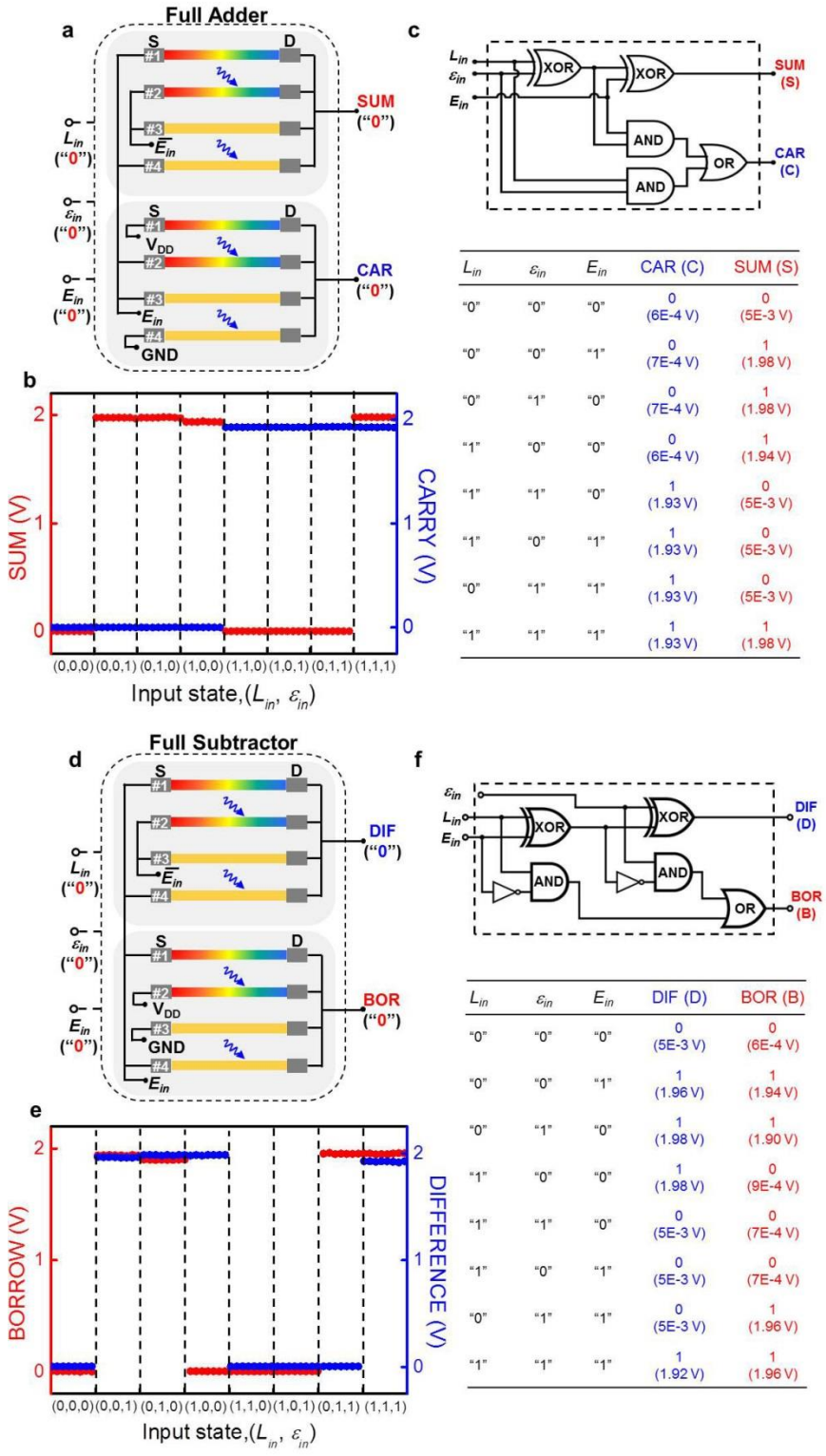

L_{in}	ε_{in}	E_{in}	CAR (C)	SUM (S)
"0"	"0"	"0"	0 (6E-4 V)	0 (5E-3 V)
"0"	"0"	"1"	0 (7E-4 V)	1 (1.98 V)
"0"	"1"	"0"	0 (7E-4 V)	1 (1.98 V)
"1"	"0"	"0"	0 (6E-4 V)	1 (1.94 V)
"1"	"1"	"0"	1 (1.93 V)	0 (5E-3 V)
"1"	"0"	"1"	1 (1.93 V)	0 (5E-3 V)
"0"	"1"	"1"	1 (1.93 V)	0 (5E-3 V)
"1"	"1"	"1"	1 (1.93 V)	1 (1.98 V)

L_{in}	ε_{in}	E_{in}	DIF (D)	BOR (B)
"0"	"0"	"0"	0 (5E-3 V)	0 (6E-4 V)
"0"	"0"	"1"	1 (1.96 V)	1 (1.94 V)
"0"	"1"	"0"	1 (1.98 V)	1 (1.90 V)
"1"	"0"	"0"	1 (1.98 V)	0 (9E-4 V)
"1"	"1"	"0"	0 (5E-3 V)	0 (7E-4 V)
"1"	"0"	"1"	0 (5E-3 V)	0 (7E-4 V)
"0"	"1"	"1"	0 (5E-3 V)	1 (1.96 V)
"1"	"1"	"1"	1 (1.92 V)	1 (1.96 V)

Figure 3.17 Light-strain controlled piezo-phototronic combinational logic circuits. Schematic configuration, electric output signals, logic diagram and experimental truth table with physical values of (a-c) piezo-phototronic one-bit full adder and (d-f) piezo-

phototronic one-bit full subtractor. Electric inputs E_{in} follows the conventional definition, logic "0" state is defined as low voltage, logic "1" state is defined as high voltage.[118]

By introducing a third controlling signal, E_{in} for electrical input, to the cascaded network of LSGTs, more complex piezo-phototronic units such as one-bit full adder and subtractor has also be demonstrated, which are important components for arithmetic logic operations in modern digital electronics. Experimental results show that these piezo-phototronic combinational circuits are capable of logically processing information carried by input signals from different domains through a set of Boolean functions. Figure 3.17a illustrates the configuration of one-bit full-adder by cascading XOR and AND logic gates with specifically designed wiring layout, which computes the summation of three inputs, L_{in}, ε_{in} and E_{in}. The outputs SUM (S) and CAR (C) represent the sum and carry-out of the summation of these three inputs, respectively, with $S=L_{in} \oplus \varepsilon_{in} \oplus E_{in}$ and $C=(L_{in} \cdot \varepsilon_{in}) + (E_{in} \cdot (L_{in} \oplus \varepsilon_{in}))$. The symbols '$\oplus$', '$\cdot$' and '+' represent logical XOR, AND and OR. Measurements of S and C for different input combinations (Figure 3.17b) show that the output voltage levels for logic state '0' (0.001-0.005 V) and logic state '1' (1.93-1.98 V) are well separated. The truth table summarizing the expected and experimental results for the full adder (Figure 3.17c) shows good consistency for this arithmetic logic unit. Similarly, operation of one-bit piezo-phototronic full-subtractor is realized (Figure 3.17d-f) for computing the subtraction of inputs L_{in}-ε_{in}-E_{in}, with $D=L_{in} \oplus \varepsilon_{in} \oplus E_{in}$ and $B=E_{in} \cdot \overline{(L_{in} \oplus \varepsilon_{in})} + \overline{L_{in}} \cdot \varepsilon_{in}$, where $\overline{L_{in}}$ is the logical negation of L_{in}. Physical values of output D and B are measured and summarized in Figures 3.17f and 3.17e, showing robust states as well as good consistency for this unit with output voltage levels for logic state '0' (0.001-0.005 V) and logic state '1' (1.90-1.98 V) well separated. These results show the

capability and flexibility of the cascaded network of LSGTs to achieve the critical functions of combinational circuit elements, which also present the potential to integrate these prototype devices into even larger-scale integrated circuits such as multi-bit arithmetic computations in an integrated configuration.

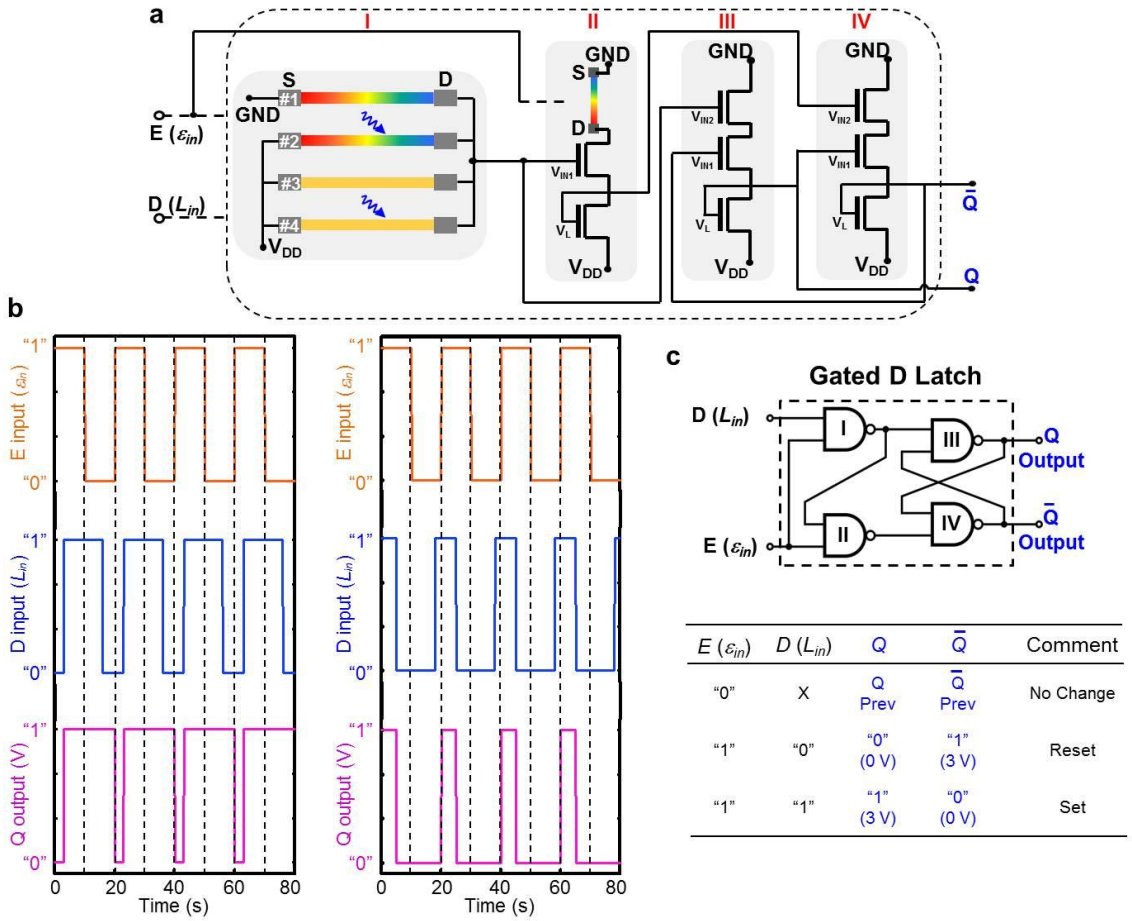

E (ε_{in})	D (L_{in})	Q	$\bar{Q}$	Comment
"0"	X	Q Prev	$\bar{Q}$ Prev	No Change
"1"	"0"	"0" (0 V)	"1" (3 V)	Reset
"1"	"1"	"1" (3 V)	"0" (0 V)	Set

Figure 3.18 Light-strain controlled piezo-phototronic sequential logic circuits. Piezo-phototronic gated D latch. (a) Schematic configuration of a piezo-phototronic gated D latch composing of four NAND gates labeled as "I", "II", "III" and "IV"; (b) Two sets electric output signals of a gated D latch, output Q follows input data D when clock signal E is set to logic "1"; output Q retains its previous state when clock signal E is set to logic "0", V_{DD} = 3 V; (c) Logic diagram and experimental truth table with physical values of a gated D latch.[118]

Notably, the assembled LSGTs units can also be configured as a sequential circuit element such as D latch[151], which represents an important component beyond the scope

of combinational elements for information storage in digital circuits and communications. The outputs of D latch depend not only on the present inputs, but also on the states of memory elements (past inputs). Figure 3.18a shows the piezo-phototronic D-latch circuit composed of one LSGTs based NAND gate (I) and three conventional FETs based NAND gates (II, III and IV) with two feedback connections between output Q and input to NAND gate IV, as well as output $\overline{Q}$ and input to NAND gate III. As a consequence, output signal Q equals input D (optical input, L_{in}) when the clock signal E (mechanical input, ε_{in}) is set to logic '1', but remains its previous state if the clock signal E is set to logic '0'. Both the optical and mechanical inputs here follow the universal definition mentioned previously. We applied 3 V to all V_{DD} terminals labeled in Figure 3.18a to match input and output signal levels. Repetitive E and D inputs pulses were programmed to test the operation of piezo-phototronic D latch, by applying strains and turning on laser beams periodically to the devices. The measured output Q (Figure 3.18b, left) clearly followed input data D when E was switched to logic '1' (-0.58% compressive strains on #3 and #4 LSGTs), and retained its previous value when clock E was set to logic '0' (-0.58% compressive strains on #1 and #2 LSGTs). A second input waveform has been designed to confirm the robust operation of this piezo-phototronic sequential logic circuit (Figure 3.18b, right). The corresponding truth table summarizing the expected and experimental results as well as comments for the D latch is shown in Figure 3.18c with good consistency of the logic. These results suggest that the demonstrated piezo-phototronic D latch can process and store the information carried by external stimuli such as mechanical strains and optical illumination.

These LSGTs and cascaded piezo-phototronic circuits possess novel, unique and complement features in comparison with existing electronics circuits based on top-down or bottom-up approaches[1, 152, 153]. First, the demonstrated design and results are different from the electrically-gated FET, by replacing the external gating voltage with strain-induced polarization charges for controlling transport and other optoelectronic processes of charge carriers through the piezo-phototronic effect. This is a fundamentally new mechanism which enables the multi-functionality of assembled devices complementary to standard electrical operations realized using thin-film semiconductors and nanomaterials[2, 84, 151, 152, 154, 155]. Second, the presented piezo-phototronic device eliminates the gate electrode and offers a new approach for 3D structuring and integration. The structural transformation from three-terminal configuration into two-terminal one may significantly simplify the layout design and circuitry fabrication for high-density device while maintaining effective control over individual devices. Third, the direct processing and storage of information carried by external stimuli other than electrical signals by piezo-phototronic circuits, which is not available in existing technologies, provides great versatility and potential for developing tunable/adaptive electronics and optoelectronics to carry out intelligent-bearing interactions with the ambient[9]. The electronic output signals from piezo-phototronic circuits after processing the encoded information in ambient stimuli may make possible the control of embedded electronics and sensors for intelligent and adaptive operations in human-electronics interfacing, optical micro- and nano-electromechanical systems, bio-probes and therapeutic device.

3.2.3 Temperature Dependence of Piezo-Phototronics[57, 81]

In this section, temperature dependence of the piezo-phototronic effect in CdS nanowires[81] and *a*-axis GaN nanobelts[57] are studied to better understand the fundamental physics about the three-way coupling piezo-phototronic effect in low ambient temperatures.

3.2.3.1 CdS Nanowires[81]

In this work, the temperature dependence of the piezo-phototronic effect in CdS NWs is systematically investigated by varying the temperature from 77 K to 300 K. Optoelectronic behaviors of CdS NWs are carefully measured by applying a series of light illuminations and straining conditions at each temperature. Under mechanical strains, the corresponding energy band diagrams indicate that the piezo-phototronic effect dominates the transport and separation processes of charge carriers by utilizing strain-induced piezoelectric polarization charges at local interface/junction to modulate the energy band structures of CdS NWs. The piezo-phototronic effect is significantly enhanced by over 550% as lowering the system temperature, since the effective piezoelectric polarization surface/interface charge density is increased due to the reduced screening effect by decreased mobile charge carrier density in CdS NWs at lower temperature. The conductivity, mobile charge carrier density, effective polarization charge density and the corresponding changes of Schottky barrier height (SBH) of CdS NWs are calculated based on theoretical simulations at various temperatures. This work explores the temperature dependence and the fundamental working mechanism of the piezo-phototronic effect, guiding the future design and fabrication of piezo-phototronic

devices for optical communications, human-machine interfacing, health monitoring systems and implantable surgical instruments

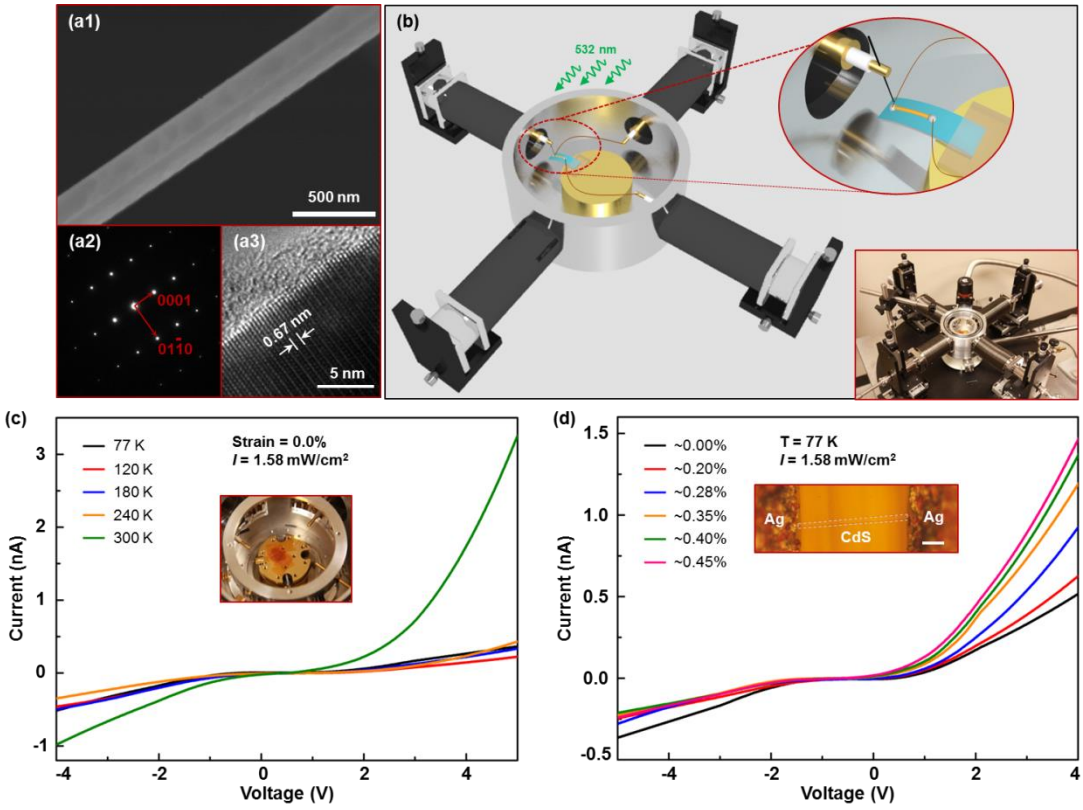

Figure 3.19 Structure and transport characterizations of CdS NWs. (a1) SEM image, (a2) SAED pattern and (a3) HRTEM image of the as-synthesized CdS NW. (b) Schematic illustration and digital image of the micro-manipulation cryogenic probe station system as experimental set-up. (c, d) *I-V* characteristics of CdS NW devices under various (c) temperatures and (d) straining conditions.[81]

CdS NWs used in this work are synthesized through a vapor-liquid-solid (VLS) process described elsewhere.[145] A typical scanning electron microscope (SEM, Hitachi SU8010) image of the as-synthesized CdS NW is shown in Figure 3.19a1, with the diameter of CdS NWs near 300 nm and the length in several hundred micrometers. The corresponding selected area electron diffraction (SAED, Tecnai G2) patterns and high-resolution transmission electron microscope (HRTEM, FEI F30) image are presented in

Figures 3.19a2 and 3.19a3, respectively, indicating that the single crystalline CdS NWs grow along [0001] direction (*c*-axis) and possess non-centrosymmetric wurtzite structure.[146] Optoelectronic performances of the CdS NW devices are measured in a micro-manipulation cryogenic probe system (Janis, model ST-500-2) as schematically shown in Figure 3.19b. Using liquid nitrogen as the cryostat, the temperature of the whole system is ranging from 77 K to 300 K. To maintain reliable thermal equilibrium between the CdS NW and the cryostat, aluminum foil (76 μm in thickness) covered with a layer of Kapton tape (30 μm in thickness) is adopted as the substrate, which features with excellent thermal conductivity, an insulating surface and satisfactory mechanical flexibility. The thermal expansion coefficients of aluminum and Kapton tape are $23.1\times10^{-6}/℃$ and $20\times10^{-6}/℃$,[109] respectively. Substrate deformations due to the mismatch of thermal expansion coefficients can therefore be neglected. The device is fabricated by transferring and bonding an individual CdS NW laterally on this substrate with its *c*-axis in the plane of the substrate. Silver paste are applied to fix both ends of the NW, serving as source and drain electrodes to form a M-S-M structure with two Schottky contacts. By fixing the device at the edge of the cryostat (Figure 3.19b, upper right corner), mechanical strains are introduced through a micro-manipulating probe attached to one of the probing station arms moving in three dimensions. The values of the externally applied tensile strains are calculated following the method reported previously by *Yang et al*.[87] A beam of green laser light with wavelength of 532 nm is shined on the device to provide optical stimuli. The electric output signals are measured and collected by computer-controlled program through a GPIB controller.

Two sets of typical *I-V* characteristics are presented in Figures 3.19c and 3.19d, showing the temperature and strain response of the CdS NW devices, respectively. Under strain free condition and green laser illumination with power density of 1.58 mW/cm^2, the devices display larger output currents at room temperatures (Figure 3.19c), indicating that the conductivity of the CdS NWs increases significantly at room temperature compared to that at low temperature. At 77 K, by applying a beam of green laser with power density of 1.58 mW/cm^2, the output currents increase at positive biased voltages while decrease at the negative side when increasing the externally applied tensile strains from 0% to 0.45%, as shown in Figure 3.19d. These observed results represent the typical transport properties of CdS NWs dominated by the piezotronic effect,[49] which leads to asymmetric changes of barrier heights and thus the output currents at two Schottky contacts. An optical image of the as-fabricated CdS NW device is presented as the inset of Figure 3.19d.

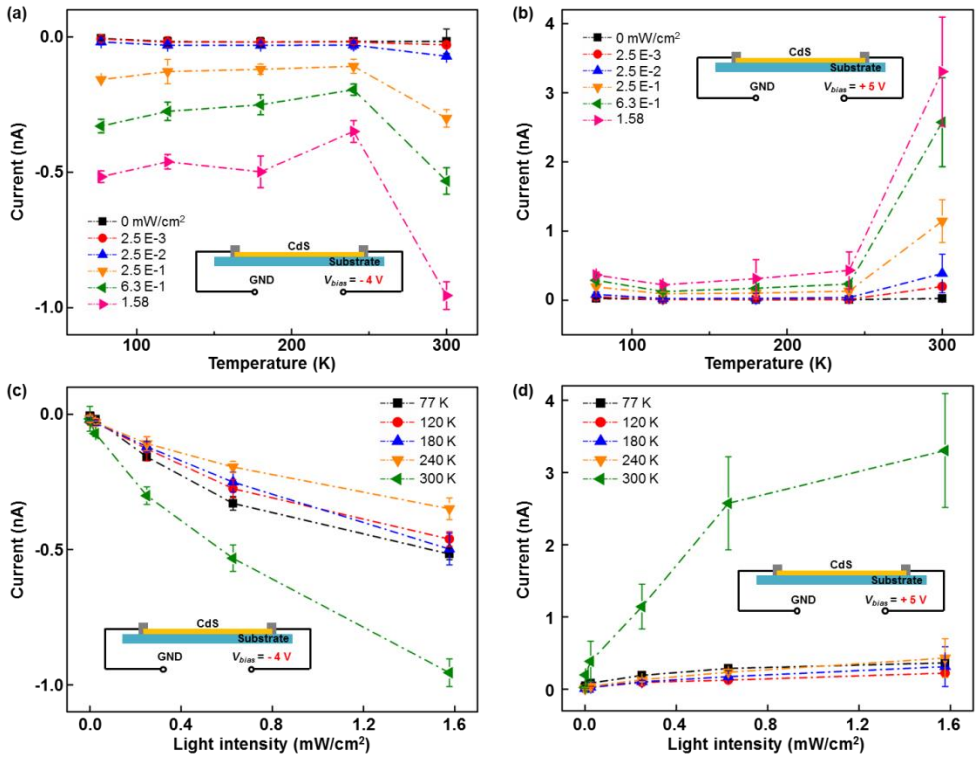

Figure 3.20 Current response of CdS NW devices to temperatures and illuminations. (a, b) Current response of CdS NW devices to various temperatures under a series of illumination intensities and strain free condition at (a) -4 V and (b) +5 V biased voltage. (c, d) Current response of CdS NW devices to various illuminations at different temperatures and under strain free condition by applying a bias voltage of (c) -4 V and (d) +5 V.[81]

The output currents response of CdS NW devices to various temperatures and illumination intensities at both positive and negative biased voltages are systematically investigated and summarized in Figure 3.20, under strain free condition. Figures 3.20a and 3.20b display the temperature response of CdS NW devices under different illumination conditions at -4 V and +5 V biased voltages, respectively. It is obvious that the output currents increase significantly at room temperature compared to those under low temperatures under each illumination intensity for both negative (Figure 3.20a) and positive (Figure 3.20b) biased voltages. These results are reasonable since the carrier density of CdS NWs is determined by ionization of shallow level dopants. As decreasing the temperature, the carrier density decreases due to the freeze-out, leading to a decreased conductance and output currents at lower temperature. By fixing the measurement temperature at 77 K, 120 K, 180 K, 240 K and 300 K, the output current responses of CdS NW devices to illumination intensities are presented in Figures 3.20c (-4 V biased voltage) and 3.20d (+5 V biased voltage). It is straightforward to observe increased currents under stronger laser illuminations at each temperature.

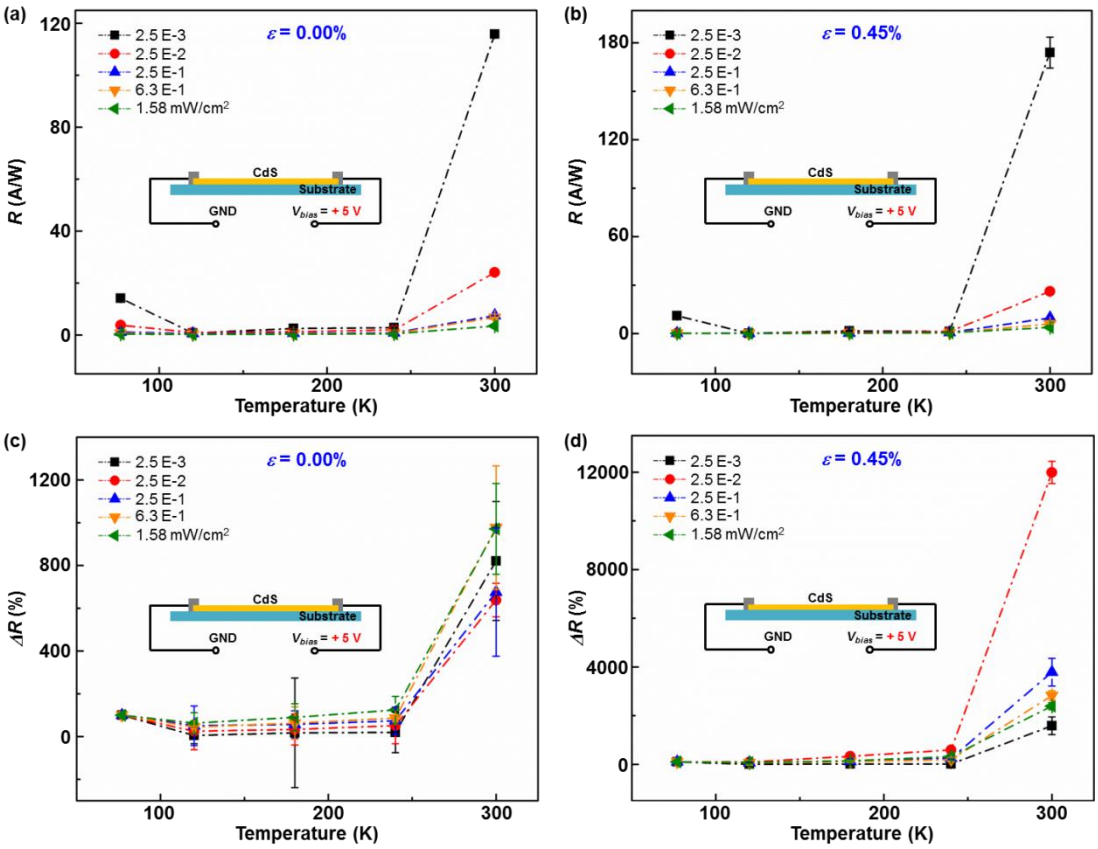

Figure 3.21 Temperature dependence of the photoresponsivity. Photoresponsivity of the device under various illuminations and temperatures, by applying (a) 0.00% and (b) 0.45% strain, biased at +5 V. Relative changes of the photoresponsivity under various illuminations and temperatures, by applying (c) 0.00% and (d) 0.45% strain, biased at +5 V.[81]

As a critical parameter to characterize the optoelectronic performances of CdS NW devices, the photoresponsivity *R* under various temperatures and illumination intensities is calculated and summarized in Figure 3.21 for strain-free (Figures 3.21a, c) and 0.45% external strain (Figures 3.21b, d) conditions at a biased voltage of +5 Volts. From Figures 3.21a and b, it is obvious that higher *R* is observed at room temperature under various illuminations and both strain conditions. Moreover, the highest value of 174 A/W is derived at 2.5×10^{-3} mW/cm^2 and 300 K by applying a 0.45% external strain, indicating the enhancements on the photoresponsivity by the piezo-phototronic effect

compared with the strain-free condition (Figure 3.21a). Besides, relative changes of the photoresponsivity R with respect to R_0 (corresponding photoresponsivity at 77 K) are calculated along the temperature-axis under both strain-free and 0.45% strain conditions as shown in Figures 3.21c and d, respectively. At room temperature (300 K), the largest relative change of R is 976.7% under strain-free condition (6.3×10^{-1} mW/cm^2, Figure 3.21c), and 11990% under 0.45% tensile strain (2.5×10^{-2} mW/cm^2, Figure 3.21d).

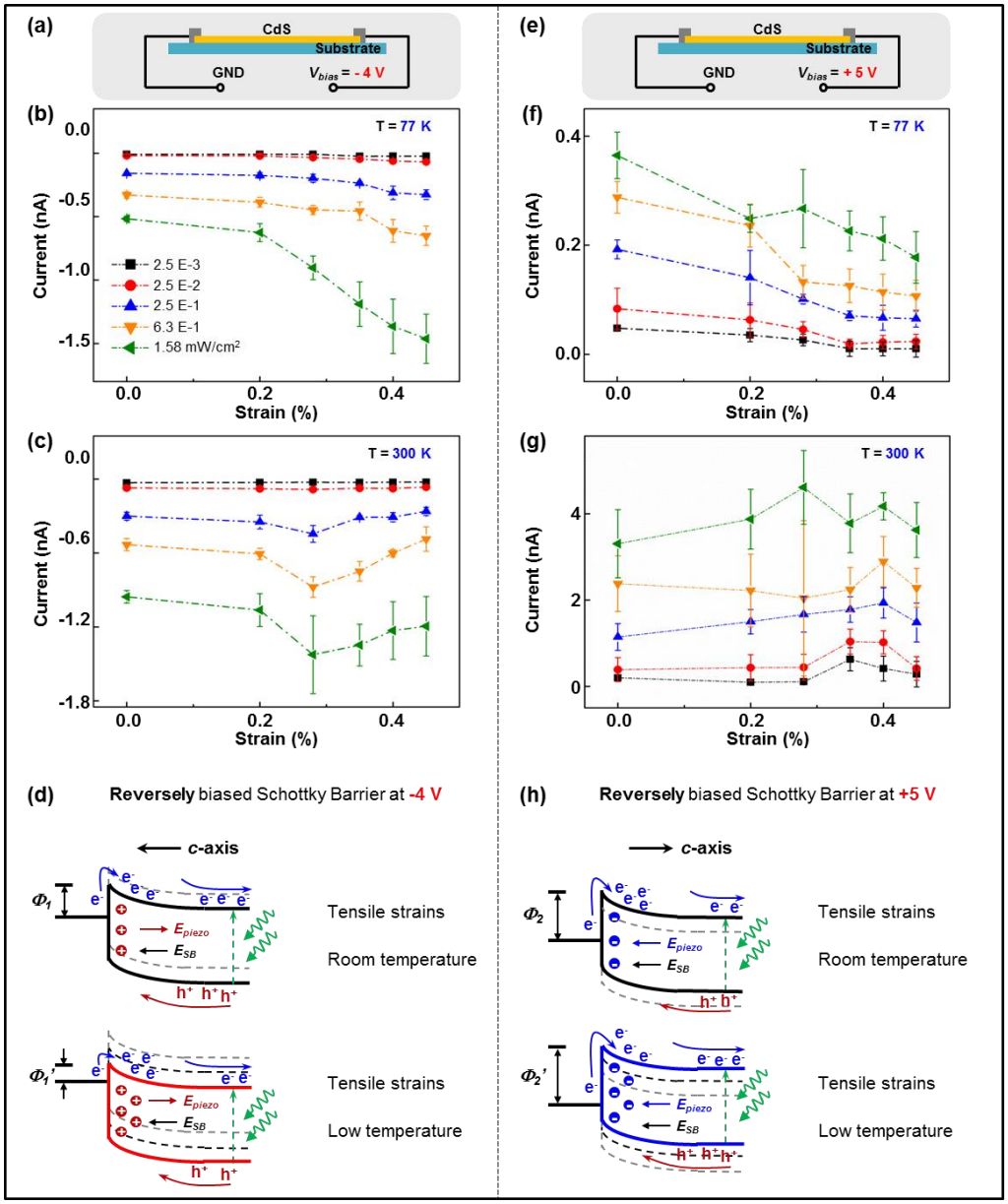

Figure 3.22 Temperature dependence of the piezo-phototronic effect and the working mechanism. (a) At a bias voltage of -4 V, the current *I vs.* strains curve under a series of illumination intensities at (b) 77 K and (c) 300 K, and (d) the corresponding energy band diagrams of CdS NWs under tensile strains at room temperature (top panel) and low temperature (bottom panel). (e) At a bias voltage of +5 V, the current *I vs.* strains curve under a series of illumination intensities at (f) 77 K and (g) 300 K, and (h) the corresponding energy band diagrams of CdS NWs under tensile strains at room temperature (top panel) and low temperature (bottom panel). The figure legends presented in (b) are adopted for plots in (c, f, g).[81]

The piezo-phototronic effect on the output currents of CdS NW devices is carefully studied under a series of light illuminations and straining conditions at different temperatures, ranging from 77 K to 300 K, for both negative and positive biased voltages as shown in Figure 3.22. At -4 V biased voltage (Figures 3.22a-c), the current responses of CdS NW devices to external strains are measured under laser illuminations with power density ranging from 2.5×10^{-3} mW/cm^2 to 1.58 mW/cm^2 at 77 K, 120 K, 180 K, 240 K and 300 K. From these experimental results, the changes of currents present a transition from monotonously increase with increasing the externally applied tensile strains to the existence of a local maximum current at certain tensile strain as raising the measurement temperature from 77 K to 300 K. Besides, the value of the tensile strain corresponding to the local maximum current decreases as increasing the temperature. Considering the fact that the piezo-phototronic effect is a polarized interfacial effect leading to asymmetric changes of barrier heights and the output currents at two Schottky contacts, the currents responses of CdS NW devices to external strains at +5 V biased voltage (Figures 3.22e-g) display a transition from monotonously decrease with increasing the tensile strains to the presenting of a local minimum current at certain tensile straining conditions as heating up the system from 77 K to 240 K. At 300 K (Figure 3.22g), the currents show a local maximum value as reversing the trend of current changes.

Energy band diagrams of CdS NWs are schematically shown in Figures 3.22d and h to systematically explain the observed optoelectronic performances of CdS devices controlled by the piezo-phototronic effect at different temperatures. Upon straining, two of the optoelectronic processes within the CdS NW devices are tuned/controlled by the piezo-phototronic effect. First, the transport of the charge carriers across a reversely biased local M-S Schottky contact is dominated by the SBH, which is controlled by the effective piezoelectric polarization charges presented at the vicinity of the local interface. The density of effective piezo-charges is affected by environment temperatures due to the screening effect of the local free charge carriers to the static piezoelectric charges. Second, the separation process of photo-generated charge carriers near the local contact is affected by the piezoelectric field induced by polarizations. Under a bias voltage of -4 V, positive piezoelectric polarization charges are presented at the reversely biased local Schottky contact under tensile strains (Figure 3.22d). Thus, on one hand, the SBH is reduced by positive piezo-charges (Figure 3.22d), which enhances the carrier transport across the reversely biased local Schottky barrier; on the other hand, the piezoelectric field is in an opposite direction of the current flow and hence reducing the separation efficiency of light-generated electron holes. A competition mechanism is formed between these two processes. At low temperature (Figure 3.22d, bottom), the separation of electron-hole pairs is almost complete with little recombination, and the screening effect to the piezoelectric charges is minimized,[156] the overall output currents are predominantly controlled by the SBH which dominates the carriers' transport across the reversely biased local Schottky contact. The more external tensile strains are applied, the lower SBH is formed. Therefore the currents increase monotonously with increasing the tensile strains

at low temperature as shown in Figure 3.22b. At room temperature (Figure 3.22d, top), the SBH at reversely biased contact is less reduced due to the enhanced screening effect by increased free electron density in CdS NWs. Moreover, the retarding of the electron-hole separation process by the piezoelectric field is becoming considerable. The combination of these two processes results in the observation of a local maximum current at room temperature as shown in Figure 3.22c. A transition from monotonous increase in current to local maximum current at certain straining conditions is therefore observed as raising the temperature from 77 K to 300 K.

Similarly, under a bias voltage of +5 V, negative polarization charges are presented at the vicinity of the local Schottky contact under tensile strains (Figure 3.22h), but with reduced magnitude due to the enhanced screening effect at room temperature. In this scenario, the SBH at local interface is increased by negative piezo-charges (Figure 3.22h) and thus hinder the carrier transport across the reversely biased local Schottky barrier. Meanwhile, the piezoelectric field is in the same direction as the current flow and improving the separation efficiency of light-generated charge carriers. There exists a competition mechanism between these two processes. Therefore, at low temperature (Figure 3.22h, bottom), due to the almost complete separations of electron-hole pairs,[156] the currents decrease monotonously with increasing the tensile strains as shown in Figure 3.22f. At room temperature (Figure 3.22h, top), the SBH at reversely biased M-S contact is slightly increased due to the less effective piezo-charges resulted from the enhanced screening effect; while the separation efficiency of the electron-hole pairs is substantially improved by the piezoelectric field, which is in the same direction as the current flow. The combination of these two processes results in the appearance of a local minimum

current. At 300 K, the separation efficiency of photo-generated charge carriers is improved so significantly by the piezoelectric field to overcome the influence of the increased SBH and start dominating the overall output currents of CdS NW devices. Therefore, a local maximum current is observed as shown in Figure 3.22g.

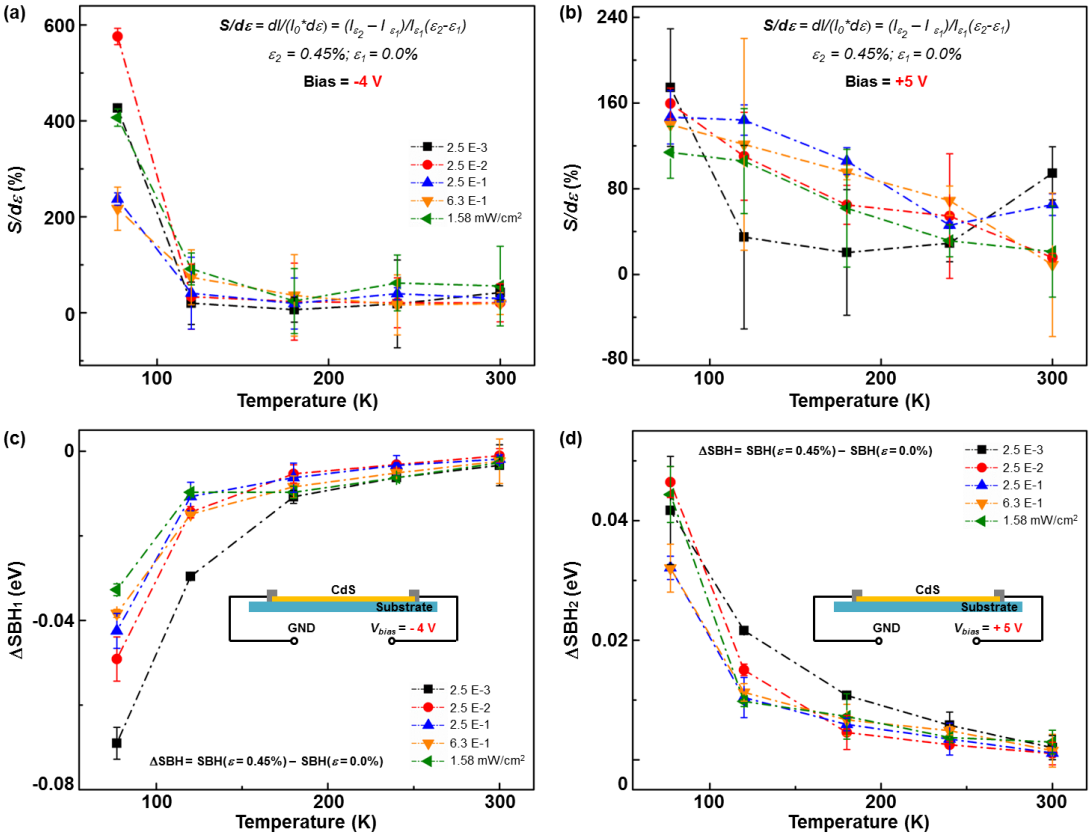

Figure 3.23 Temperature dependence of the piezo-phototronic factor at (a) -4 V and (b) +5 V biased voltage. The piezo-phototronic factor is defined as the response sensitivity per unit strains: $S/d\varepsilon$. The figure legends presented in (a) are adopted for plots in (b). (c, d) Calculated changes of SBH as a function of temperatures at the reversely biased Schottky contact under (c) -4 V and (d) +5 V between 0.45% tensile strain and strain-free condition.[81]

Temperature dependence of the piezo-phototronic effect is further investigated by defining a physical parameter, piezo-phototronic factor, as the response sensitivity per unit strain: $\boldsymbol{S/d\varepsilon} = dI/(I_0*d\varepsilon) = (I_{\varepsilon 2} - I_{\varepsilon 1})/I_{\varepsilon 1}(\varepsilon_2-\varepsilon_1)$, where $I_{\varepsilon 2}$ and $I_{\varepsilon 1}$ correspond to the

currents derived under ε_2 and ε_1 straining conditions at the same illumination intensity, respectively. The piezo-phototronic factors derived at -4 V and +5 V biased voltages are summarized and plotted as a function of temperatures in Figures 3.23a and 3.23b, respectively. Obviously, for both biased voltages, larger piezo-phototronic factor is achieved at lower temperature under all the illumination intensity, with the largest value of 576.2% derived under 2.5×10^{-2} mW/cm^2 illumination at 77 K (Figure 3.23a). These results clearly indicate the significantly enhanced piezo-phototronic effect at low temperatures, and are further confirmed by theoretically calculating the changes of SBH at the reversely biased local Schottky contact for both -4 V and +5 V biased voltages, as shown in Figures 3.23c and 3.23d, respectively. An M-S-M physical model is applied to quantitatively simulate the transport properties of CdS NWs, and the changes of SBH are calculated through a well-developed Matlab based program PKUMSM.[62] As expected, more changes of SBH are obtained at lower temperature for both biased voltages (Figures 3.23c and 3.23d), which further prove the fact that the piezo-phototronic effect is significantly enhanced at low temperature.

3.2.3.2 *a*-Axis GaN Nanobelts[57]

In this work, the temperature dependence of the piezo-phototronic effect is investigated in GaN NBs synthesized along the non-polar *a*-axis orientation. Two independent processes are discovered to form a competing mechanism through the investigation of the temperature dependence of the piezo-phototronic effect in *a*-axis GaN. The corresponding energy band diagrams at both low and room temperatures are carefully analyzed to explain the working mechanism of the piezo-phototronic effect at

different temperatures. This study presents in-depth understandings about the temperature dependence of the piezo-phototronic effect in *a*-axis GaN and provides guidance to their potential applications in high-performances electromechanical/optoelectronic devices.

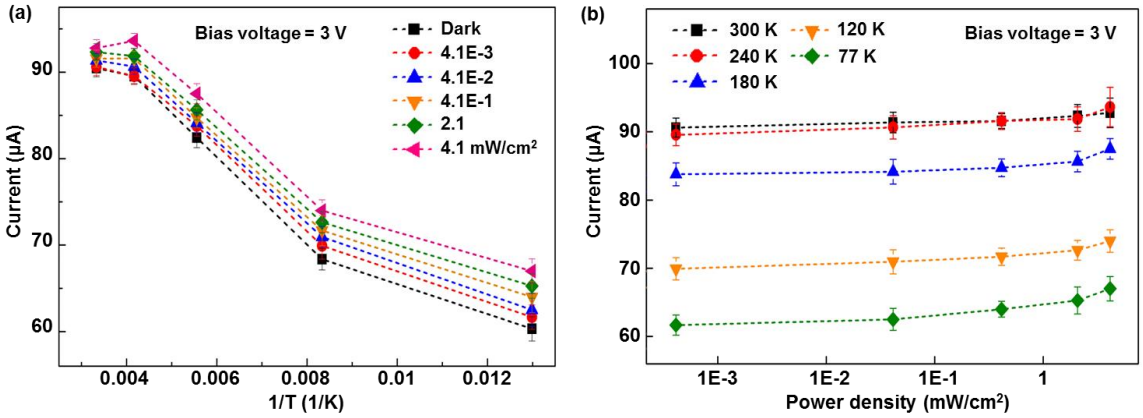

Figure 3.24 Current response of GaN NBs devices. Under strain free condition and a bias voltage of 3 V, (a) the current response of GaN NB devices to various temperatures and (b) illumination intensities.[57]

GaN NBs used in this study is the same as those used in previous section 2.2.4, where detailed materials properties have already been carefully characterized. Under strain-free condition and a bias voltage of 3 V, the current response of the GaN NB devices to various temperatures (illumination intensities) at different illumination intensities (temperatures) are summarized and plotted in Figure 3.24a (3.24b). Higher output currents are observed under stronger illumination intensities at each temperature (Figure 3.24b) since more charge carriers are generated by stronger optical stimuli. Furthermore, under certain illumination intensity, the current response increases drastically with the temperature from 77 K to 240 K as shown in Figure 3.24a due to the gradually release of freeze-out carriers on shallow donor energy states. No significant current increase, however, is observed when the temperature increases from 240 K to 300 K. It is because most of the trapped charge carriers are released at about 200 K[157, 158], as

heating up the system to 300 K, enhanced scattering by the lattice vibration decreases the mobility of free charge carriers[74] and thus reduce the conductivity of the GaN NB devices.

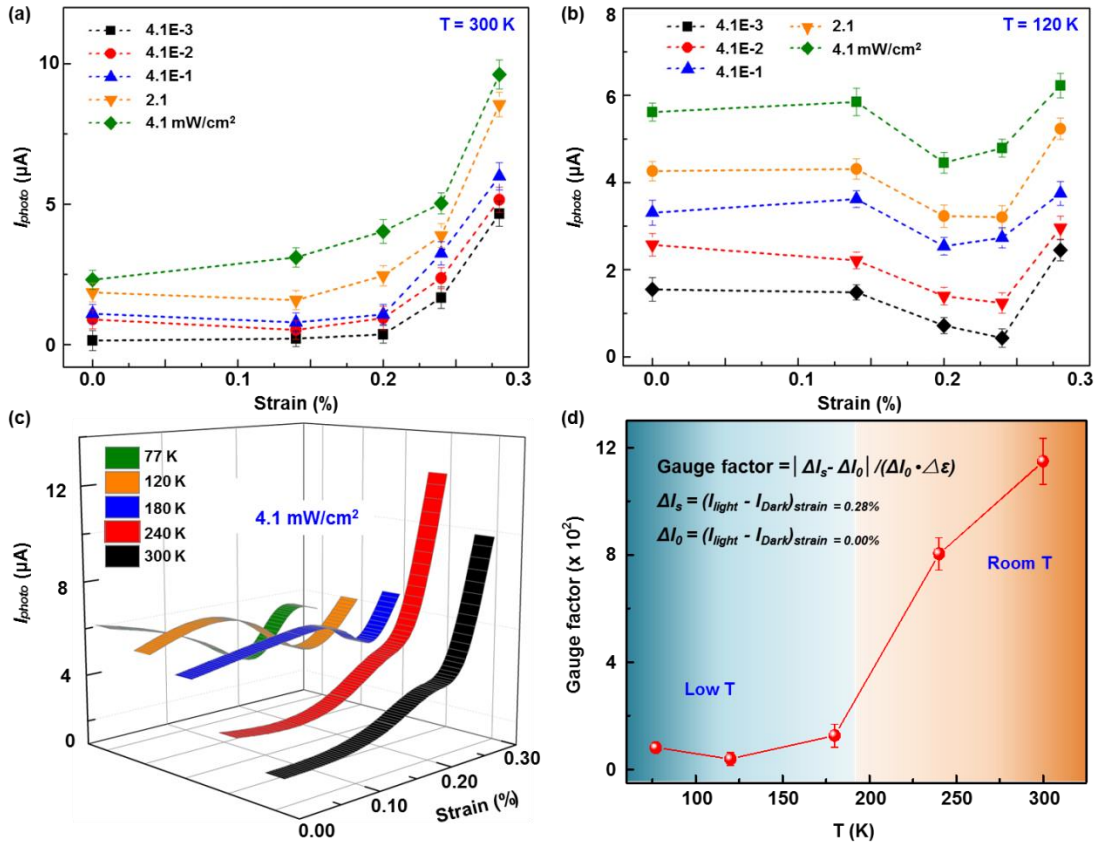

Figure 3.25 Temperature dependence of the piezo-phototronic effect in *a*-axis GaN NB. Photocurrent *vs.* externally applied strains under a series of illumination intensity at (a) 300 K and (b) 120 K. (c) Under the illumination identity of 4.1 mW/cm^2, the photocurrent (I_{photo}= I_{light} –I_{dark}) *vs.* tensile strains at various temperatures. (d) Photocurrent gauge factor as a function of system temperature.[57]

Temperature dependence of the piezo-phototronic effect on the output currents of GaN NB devices is carefully studied under a series of light illuminations and straining conditions from 77 K to 300 K as shown in Figure 3.25. Photocurrents (I_{photo} = I_{light} - I_{dark}) are calculated to evaluate the change of current response to various UV illuminations at 300 K, 240 K, 180 K, 120 K and 77 K. These results clearly show that, at 300 K and 240 K, the photocurrents I_{photo} increase monotonically as increasing the tensile strains,

although there exist fluctuations under weak illuminations and small straining conditions; while at low temperature of 180 K, 120 K and 77 K, I_{photo} decrease as increasing strains at first and then increase with a local minimum observed at a certain straining condition. Under 4.1 mW/cm^2 illumination identity, the photocurrent I_{photo} as a function of tensile strains at various temperatures are summarized and shown in Figure 3.25c. The temperature dependence of the piezo-phototronic effect is quantitatively evaluated by defining a photocurrent gauge factor as the changes of photocurrent per unit strain: $\left|\Delta I_1 - \Delta I_0\right| / (\Delta I_0 \bullet \Delta\varepsilon)$, where ΔI_1 and ΔI_0 correspond to the photocurrent of devices under 0.28% and 0.00% strains, respectively. Figure 3.25d shows that the value of photocurrent gauge factor remains small below 180 K and increases significantly at 240 K and 300 K, with the value at 300 K more than 14 times in magnitude larger than that at 77 K. These results suggest that in the *a*-axis GaN NB devices, the enhancement of photocurrent by the piezo-phototronic effect at room temperature is more significant than that at low temperature. In previous section 3.2.3.1, the temperature dependence of the piezo-phototronic effect in *c*-axis CdS nanowire exhibited an completely opposite trend, in which the piezo-phototronic effect was significantly enhanced as cooling down the temperature from 300 K to 77 K. This novel observation presented here indicates that the physical mechanism of temperature dependence of the piezo-phototronic effect is different in *a*-axis nanostructures compared to that in *c*-axis nanostructures.

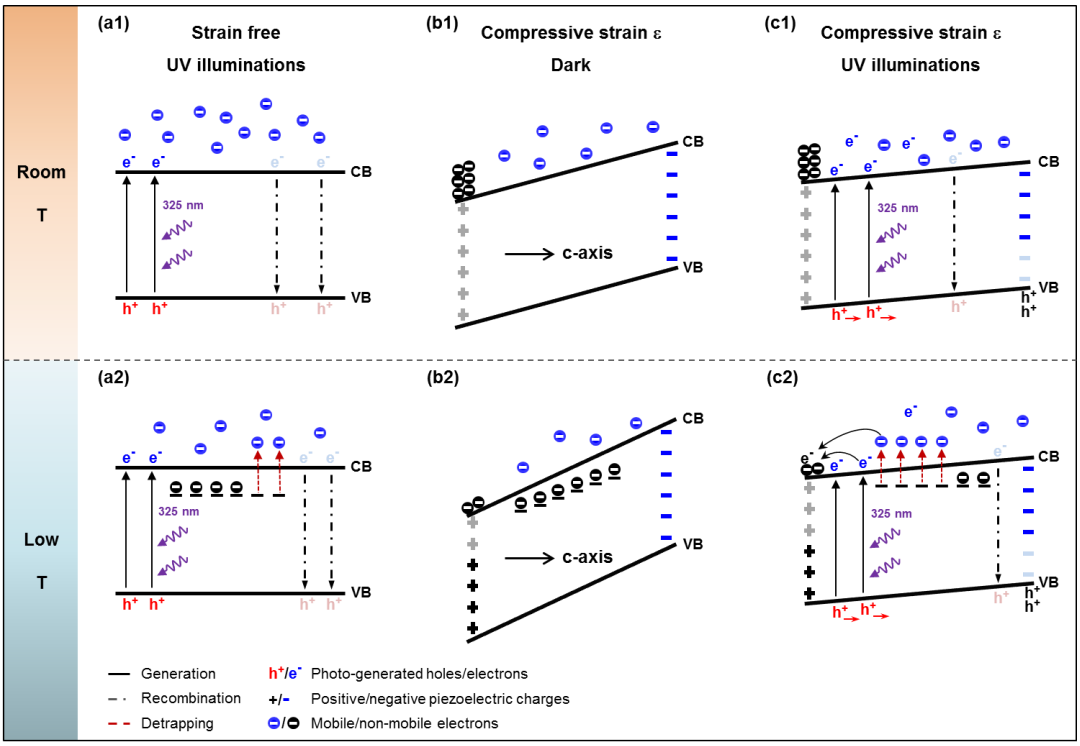

Figure 3.26 Working mechanisms of temperature dependence of the piezo-phototronic effect. At room temperature, the energy band diagram under (a1) strain free condition, (b1, c1) compressive strains along the *c*-axis (b1) in dark, and (c1) UV illuminations. At low temperature, the energy band diagram under (a2) strain free condition, (b2, c2) compressive strains along the *c*-axis (b2) in dark, and (c2) UV illuminations.[57]

Energy band diagrams across the width of GaN NBs along *c*-axis are schematically presented in Figure 3.26 to systematically explain the temperature dependence of the piezo-phototronic effect in *a*-axis GaN. At room temperature, under strain-free condition, both photo-generation and recombination of electron-holes occur normally upon 325 nm UV illumination as shown in Figure 3.26a1. By applying compressive strains along the *c*-axis (*i.e.* tensile strains along the *a*-axis), under dark condition, positive piezo-charges induced at the *–c* plane are screened by local free electrons in GaN, while the negative piezo-charges at *+c* plane are only partially screened and thus tilt the energy band as shown in Figure 3.26b1. Upon UV illuminations (Figure

3.26c1), the photo-generated holes are readily attracted by the negative piezo-charges and the recombination of electron-hole pairs is therefore greatly suppressed. As a result, the unpaired photo-excited electrons drift along *a*-axis direction under the bias voltage and are collected at the anode to contribute to the photocurrent I_{photo}. By increasing the externally applied strains, more photo-generated holes are attracted by increased negative piezo-charges, leaving more unpaired photo-generated electrons to contribute to the I_{photo}. Therefore, the I_{photo} monotonically increase with the external strains at room temperature as experimentally observed in Figures 3.25a and 3.25c.

At low temperature, under strain free condition (Figure 3.26a2), some free electrons are trapped in impurities centers due to the freeze-out effect[159], leading to reduced carrier density and output currents compared to those at room temperature as shown in Figure 3.24a. The activation energy of these impurities is typically 20-30 meV[157], which is much smaller than the energy of the incident 325 nm UV laser. Consequently, the trapped electrons are de-trapped/activated back into conduction band by absorbing the photon energy under UV illuminations (Figure 3.26a2). In this scenario, the photo current I_{photo} consist of both the band gap excitation and the de-trapping/activation of the bounded electrons. In contrast, no defect related de-trapping/activation process exists at room temperature since the vast majority of electrons are inherently ionized[74]. Therefore, under strain free condition, the I_{photo} at low temperature is larger than that at room temperature as shown in Figure 3.25c. By applying compressive strains along the *c*-axis (*i.e.* tensile strains along the *a*-axis), positive and negative piezoelectric polarization charges are induced near $-c$ and $+c$ plane, respectively. At low temperature under dark condition, the positive piezo-charges are

only partially screened due to the decreased density and mobility of free electrons caused by the freeze-out effect, leading to a more significant tilting of energy band than that at room temperature, as shown in Figure 3.26b2. Upon UV illuminations (Figure 3.26c2), two processes form a competition mechanism: (i) Part of the photo-generated electrons and/or free electrons tend to be attracted by the non-completely screened positive piezo-charges near $-c$ plane. This process reduces the photocurrent I_{photo}. (ii) The obviously tilted energy band caused by piezoelectric polarizations makes the donor energy level closer to or into the conduction band; the de-trapping/activation of bounded electrons is thus greatly enhanced under UV illuminations. More de-trapped/activated electrons contribute to the I_{photo} and this process increases the photocurrent I_{photo}. In addition, as increasing the external strains, both process (i) and (ii) are enhanced. The increasing of effective positive polarization charges leads to a more significant tilting energy band. This, in turn, facilitates the trapping of photo-generated electrons and/or free electrons at the positive piezo-charges side. Therefore, a local minimum of I_{photo} is observed with the increasing of strains by considering the competition mechanism between these two processes at low temperature.

Based on the experimental results and the theoretical analysis provided above, it is clear to see that under mechanical strains, the piezo-charges of *a*-axis GaN nanobelt are induced at the polar faces ($+c$ and $-c$ planes) along the *c*-axis direction. The energy band profile, charge carrier distributions and the transport property of *a*-axis GaN are modulated in the whole body of the nanobelt as a volumetric effect. This is fundamentally distinguishable from the piezo-phototronic effects in *c*-axis nanostructures, which are interfacial effects with the piezoelectric polarizations created at the local metal-

semiconductor contact formed near the end faces of the nanostructures to tune/control the carriers transport across the interface.

CHAPTER 4

CONCLUSIONS

In this dissertation, I have presented my major research achievements in the past five years as a PhD student and a graduate research assistant at Georgia Tech. During my doctoral research, I was dedicated to investigating the fundamental physics of the piezotronic and piezo-phototronic effects by understanding the piezoelectric polarization charges modified energy band profiles and charge carrier transport processes both theoretically and experimentally. Temperature dependence of the piezotronic and piezo-phototronic effects is studied to derive insights about the charge carriers' transport process at various ambient temperatures. Following the fundamental working principles of these two effects, several applications have been demonstrated to investigate the piezotronic and piezo-phototronic effects on a wide range of electronic and optoelectronic devices based on the piezoelectric semiconductors, including nanowire/microwire transistors, nanowire logic circuits, bio/chemical sensors and photo detectors. These results indicate the universality of piezotronic and piezo-phototronic effects as effective approaches to modify the physical properties of charge carriers in piezoelectric semiconductors. In this chapter, my research achievements and technological innovations are summarized, and several suggestions on future developments in this field are given for potential researchers who will continue investigations in both piezotronics and piezo-phototronics.

4.1 Piezotronics

The fundamental physics about the piezotronic effect has been carefully studied in this section, followed by several applications of the piezotronic effect to various electronic devices. By applying mechanical strains to M-S-M structured two terminal electronics based on GaN nanobelts[49, 50], the piezotronic effect has been applied to control the carriers' transport processes of NBs transistors through modifying the energy band profiles at local M-S contacts. Besides, the piezotronic effect has also been applied to modify the physical properties of electron gas in AlGaN/AlN/GaN heterostructures as a promising approach to enhance the electric transport properties of high electron mobility transistors (HEMTs). Furthermore, we have applied the piezotronic effect to achieve universal logic operations and simple logic computations in nanowire transistors networks[51] by directly utilizing mechanical signals as inputs to control the electric outputs of strain-gated transistors. By applying strains to Schottky-contacted ZnO NWs sensors, the piezotronic effect has been applied to enhance/optimize the sensing performances of different types of NW sensors, including pH sensors[52], glucose sensors[54], protein sensors[53], gas sensors[56] and humidity sensors[55]. Finally, we presented the fundamental study about the temperature dependence of the piezotronic effect in GaN nanobetls to better understand the physical mechanism of piezo-charges modulation of energy band profiles at various ambient temperatures. Generally, the results indicate that the piezotronic effect is universal to different types of electronics and effective to modify the charge transport processes as long as energy barriers are formed between piezoelectric semiconductors and other materials.

4.2 Piezo-Phototronics

The fundamental physics about the piezo-phototronic effect has been systematically investigated in this section at first; the the temperature dependence of the piezo-phototronic effect in *c*-axis CdS nanowires and *a*-axis GaN nanobetls are studied to better understand the physical mechanism of piezo-charges modulation of energy band profiles at various ambient temperatures in different oriented crystals. The modifications of optoelectronic processes, such as generation, separation, recombination and transportation of photo-induced charge carriers by the piezo-phototronic effect are further explored by applying mechanical strains to various photodetectors based on piezoelectric semiconductors. We have shown that the photo sensing performances of GaN nanobelts PDs[115], p-Si/n-ZnO PDs[116] and optical fiber/NWs hybridized PDs[117] are significantly enhanced by the piezo-phototronic effect following the physical working mechanism described above. Finally, the piezo-phototronic effect has also been applied to achieve light-strain dual gated transistors (LSGTs) based on cascaded CdS NWs networks for logic operations, computations and information processing[118]. We successfully applied both mechanical and optical signals as inputs to control the electric output of LSGTs and realized some complicated logic computing and information processing functions in semiconductor nanowires devices. These results also indicate the universality of the piezo-phototronic effect in modifying the optoelectronic processes in different types of devices and various materials.

4.3 Future Developments

Since the establishment of the field of piezotronics in year 2007 and piezo-phototronics in year 2010, the fundamental physics of these two effects have been carefully studied and a number of applications have been demonstrated to advance this relatively new field during the past few years. However, there are still many open questions remain to be investigated to push this field one step further towards commercialization in the future. A few problems and suggested investigation areas are listed below to assist future research in this field

1. The fundamental understanding of piezoelectric polarizations in micro-scale still needs more investigations. To better understand the basics of these two effects, it is essential to conduct *in-situ* explorations about the formation of piezo-charges and the modulation process of energy states by the piezo-charges.

2. It is of great importance to find a way to dynamically apply mechanical strains to existing electronics/optoelectronics for product-level applications of these two effects. Since all the practical applications of piezotronics and piezo-phototronics so far are based on lab-scale flexible devices, it is significant to demonstrate the feasibility to apply these two effects to commercialized devices dynamically. This could bring the piezotronic and piezo-phototronic effects one step closer to commercialization.

3. Expanding the materials system is urgent. Theoretically, the piezotronic and piezo-phototronic effects are applicable to all piezoelectric semiconductor materials. However, we have only demonstrated these two effects in a few materials, such as ZnO, GaN, CdS, CdSe etc. There are a huge number of materials to be studied to verify the universality of these two effects.

4. There is a great opportunity to study the piezo-phototronic effect on solar cells. Three most-widely used optoelectronics are photodetectors, LEDs and solar cells. As for now, the piezo-phototronic effect on both photodetectors and LEDs has been carefully studied by several researchers. However, reports about the piezo-phototronic effect on solar cells are still limited and incomplete. Therefore, there exists a great opportunity right now to systematically study the piezo-phototronic effect on different types of solar cells.

REFERENCES

[1]. Cui, Y.; Lieber, C. M. Functional nanoscale electronic devices assembled using silicon nanowire building blocks. *Science* **2001,** 291, (5505), 851-853.

[2]. Huang, Y.; Duan, X. F.; Cui, Y.; Lauhon, L. J.; Kim, K. H.; Lieber, C. M. Logic gates and computation from assembled nanowire building blocks. *Science* **2001,** 294, (5545), 1313-1317.

[3]. Sanders, D. Environmental sensors and networks of sensors. *Sensor Rev* **2008,** 28, (4), 273-274.

[4]. Hao, Y.; Foster, R. Wireless body sensor networks for health-monitoring applications. *Physiol Meas* **2008,** 29, (11), R27-R56.

[5]. Kim, D. H.; Ghaffari, R.; Lu, N. S.; Rogers, J. A. Flexible and Stretchable Electronics for Biointegrated Devices. *Annu Rev Biomed Eng* **2012,** 14, 113-128.

[6]. Alivisatos, A. P.; Andrews, A. M.; Boyden, E. S.; Chun, M.; Church, G. M.; Deisseroth, K.; Donoghue, J. P.; Fraser, S. E.; Lippincott-Schwartz, J.; Looger, L. L.; Masmanidis, S.; McEuen, P. L.; Nurmikko, A. V.; Park, H.; Peterka, D. S.; Reid, C.; Roukes, M. L.; Scherer, A.; Schnitzer, M.; Sejnowski, T. J.; Shepard, K. L.; Tsao, D.; Turrigiano, G.; Weiss, P. S.; Xu, C.; Yuste, R.; Zhuang, X. W. Nanotools for Neuroscience and Brain Activity Mapping. *Acs Nano* **2013,** 7, (3), 1850-1866.

[7]. Wang, Z. L. Self-Powered Nanosensors and Nanosystems. *Adv Mater* **2012,** 24, (2), 280-285.

[8]. Wang, Z. L. Toward self-powered sensor networks. *Nano Today* **2010,** 5, (6), 512-514.

[9]. Wang, Z. L.; Wu, W. Z. Nanotechnology-Enabled Energy Harvesting for Self-Powered Micro-/Nanosystems. *Angew Chem Int Edit* **2012,** 51, (47), 11700-11721.

[10]. Ko, H. C.; Stoykovich, M. P.; Song, J. Z.; Malyarchuk, V.; Choi, W. M.; Yu, C. J.; Geddes, J. B.; Xiao, J. L.; Wang, S. D.; Huang, Y. G.; Rogers, J. A. A hemispherical electronic eye camera based on compressible silicon optoelectronics. *Nature* **2008,** 454, (7205), 748-753.

[11]. Tian, B. Z.; Liu, J.; Dvir, T.; Jin, L. H.; Tsui, J. H.; Qing, Q.; Suo, Z. G.; Langer, R.; Kohane, D. S.; Lieber, C. M. Macroporous nanowire nanoelectronic scaffolds for synthetic tissues. *Nat Mater* **2012,** 11, (11), 986-994.

[12]. Wang, C.; Hwang, D.; Yu, Z. B.; Takei, K.; Park, J.; Chen, T.; Ma, B. W.; Javey, A. User-interactive electronic skin for instantaneous pressure visualization. *Nat Mater* **2013,** 12, (10), 899-904.

[13]. Keplinger, C.; Sun, J. Y.; Foo, C. C.; Rothemund, P.; Whitesides, G. M.; Suo, Z. G. Stretchable, Transparent, Ionic Conductors. *Science* **2013,** 341, (6149), 984-987.

[14]. Dvir, T.; Timko, B. P.; Brigham, M. D.; Naik, S. R.; Karajanagi, S. S.; Levy, O.; Jin, H. W.; Parker, K. K.; Langer, R.; Kohane, D. S. Nanowired three-dimensional cardiac patches. *Nat Nanotechnol* **2011,** 6, (11), 720-725.

[15]. Wu, W. Z.; Wen, X. N.; Wang, Z. L. Taxel-Addressable Matrix of Vertical-Nanowire Piezotronic Transistors for Active and Adaptive Tactile Imaging. *Science* **2013,** 340, (6135), 952-957.

[16]. Wang, Z. L. Progress in Piezotronics and Piezo-Phototronics. *Adv Mater* **2012,** 24, (34), 4632-4646.

[17]. G. Gautschi, *Piezoelectric Sensorics: Force, Strain, Pressure, Acceleration and Acoustic Emission Sensors, Materials and Amplifiers*. Springer: Berlin, Heidelberg, 2002.

[18]. Wang, Z. L. Piezopotential gated nanowire devices: Piezotronics and piezo-phototronics. *Nano Today* **2010,** 5, (6), 540-552.

[19]. Zhou, J.; Gu, Y. D.; Fei, P.; Mai, W. J.; Gao, Y. F.; Yang, R. S.; Bao, G.; Wang, Z. L. Flexible piezotronic strain sensor. *Nano letters* **2008,** 8, (9), 3035-3040.

[20]. Wang, Z. L. Piezotronic and Piezophototronic Effects. *J Phys Chem Lett* **2010,** 1, (9), 1388-1393.

[21]. Wu, W. Z.; Wei, Y. G.; Wang, Z. L. Strain-Gated Piezotronic Logic Nanodevices. *Adv Mater* **2010,** 22, (42), 4711-4715.

[22]. Yang, Q.; Guo, X.; Wang, W. H.; Zhang, Y.; Xu, S.; Lien, D. H.; Wang, Z. L. Enhancing Sensitivity of a Single ZnO Micro-/Nanowire Photodetector by Piezo-phototronic Effect. *Acs Nano* **2010,** 4, (10), 6285-6291.

[23]. Wang, Z. L.; Hu, Y. F.; Yang, Q.; Liu, Y. Piezo-phototronic Effect and Its Applications in Flexible Optoelectronic and Energy Technologies. *2011 Ieee Photonics Conference (Pho)* **2011**, 625-625.

[24]. Yang, Q.; Wang, W. H.; Xu, S.; Wang, Z. L. Enhancing Light Emission of ZnO Microwire-Based Diodes by Piezo-Phototronic Effect. *Nano letters* **2011,** 11, (9), 4012-4017.

[25]. Wang, Z. L. Towards Self-Powered Nanosystems: From Nanogenerators to Nanopiezotronics. *Advanced Functional Materials* **2008,** 18, (22), 3553-3567.

[26]. Wang, Z. L.; Yang, R. S.; Zhou, J.; Qin, Y.; Xu, C.; Hu, Y. F.; Xu, S. Lateral nanowire/nanobelt based nanogenerators, piezotronics and piezo-phototronics. *Mat Sci Eng R* **2010,** 70, (3-6), 320-329.

[27]. Wang, Z. L.; Song, J. H. Piezoelectric nanogenerators based on zinc oxide nanowire arrays. *Science* **2006,** 312, (5771), 242-246.

[28]. Zhou, J.; Fei, P.; Gu, Y. D.; Mai, W. J.; Gao, Y. F.; Yang, R.; Bao, G.; Wang, Z. L. Piezoelectric-Potential-Control led Polarity-Reversible Schottky Diodes and Switches of ZnO Wires. *Nano letters* **2008,** 8, (11), 3973-3977.

[29]. Boxberg, F.; Sondergaard, N.; Xu, H. Q. Elastic and Piezoelectric Properties of Zincblende and Wurtzite Crystalline Nanowire Heterostructures. *Adv Mater* **2012,** 24, (34), 4692-4706.

[30]. Boxberg, F.; Sondergaard, N.; Xu, H. Q. Photovoltaics with Piezoelectric Core-Shell Nanowires. *Nano letters* **2010,** 10, (4), 1108-1112.

[31]. Gao, Y.; Wang, Z. L. Electrostatic potential in a bent piezoelectric nanowire. The fundamental theory of nanogenerator and nanopiezotronics. *Nano letters* **2007,** 7, (8), 2499-2505.

[32]. Gao, Z. Y.; Zhou, J.; Gu, Y. D.; Fei, P.; Hao, Y.; Bao, G.; Wang, Z. L. Effects of piezoelectric potential on the transport characteristics of metal-ZnO nanowire-metal field effect transistor. *J Appl Phys* **2009,** 105, (11), 113707.

[33]. Yang, S. Z.; Wang, L. F.; Tian, X. Z.; Xu, Z.; Wang, W. L.; Bai, X. D.; Wang, E. G. The Piezotronic Effect of Zinc Oxide Nanowires Studied by In Situ TEM. *Adv Mater* **2012,** 24, (34), 4676-4682.

[34]. Gao, Y.; Wang, Z. L. Equilibrium Potential of Free Charge Carriers in a Bent Piezoelectric Semiconductive Nanowire. *Nano letters* **2009,** 9, (3), 1103-1110.

[35]. Lu, M. P.; Song, J.; Lu, M. Y.; Chen, M. T.; Gao, Y.; Chen, L. J.; Wang, Z. L. Piezoelectric Nanogenerator Using p-Type ZnO Nanowire Arrays. *Nano letters* **2009,** 9, (3), 1223-1227.

[36]. Schmidt-Mende, L.; MacManus-Driscoll, J. L. ZnO - nanostructures, defects, and devices. *Mater Today* **2007,** 10, (5), 40-48.

[37]. Vetury, R.; Zhang, N. Q. Q.; Keller, S.; Mishra, U. K. The impact of surface states on the DC and RF characteristics of A1GaN/GaN HFETs. *Ieee T Electron Dev* **2001,** 48, (3), 560-566.

[38]. Yuan, G. D.; Zhang, W. J.; Jie, J. S.; Fan, X.; Zapien, J. A.; Leung, Y. H.; Luo, L. B.; Wang, P. F.; Lee, C. S.; Lee, S. T. p-type ZnO nanowire arrays. *Nano letters* **2008,** 8, (8), 2591-2597.

[39]. Wang, F.; Seo, J. H.; Bayerl, D.; Shi, J. A.; Mi, H. Y.; Ma, Z. Q.; Zhao, D. Y.; Shuai, Y. C.; Zhou, W. D.; Wang, X. D. An aqueous solution-based doping strategy for large-scale synthesis of Sb-doped ZnO nanowires. *Nanotechnology* **2011,** 22, (22), 225602.

[40]. Pradel, K. C.; Wu, W. Z.; Zhou, Y. S.; Wen, X. N.; Ding, Y.; Wang, Z. L. Piezotronic Effect in Solution-Grown p-Type ZnO Nanowires and Films. *Nano letters* **2013,** 13, (6), 2647-2653.

[41]. Yankovich, A. B.; Puchala, B.; Wang, F.; Seo, J. H.; Morgan, D.; Wang, X. D.; Ma, Z. Q.; Kvit, A. V.; Voyles, P. M. Stable p-Type Conduction from Sb-Decorated Head-to-Head Basal Plane Inversion Domain Boundaries in ZnO Nanowires. *Nano letters* **2012,** 12, (3), 1311-1316.

[42]. Wang, Z. L. From nanogenerators to piezotronics-A decade-long study of ZnO nanostructures. *Mrs Bull* **2012,** 37, (9), 814-827.

[43]. Wang, Z. L. Preface to the Special Section on Piezotronics. *Adv Mater* **2012,** 24, (34), 4630-4631.

[44]. Tung, R. T. Recent advances in Schottky barrier concepts. *Mat Sci Eng R* **2001,** 35, (1-3), 1-138.

[45]. Brillson, L. J.; Lu, Y. C. ZnO Schottky barriers and Ohmic contacts. *J Appl Phys* **2011,** 109, (12), 121301.

[46]. Rhoderick, E.; Williams, R., *Metal-semiconductor contacts*. 2nd ed.; Clarendon Press: Oxford, 1988.

[47]. Zhang, Y.; Liu, Y.; Wang, Z. L. Fundamental Theory of Piezotronics. *Adv Mater* **2011,** 23, (27), 3004-3013.

[48]. Crowell, C. R.; Sze, S. M. Current Transport in Metal-Semiconductor Barriers. *Solid State Electron* **1966,** 9, (11-1), 1035-1048.

[49]. Yu, R. M.; Dong, L.; Pan, C. F.; Niu, S. M.; Liu, H. F.; Liu, W.; Chua, S.; Chi, D. Z.; Wang, Z. L. Piezotronic Effect on the Transport Properties of GaN Nanobelts for Active Flexible Electronics. *Adv Mater* **2012,** 24, (26), 3532-3537.

[50]. Yu, R. M.; Wang, X. F.; Peng, W. B.; Wu, W. Z.; Ding, Y.; Li, S. T.; Wang, Z. L. Piezotronic Effect in Strain-Gated Transistor of a-Axis GaN Nanobelt. *Acs Nano* **2015,** 9, (10), 9822-9829.

[51]. Yu, R. M.; Wu, W. Z.; Ding, Y.; Wang, Z. L. GaN Nanobelt-Based Strain-Gated Piezotronic Logic Devices and Computation. *Acs Nano* **2013,** 7, (7), 6403-6409.

[52]. Pan, C. F.; Yu, R. M.; Niu, S. M.; Zhu, G.; Wang, Z. L. Piezotronic Effect on the Sensitivity and Signal Level of Schottky Contacted Proactive Micro/Nanowire Nanosensors. *Acs Nano* **2013,** 7, (2), 1803-1810.

[53]. Yu, R. M.; Pan, C. F.; Wang, Z. L. High performance of ZnO nanowire protein sensors enhanced by the piezotronic effect. *Energ Environ Sci* **2013,** 6, (2), 494-499.

[54]. Yu, R. M.; Pan, C. F.; Chen, J.; Zhu, G.; Wang, Z. L. Enhanced Performance of a ZnO Nanowire-Based Self-Powered Glucose Sensor by Piezotronic Effect. *Advanced Functional Materials* **2013,** 23, (47), 5868-5874.

[55]. Hu, G. F.; Zhou, R. R.; Yu, R. M.; Dong, L.; Pan, C. F.; Wang, Z. L. Piezotronic effect enhanced Schottky-contact ZnO micro/nanowire humidity sensors. *Nano Res* **2014,** 7, (7), 1083-1091.

[56]. Zhou, R. R.; Hu, G. F.; Yu, R. M.; Pan, C. F.; Wang, Z. L. Piezotronic effect enhanced detection of flammable/toxic gases by ZnO micro/nanowire sensors. *Nano Energy* **2015,** 12, 588-596.

[57]. Wang, X. F.; Yu, R. M.; Peng, W. B.; Wu, W. Z.; Li, S. T.; Wang, Z. L. Temperature Dependence of the Piezotronic and Piezophototronic Effects in a-axis GaN Nanobelts. *Adv Mater* **2015,** 27, (48), 8067-8074.

[58]. Liu, H. F.; Liu, W.; Chua, S. J.; Chi, D. Z. Fabricating high-quality GaN-based nanobelts by strain-controlled cracking of thin solid films for application in piezotronics. *Nano Energy* **2012,** 1, (2), 316-321.

[59]. Zhang, Z. Y.; Jin, C. H.; Liang, X. L.; Chen, Q.; Peng, L. M. Current-voltage characteristics and parameter retrieval of semiconducting nanowires. *Appl Phys Lett* **2006,** 88, (7), 073102.

[60]. Zhang, Z. Y.; Yao, K.; Liu, Y.; Jin, C. H.; Liang, X. L.; Chen, Q.; Peng, L. M. Quantitative analysis of current-voltage characteristics of semiconducting nanowires: Decoupling of contact effects. *Advanced Functional Materials* **2007,** 17, (14), 2478-2489.

[61]. Freeouf, J. L.; Woodall, J. M. Schottky Barriers - an Effective Work Function Model. *Appl Phys Lett* **1981,** 39, (9), 727-729.

[62]. Liu, Y.; Zhang, Z. Y.; Hu, Y. F.; Jin, C. H.; Peng, L. M. Quantitative fitting of nonlinear current-voltage curves and parameter retrieval of semiconducting nanowire, nanotube and nanoribbon devices. *J Nanosci Nanotechno* **2008,** 8, (1), 252-258.

[63]. Liu, Y.; Kauser, M. Z.; Nathan, M. I.; Ruden, P. P.; Dogan, S.; Morkoc, H.; Park, S. S.; Lee, K. Y. Effects of hydrostatic and uniaxial stress on the Schottky barrier heights of Ga-polarity and N-polarity n-GaN. *Appl. Phys. Lett.* **2004,** 84, (12), 2112-2114.

[64]. Litimein, F.; Bouhafs, B.; Dridi, Z.; Ruterana, P. The electronic structure of wurtzite and zincblende AlN: an ab initio comparative study. *New J Phys* **2002,** 4, 64.

[65]. Li, Y. F.; Yao, B.; Lu, Y. M.; Wei, Z. P.; Gai, Y. Q.; Zheng, C. J.; Zhang, Z. Z.; Li, B. H.; Shen, D. Z.; Fan, X. W.; Tang, Z. K. Realization of p-type conduction in undoped Mg(x)Zn(1-x)O thin films by controlling Mg content. *Appl Phys Lett* **2007,** 91, (23), 232115.

[66]. Lin, R. C.; Ding, L.; Casola, C.; Ripoll, D. R.; Feschotte, C.; Wang, H. Y. Transposase-derived transcription factors regulate light signaling in Arabidopsis. *Science* **2007,** 318, (5854), 1302-1305.

[67]. Liu, Y.; Kauser, M. Z.; Schroepfer, D. D.; Ruden, P. P.; Xie, J.; Moon, Y. T.; Onojima, N.; Morkoc, H.; Son, K. A.; Nathan, M. I. Effect of hydrostatic pressure on the current-voltage characteristics of GaN/AlGaN/GaN heterostructure devices. *J Appl Phys* **2006,** 99, (11), 113706.

[68]. WANG, Z. L. Progress in Piezotronics and Piezo-Phototronics *Adv. Mater.* **2012,** 24, (34), 4632-4646.

[69]. Santhanam, G.; Ryu, S. I.; Yu, B. M.; Afshar, A.; Shenoy, K. V. A high-performance brain-computer interface. *Nature* **2006,** 442, (7099), 195-198.

[70]. Tee, B. C. K.; Wang, C.; Allen, R.; Bao, Z. N. An electrically and mechanically self-healing composite with pressure- and flexion-sensitive properties for electronic skin applications. *Nat Nanotechnol* **2012,** 7, (12), 825-832.

[71]. Kaltenbrunner, M.; Sekitani, T.; Reeder, J.; Yokota, T.; Kuribara, K.; Tokuhara, T.; Drack, M.; Schwodiauer, R.; Graz, I.; Bauer-Gogonea, S.; Bauer, S.; Someya, T. An ultra-lightweight design for imperceptible plastic electronics. *Nature* **2013,** 499, (7459), 458-463.

[72]. Gao, Y.; Wang, Z. L. Equilibrium Potential of Free Charge Carriers in a Bent Piezoelectric Semiconductive Nanowire. *Nano letters* **2009,** 9, (3), 1103-1110.

[73]. Peng, B. Mechanical Characterization of One-dimensional Nanomaterials. Northwestern University, 2008.

[74]. Sze, S. M., *Physics of semiconductor devices*. John Wiley & Sons: New York, 1981.

[75]. Ambacher, O.; Foutz, B.; Smart, J.; Shealy, J. R.; Weimann, N. G.; Chu, K.; Murphy, M.; Sierakowski, A. J.; Schaff, W. J.; Eastman, L. F.; Dimitrov, R.; Mitchell, A.; Stutzmann, M. Two dimensional electron gases induced by spontaneous and piezoelectric polarization in undoped and doped AlGaN/GaN heterostructures. *J Appl Phys* **2000,** 87, (1), 334-344.

[76]. Li, Y.; Xiang, J.; Qian, F.; Gradecak, S.; Wu, Y.; Yan, H.; Yan, H.; Blom, D. A.; Lieber, C. M. Dopant-free GaN/AlN/AlGaN radial nanowire heterostructures as high electron mobility transistors. *Nano letters* **2006,** 6, (7), 1468-1473.

[77]. Vandenbrouck, S.; Madjour, K.; Theron, D.; Dong, Y. J.; Li, Y.; Lieber, C. M.; Gaquiere, C. 12 GHz F-MAX GaN/AlN/AlGaN Nanowire MISFET. *Ieee Electr Device L* **2009,** 30, (4), 322-324.

[78]. Smorchkova, I. P.; Chen, L.; Mates, T.; Shen, L.; Heikman, S.; Moran, B.; Keller, S.; DenBaars, S. P.; Speck, J. S.; Mishra, U. K. AlN/GaN and (Al,Ga)N/AlN/GaN two-dimensional electron gas structures grown by plasma-assisted molecular-beam epitaxy (vol 90, pg 5196, 2001). *J Appl Phys* **2002,** 91, (7), 4780-4780.

[79]. Zhang, Y. F.; Singh, J. Charge control and mobility studies for an AlGaN/GaN high electron mobility transistor. *J Appl Phys* **1999,** 85, (1), 587-594.

[80]. Ambacher, O.; Dimitrov, R.; Stutzmann, M.; Foutz, B.; Murphy, M.; Smart, J.; Shealy, J. R.; Weimann, N. G.; Eastman, L. F. Two-dimensional electron gases induced by spontaneous and piezoelectric polarization in undoped AlGaN/GaN HETS. *Compound Semiconductors 1999* **2000**, (166), 493-497.

[81]. Yu, R. M.; Wang, X. F.; Wu, W. Z.; Pan, C. F.; Bando, Y.; Fukata, N.; Hu, Y. F.; Peng, W. B.; Ding, Y.; Wang, Z. L. Temperature Dependence of the Piezophototronic Effect in CdS Nanowires. *Advanced Functional Materials* **2015,** 25, (33), 5277-5284.

[82]. Lee, S. Y.; Park, K. I.; Huh, C.; Koo, M.; Yoo, H. G.; Kim, S.; Ah, C. S.; Sung, G. Y.; Lee, K. J. Water-resistant flexible GaN LED on a liquid crystal polymer substrate for implantable biomedical applications. *Nano Energy* **2012,** 1, (1), 145-151.

[83]. Zhou, J.; Fei, P.; Gu, Y. D.; Mai, W. J.; Gao, Y. F.; Yang, R.; Bao, G.; Wang, Z. L. Piezoelectric-Potential-Control led Polarity-Reversible Schottky Diodes and Switches of ZnO Wires. *Nano letters* **2008,** 8, (11), 3973-3977.

[84]. Xiang, J.; Lu, W.; Hu, Y. J.; Wu, Y.; Yan, H.; Lieber, C. M. Ge/Si nanowire heterostructures as high-performance field-effect transistors. *Nature* **2006,** 441, (7092), 489-493.

[85]. Wei, T. Y.; Yeh, P. H.; Lu, S. Y.; Lin-Wang, Z. Gigantic Enhancement in Sensitivity Using Schottky Contacted Nanowire Nanosensor. *J Am Chem Soc* **2009,** 131, (48), 17690-17695.

[86]. Xu, S.; Qin, Y.; Xu, C.; Wei, Y. G.; Yang, R. S.; Wang, Z. L. Self-powered nanowire devices. *Nat Nanotechnol* **2010,** 5, (5), 366-373.

[87]. Yang, R. S.; Qin, Y.; Dai, L. M.; Wang, Z. L. Power generation with laterally packaged piezoelectric fine wires. *Nat Nanotechnol* **2009,** 4, (1), 34-39.

[88]. Han, X. D.; Zheng, K.; Zhang, Y. F.; Zhang, X. N.; Zhang, Z.; Wang, Z. L. Low-temperature in situ large-strain plasticity of silicon nanowires. *Adv Mater* **2007,** 19, (16), 2112-2118.

[89]. Pan, Z. W.; Dai, Z. R.; Wang, Z. L. Nanobelts of semiconducting oxides. *Science* **2001,** 291, (5510), 1947-1949.

[90]. Eichenfield, M.; Chan, J.; Camacho, R. M.; Vahala, K. J.; Painter, O. Optomechanical crystals. *Nature* **2009,** 462, (7269), 78-82.

[91]. Sung, Y. M.; Noh, K.; Kwak, W. C.; Kim, T. G. Enhanced glucose detection using enzyme-immobilized ZnO/ZnS core/sheath nanowires. *Sensor Actuat B-Chem* **2012,** 161, (1), 453-459.

[92]. Zhou, J.; Gu, Y. D.; Fei, P.; Mai, W. J.; Gao, Y. F.; Yang, R. S.; Bao, G.; Wang, Z. L. Flexible piezotronic strain sensor. *Nano letters* **2008,** 8, (9), 3035-3040.

[93]. Mao, S.; Lu, G. H.; Yu, K. H.; Bo, Z.; Chen, J. H. Specific Protein Detection Using Thermally Reduced Graphene Oxide Sheet Decorated with Gold Nanoparticle-Antibody Conjugates. *Adv Mater* **2010,** 22, (32), 3521-3526.

[94]. Chen, J. X.; Ding, L. W.; Zhang, X. H.; Chu, L.; Liu, N. S.; Gao, Y. H. Strain-enhanced cable-type 3D UV photodetecting of ZnO nanowires on a Ni wire by coupling of piezotronics effect and pn junction. *Opt Express* **2014,** 22, (3), 3661-3668.

[95]. Pan, C. F.; Li, Z. T.; Guo, W. X.; Zhu, J.; Wang, Z. L. Fiber-Based Hybrid Nanogenerators for/as Self-Powered Systems in Biological Liquid. *Angew Chem Int Edit* **2011,** 50, (47), 11192-11196.

[96]. Fryberger, T. B.; Semancik, S. CONDUCTANCE RESPONSE OF PD/SNO2 (110) MODEL GAS SENSORS TO H2 AND O2. *Sensors and Actuators B-Chemical* **1990,** 2, (4), 305-309.

[97]. Kolmakov, A.; Klenov, D. O.; Lilach, Y.; Stemmer, S.; Moskovits, M. Enhanced gas sensing by individual SnO2 nanowires and nanobelts functionalized with Pd catalyst particles. *Nano Letters* **2005,** 5, (4), 667-673.

[98]. Chen, M.; Wang, Z.; Han, D.; Gu, F.; Guo, G. Porous ZnO Polygonal Nanoflakes: Synthesis, Use in High-Sensitivity NO2 Gas Sensor, and Proposed Mechanism of Gas Sensing. *The Journal of Physical Chemistry C* **2011,** 115, (26), 12763-12773.

[99]. Yang, R.; Qin, Y.; Dai, L.; Wang, Z. L. Power generation with laterally packaged piezoelectric fine wires. *Nat. Nanotechnol.* **2009,** 4, (1), 34-9.

[100]. Janotti, A.; Van de Walle, C. G. Oxygen vacancies in ZnO. *Appl. Phys. Lett.* **2005,** 87, (12), 122102.

[101]. Schaub, R.; Thostrup, P.; Lopez, N.; Lægsgaard, E.; Stensgaard, I.; Nørskov, J. K.; Besenbacher, F. Oxygen Vacancies as Active Sites for Water Dissociation on Rutile TiO_ [1](110). *Physical Review Letters* **2001,** 87, (26), 266104.

[102]. Wang, Z. L. Piezotronic and piezophototronic effects. *The Journal of Physical Chemistry Letters* **2010,** 1, (9), 1388-1393.

[103]. Zhou, J.; Fei, P.; Gu, Y.; Mai, W.; Gao, Y.; Yang, R.; Bao, G.; Wang, Z. L. Piezoelectric-potential-controlled polarity-reversible Schottky diodes and switches of ZnO wires. *Nano Lett.* **2008,** 8, (11), 3973-3977.

[104]. Geissler, P. L.; Dellago, C.; Chandler, D.; Hutter, J.; Parrinello, M. Autoionization in liquid water. *Science* **2001,** 291, (5511), 2121-2124.

[105]. Dulub, O.; Meyer, B.; Diebold, U. Observation of the dynamical change in a water monolayer adsorbed on a ZnO surface. *Phys. Rev. Lett.* **2005,** 95, (13), 136101.

[106]. Du, Y.; Deskins, N. A.; Zhang, Z.; Dohnalek, Z.; Dupuis, M.; Lyubinetsky, I. Two Pathways for Water Interaction with Oxygen Adatoms on TiO2(110). *Phys. Rev. Lett.* **2009,** 102, (9), 096102.

[107]. Liu, Y.; Zhang, Z. Y.; Hu, Y. F.; Jin, C. H.; Peng, L. M. Quantitative Fitting of Nonlinear Current–Voltage Curves and Parameter Retrieval of Semiconducting Nanowire, Nanotube and Nanoribbon Devices. *J Nanosci. Nanotechno.* **2008,** 8, (1), 252-258.

[108]. Wang, X. F.; Tong, J. H.; Chen, X.; Zhao, B. J.; Ren, Z. W.; Li, D. W.; Zhuo, X. J.; Zhang, J.; Yi, H. X.; Liu, C.; Fang, F.; Li, S. T. Highly ordered GaN-based nanowire arrays grown on patterned (100) silicon and their optical properties. *Chem Commun* **2014,** 50, (6), 682-684.

[109]. Hu, Y. F.; Klein, B. D. B.; Su, Y. J.; Niu, S. M.; Liu, Y.; Wang, Z. L. Temperature Dependence of the Piezotronic Effect in ZnO Nanowires. *Nano letters* **2013,** 13, (11), 5026-5032.

[110]. Pan, C. F.; Dong, L.; Zhu, G.; Niu, S. M.; Yu, R. M.; Yang, Q.; Liu, Y.; Wang, Z. L. High-Resolution Electroluminescent Imaging of Pressure Distribution Using a Piezoelectric Nanowire LED Array. *Nat Photonics* **2013,** 7, (9), 752-758.

[111]. Zhang, Y.; Yang, Y.; Wang, Z. L. Piezo-phototronics effect on nano/microwire solar cells. *Energ Environ Sci* **2012,** 5, (5), 6850-6856.

[112]. Pan, C. F.; Niu, S. M.; Ding, Y.; Dong, L.; Yu, R. M.; Liu, Y.; Zhu, G.; Wang, Z. L. Enhanced Cu2S/CdS Coaxial Nanowire Solar Cells by Piezo-Phototronic Effect. *Nano letters* **2012,** 12, (6), 3302-3307.

[113]. Muller, R.; Kamins, T.; Chan, M., *Device electronics for integrated circuits*. 3rd ed.; Wiley: Hoboken, NJ, 2002.

[114]. Sze, S., *Physics of semiconductor devices*. 2nd ed.; Wiley: New York, 1981.

[115]. Yu, R. M.; Pan, C. F.; Hu, Y. F.; Li, L.; Liu, H. F.; Liu, W.; Chua, S.; Chi, D. Z.; Wang, Z. L. Enhanced performance of GaN nanobelt-based photodetectors by means of piezotronic effects. *Nano Res* **2013,** 6, (10), 758-766.

[116]. Wang, Z. N.; Yu, R. M.; Wen, X. N.; Liu, Y.; Pan, C. F.; Wu, W. Z.; Wang, Z. L. Optimizing Performance of Silicon-Based p-n junction Photodetectors by the Piezo-Phototronic Effect. *Acs Nano* **2014,** 8, (12), 12866-12873.

[117]. Wang, Z. N.; Yu, R. M.; Pan, C. F.; Liu, Y.; Ding, Y.; Wang, Z. L. Piezo-Phototronic UV/Visible Photosensing with Optical-Fiber-Nanowire Hybridized Structures. *Adv Mater* **2015,** 27, (9), 1553-1560.

[118]. Yu, R. M.; Wu, W. Z.; Pan, C. F.; Wang, Z. N.; Ding, Y.; Wang, Z. L. Piezo-phototronic Boolean Logic and Computation Using Photon and Strain Dual-Gated Nanowire Transistors. *Adv Mater* **2015,** 27, (5), 940-947.

[119]. Yang, Y.; Zhang, H. L.; Chen, J.; Lee, S. M.; Hou, T. C.; Wang, Z. L. Simultaneously Harvesting Mechanical and Chemical Energies by a Hybrid Cell for Self-Powered Biosensors and Personal Electronics. *Energ Environ Sci* **2013,** 6, (6), 1744-1749.

[120]. Zhang, F.; Niu, S. M.; Guo, W. X.; Zhu, G.; Liu, Y.; Zhang, X. L.; Wang, Z. L. Piezo-Phototronic Effect Enhanced Visible/UV Photodetector of a Carbon-Fiber/ZnO-CdS Double-Shell Microwire. *Acs Nano* **2013,** 7, (5), 4537-4544.

[121]. Liu, Y.; Das, A.; Xu, S.; Lin, Z. Y.; Xu, C.; Wang, Z. L.; Rohatgi, A.; Wong, C. P. Hybridizing ZnO Nanowires with Micropyramid Silicon Wafers as Superhydrophobic High-Efficiency Solar Cells. *Adv Energy Mater* **2012,** 2, (1), 47-51.

[122]. Dutta, M.; Basak, D. P-ZnO/n-Si Heterojunction: Sol-gel Fabrication, Photoresponse Properties, and Transport Mechanism. *Appl Phys Lett* **2008,** 92, (21), 212112.

[123]. Liu, Y.; Niu, S.; Yang, Q.; Klein, B. D.; Zhou, Y. S.; Wang, Z. L. Theoretical Study of Piezo-Phototronic Nano-LEDs. *Adv Mater* **2014,** 26, (42), 7209-7216.

[124]. Sze, S. M. Physics of Semiconductor-Devices. *Cc/Eng Tech Appl Sci* **1982**, (27), 28-28.

[125]. Aranovich, J. A.; Golmayo, D.; Fahrenbruch, A. L.; Bube, R. H. Photo-Voltaic Properties of Zno-Cdte Heterojunctions Prepared by Spray Pyrolysis. *J Appl Phys* **1980,** 51, (8), 4260-4268.

[126]. Konstantatos, G.; Sargent, E. H. Nanostructured Materials for Photon Detection. *Nat Nanotechnol* **2010,** 5, (12), 391-400.

[127]. Kasap, S. O. Optoelectronics and Photonics: Principles and Practices[M]. *New Jersey: Prentice Hall* **2001,** 37.

[128]. Sun, K.; Jing, Y.; Park, N.; Li, C.; Bando, Y.; Wang, D. L. Solution Synthesis of Large-Scale, High-Sensitivity ZnO/Si Hierarchical Nanoheterostructure Photodetectors. *Journal Of The American Chemical Society* **2010,** 132, (44), 15465-15467.

[129]. Manna, S.; Das, S.; Mondal, S. P.; Singha, R.; Ray, S. K. High Efficiency Si/CdS Radial Nanowire Heterojunction Photodetectors Using Etched Si Nanowire Templates. *J Phys Chem C* **2012,** 116, (12), 7126-7133.

[130]. Hu, Y. F.; Zhang, Y.; Xu, C.; Lin, L.; Snyder, R. L.; Wang, Z. L. Self-Powered System with Wireless Data Transmission. *Nano Lett* **2011,** 11, (6), 2572-2577.

[131]. Xu, Y.; Schoonen, M. A. A. The absolute energy positions of conduction and valence bands of selected semiconducting minerals. *Am Mineral* **2000,** 85, (3-4), 543-556.

[132]. Soci, C.; Zhang, A.; Xiang, B.; Dayeh, S. A.; Aplin, D. P. R.; Park, J.; Bao, X. Y.; Lo, Y. H.; Wang, D. ZnO nanowire UV photodetectors with high internal gain. *Nano letters* **2007,** 7, (4), 1003-1009.

[133]. Ni, P. N.; Shan, C. X.; Wang, S. P.; Liu, X. Y.; Shen, D. Z. Self-powered spectrum-selective photodetectors fabricated from n-ZnO/p-NiO core-shell nanowire arrays. *J Mater Chem C* **2013,** 1, (29), 4445-4449.

[134]. Yadav, H. K.; Sreenivas, K.; Gupta, V. Persistent photoconductivity due to trapping of induced charges in Sn/ZnO thin film based UV photodetector. *Appl Phys Lett* **2010,** 96, (22), 223507.

[135]. Zhou, J.; Gu, Y.; Hu, Y.; Mai, W.; Yeh, P. H.; Bao, G.; Sood, A. K.; Polla, D. L.; Wang, Z. L. Gigantic enhancement in response and reset time of ZnO UV nanosensor by utilizing Schottky contact and surface functionalization. *Appl Phys Lett* **2009,** 94, (19), 191103.

[136]. Monroy, E.; Omnes, F.; Calle, F. Wide-bandgap semiconductor ultraviolet photodetectors. *Semicond Sci Tech* **2003,** 18, (4), R33-R51.

[137]. Zou, J. P.; Zhang, Q.; Huang, K.; Marzari, N. Ultraviolet Photodetectors Based on Anodic TiO2 Nanotube Arrays. *J Phys Chem C* **2010,** 114, (24), 10725-10729.

[138]. Konstantatos, G.; Howard, I.; Fischer, A.; Hoogland, S.; Clifford, J.; Klem, E.; Levina, L.; Sargent, E. H. Ultrasensitive solution-cast quantum dot photodetectors. *Nature* **2006,** 442, (7099), 180-183.

[139]. Sargent, E. H. Solar Cells, Photodetectors, and Optical Sources from Infrared Colloidal Quantum Dots. *Adv Mater* **2008,** 20, (20), 3958-3964.

[140]. McDonald, S. A.; Konstantatos, G.; Zhang, S. G.; Cyr, P. W.; Klem, E. J. D.; Levina, L.; Sargent, E. H. Solution-processed PbS quantum dot infrared photodetectors and photovoltaics. *Nat Mater* **2005,** 4, (2), 138-142.

[141]. Sarasqueta, G.; Choudhury, K. R.; So, F. Effect of Solvent Treatment on Solution-Processed Colloidal PbSe Nanocrystal Infrared Photodetectors. *Chem Mater* **2010,** 22, (11), 3496-3501.

[142]. Sarasqueta, G.; Choudhury, K. R.; Subbiah, J.; So, F. Organic and Inorganic Blocking Layers for Solution-Processed Colloidal PbSe Nanocrystal Infrared Photodetectors. *Adv Funct Mater* **2011,** 21, (1), 167-171.

[143]. Chen, M. W.; Retamal, J. R. D.; Chen, C. Y.; He, J. H. Photocarrier Relaxation Behavior of a Single ZnO Nanowire UV Photodetector: Effect of Surface Band Bending. *Ieee Electr Device L* **2012,** 33, (3), 411-413.

[144]. Liu, C.; Zhang, B. P.; Lu, Z. W.; Binh, N. T.; Wakatsuki, K.; Segawa, Y.; Mu, R. Fabrication and characterization of ZnO film based UV photodetector. *J Mater Sci-Mater El* **2009,** 20, (3), 197-201.

[145]. Gu, F. X.; Yang, Z. Y.; Yu, H. K.; Xu, J. Y.; Wang, P.; Tong, L. M.; Pan, A. L. Spatial Bandgap Engineering along Single Alloy Nanowires. *J. Am. Chem. Soc.* **2011,** 133, (7), 2037-2039.

[146]. Lin, Y. F.; Song, J.; Ding, Y.; Lu, S. Y.; Wang, Z. L. Alternating the output of a CdS nanowire nanogenerator by a white-light-stimulated optoelectronic effect. *Adv. Mater.* **2008,** 20, (16), 3127-3130.

[147]. Li, Q. G.; Penner, R. M. Photoconductive cadmium sulfide hemicylindrical shell nanowire ensembles. *Nano Lett.* **2005,** 5, (9), 1720-1725.

[148]. Soole, J. B. D.; Schumacher, H. Ingaas Metal-Semiconductor-Metal Photodetectors for Long Wavelength Optical Communications. *IEEE J. Quantum Electron.* **1991,** 27, (3), 737-752.

[149]. Rhoderick, E. H.; Williams, R. H., *Metal-semiconductor contacts*. 2nd ed.; Clarendon Press New York, 1988; p xiii, 252 p.

[150]. Wu, W. Z.; Wang, Z. L. Piezotronic Nanowire-Based Resistive Switches As Programmable Electromechanical Memories. *Nano letters* **2011,** 11, (7), 2779-2785.

[151]. Allen, P. E.; Holberg, D. R., *CMOS analog circuit design*. 3rd ed.; Oxford University Press, USA: New York ; Oxford, 2012; p xvi, 757 p.

[152]. Muller, R. S.; Kamins, T. I.; Chan, M., *Device electronics for integrated circuits*. 3rd ed.; John Wiley & Sons, Inc.: New York, NY, 2003; p xviii, 528 p.

[153]. Bachtold, A.; Hadley, P.; Nakanishi, T.; Dekker, C. Logic circuits with carbon nanotube transistors. *Science* **2001,** 294, (5545), 1317-1320.

[154]. Javey, A.; Kim, H.; Brink, M.; Wang, Q.; Ural, A.; Guo, J.; McIntyre, P.; McEuen, P.; Lundstrom, M.; Dai, H. J. High-kappa dielectrics for advanced carbon-nanotube transistors and logic gates. *Nat. Mater.* **2002,** 1, (4), 241-246.

[155]. Lin, Y. M.; Valdes-Garcia, A.; Han, S. J.; Farmer, D. B.; Meric, I.; Sun, Y. N.; Wu, Y. Q.; Dimitrakopoulos, C.; Grill, A.; Avouris, P.; Jenkins, K. A. Wafer-Scale Graphene Integrated Circuit. *Science* **2011,** 332, (6035), 1294-1297.

[156]. Hecht, M. H. Role of Photocurrent in Low-Temperature Photoemission-Studies of Schottky-Barrier Formation. *Phys Rev B* **1990,** 41, (11), 7918-7921.

[157]. Molnar, R. J.; Lei, T.; Moustakas, T. D. Electron-Transport Mechanism in Gallium Nitride. *Appl Phys Lett* **1993,** 62, (1), 72-74.

[158]. Anwar, A. F. M.; Wu, S. L.; Webster, R. T. Temperature dependent transport properties in GaN, A1(x)Ga(1-x)N, and InxGa1-xN semiconductors. *Ieee T Electron Dev* **2001,** 48, (3), 567-572.

[159]. Slack, G. A.; Schowalter, L. J.; Morelli, D.; Freitas, J. A. Some effects of oxygen impurities on AlN and GaN. *J Cryst Growth* **2002,** 246, (3-4), 287-298.

VITA

RUOMENG YU

RUOMENG YU was born in Qinhuangdao, Hebei, P. R. China. He attended Huzhong University of Science and Technology, Wuhan, P. R. China in 2006 and received a B.S. in Applied Physics in 2010. He then came to Georgia Institute of Technology to pursue a M.S. in Physics and a PhD in Materials Science and Engineering under the supervision of Prof. Zhong Lin Wang. Ruomeng Yu's research interests include functional electronic and optoelectronic devices based on semiconductors for piezotrnoics and piezo-phototronics. When he is not working, Ruomeng enjoys playing basketball and traveling.